This electronic thesis or dissertation has been downloaded from Explore Bristol Research, http://research-information.bristol.ac.uk

Author:
Cheng, Jingwei

Title:
Nonlinear Ultrasonic Imaging Techniques for Non-Destructive Testing

General rights
Access to the thesis is subject to the Creative Commons Attribution - NonCommercial-No Derivatives 4.0 International Public License. A copy of this may be found at https://creativecommons.org/licenses/by-nc-nd/4.0/legalcode This license sets out your rights and the restrictions that apply to your access to the thesis so it is important you read this before proceeding.

Take down policy
Some pages of this thesis may have been removed for copyright restrictions prior to having it been deposited in Explore Bristol Research. However, if you have discovered material within the thesis that you consider to be unlawful e.g. breaches of copyright (either yours or that of a third party) or any other law, including but not limited to those relating to patent, trademark, confidentiality, data protection, obscenity, defamation, libel, then please contact collections-metadata@bristol.ac.uk and include the following information in your message:

- Your contact details
- Bibliographic details for the item, including a URL
- An outline nature of the complaint

Your claim will be investigated and, where appropriate, the item in question will be removed from public view as soon as possible.

Nonlinear Ultrasonic Imaging Techniques for Non-Destructive Testing

by

Jingwei Cheng

Department of Mechanical Engineering

A dissertation submitted to the University of Bristol in accordance with the requirements for award of the degree of the Doctor of Philosophy in the Faculty of Engineering in October 2018.

Word count: 40227

Abstract

Nonlinear imaging techniques have recently emerged which have the potential to detect cracks at a much earlier stage than was previously possible. This thesis describes a group of novel nonlinear phased array imaging techniques for non-destructive testing. In contrast to conventional nonlinear techniques, these techniques have the potential to reliably image tightly closed cracks and quantify their nonlinearities without bespoke and complicated setups. The underlying engineering science, the experimental procedure and the fundamental findings for each technique are discussed.

The nonlinear ultrasonic diffuse energy imaging (NUI) technique was recently proposed to allow nonlinearity to be isolated and located in an image. Its performance for monitoring fatigue crack growth is first investigated. The results suggest that NUI is more sensitive than conventional ultrasonic imaging to the microscale changes occurring at the early stages of failure. The potential for NUI to deliver accurate sizing of fatigue cracks is also demonstrated. In addition, an investigation into the performance of NUI by optimising the key parameters with the proposed methodology is presented. The results suggest that the performance of NUI significantly depends on the parameters and the adaptive optimisation methods can be used to select the optimum parameters and expand the applications of NUI for different structures and materials.

A family of nonlinear coherent imaging (NCI) techniques are explored and developed based on the coherently scattered amplitude subtraction at the fundamental or subharmonic frequency of two focusing modes. The novel nonlinear phenomena in the form of phase change or amplitude loss are investigated and exploited to yield two separate NCI metrics (phase and amplitude). The NCI methods using pulse-echo and pitch-catch configurations are then examined on a broad range of fatigue cracks grown in multiple samples. The results suggest that the NCI techniques, in conjunction with the proposed noise compensation approach, significantly enhance selectivity, sensitivity and practicality of crack detection and characterisation.

Dedication and Acknowledgements

I would like to express my sincere gratitude to my project supervisor Prof. Bruce Drinkwater and Dr. Jack Potter, for their precious guidance and comprehensive support throughout the duration of my PhD study. In addition, I would like to thank Prof. Anthony Croxford for his contribution to this research project.

I would like to thank Mr. Guy Pearn, Mr. Peter Whereat and Mr. Stephen Iles for their support and expertise on the fabrication of the specimens and the setup of the experimental rigs.

Great thanks also to my supervisor Prof. Bruce Drinkwater for providing the financial support from UNDT scholarship.

Last but not the least, I would like to express my great appreciation to my parents for their financial support and encouragement during my study in Bristol. Also thank my fiancée Qiujie and all my friends for their encouragement and help.

Author's Declaration

I declare that the work in this dissertation was carried out in accordance with the requirements of the University's *Regulations and Code of Practice for Research Degree Programmes* and that it has not been submitted for any other academic award. Except where indicated by specific reference in the text, the work is the candidate's own work. Work done in collaboration with, or with the assistance of, others, is indicated as such. Any views expressed in the dissertation are those of the author.

SIGNED: .... **DATE:..........................**

Table of Contents

List of Figures

List of Tables

List of Symbols

t: time of wave propagation
$f_{n,m}(t)$: time-domain received signals for each combination of transmitter (n) and receiver (m) elements in the full matrix capture
r: location of a pixel in the x-z image plane
$I(x, z)$: intensity of the total focusing image at any point in the x-z image plane
$h_{n,m}$: complex Hilbert transform of time-domain received signals
ρ: density of a material
u: particle displacement
σ_{xx}: uniaxial stress in direction of x coordinate
σ_0: initial static stress
v: Poisson’s ratio
E_1: second order of elastic constant (i.e. Young’s modulus of the material)
E_2: third order of elastic constant
E_3: fourth order of elastic constant
c: longitudinal wave velocity in the material
β: acoustic nonlinearity parameter
A_0: first Landau-Lifshitz third order elastic constant
B_0: second Landau-Lifshitz third order elastic constant
C_0: third Landau-Lifshitz third order elastic constant
l: first Murnaghan constant
m: second Murnaghan constant
n: third Murnaghan constants
H: Heaviside unit step function
ε_0: initial static strain at the interface
σ: applied stress
ε: strain
A_1: amplitude of the first harmonic wave
ω: radial frequency

f: frequency

k: wave number

A_2: amplitude of the second harmonic wave

k_1: wave vector of the first incident wave

k_2: wave vector of the second incident wave

f_1: incident frequency of the first transmitter

f_2: incident frequency of the second transmitters

q: ratio of longitudinal and shear velocities

ϕ: relative angle of two transmitters

A: amplitude of wave

δ_n^T: transmission delay applied to the n^{th} element to achieve a focus

$g_m(t)$: time-domain signal received on element m for the parallel transmission

γ: nonlinear metric used in nonlinear ultrasonic diffuse energy imaging

K_{max}: maximum stress intensity factor

K_{IC}: nominal fracture toughness of material

K_{min}: minimum stress intensity factor

R: stress ratio of the minimum and maximum load

P_{min}: minimum load

P_{max}: maximum load

ΔK: stress intensity factor range

a: distance from load bearing point to the notch or the crack tip of a compact tension specimen

W: width of a compact tension specimen

α: ratio of the distance from the load bearing point to the notch or crack tip and the width of a compact tension specimen

B: thickness of a compact tension specimen

t_r: gate start time

T: window length

N: number of elements (i.e. number of firings)

ϵ: a proportion of noise to the acoustic energy of a single sequential response

η_{area}: metric for evaluating variations in energy area of windowed signals

η_{max}: metric for evaluating variations in maximum energy

N_n: the number pf transmit (n) elements

N_n: the number pf transmit (n) elements

$f_{n,m}^{max}$: maximum amplitude in each window of full matrix capture signals

n: number of component waveforms

η_{phase}: metric for evaluating the degree of phase coherence between two signals

$f_{n,m}^{F}(t)$: finite element simulated signals in time-domain for each combination of transmitter (n) and receiver (m) elements

$f_{n,m}^{W}(t)$: received white noise in time-domain for each combination of transmitter (n) and receiver (m) elements

o_1: first amplitude factor for calculating decay rate

o_2: second amplitude factor for calculating decay rate

b: first decay coefficient

d: second decay coefficient

$y_{n,m}(t)$: two-term exponential model of time-domain signal for each combination of transmitter (n) and receiver (m) elements

$\hat{f}_{n,m}^{W}(t)$: decayed white noise in time-domain for each combination of transmitter (n) and receiver (m) elements

x_a is the position of reference element in x-axis for the transmission delay law

x_b is the position of reference element in x-axis for the reception delay law

$F_{n,m}(\omega)$: received signals in frequency domain for each combination of transmitter (n) and receiver (m) elements in the full matrix capture

$G_m(\omega)$: received signals in frequency domain on element m for the parallel transmission

δ_m^R: reception delay applied to the m^{th} element to achieve the focus

ω_0: nominal centre frequency of the array probe at reception

A_s: received time series in the sequential focusing case

A_p: received time series in the parallel focusing case

t_f: focal time

$\delta_A(\omega)$: amplitude ratio in frequency domain between sequential and parallel focusing

$\delta_\varphi(\omega)$: relative phase in frequency domain between sequential and parallel focusing

I_s: complex amplitude of the focal point in the sequential case

I_p: complex amplitude of the focal point in the parallel case

ζ: nonlinear amplitude metric of nonlinear coherent imaging

$\hat{\delta}_A$: baseline of amplitude ratio from linear points between sequential and parallel focusing

$\hat{\delta}_\varphi$: baseline of relative phase from linear points between sequential and parallel focusing

$\hat{A}_s$: corrected time series in the sequential focusing case with amplitude and phase compensation

$\hat{I}_s$: corrected complex amplitude in time domain of the focal point in the sequential case

$\hat{\zeta}$: corrected nonlinear amplitude metric $\hat{\zeta}$ of nonlinear coherent imaging

φ_s: phase component of complex amplitude at every pixel in sequential case

φ_p: phase component of complex amplitude at every pixel in parallel case

ζ_φ: nonlinear phase metric of nonlinear coherent imaging

$\tilde{A}_s$: corrected time series in the sequential focusing case with phase compensation

$\tilde{\zeta}_\varphi$: corrected nonlinear phase metric

List of Abbreviations

AE: acoustic emission

AM: amplitude modulation

CAN: contact acoustic nonlinearity

CT: compact tension

dB: decibel

EDM: electrical discharge machining

FAD: fundamental wave amplitude difference

FE: finite element

FMC: full matrix capture

MUSIC: multiple signal classification

NCI: nonlinear coherent imaging

NDT: non-destructive testing

NEWS: nonlinear elastic wave spectroscopy

NRUS: nonlinear resonant ultrasound spectroscopy

NUI: nonlinear ultrasonic diffuse energy imaging

NWMS: nonlinear wave modulation spectroscopy

PI: phase inversion

PIAM: combination of phase inversion and amplitude modulation

RMS: root mean square

SBC: surface breaking crack

SHG: second harmonic generation

SHM: structural health monitoring

SNR: signal-to-noise ratio

TFM: total focusing method

TR-NEWS: time reversal nonlinear elastic wave spectroscopy

1D: one-dimensional

2D: two-dimensional

3D: three-dimensional

CHAPTER 1-INTRODUCTION

1.1 Introduction

This thesis is concerned with the development and the implementation of multiple nonlinear ultrasonic phased array imaging techniques as well as investigations into their capabilities for structural health monitoring (SHM) throughout the crack growth. The research in this thesis aims to explore some novel nonlinear imaging techniques and deliver a clear understanding of their efficacy and practicality in non-destructive testing (NDT) applications by investigating their performance on a wide range of samples with various nonlinear damage.

The integrity and the reliability of structural components are critical to ensure their safe operation (e.g. in aviation, power generation and transportation industries). It is known as that as materials (e.g. metals used in pressure vessel welds, railways and pipelines) age, in terms of fatigue, thermal aging, creep, plasticity and radiation damage, they become increasingly more nonlinear (e.g. Matlack et al. [2015]). There are numerous unpredictable factors of material failure such as potential flaws in fabrication processes and environmental deterioration. As a consequence, *in situ* or permanent inspection of the critical structures by detecting the defects at an earlier stage and quantitatively evaluating their remaining life is highly desirable in every engineering industry.

Notably, crack growth generated by fatigue loading is the most common failure of many aged engineering structures. Early detection is therefore important to plan maintenance and guarantee the safety of structures. Conventional ultrasonics using various arrangements of transmitting and receiving transducers represents a suite of approaches to crack detection and sizing that are widely used in industry. However, it is well known that these techniques are inaccurate if the crack is small or partially closed [Tsuda et al., 2006, Thomas et al. 2005, Papazian et al., 2007]. This means that the detection of fatigue in its early stages is not currently possible and necessarily non-destructive inspection is focused on monitoring cracks towards the middle and end of a component's fatigue life. The consequence is that inspection intervals must be shortened and/or designs must have higher margins of safety, reducing structural efficiency and adding cost.

Nonlinear ultrasonic methods are sensitive to the microstructural material changes which precede macroscopic crack growth (e.g. Nagy [1998] and Matlack et al. [2015]). As cracks initiate and start to grow, the nonlinearity due to crack opening and closing (often called non-classical nonlinearity) becomes the dominant feature and leads to a measurable nonlinearity prior to the formation of the large volumetric defects, which may then be detected effectively by conventional linear ultrasonic inspection. This non-classical nonlinearity is described as a contact-acoustic nonlinearity or clapping nonlinearity, which in the simplest case describes the ability of a partially contacting interface to transmit only the compressive component of a wave [Solodov, 1998, Solodov et al., 2002, Solodov et al., 2004]. Recently, several techniques which implement harmonic generation and frequency modulation using ultrasonic transducers to measure elastic nonlinearity have demonstrated the capability to spatially isolate fatigue cracks and effectively monitor their early growth [Su et al., 2014, Lim et al., 2015, Fierro and Meo, 2015, Lim and Sohn, 2015, Amura, 2011]. However, the use of complicated bespoke setups and the lack of robust quantification of measurement errors have led to a significant gap between laboratory results and application by industry [Kim et al. 2006, Cantrell and Yost, 2001, Solodov and Korshak, 2003, Solodov et al., 2004, Croxford et al., 2009, Ohara et al., 2010, Yan and Nagy, 2000, Jiao et al., 2009, Ohara et al., 2017].

Recent advances have enabled the formation of nonlinear ultrasonic images, allowing the nonlinearity to be isolated spatially whilst requiring a similar experimental setup to conventional linear array imaging (e.g. Potter et al. 2014 and Haupert et al. 2017). Nonlinear imaging methods using ultrasonic phased arrays have recently emerged which have the potential to detect material degradation and challenging defects, such as closed cracks. These techniques can be divided into three types: 1) subharmonic amplitude imaging (e.g. Ohara et al. [2007]), 2) amplitude modulation approach (e.g. Ikeuchi et al. [2013] and Haupert et al. [2017]) and 3) nonlinear ultrasonic diffuse energy imaging (NUI) (e.g. Potter et al. [2014]). In the first two techniques the scattered amplitude used to improve detectability of partially closed cracks does not suppress linear scattering features in the resultant images. The third technique uses an off-the-shelf phased array to create much higher resolution nonlinear images than was previously possible. It measures the diffuse ultrasonic field which is a regime created after long time in which the ultrasonic waves are spatially uncorrelated and uniformly distributed in the sample. Measurements of nonlinearity in this diffuse regime have been shown to have high sensitivity to crack-like defects as well as suppressing linear geometry features.

Consequently, Chapter 2 builds on this NUI technique. Its sensitivity to very small defects within noisier materials (e.g. mild steel) as well as the accuracy of crack sizing are explored on some fatigue crack samples. In addition, the earliest point at which detection is achieved in a fatigue test is quantified. The NUI technique is used in conjunction with a standard linear imaging technique, known as total focusing method (TFM) [Holmes et al., 2005] for a comparison study. As a consequence of co-located linear and nonlinear images produced by the same phased array system, the nonlinear one can be used to deliver complementary information with confidence, when the area of interest is identified, but barely detectable from linear information. Note that here the ultrasonic testing is performed alongside micrographic study to examine its capability of sizing cracks.

However, the parameters used in NUI to capture and analyse the diffuse waves necessitate a systematic process to identify their optimum values on a case-by-case basis. This is because the material properties, specimen geometry, boundary condition and instrumentation noise all affect the time taken to establish a diffuse field. Furthermore, an early estimation of a diffuse field, associated with an appropriate size of time window significantly determine the performance of NUI because of a compromise between the degree of diffuseness and signal-to-noise ratio. Last, the volumetric defects would require an advanced NUI in three-dimensional (3D) space using a two-dimensional (2D) array, thereby increasing inspection efficacy and efficiency. In Chapter 3, its performance is first, therefore, optimised by a suite of parametric studies (e.g. on effect of frequency bandwidth). In addition, some diffuse field prediction techniques as well as a novel 3D NUI approach are proposed to improve its applicability.

Although the NUI technique has presented high detectability in some laboratorial cases, the actual structures in heavy industries are often large in size (e.g. aircraft or pressure vessels in a power plant) or are sometimes made of highly attenuating materials (e.g. copper), so that a detectable diffuse field cannot be generated. This weakness led to the development of coherent field imaging methods based on conventional approaches, such as subharmonic scattering and amplitude modulation. In Chapter 4, a board family of nonlinear coherent imaging (NCI) approaches using an ultrasonic phased array system are explored and developed by observing the novel nonlinear phenomena in terms of phase change and amplitude loss primarily at the fundamental or subharmonic frequency of the two focusing modes: *parallel*, in which the elements are fired together with a delay law and *sequential*, in which elements are fired independently. In addition, an approach of the instrumentation nonlinearity compensation is proposed to significantly improve the detectability of microcracks. In Chapter 5, the applicability and the efficacy of the NCI techniques for NDT are investigated by rigorously examining their performance on monitoring crack growth and detecting various surface breaking cracks. The investigations also enhance the appreciation of the relationship between the novel nonlinear phenomena and the mechanical characteristics of cracks.

1.2 Thesis objectives

1) This project aims to identify the most effective ultrasonic imaging approach by which the acoustic nonlinearities induced by the nonlinear defects (e.g. closed fatigue cracks) can be measured. Firstly, the recently developed nonlinear ultrasonic imaging (NUI) technique is investigated to assess its potential for selectively detecting partially closed fatigue cracks. This is achieved through a series of investigations on monitoring fatigue crack growth leading to an understanding of its efficacy for early detection and crack sizing for structural health monitoring.

2) The next step is to optimise the NUI in terms of the signal-to-noise performance and the practicality for different NDT applications. These improvements necessitate parametric studies, in conjunction with proposed nonlinear metrics used to indicate the NUI performance. Consequently, the complete set-up optimisation process is integrated with the imaging technique, in order to allow practical inspection without prior knowledge of the test structure.

3) Furthermore, despite the high detectability of the fatigue cracks in some cases by using the NUI method, its performance and applicability are considerably dependent on the measurable diffuse wave field. As a consequence of practical difficulties in generating a diffuse field in some cases (e.g. in pipelines and pressure vessels), an alternative approach is explored based on the measurement of the coherent field, i.e. that scattered directly from the geometry and defects. This nonlinear coherent imaging (NCI) technique is expected to combine the favourable transmission modes used in NUI with the unexplored nonlinear phenomena of their coherently scattered waves, thereby significantly improving the detectability of closed cracks as well as the practicality for the NDT applications.

4) Finally, multiple feasibility studies will be conducted by examining a family of NCI techniques on monitoring crack growth and detecting various surface breaking cracks. Therefore, its capabilities of structural health monitoring can be identified, in order to make full use of the nonlinear ultrasonic phased array techniques for NDT.

1.3 Thesis outline

In compliance with the objectives described above in sequence, the structure of this thesis can be divided into 6 chapters as follows:

Section 1.4 of Chapter 1 reviews the literature principally relevant to the subject of this thesis. The development of an ultrasonic phased array system for non-destructive testing (NDT) including the different transmission techniques and the conventional linear phased array imaging approach is first introduced. Subsequently, previous works on the existing nonlinear ultrasonic techniques (e.g. second harmonic generation and non-collinear mixing) are reviewed and compared. Based on an understanding of those, a recent nonlinear ultrasonic phased array imaging (NUI) method is then explained.

Following the preliminary research of the NUI technique, Chapter 2 introduces a series of investigations into the capabilities of NUI for monitoring fatigue crack growth. In particular compact tension specimens, made of mild steel, are fabricated and the standardised high-cycle fatigue test is carefully designed to allow the early detection and the sizing of the fatigue cracks. This technique, in conjunction with conventional array imaging, is applied to the periodic monitoring of the specimens under high-cycle fatigue loading. The detection limits of these techniques are investigated. Their abilities to localise and detect small cracks are further quantified with the aid of micrography.

Chapter 3 describes a chain of optimisation approaches for NUI technique. Initially, the key parameters used in NUI (e.g. aperture size, data averaging, reception bandwidth and centre frequency) are studied by investigating the corresponding signal-noise performance with the proposed metrics. Then, three different metrics are proposed to evaluate the diffusivity of a wave field (i.e. predict the gate start time and the window length used in NUI method) in terms of the spatial energy distribution and the phase coherence. Further, three different models are developed to provide experimental, numerical and analytical data respectively for comparison purpose. Hence, the efficacy of the proposed metrics is identified by examining them on those data generated from simulations and well-known samples. Last, a novel NUI technique for volumetric evaluation (termed three-dimensional NUI) is developed and then discussed about its imaging performance and the applications for NDT.

Chapter 4 introduces the development of some novel nonlinear coherent imaging (NCI) techniques. First, the nonlinear ultrasonic phenomena of the resultant coherently scattered wave distorted by closed fatigue cracks are explored experimentally from the pulse-echo ultrasonic measurements using the same phased array system. Following the observations of nonlinear change in amplitude or phase, the amplitude and phase metrics used in NCI methods are proposed. Furthermore, a novel approach of instrumentation nonlinearity compensation for NCI is developed and then discussed in terms of its efficacy of noise suppression. Finally, the pitch-catch NCI technique alongside the measurements at subharmonic and fundamental frequencies are investigated.

Chapter 5 further investigates the capabilities of NCI techniques for NDT applications. First, all the NCI techniques, in conjunction with the NUI method are implemented to monitor the fatigue crack growth in multiple fatigue crack specimens. Their relative performances are then compared and discussed. Subsequently, the detectability of surface breaking cracks using the pulse-echo NCI technique is explored. Finally, the benefits and the limitations of the NCI techniques are described.

Chapter 6 suggests the future works and the direction of further research. This includes the technology transfer of the proposed methods, the unexplored fundamental research to be followed up as well as their potential applications in biomedical field.

1.4 Literature review

1.4.1 Background of ultrasonic arrays and non-destructive testing

An ultrasonic array is a transducer that consists of a number of individual piezoelectric elements. The independently controlled parallel transmission circuits in an array controller enable separate firings of transmitter elements in a pre-set sequence based on a delay law, whereby the beam forming into a test structure can be controlled to achieve translating, steering and focusing. Recent developments of controller systems and high-speed post-processing have realised real-time imaging and hence visualisation of the internal structure. Furthermore, a one-dimensional (1D) array (in which its elements is arranged in one row) and a two-dimensional (2D) array (in which the layout of its elements has multiple rows) allow the cross-sectional and the volumetric images to be produced respectively. Most importantly, ultrasonic arrays deliver two considerable benefits over conventional monolithic transducers. Firstly, an array is able to focus or steer the ultrasonic beam over a broad range of depths and angles, which enables multiple inspections with a single transducer. Secondly, it can image a significant volume of the target from a single location, thereby increasing the speed of inspection.

Ultrasonic array systems were originally implemented in medical diagnostic imaging where the target generally varies with time due to movement of the human body [Macovski, 1979, Well, 1992]. The development of contrast-enhanced ultrasound has achieved the visualisation and the quantification of blood flow and tissue perfusion, delivering considerable benefits (e.g. ultrafast imaging and low cost) [Becher et al., 2000, Cosgrove et al.,2010, Wilson et al., 2010, Sboros et al., 2010]. Medical imaging is a compromise between frame rate (the frequency at which an imaging device displays successive images) and imaging performance (indicated by the signal-to-noise ratio) [Angelsen et al., 1995]. For instance, the number of focal points in parallel transmission (i.e. the number of firings using an aperture, sub-set of array elements) is limited to the requirement of real-time imaging. Note that the parallel transmission can be principally classified as three modalities (plane swept B-scan, focused swept B-scan and sector B-scan, as illustrated in figures 1.1(a-c)). Whilst the plane B-scan can increase the inspection speed by simultaneously firing all the elements the detectability of targets is significantly lower than that of focused B-scan, because of smaller detection coverage and lower transmission energy at each imaging pixel.

In non-destructive testing (NDT) applications, the target specimen is usually static (time-invariant) over the timescale of the measurements. It is then realistic to capture and store the time-domain signals sequentially from all the combinations of transmitter-receiver pairs of array elements, referred as full matrix capture (FMC) [Holmes et al., 2005]. Their further works have presented that the equivalent plane B-scan, focused B-scan and sector B-scan images can be produced by extracting the corresponding time-domain signals from the FMC data. Most importantly, an optimised imaging algorithm, termed total focusing method (TFM), was proposed to fully exploit the FMC data, thereby maximising the signal-to-noise performance by synthetically focusing at every pixel with all the array elements in post-processing (see figure 1.1(d)) [Holmes et al., 2005]. The scientific research of TFM algorithms [Zhang et al., 2010, Zhang et al., 2011, Bannouf et al. 2013, Felice et al. 2014], combined with the development of computing technology (e.g. graphics processing units) [Lambert et al. 2012, Njiki et al. 2013], have realised their broad industrial use in real-time imaging of defects.

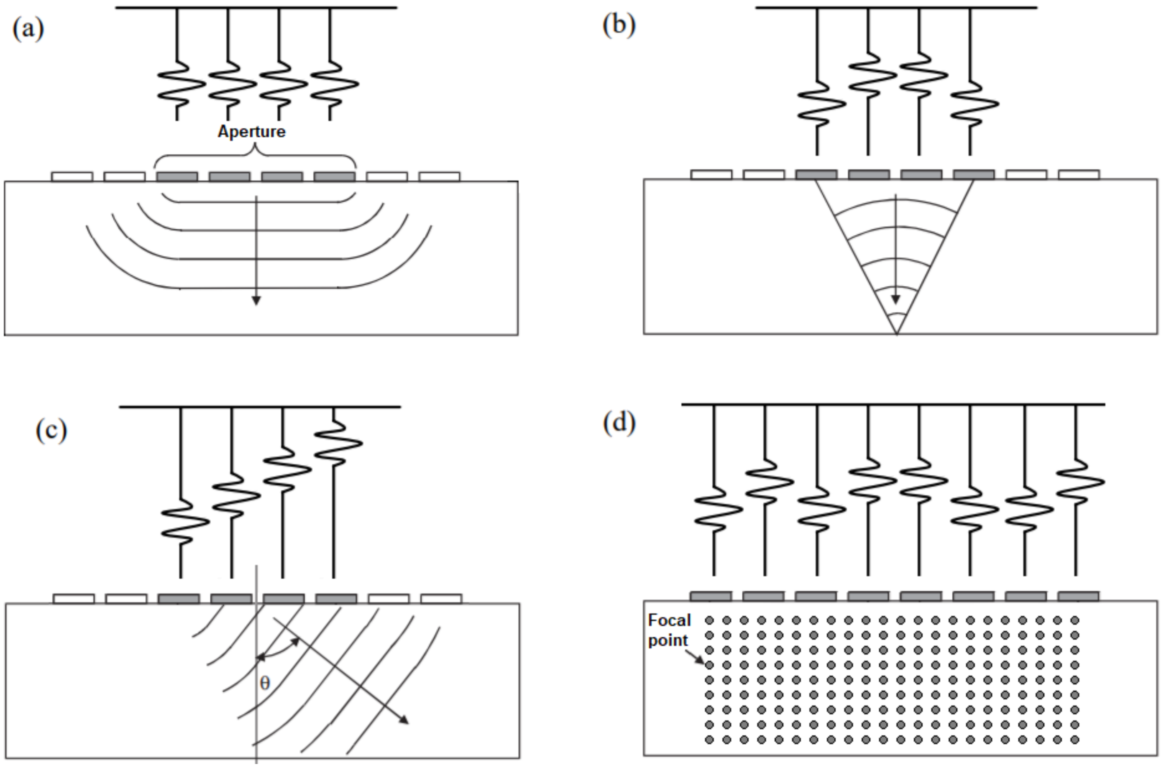

Figure 1.1. Schematic diagram of the (a) plane swept B-scan, (b) focused swept B-scan, (c) sector B-scan and (d) total focusing method.

It should be noted that the approaches of plane B-scan, focused B-scan and sector B-scan can be identically achieved either by post-processing the FMC data or through physical beam forming. Nevertheless, the TFM exploits all the information in the FMC data, so that it is only practically achievable in post-processing. The signals selected from all the time traces in FMC, by calculating their corresponding time of flight, are then summed to construct a focus at every pixel in the image. Assuming $f_{n,m}(t)$ are the time-domain received signals for each combination of transmitter (n) and receiver (m) elements in the FMC case, the intensity of the image, $I(x, z)$ at any point in the image plane (as illustrated in figure 1.2) is given by:

$$I(x,z) = \left| \sum h_{n,m} \left(\frac{\sqrt{(x_n - x)^2 + z^2} + \sqrt{(x_m - x)^2 + z^2}}{c} \right) \right|, \tag{1.1}$$

where $h_{n,m}$ is the complex Hilbert transform of, $f_{n,m}$ [Kino, 1987], the position of focal point $\boldsymbol{r}$ is defined in terms of x and z coordinates, c is the speed of sound in the target material and the summation is performed over all transmitters (n) and receivers (m). Note that linear interpolation is necessary to extract information from discretely sampled time-domain signals. Consequently, each point in the image contains the maximum amount of information from FMC. Last but not least, previous works further developed the imaging techniques using 2D phased arrays which can be implemented to produce three-dimensional (3D) images of the target structure and deliver an enhanced characterisation of volumetric defects [Mendelsohn and Wiener-Avnear, 2002, Martinez et al., 2003, Blum et al., 2005].

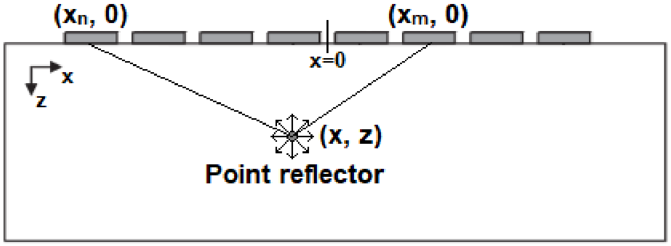

Figure 1.2. Configuration of phased array measurement.

1.4.2 A review of nonlinear ultrasonic techniques

Unlike the reliance of a macroscopic interface in linear ultrasonic measurements, all the nonlinear ultrasonic techniques are based on the evaluation of elastic nonlinearity, which indicates a material property in which the change in stress is not directly proportional to the change in strain. Therefore, the nonlinear ultrasonic techniques are much more sensitive to the microscale change in materials. The most well-known effect of elastic nonlinearity on a propagating ultrasound is spectral migration (i.e. harmonic generation). As a consequence of this nonlinear effect, some of the energy at the incident frequency is converted into its subharmonics and superharmonics. Furthermore, the acousto-elastic effect, in which the ultrasonic velocity is dependent on an external stress applied to the test structure, has been discovered as an additional type of nonlinear distortion. In the existence of nonlinear elasticity, the linear acoustic properties (e.g. additivity, homogeneity and reciprocity) no longer holds true. The key distinction between the principles of nonlinear and linear systems is exploited to characterise the material.

The interaction between elastic nonlinearity and acoustic wave has been studied by a significant amount of research in a multidisciplinary field (e.g. with the applications of NDT and biomedical diagnosis) [Murnaghan, 1937, Hughes, 1953, Toupin and Bernstein, 1961, Bateman et al., 1961, Johnson, 1981, Becher and Burns, 2000]. Notably, the microstructural features of crystalline metallic materials (e.g. dislocations, precipitates and microcracks) have been found to yield the elastic nonlinearity, which were firstly observed to be detected by acousto-elastic techniques [Cantrell, 2004, Nagy, 1998]. Additionally, the quantitative change in microstructure can be measured by the nonlinear ultrasonic techniques, such that the early material degradation and the residual life of critical assets are estimated. It is also worth noting that the defects (e.g. fatigue cracks) at late stages are undetectable by conventional linear ultrasonic techniques due to access limitations in some cases. Since the crack tip is usually tightly closed, the linear scattering from the tip is too weak to be distinguished from coherent noise (e.g. scattering from local grain boundaries). However, the nonlinear techniques have potentials to reveal those hidden defects by suppressing the linear interference and isolating the localised elastic nonlinearity from an interested source.

This subsection reviews a broad family of nonlinear ultrasonic testing approaches. The review starts from the fundamental theory of elastic nonlinearity, followed by their applications as well as comparative study. In particular the theoretical overview of elastic nonlinearity in two different forms (classical and non-classical modalities) is first presented. Whilst a significant number of relevant techniques have been developed for the measurement of nonlinear elasticity, some of them are selected to be reviewed because of their viability in industrial operation. The underlying physics, experimental setup and key findings for each method are discussed.

The ultrasonic testing techniques can be broadly classified as three groups: harmonic generation measurement, nonlinear spectroscopy and nonlinear ultrasonic phased array imaging. Briefly, the first nonlinear method measures either the generation of harmonics (e.g. a second harmonic wave) or a third wave at a resulting frequency induced by two incident waves (known as wave mixing). This technique is primarily dependent on the global measurement of weak classic nonlinearity, such that the early damage (e.g. dislocations) in a region can be estimated. Secondly, the nonlinear spectroscopy technique directly measures the elastic nonlinearity by evaluating the frequency spectra at the point of interest. This class of technique can be implemented with complicated instrumentation to detect damage precursors or discrete defects (e.g. fatigue cracks and delaminations) on a substantial surface. Finally, the latest generation of nonlinear ultrasonic technique utilises state-of-the-art phased array system to accomplish the imaging of non-classical nonlinearity (e.g. tightly closed cracks). Despite promising results obtained from multiple existing techniques, in which various types of transmission and post-processing are applied, considerable lack of quantitative studies on abundant samples as well as knowledge of underlying physics limits their practical applications and scientific development.

1.4.2.1 Classical nonlinearity

Assuming a longitudinal wave propagates through an isotropic elastic medium, the equation of motion can be derived in one-dimension:

$$\rho\frac{\partial^2 u}{\partial t^2} = \frac{\partial \sigma_{xx}}{\partial x}, \tag{1.2}$$

where ρ is the density of a material, u is the particle displacement, σ_{xx} is the uniaxial stress in direction of x coordinate, and t is the time of propagation. For a linearly elastic material the applied stress is directly proportional to the resulting strain. Its mathematical expression is given by:

$$\sigma = \sigma_0 + E_1 \left(\frac{\partial u}{\partial x}\right), \tag{1.3}$$

where σ_0 is the initial static stress and E_1 is the appropriate second-order elastic constant (i.e. Young's modulus of the material). Whilst this ordinary theory of elasticity is adequate for many problems and materials the actual elastic response of materials is anelastic [Zener, 1948] or plastic in varying degrees. Therefore, this nonlinear relationship can be approximated by using further terms in the Taylor series expansion. The constitutive equation for a higher order nonlinearity is generalised as follows:

$$\sigma = \sigma_0 + E_1 \left(\frac{\partial u}{\partial x}\right) + \frac{1}{2} E_2 \left(\frac{\partial u}{\partial x}\right)^2 + \frac{1}{6} E_3 \left(\frac{\partial u}{\partial x}\right)^3 + \ldots, \tag{1.4}$$

where E_2 and E_3 are the elastic constants of third- and fourth-order respectively. It should be noted that the strain induced by ultrasonic waves are in general small (of the order 10^{-6}), so that it is unnecessary to consider the high order terms in equation (1.4) for the further theoretical analysis. Ultimately, by substituting the simplified equation (1.4), including a quadratic nonlinearity (indicated by the third term in equation. (1.4)), to equation (1.2), the nonlinear wave equation can therefore be derived as:

$$\frac{\partial^2 u}{\partial t^2} = c^2 \left(1 - \beta \frac{\partial u}{\partial x}\right) \frac{\partial^2 u}{\partial x^2}, \tag{1.5}$$

where c is the longitudinal wave velocity in the material, and β is the acoustic nonlinearity parameter, which can be expressed in different forms. In general a quadratic strain energy is solved in three dimensions. Hence, the first approach to formulate β is the use of three independent parameters (A_0, B_0 and C_0) of a specific material, termed the Landau-Lifshitz third order elastic constants (TOECs) [Landau and Lifshitz, 1986]. Alternatively, these can also be described in terms of the Murnaghan constants as $l = B_0 + C_0$, $m = \frac{A_0}{2} + B_0$ and $n = A_0$ [Murnaghan, 1937]. The acoustic nonlinearity parameter β is therefore expressed in terms of TOECs as:

$$\beta = -\left(\frac{\dfrac{3E(1-v)}{(1+v)(1-2v)} + 2A + 6B + 2C}{\sigma_0 + \dfrac{E(1-v)}{(1+v)(1-2v)}}\right), \tag{1.6}$$

where v is Poisson's ratio. Note that β relies on the crystalline structure and symmetry of the material (i.e. the lattice anharmonicity itself). Additionally, various micro-structural defects give rise to measurable changes in the classical nonlinearity, whereby the changes can be quantitatively measured by the proposed nonlinear parameter β. The microscale defects are principally known as dislocation pinning, dislocation dipoles, precipitate pinned dislocations and microcracks.

Dislocations lead to the nonlinear relationship between the glide displacement of a dislocation and an applied stress regardless of dislocation pinning [Suzuki et al., 1964]. The pinning is a mechanical behavior to prevent the materials from a movement of dislocation, because of different stress fields (induced by alloy elements and other point defects), grain boundaries, precipitates or inclusions. In the existence of the local stress fields of these pinning points, bowing out of dislocations occurs. Therefore, the overall strain is the sum of both lattice strain and that of the bowed dipole, which refers to a nonlinear stress-strain relationship. Furthermore, these dislocation line segments behaves similar to that of a string model, which produces an additional nonlinear effect [Granato and Lucke, 1956]. It is worth noting that the nonlinear parameter β is dependent on the type of dislocations. For instance, it has been experimentally demonstrated that edge dislocations contribute more to β values than screw dislocations [Zhang et al., 2013].

The formation of dipoles (i.e. pairs of parallel dislocations with opposite Burger vectors) predominantly relies on two different processes (the motions of edge and screw dislocations). In most cases, the stress-strain relationship of these dipoles is intrinsically nonlinear, so that the nonlinear elasticity of bulk materials is primarily dependent on the volumetric density of dislocation dipoles. A few theoretical models, associated with experimental validations, for the contribution of dislocation dipoles to the acoustic harmonic generation (measured by the acoustic nonlinearity parameter β) have been developed [Cantrell and Yost, 1994, Cantrell, 2004]. In addition, dislocation dipoles are the main sources of the elastic nonlinearity induced from fatigue. In general cyclic loading contributes to the generation of dislocated microstructures. These microscale features are observed as branching patterns in high spatial density, which ultimately evolve into slip-bands. Note that the dislocation in high density leads to the formation of dipoles.

The presence of precipitates also determines the value of β. It is worth noting that precipitates implicitly contribute to an increase in elastic nonlinearity by creating the local stress field. Therefore, the total bulk nonlinear response is a function of the volumetric density and spatial distribution of precipitates and dipoles. The most types of damage (such as fatigue, creep, thermal aging and radiation) are related to the generation of dislocations and precipitates, so that their nonlinear changes can be reflected by the magnitude of β. However, a more accurate estimation of β requires comprehensive considerations of both the microstructure and the damage type.

1.4.2.2 Non-classical nonlinearity

In an idealised elastic solids bulk material oscillations behave weakly nonlinear due to the classical nonlinearity described above. However, previous works reported that the contact acoustic nonlinearity (CAN), known as non-classical nonlinearity, local to a non-bonded interface in contact was observed at a much higher level due to a hysteretic behaviour [Moussatov et al., 2003] or a clapping effect [Solodov, 1998, Solodov et al., 2002, Solodov et al., 2004]. The CAN generally occurs at later stages of defects followed by the formation of microscale dislocations, but prior to the presence of the linearly detectable defects with non-contact geometries. These characteristics are commonly found in well-known defects such as fatigue cracks and weakly bonded joints (kissing bonds) [Korshak et al., 2002, Brotherhood et al., 2003]. Therefore, early detections of the damage associated with CAN will be achievable if appropriate ultrasonic techniques are proposed to identify the source of CAN.

Assuming a longitudinal wave is vertically incident to the surface of the interface, the tensile stress of the wave results in opening of the interface, such that the contact between surfaces is weakened. However, the compressional component leads to an increase in the elasticity by strengthening the contact. As a consequence, the asymmetric (i.e. bilinear) stiffness characteristics of the interface may be formulated by a piece-wise stress-strain relationship (as illustrated in figure 1):

$$\sigma = E\left(1 - H(\varepsilon - \varepsilon_0)\frac{\Delta E}{E}\right)\varepsilon, \tag{1.7}$$

where $H(-)$ is a Heaviside unit step function and ε_0 denotes the initial static strain at the interface.

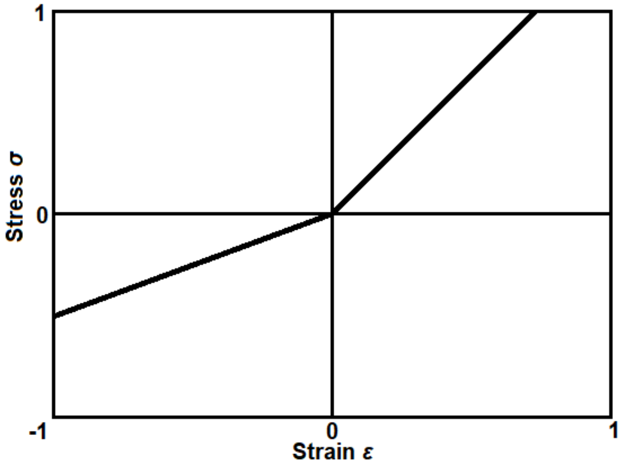

Figure 1.3. Bi-linear stress-strain relationship of CAN.

Such bi-linear response contributes to a broad range of nonlinear dynamics. These non-classical nonlinearities contributes to the formation of super-harmonics, consistent with the classical nonlinear effects [Blanloeuil et al., 2016]. Likewise frequency mixing exists in non-classical nonlinear dynamics, however it is not in compliance with the resonance criteria of classical wave mixing. Notably, the non-classical nonlinearity in clapping mode contributes to the generation of subharmonic waves at frequencies of $\omega_0/2$, $3\omega_0/2$, $\omega_0/3$ and $2\omega_0/3$ (ω_0 denotes fundamental frequency of the incident wave) [Ohara et al., 2006, Yamanaka et al., 2004, Sasaki et al., 2005]. This form of nonlinearity can be simply distinguished from that of classical elastic or instrumentation nonlinearity, so that this distinction is a unique tool for characterisation of nonlinear defects. In addition, such nonlinear responses may be subject to amplitude thresholding effect in the existence of static or residual stress. Consequently, the stress generated from ultrasonic waves needs to be strong enough to compensate for the initial compressive stress, in order for exciting the nonlinear response.

Further, non-bonded interfaces also involve in nonlinear frictional contact induced by normal shear waves [Meziane et al., 2011]. Assuming a shear wave is incident normal to the rough interface and propagates through the contact, two friction mechanisms are taken into account: Coulomb's law with an invariable friction coefficient and a slip-weakening friction law which includes static and dynamic friction coefficients. The state of this stick-slip behaviour is dependent on the size of the applied shear stress, because strong shear stresses are required to initiate the slip (also known as amplitude thresholding effect). Additionally, this nonlinear effect is independent of loading direction, so that their symmetric nonlinear relationships between shear stress and strain are produced and presented in figure 1.4(a) and (b). Consequently, the frictional nonlinearity parallel to the interface, associated with the clapping effect in normal direction give rise to sophisticated nonlinear dynamics in non-classical mode (i.e. CAN).

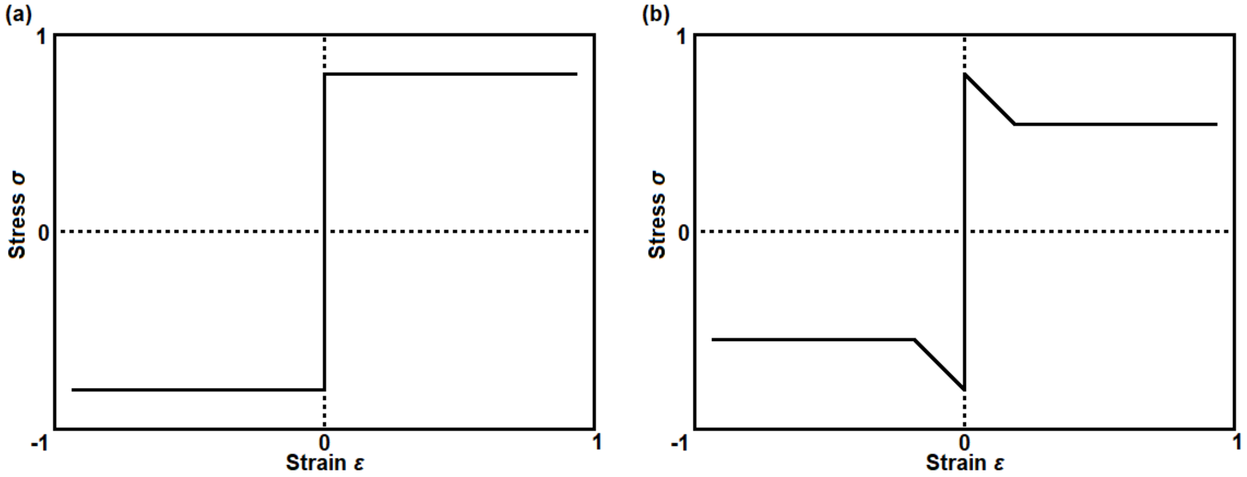

Figure 1.4. Shear stress-strain relationship for (a) Coulomb friction law and (b) slip-weakening friction law.

The CAN leads to small displacements on the order of 10s or 100s of nanometers. The surface profile of cracks on this length scale is significantly irregular (i.e. the local surface roughness is high). Extensive models of cracks used in previous studies were built under the assumption of flat interfaces. Therefore, the deviations from actual nonlinear scattering directivity and non-classical nonlinear dynamics are expected to occur. However, these simplified models have made good approximations to the principle of fundamental contact nonlinearity, in which the fundamental energy dissipation and the generation of harmonics are taken into account.

1.4.2.3 Second harmonic generation measurement technique

One of the most conventional techniques for measuring classical nonlinearity is second harmonic generation (SHG) measurement, which has been presented to effectively detect and monitor microstructural changes in metals such as dislocations and precipitates [Breazeale and Thompson, 1963, Breazeale and Ford, 1965, Gedroitz and Krasilnikov, 1963]. As a sinusoidal ultrasonic wave propagates through a medium with quadratic nonlinearity, the interaction of this wave with microstructural features leads to the energy transfer from the fundamental frequency to the second harmonic component. Additionally, this physical mechanism continuously occurs with distance travelled, causing a cumulative effect. The principle of SHG measurement is the estimation of the acoustic nonlinearity parameter by evaluating the relative amplitude of the fundamental and second harmonic components of a measured wave at a given propagation distance.

In the simplest case of SHG, bulk longitudinal plane waves are assumed to propagate in the medium, a simple relation may be established between the relative harmonic amplitude and the acoustic nonlinearity parameter, β. If a monochromatic ultrasonic pulse of first harmonic amplitude A_1, radial frequency ω ($=2\pi f$) at frequency f and wave number k ($=\omega/c$) is propagating through bulk material with a constant quadratic nonlinearity parameter β, then the time harmonic solution to equation (1.3) of the wave measured at some distance x from the source may be written as:

$$u(t) = A_1 sin(kx - \omega t) + A_2 cos(2kx - 2\omega t), \tag{1.8}$$

where the amplitude of the second harmonic wave is

$$A_2 = \frac{\beta A_1^2 x k^2}{8}. \tag{1.9}$$

By simply rearranging this amplitude term, the acoustic nonlinearity parameter may be expressed as a function of the measured first and second harmonic amplitude as follow:

$$\beta = \frac{8A_2}{A_1^2 x k^2}. \tag{1.10}$$

Note that higher order elastic constants can be taken into account by applying an asymptotic iterative procedure, in order to provide a more accurate approximation [Thompson and Tiersten, 1977]. However, some experimental results suggest that only the quadratic nonlinearity is significantly indicative of harmonic generation.

Furthermore, the analytical solution of β states that this parameter represent a cumulative effect of nonlinearity along the propagation path. Consequently, SHG of bulk waves cannot localise the source of elastic nonlinearity, due to measurement of a spatially averaged value. For instance, such measurements cannot distinguish weak nonlinearity along the propagation path from strong nonlinearity of a localised defect. Additionally, since the bulk wave cannot be measured at any point inside the structure, SHG method is then limited to the surface measurements.

The requirement for the bulk wave to be measured at some points along its entire distance usually limits SHG to applications for which two-sided access (i.e. through-transmission setup) to a structure is available. Although previous works report that [Best et al., 2014, Jeong et al., 2018] SHG using a single-sided pulse-echo setup delivers the potential to measure β in solids or liquids. However, the SHG along with the backward propagation followed by reflection is out of phase with that which happens on the forward path. Therefore, the SHG during the backward propagation interferes destructively with existing second harmonic components from the forward path, significantly lowering the measurability of the second harmonic component from the pulse at reception. As a consequence of attenuation and acoustic beam diffraction, the first harmonic amplitude differs slightly along the two paths, contributing to small differences in the entire SHG. In practice there is some measurable harmonic component remaining in the received signal but it is much less effective than through-transmission (pitch-catch) measurements.

The pitch-catch experiments for SHG measurement are generally accomplished by using two piezo-electric transducers either bonded or gel coupled to each side of structure. As presented in figure 1.5, a typical SHG measurement necessitates a narrow-band transmitter with long excitation pulses (in the order of 10 or more cycles) and a broad-band receiver with high frequency response at both first and second harmonics. In addition, a powerful amplifier is necessary for an implementation of SHG method due to considerably weak harmonic component relative to the incident amplitude. When the signals are received by a broad-band transducer a series of signal processing methods are then employed to extract the desired information. The first and second harmonic components can be obtained through analogue filtering or post-processing of the digitalised waveform. Whilst a single measurement can imply an approximate value of β, more accurate estimation is achieved by repeating the measurement for a wide range of voltage input. In compliance with equation (1.9), the generated second harmonic amplitude is expected to increase with the square of the fundamental amplitude. Therefore, through multiple values of A_2 obtained at different excitation voltages (i.e. A_1), the relationship between A_2 and A_1^2 can be described by a linear fit line through their points on a 2-D plot. The gradient of this linear fit line precisely predicts the value of β.

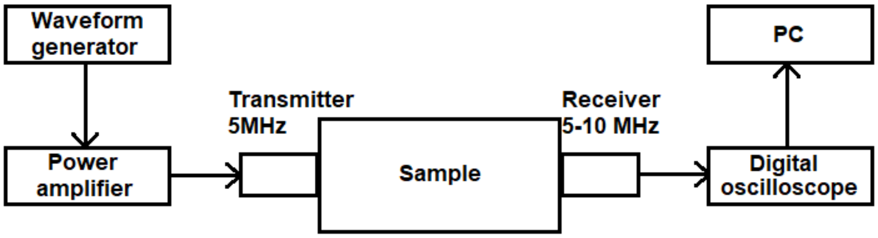

Figure 1.5. Schematic diagram of a typical SHG experimental setup.

Notably, inconsistency in coupling force can influence transmission energy and consequently reduce measurement repeatability [Liu et al., 2011, Sun et al., 2006]. The air-coupled transducers are available for ultrasonic measurements, whereas the substantial reduction in transmission energy leads to impracticality for SHG method. At reception, both capacitive and laser methods allow the signals to be measured without contact [Yost and Breazeale, 1974, Blackshire et al., 2003]. In spite of that, the complicated instrumentation significantly limits their practical use. Last but not least, experimental results have also shown the similar relationship between A_2 and the square of A_1 for Rayleigh or Lamb waves [Shull et al., 1995, Beremes et al., 2007, Deng and Pei, 2007, Pruell et al., 2009].

Most of previous results suggest that the SHG measurement may be an efficient technique for quantitatively measuring early stages of degradation (e.g. fatigue and creep) in metals [Cantrell and Yost, 2001, Baby et al., 2008], but it cannot distinguish the source of nonlinear defects from bulk material nonlinearity along the propagation path as well as instrumentation nonlinearity. Furthermore, the consistency of results (i.e. measurement repeatability) is strongly influenced by coupling condition. The difference in attenuation rate and diffraction for the first and second harmonic necessitates effective corrections in post-processing (e.g. modifications for frequency-dependent attenuation and amplitude ratio) [Cantrell, 2003, Hurley and Fortunko, 1997].

1.4.2.4 Wave mixing techniques for nonlinear ultrasonic detection

In addition to SHG (seen as self-interaction of a wave), material nonlinearities have been found to trigger the interaction between two incident ultrasonic waves (known as collinear or non-collinear interaction) [Taylor and Rollins, 1964, Chen et al., 2014]. This wave mixing technique possesses two overwhelming advantages over SHG method, which are the separation of material and instrumentation nonlinearities as well as the localised measurement of elastic nonlinearity in the region of intersection. In particular, quadratic nonlinearity results in three-wave interactions in which the intersection of two incident waves generates a third wave at a resulting frequency. The focus here has been selected as the non-collinear interaction due to its practical simplicity for NDT applications (e.g. single-sided access required).

Under certain circumstances, the elastic nonlinearity (local to the intersecting area of two unparalleled waves) can induce the generation of a third wave with a frequency and wave vector equal to either the sum or difference of the incident wave frequencies and wave vectors respectively. In practice, the interaction of two shear waves generating a longitudinal wave is the most applicable one. More specifically, a longitudinal wave with substantial amplitude will be produced in the direction of the resulting wave vector ($=k_1 + k_2$, where k_1 and k_2 denote the wave vectors of the first and second incident waves respectively) given that the interaction angle ϕ and ratio of transmission frequencies α ($=f_1 / f_2$, where f_1 and f_2 represent incident frequencies of two different transmitters) satisfy the resonance condition below:

$$\cos\phi = \alpha^2 + \frac{1}{2}\left(q + \frac{1}{q}\right)(\alpha^2 - 1), \tag{1.11}$$

where q is the ratio of longitudinal and shear velocities. As a consequence of multiple satisfactory interaction angles, the frequency ratio can be flexibly chosen to accommodate a given test structure. There are nevertheless restrictions because solutions to equation (1.11) are only valid for frequency ratios between $(1 - q)/\,(1 + q)$ and $(1 + q)/\,(1 - q)$.

A typical double-sided arrangement for such an inspection is illustrated in Figure 1.6(a). Two transmitters are placed at an angle to top surface through wedges, in order to transmit shear waves in the test structure. The angle of the wedges is chosen such that refracted shear waves are produced at the interface with a required relative angle ϕ. The interaction depth is dependent on the distance between the transmitters. A scattered longitudinal wave is produced within the volume of intersected shear waves and is then measured using a receiving transducer on the opposite surface.

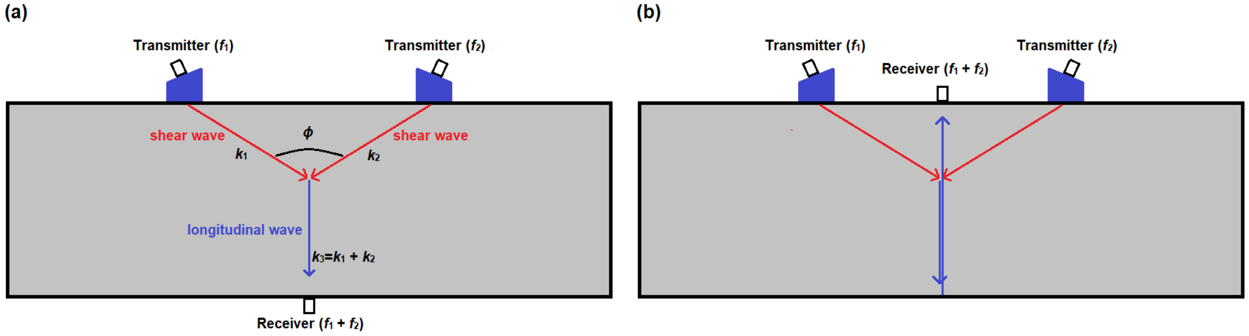

Figure 1.6. Schematic diagram of a typical experimental setup for non-collinear wave mixing through (a) double-sided measurement or (b) single-sided measurement.

One-sided access configuration of this test is also achievable as displayed in Fig. 1.6(b). For this symmetric arrangement, a frequency ratio of unity generates a scattered wave perpendicular to the surface. The generated wave will then become the first reflection from the back wall, received by probe positioned centrally on the transmission surface. If a frequency ratio is not equivalent to unity the generated wave will be steered away from centre, requiring an appropriate calibration of receiving position. Furthermore, depth scanning may be achieved through either changing the distance of the transmitters or adjusting the angle of the transmitters, however the change in the interaction angle requires the frequency ratio to be modified.

Recent works have investigated the potentials of this non-collinear mixing technique for sizing the classical nonlinearities (such as plasticity and fatigue) [Croxford et al., 2009, Demcenko et al., 2012] as well as non-classical nonlinearities (e.g. fatigue cracks and kissing bonds) [Jiao et al., 2017, Alston et al., 2018]. Similarly, this method necessitates a nonlinear metric for quantifying the size of nonlinearities. The metric can be simply defined as the ratio of amplitude of the generated wave to the product of two incident amplitudes. However, it has been observed that there is little sensitivity to high cycle fatigue, only to very low cycle fatigue above the yield stress. The wave mixing technique provides more localised measurement over SHG method, whereas the metric is still limited to a spatially averaged value in volume of interaction. Furthermore, the instrumentation required for this method is significantly more complicated than those for other nonlinear techniques, leading to impracticality of *in-situ* testing and monitoring.

1.4.2.5 Nonlinear spectroscopy

Spectroscopy is described as the study of an interaction between a wave and a medium as a function of its wavelength or frequency. According to that broad definition all nonlinear ultrasonic techniques might fall into the category of spectroscopy. The predominant difference between the nonlinear spectroscopy and other nonlinear ultrasonic approaches is that it implies elastic nonlinearity through analysis of the wave field measured directly at the point of interest, instead of some later components of the propagating field. These methods necessitate excitation of a structure in some vibrational modes and then evaluate the frequency response at an interested point. The type of excitation accounts for the scope of nonlinear measurement, in which a global or local nonlinearity can be identified. If the excitation frequency is chosen to be close to natural frequency of the structure, the measured response infers nonlinear elasticity throughout the material. Conversely, the local nonlinear response is estimated by exciting off-resonance.

One classical group of nonlinear ultrasonic techniques for global measurements is nonlinear elastic wave spectroscopy (NEWS), which principally has two types: nonlinear resonant ultrasound spectroscopy (NRUS) and nonlinear wave modulation spectroscopy (NWMS). A linear system has fixed natural frequencies and mode shapes, whereas the modal frequency response is dependent on input amplitude and frequency for nonlinear systems. NRUS quantifies a spatially-averaged size of nonlinear elasticity through the analysis of relationship between excitation amplitudes and resonant frequencies. An example of the NRUS measurements, in which the damage state of the material could be obtained from the nonlinear amplitude-dependent resonance, was described by [Abeele et al., 2000]. Two rectangular beams, in damaged and undamaged conditions respectively, were excited by multiple frequency sweeps at around the first natural (300 Hz) and the peak acceleration was recorded by an accelerometer. This was repeated for successively increasing drive voltages. The experimental results are presented in figure 1.7. Although both of samples exhibit an increase in measured acceleration with increasing excitation amplitude, the resonant frequency response of the damaged sample significantly differs from that of the intact one. The microcracking leads to a decreasing frequency shift with increasing amplitude.

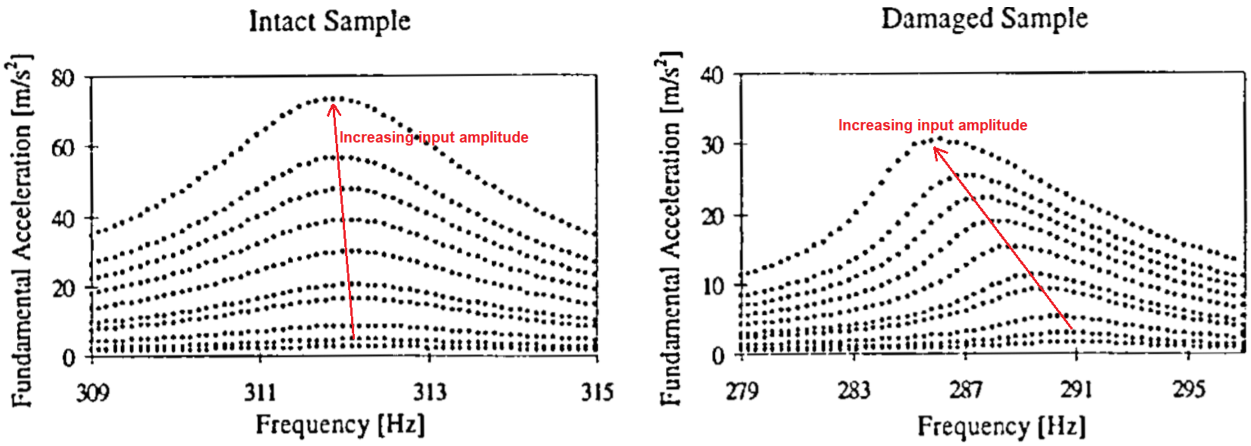

Figure 1.7. An example of NRUS experimental results (Image reproduced from [Abeele et al., 2000]).

Consistent results have also been obtained for aluminium plates including residual stresses [Korobov et al., 2015]. The NWMS generally apply two continuous waves at different frequencies, whereby the existence of nonlinear system leads to various nonlinear modulation effects. A systematic study into bispectral analysis, rather than power-spectral analysis, has demonstrated that global measurement necessitates the excitation of multiple modes [Courtney et al., 2008]. Some promising results in which NWMS appears to be highly sensitive to various damages have been observed in different materials [Meo and Zumpano, 2005, Meo et al., 2008, Courtney et al., 2008]

Whilst global measurement technique allows a structure to be inspected rapidly, localised measurements are generally favoured in order to facilitate follow-up maintenance. Previous works have developed a nonlinear spectroscopy technique for detecting a fatigue crack using a scanning laser vibrometer [Solodov et al., 2004]. In this study, analysis of the spectra reveal both the subharmonic generation and self-modulation (i.e. generated components at mixed transmission frequencies), which deliver an accurate localisation of the defect.

Another variant of nonlinear spectroscopy for localising the source of elastic nonlinearity is known as time reversal nonlinear elastic wave spectroscopy (TR-NEWS), which was initially developed by [Ulrich et al., 2007]. Time reversal method relies on a linear feature (reciprocity property). The principle is as follows: assuming two incident surface waves at different frequencies are propagating through a damaged structure, the two waves coincidentally interact with the nonlinear defect simultaneously. As a consequence of nonlinear distortion, a generated wave component at their sum and the difference frequencies will be scattered and eventually received by some transducers. The received signals are then filtered at the sum and the difference, time reversed, re-transmitted and found to focus on the nonlinear scatter in sequence. Consider an ultrasonic signal transmitted or emitted from some point in a structure. The field this produces can be recorded at a single or multiple points elsewhere in the structure. Their experimental results show that the time reversed waves successfully refocused on the target crack, detected by a laser vibrometer.

In summary, nonlinear spectroscopy techniques can be used to measure the global nonlinearity or the local nonlinearity. The surface measurements may necessitate scanning laser vibrometers to identify and image the target signal at the point of interest. Such techniques require complicated instrumentation and involve substantial scanning for a large structure.

1.4.2.6 Nonlinear ultrasonic phased array imaging techniques

As a consequence of impracticality of the complicated bespoke setups required for the localisation of elastic nonlinearity, the SHG, wave mixing, nonlinear spectroscopy techniques have yet to become accepted by industry. Recently, some nonlinear imaging techniques using ultrasonic phased arrays have however emerged with the ability to localise and size closed cracks. These techniques can broadly be classified into three groups. Firstly, subharmonic imaging [Ohara et al., 2007] which is conceptually similar to conventional linear array imaging, but which evaluates the subharmonic rather than fundamental component of the received signals. These methods are well suited to imaging of closed cracks since subharmonic generation is associated only with the defect and not nonlinearity of the bulk material or instrumentation. Secondly, an approach, referred to as amplitude modulation, evaluates the nonlinear amplitude dependence of the fundamental frequency component backscattered from the inspection point. Amplitude modulation at the inspection point has been achieved in two ways: by modulating the transmission amplitude [Ikeuchi et al., 2013] and by changing the number of transmitting elements [Haupert et al., 2017]. In the latter technique the scattered amplitude from transmission of all elements simultaneously is subtracted from that recorded using just the odd and even subsets of the elements. Such methods have been shown to increase detectability of closed cracks but imperfectly suppress linear scattering features in the resultant images. Thirdly, nonlinear diffuse energy imaging [Potter et al., 2014] contrasts the statistical diffuse energy of fields produced by sequential and parallel transmission focusing. Whilst this approach has shown high sensitivity in some cases, when the test structures become large in size or are made of highly attenuating materials, a measurable diffuse field cannot be produced thereby limiting the applicability. Such applications necessitate the use of coherent field imaging methods such as subharmonic scattering and amplitude modulation.

1.4.2.6.1 Subharmonic imaging

One classical group of nonlinear phased array imaging techniques are developed to perform the analysis of subharmonic component in the measured waves scattered from the focal point. This class of method is technically similar to forms of linear array imaging, but the focus here is the scattered amplitude at subharmonic frequency, rather than fundamental frequency. As described in Subsection 1.4.2.2, the form of contact acoustic nonlinearity induced by closed cracks can generate both sub-harmonic and super-harmonic components of an incident ultrasonic wave.

As an imaging metric for non-classical nonlinearities, subharmonic scattering offers a considerable advantage over other harmonic components. Subharmonic generation can be clearly distinguished from either instrumentation nonlinearity or bulk material nonlinearity (i.e. second harmonic generation). Consequently received subharmonic amplitude might be predominantly induced by nonlinear defects. Therefore, the nonlinear selectivity is expected to be higher for the subharmonic imaging.

The distorted waves are required to be scattered toward a receiving probe, in order to localise the source of nonlinear distortion. For a single-sided access, this can be achieved in two ways. Firstly some weak nonlinear components can be directly backscattered at interface in contact. Secondly, distortion induced by closed crack can be acquired through the forward field later backscattered by open crack regions, grain boundaries and other close scatterers such as a back wall. Furthermore, the efficacy of backscattering is also dependent on incident angle relative to their interface. Therefore, the distorted field is theoretically measurable in a single-sided configuration, but, there is uncertainty in the actual directivity function of the process due to reliance on the existence of desired geometric features in the specific sample. As a result, physical variance is existing between nominally identical cracks, leading to the difference in their detectability.

Idealised nonlinear measurements necessitate both narrow-band amplitude in high transmission intensity and great sensitivity to the evaluated frequency component. For subharmonic imaging this generally requires the involvement of two different transducers in transmission and reception respectively, increasing the operational complexity. Note that a phased array is preferably employed to increase the signal detectability due to wide scattering angle. The earliest implementation was performed by [Ohara et al., 2007]. The subharmonic measurement employed a scanning monolithic transducer for transmission and an ultrasonic phased array for reception, as illustrated in figure 1.8(a). The image is then produced by moving the transmitter along the surface and post-processing of the received signals with reception focal law at each imaging pixel. Through evaluating the filtered signals at the desired frequency, fundamental and subharmonic images can be formed. The bandwidth of the receiver is typically sufficiently wide for providing good sensitivity to both fundamental and subharmonic signals.

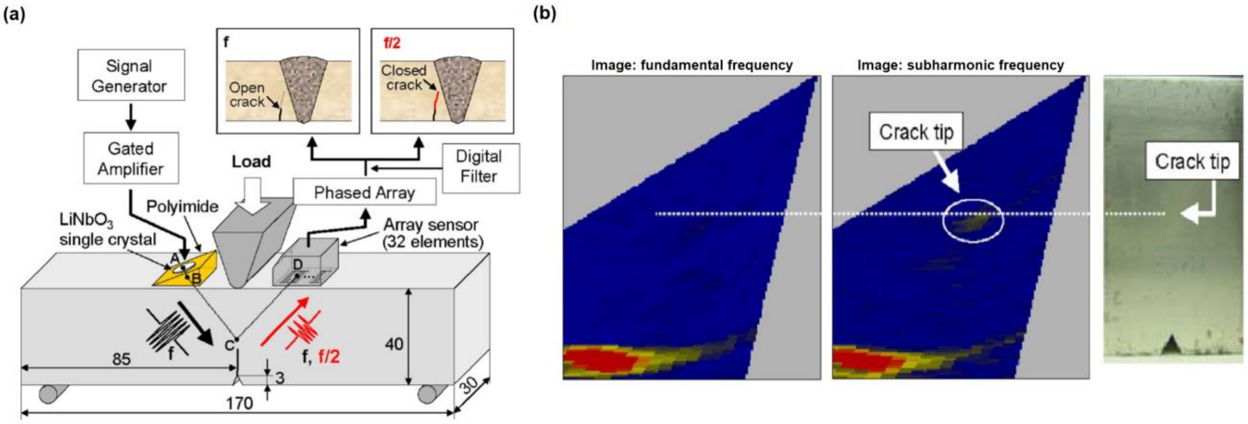

Figure 1.8. (a) A schematic illustration of subharmonic imaging experiment, and (b) imaging results of a high cycle fatigue crack (Image reproduced from [Ohara et al., 2007]).

This technique was then implemented to the imaging of high or low-cycle fatigue cracks grown in both aluminium (Al17075) and stainless steel (SUS316L) specimens subjected to three point bending test. Their results suggest that the low-cycle fatigue crack in the aluminium sample was detected by both fundamental and subharmonic imaging methods. However, under high cycle fatigue loading, the crack tip was only visible in the subharmonic image, as displayed in figure 1.8(b). This might be due to the crack closure, increasing contact acoustic nonlinearity. To manifest this hypothesis, another experiment was conducted to demonstrate that less of the crack region was identified in the subharmonic image when the crack grown in the stainless steel sample became more open with increasing applied static load.

The detectability of closed crack is seen to be improved significantly by comparing with the fundamental imaging results, whereas the linear scattering features, such as the back wall, remain at high level within the subharmonic image. This indicates that this subharmonic imaging cannot separate the nonlinear source from the linear scatterers. This is possibly attributed to the forward distorted field backscattered by the back wall, the subharmonic generation at the probe-sample interface or existence of subharmonic components within transmission bandwidth. This class of nonlinear imaging was then widely studied in terms of its performance on a range of damaged samples. Similar detectability of subharmonic and fundamental imaging was seen in the results of crack growth monitoring [Ohara et al., 2010] and detection of different stress corrosion cracks [Ohara et al., 2009, Ohara et al., 2010, Horinouchi et al., 2012]. An optimisation approach using multiple signal classification (MUSIC) algorithm was proposed to enhance the resolution of nonlinear subharmonic imaging by significantly reducing point spread function [Park et al., 2016].

Another type of subharmonic imaging was developed by [Potter et al., 2016]. Specifically, the arrangement is similar to those for previous subharmonic imaging, but monolithic transmitter was replaced by an additional phased array to realise synthetic and physical focusing through delay law used in both transmission and reception. Since the majority of commercially available array controllers possess broadband pulse excitation rather than arbitrary waveform generation, transmitted signals inherently contain a considerable amount of subharmonic component, causing nonlinear defects indistinguishable with linear features. Consequently, this class of method necessitates suppression of the effect of the overlap between fundamental and subharmonic frequency components. To this end, the principle of parallel-sequential field subtraction used in nonlinear diffuse energy imaging technique (see Subsection 1.4.2.6.3) was applied to this subharmonic imaging.

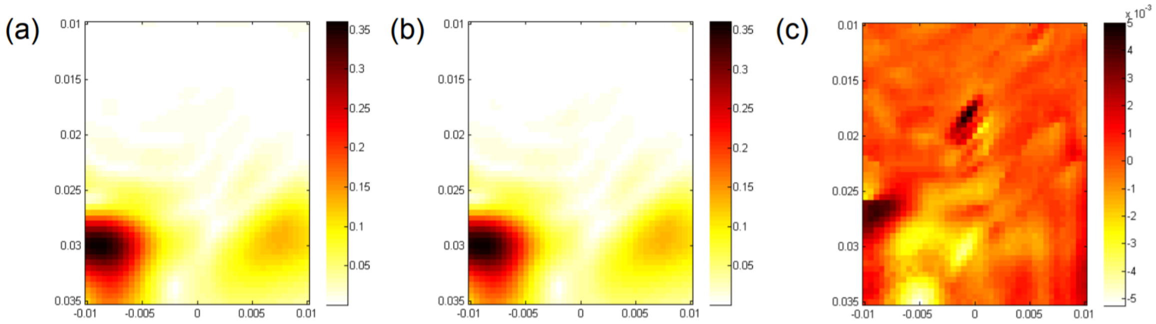

Figure 1.9. (a) Parallel subharmonic image, (b) sequential subharmonic image and (c) subtracted subharmonic image (Image reproduced from [Potter et al., 2016]).

The fundamental process of this imaging is as follows. Firstly an image is produced by physically focusing at each pixel in sequence through a 5 MHz transmitter and a 2.5 MHz receiver. The imaging process is conceptually similar to the total focusing method [Holmes et al., 2005] for the two array configuration filtered at the subharmonic. Secondly the synthetic focusing is achieved through post processing of a sequentially captured full matrix. These two focusing are expected to be linearly equivalent, inferring that the subharmonic components within transmission band will be removed after parallel-sequential subtraction. Harmonic generation is by definition an amplitude dependent process, implying subharmonic scattering will be greater for the parallel transmission case due to much larger fundamental energy at the focal point. Consequently through subtracting these two images from each other, linear geometric features should be removed and only nonlinear scatterer should remain. In addition, any subharmonic generation at the array-specimen interface should also be removed.

This is demonstrated experimentally in figure 1.9 in application to a high cycle fatigue crack grown in an aluminium sample. The parallel and sequentially focused images are seen to be nominally identical and are dominated by linear scattering from the back wall induced by the overlap between transmission and reception bandwidths. However, when the two images are subtracted these linear features are significantly suppressed and a nonlinear feature corresponding to the crack tip becomes prominent within the image. Note that the back wall is not removed completely by this process. This might be attributed to the instrumentation nonlinearity (i.e. the inability to transmit identically in parallel and sequential modes). Another key finding was that the longitudinal-shear mode conversion at contact interface of closed fatigue crack occurred in the same experiment. The results suggest that the use of generated shear wave can lead to higher selectivity of closed crack in this arrangement. This is likely due to the oblique incident angle relative to the crack interface, causing strong frictional (i.e. rubbing) contact nonlinearity excited by the generated shear waves at the interface.

1.4.2.6.2 Fundamental amplitude modulation imaging

Subsection 1.4.2.6.1 described a group of imaging techniques that measures the generated subharmonic wave induced by the source of contact acoustic nonlinearity. Another class of techniques rather evaluate the remaining fundamental component to quantify elastic nonlinearity at or close to the target point. The principle is that if the transmitted waves propagates through materials of elastic nonlinearity a considerable portion of fundamental energy will transfer to some other frequency components. Therefore, when this small change in the received fundamental amplitude is measured the source of elastic nonlinearity is expected to be detected. The measurement of fundamental amplitude is advantageous because only one array probe is required for a pulse-echo configuration. Further this allows both linear and nonlinear imaging to be performed using the same instrumentation, facilitating the industrial use on existing phased array systems. Last but not least, the measurement of loss in fundamental waves provides a metric sensitive to both classical and non-classical acoustic nonlinearity at the pixel location.

This class of techniques seek to exploit a relative change in the backscattered fundamental wave through a series of measurements. Hence some form of baseline measurement is required to be performed. The general concept is to modulate some experimental parameters (such as phase and amplitude) and then evaluate how the fundamental or subharmonic imaging changes as a function of this parameter. Two of the most widely studied approaches are known as phase inversion (PI) and amplitude modulation (AM), which were initially proposed to enhance the detectability of microbubble contrast agents [Brock-Fisher et al., 1996, Simpson et al., 1999]. As presented in figure 1.10, two or three pulses in specified phase and amplitude are output in sequence from the same transmitter. Through each combination of received pulses in post-processing, the linear components are suppressed but the nonlinear echoes are preserved and accumulated. This process allows the nonlinear target (in this example microbubble) to be imaged with significantly enhanced selectivity within nonlinear image.

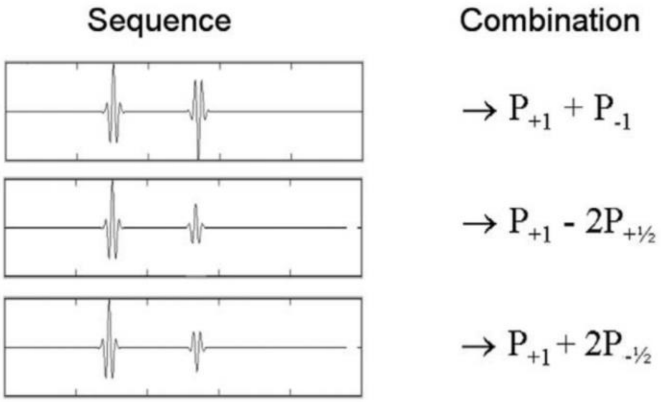

Figure 1.10. Illustration of pulse inversion (PI) approach, amplitude modulation (AM) approach and the method (PIAM) by combining PI and AM (Image reproduced from [Eckersley et al., 2005]).

A variant of AM method in application to nonlinear imaging of closed crack was implemented by [Ikeuchi et al., 2013] who called this the fundamental wave amplitude difference (FAD) technique. Similarly, the experimental procedure of this approach is to form two conventional linear images by using a phased array to fire signals at two different excitation voltages. The images are subsequently scaled by the same factor as the amplitude difference in excitation and subtracted to produce the nonlinear image. The underlying principle is that although the linear scattering followed by linear normlisation are expected to appear at the proximate level within two linear images the disproportional nonlinear response remains as relative fundamental amplitude loss in the subtracted image and can be indicative of elastic nonlinearity.

To examine the efficacy of this technique, a fatigue crack specimen made of austenitic stainless steel was inspected by a 32 element 5 MHz array. The low and high input amplitude images as well as the subtracted image for this test are presented in figures 1.11 (a-c). The fatigue crack in this sample is likely to be slightly open due to strong linear scattering of the crack tip relative to the back wall (see figures (a) and (b)). The subtracted image is seen to improve the selectivity of fatigue crack at first glance, whereas the amplitude of each feature in the subtracted image is not convincing. An example is that the back wall on the right hand side of two images (see figures 1.11(a) and (b)) exhibits the highest contrast in amplitude, but the subtracted image shows that none of the scattering can be seen in the same area, and the peak amplitude of scattering within the image in figure 1.11(c) is approximately three quarters of the highest value in its dynamic range.

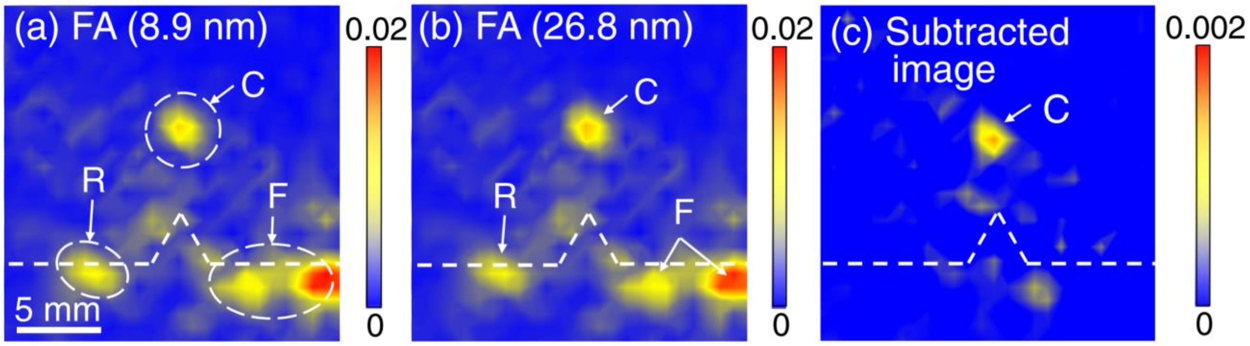

Figure 1.11. Fundamental wave amplitude difference technique (a) low amplitude image (b) high amplitude image (c) subtracted image. (Image reproduced from [Ikeuchi et al., 2013]).

Another class of AM method was proposed by Haupert et al. [2017]. This technique relies on similar principles to FAD approach. In contrast to modulated transmission amplitude used in FAD, this method instead vary the number of transmitting elements to achieve the high or low amplitude focusing at each pixel location. The principal advantage is that the effect of nonlinearity generated during propagation path between probe and target nonlinear defect can be eliminated. It is also insensitive to other sources of nonlinearity such as instrumentation nonlinearity and contact acoustic effects at the array-specimen interface because of the identical transmission energy for each element used in high and low amplitude focusing.

To form a nonlinear image, this necessitates three different acquisitions. Firstly, it employs all the elements to physically focus at each pixel on both transmission and reception to form a linear image (known as parallel focusing). A similar process is then performed using identical focal laws but transmitting in turn with only the odd elements and subsequently the even elements. The two subset measurements are first summed, then subtracted from the full transmission and finally processed to generate the nonlinear image. This is described schematically in figure 1.12 (a). For a linear system, the sum of the two subset transmission generated the equivalent field to the full parallel transmission. However, the amplitude seen by each focal point for the full transmission will be roughly twice that of the odd-even subset transmissions yielding a difference in the nonlinear response of the two at the focal point. This concept is similar to the principle of parallel-sequential field subtraction but using half of the array elements rather than single elements.

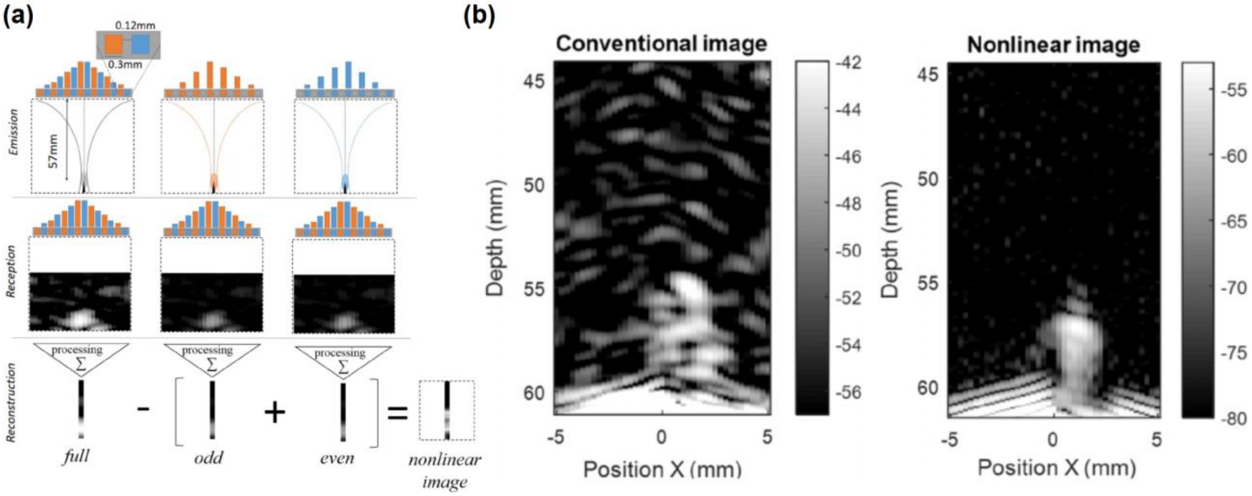

Figure 1.12. A type of amplitude modulation (a) imaging process and (b) imaging results. (Image reproduced from [Haupert et al., 2017]).

This technique was implemented to image a fatigue crack grown in a stainless steel AISI304 sample. The linear and nonlinear images generated using a 64 element 5 MHz array are presented in figure 1.12(b). The linear image exhibits substantial coherent noise (i.e. grain noise) similar to the previous example. The linear response of the crack is not restricted to the tip in this case, however exhibits considerable linear scattering along the whole crack length. The corresponding nonlinear image presents significant suppression of grain noise as well as an increase in detectability of cracked area (the quoted figure is of a 5 decibels (dB) enhancement). Notably, although this technique is expected to suppress more noise over FAD residual scattering from the linear back wall appears at much stronger level than the last example.

Both of these examples demonstrate the potentials of fundamental amplitude modulation imaging to increase signal-to-noise performance for high cycle fatigue cracks. It is evident however that some linear backscatterers from the crack is also required for the nonlinear response to be measured. It is thought that this class of technique is suited to providing complementary information in the detection of partially-closed defects that are weakly visible in a linear modality but perhaps cannot be distinguished from coherent noise and proximate linear features. However, such class of technique still necessitates further development on improving the detectability of various nonlinear defects (e.g. early stage microcracking) as well as suppression of interference from linear features. Additionally, the quantitative study is also important in order to examine their capability of sizing defects.

1.4.2.6.3 Fundamental diffuse energy imaging

The nonlinear imaging methods described in Subsections 1.4.2.6.1 and 1.4.2.6.2 are principally dependent on the measurements of coherently scattered field at subharmonic and fundamental frequencies. In theory, both of those methods only measure a small proportion of total nonlinear response due to the inability to capture the target scattering in every direction. In particular, if a microcrack is perfectly closed only the forward distorted field would exist, which is barely measurable when the receiver is not positioned on the other side. In either this case or detection of a partially closed crack, it necessitates an approach to capture all of the nonlinear information using single-sided access (also preferably with a single probe), in order to improve the detectability of these defects. A novel technique termed nonlinear ultrasonic diffuse energy technique (NUI) was recently proposed to overcome those difficulties [Potter et al., 2014]. The use of diffuse field is advantageous since it allows total nonlinear information at each pixel location to be obtained through measurement of uniformly distributed energy. Further, Subsection 1.4.2.6.2 described a technique that employs half of array elements for low amplitude focusing. This method instead fires every single element separately in order to increase energy contrast at the focal point between low and high amplitude focusing. A brief overview of this technique is given as follows.

The technique uses an off-the-shelf phased array to create much higher resolution nonlinear images than was previously possible. In addition a diffuse field nonlinear metric was explored and shown to have high sensitivity to the nonlinear signals. More specifically, the NUI technique uses an array to create a spatial map of nonlinearity by focusing in two different modes on each pixel in the image. The first mode is *parallel*, in which the elements are fired near simultaneously with an applied delay law, resulting in high intensity focus (known as physical beam forming) at the pixel location. Another mode is *sequential* in which the elements are fired independently (referred as full matrix capture) and the interference effects of focusing are emulated synthetically through a post-processing algorithm. The principle is that two resulting fields would be linearly equivalent and therefore any differences can be used to infer the elastic nonlinearity. Similarly, this difference is also insensitive to other sources of nonlinearity such as bulk material and transducer-specimen interface nonlinearities.

When parallel focusing is achieved using a large number of array elements, the absolute acoustic pressure seen by focal point is significantly higher at the focal point than that through independent firing used in sequential transmission. This can be interpreted by an example: assuming longitudinal waves transmitted by a 64 element array propagate through an isotropic elastic materials with a quadratic nonlinearity, each pulse arrives at a focal point with amplitude A. For each single transmission cycle of parallel and sequential focusing, the absolute amplitude seen at the focal point differs by a factor of 64. Since the amplitude of a generated second harmonic wave is proportional to A^2 and the wave energy is also proportional to A^2, the amount of energy lost from the fundamental wave (i.e. the amount of energy obtained in the second harmonic generation), is proportional to A^4. Consequently, the acoustic energy lost from the fundamental wave for the single transmission cycle in parallel focusing is 64^3 larger than that via the summation of the 64 transmission cycles required for the equivalent sequential focusing (see more details described in table 1.1). This considerable difference would infer the elastic nonlinearity at the focal point if all the distorted signals can be measured in subsequent propagating wave field.

Focusing type	Amplitude of fundamental harmonic at focal point	Amplitude of second harmonic at focal point	Energy lost from fundamental wave at focal point
Parallel (single transmission cycle)	$64 \times A$	$(64 \times A)^2$	$(64 \times A)^4$
Sequential (all transmission cycles)	$64 \times A$	$64 \times A^2$	$64 \times A^4$

Table 1.1. Amplitude of fundamental and second harmonic as well as energy lost from fundamental wave for parallel and sequential focusing cases of a 64 element array.

The wave field is not accessible by the measurement system at the focal point. Further, the existence of substantial diffusors and scatterers (e.g. boundaries of the structure and grain) leads to inability to capture all of the distorted wave in coherent field at a single inspection location. However, the fundamental energy loss might be inferred subsequently from a homogeneous wave field (diffuse wave field). The principle is that after multiple scattering energy sampled at any instant within the structure is proportional to the total energy in the system. Consequently, nonlinear information at the focal point in the form of energy loss is uniformly spread within the structure. Note that it is important to measure the diffuse energy over a period of time because in a statistical sense this will involve more distorted waves in the analysis of total fundamental energy lost at the focal point. The proposed approach then estimates acoustic nonlinearity at the focal point by measuring the relative loss in fundamental diffuse energy between parallel and sequential focusing. The imaging metric is then defined as the normalised difference in fundamental energy of parallel and sequential focusing.

This technique was implemented to the measurement of a high cycle fatigue crack grown in an aluminium compact tension specimen. Note that a 5 mm diameter hole was machined behind the crack tip and an equivalent hole was machined to one side as a linear reference. The linear and nonlinear images, formed using a 64 element 5 MHz array are shown in figure 1.13.

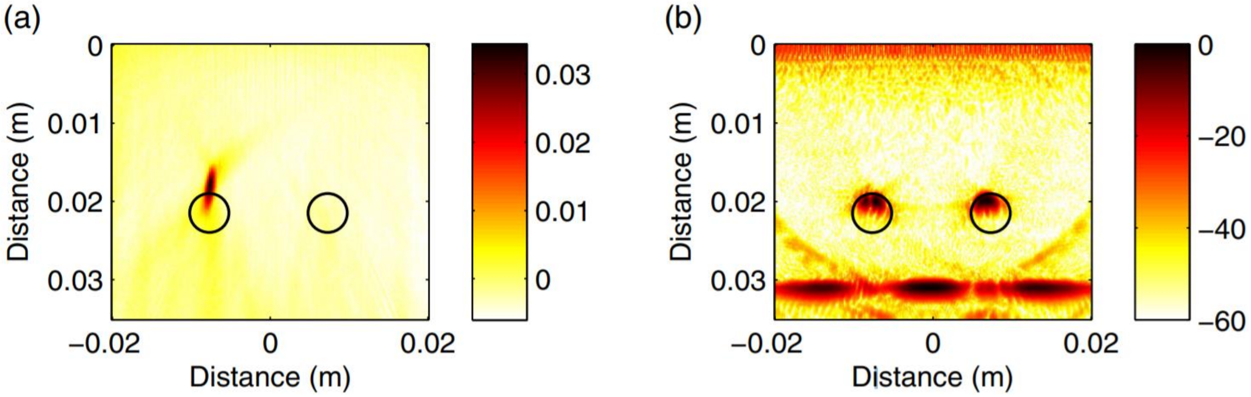

Figure 1.13. (a) Nonlinear ultrasonic diffuse energy imaging results and (b) Total focusing imaging results. (Image reproduced from [Potter et al., 2014]).

As presented in figure 1.13 (b), the linear image is seen to be dominated by the back wall and hole scattering. There are some shadowing effects on the left hole induced by diffraction at the crack tip, whereas this is a vague indication and no sizing information is provided. The nonlinear image shows a clear indication from the cracked region due to the local elastic nonlinearity. Furthermore, the linear suppression seen in this example is particularly effective, as a direct consequence of the diffuse energy measurement. Since imaging is not based upon a coherently scattered signal from the inspection point, instrumentation nonlinearity (e.g. inability to transmit the equivalent energy in two consecutive firing) does not generate artifacts from linear features as is the case with coherent nonlinear imaging techniques (described in Subsection 1.4.2.6.2). This is crucial because a geometric feature which acts as a stress raiser to initiate crack growth is itself intrinsically a strong linear scatterer. Therefore, without separation of linear and nonlinear modalities, a small nonlinear defect can be masked by the linear feature it grows from. In summary, this technique is seen to provide the highest sensitivity to closed cracks by capturing more nonlinear information at each imaging location in the diffuse field. Since it requires measurable signals in the diffuse field the application is limited to small structures or made of weakly absorbing materials.

1.4.2.6 Summary of nonlinear ultrasonic techniques

A broad variety of techniques have been proposed to measure elastic nonlinearity in various materials such as composites and metals. Each have particular experimental requirements which determine their practical applicability and each exhibit differences in sensitivity to different damage types. In general, by comparison with linear ultrasonic techniques, their uniqueness is to characterise smaller structural change prior to the formation of the large volumetric damage, which may then be detected effectively by the linear techniques. The nature of existing scientific literature makes direct comparisons of the sensitivity of these nonlinear techniques difficult. Each result is presented for different specimens and using different instrumentation. Furthermore signal-to-noise improvements are evaluated quantitatively in different ways or not at all for each case. It is possible however to draw certain conclusions regarding the various advantages and disadvantages of each method, which is summarised in table 1.2. From table 1.2, it is evident that nonlinear diffuse energy imaging technique should be further studied quantitatively as the most promising method. Furthermore, its strong reliance of a measurable diffuse field also necessitates more scientific research on the development of an alternative coherent imaging method.

Method	Damage sensitivity	Advantages	Disadvantages
Second harmonic generation	Plasticity, creep, low and high cycle fatigue, thermal aging and radiation damage	Sensitive to a broad range to microstructural damage	Spatially averaged value of bulk material. Double-sided access. Inability to separate instrument and material nonlinearity.
Wave mixing	Plasticity, kissing bond and fatigue crack	Volumetric localisation of nonlinear source. Separation of instrument and material nonlinearity	Impractical experimental requirement
Nonlinear elastic wave spectroscopy	Partially closed crack and delaminations	Long range inspection	Only surface measurements. Complicated experimental setup
Nonlinear time reversal spectroscopy	Partially closed crack and delaminations	Imaging of nonlinear scatterers over large area	Only surface measurements. Impractical experimental requirement
Subharmonic array imaging	Partially closed crack	Through depth imaging. Single-sided access	Complicated experimental setup. Analysis of limited amount of nonlinear information. Difficulty in linear suppression

Fundamental amplitude modulation imaging	Partially closed crack	Through depth imaging. Single-sided access. Single array required.	Reliance of linear scattering close to nonlinear feature. Difficulty in linear suppression
Nonlinear ultrasonic diffuse energy imaging	Partially closed or closed crack	Highest sensitivity to elastic nonlinearity. Effective linear suppression. Through depth imaging. Single-sided access. Single array required.	Measurable diffuse field required.

Table 1.2. Summary of a comparative study for existing nonlinear ultrasonic techniques.

1.4.3 Research scope based on literature review

The research scope presented in this thesis is derived from the principal gaps in the literature reviewed above, and it specifically focuses on four aspects:

1) Since nonlinear ultrasonic diffuse energy imaging (NUI) technique is seen to provide the highest sensitivity to closed fatigue crack, further quantitative study should be made to examine the detectability of early stage microcracking as well as the capability of crack sizing. In this thesis, an investigation into the performance of NUI for the monitoring of the early stages of fatigue crack growth was conducted with the aid of micrography. The detection limits and the repeatability of this technique were also explored.

2) As indicated in the literature, the NUI is based on the measurement of propagating waves over a period of time within diffuse field. In addition, all the published results were produced through the use of empirical parameters (e.g. gate start time and window size at reception) under laboratory conditions and in small specimens. Consequently, a systematic study and an effective optimisation of key parameters used in NUI were described later. In particular, an optimisation method to measure and predict a diffuse field was developed to select the optimum value of gate start time and window size for NUI in application to an unfamiliar structure. Furthermore, an

investigation into NUI in three-dimensional space was accomplished and demonstrated that it can be used to effectively evaluate elastic nonlinearity of volumetrically variant defects.

3) Since a measurable diffuse field might not exist in large structures (e.g. components in heavy industry), it would be important to develop an alternative approach. Some coherent imaging methods have been reported in the literature, whereas the inability to separate nonlinear defects from linear features is observed in most of their results. This might be attributed to a misinterpretation of an appropriate use of nonlinear information contained in coherently scattered field. Consequently, an investigation into parallel-sequential coherently scattered field was firstly launched to explore the underlying physics behind the experimental nonlinear results. Subsequently, a wide variety of novel metrics were proposed and used to deliver significantly high sensitivity to fatigue cracks as well as effective linear suppression.

4) As a consequence of promising results seen in the proposed coherent imaging method, further investigation into its efficacy of crack growth monitoring was made along with the diffuse energy technique. The capability of crack sizing and early detection was explored. Additionally, some surface breaking cracks grown in different samples were used to examine the applicability of this technique.

CHAPTER 2-MONITORING OF FATIGUE CRACK GROWTH USING NONLINEAR ULTRASONIC DIFFUSE ENERGY IMAGING

2.1. Introduction

As indicated in literature review, previous works described nonlinear ultrasonic diffuse energy imaging (NUI) technique and showed its potential for the detection of small defects within aluminium specimens [Potter et al., 2014]. In this chapter, the sensitivity of NUI to microscale defects within noisier materials (e.g. mild steel) and the quantification of the earliest point at which detection is achieved are demonstrated in a fatigue test. The accuracy of crack sizing achievable was also explored by identifying their actual sizes using micrography. The NUI technique was implemented alongside a conventional linear imaging technique, termed total focusing method (TFM) for comparison purposes [Holmes et al., 2005]. Indeed, it is shown that the same array used with a standard commercially available array controller can be used to produce co-located linear and nonlinear images. In this way, the nonlinear image can be seen as providing complementary information, which can be used in conjunction with the conventional linear information.

Specifically, the linear and nonlinear imaging techniques are applied to the periodic monitoring of steel compact tension specimens subjected to high cycle fatigue loading. The results suggest that NUI is more sensitive than conventional ultrasonic imaging to the microscale changes occurring at the early stages of failure, i.e. detectability starts c. 15% of fatigue life. In addition to early detection, the potential for NUI to deliver accurate sizing of fatigue cracks and monitor crack propagation is also presented.

2.2. Linear (TFM) and nonlinear (NUI) imaging

In a typical commercially available array controller, two alternative modes of operations are possible. In parallel mode, independently controlled circuits allow the firing of transmitter elements in a pre-set sequence termed a delay law. Similarly, these, or other, delays can be applied to the received signals on reception to form an image. The use of this mode of parallel firing and delays on transmission results in a high intensity beam forming in the specimen that can be controllably translated, steered or focused. Alternatively, sequential transmission and capture can be used and the time-domain signals from all the individual combinations of transmitter-receiver pairs captured one after the other. This so called full matrix capture (FMC) [Holmes et al., 2005] data can then be post-processed to form an image. The key difference here is that, as the signals from individual elements are transmitted separately, in this sequential mode the high amplitude focus is not physically generated in the sample. If the test structure is time invariant and the principle of linear superposition holds, these two modes of operation yield identical images.

The NUI technique capitalises on the physical difference in amplitude of the waves at the focal point if the parallel and sequential modes are compared (see fuller details in Subsection 1.4.2.6.3). It is apparent that the pressure amplitude, A, at the focus, is of the order of N times higher in the parallel case, where N is the number of elements in the array. Considering the case of classical third order strain energy, since the amplitude of any second harmonic wave generated is proportional to A^2 and the energy of the wave is proportional to A^2, the amount of energy in the second harmonic wave, is proportional to A^4. Furthermore, since the energy is conserved, the amount of energy lost from the fundamental will be N^3 times higher in the parallel case. Note that in practice higher harmonics could exist and these would result in further energy loss from the fundamental. In the NUI technique the energy in the fundamental is measured as the integral of A^2 over some time window which is set to be within the diffuse field, i.e. at a time after which the energy is uniformly distributed within the sample.

The requirement to measure the energy of the diffuse field means that the selection of reception start time t_r (the time instant when each element starts to receive signals) and window length T (the time length corresponding to duration of the time domain signal each receiver acquires) is particularly important. There are two competing effects. First, the acoustic field only slowly tends to the diffuse field condition with time. Second, as wave propagation is dissipative, the signal-to-noise ratio will decrease with time. Ultimately, compromise values of t_r and T must be found such that a diffuse field condition is achieved and the amplitude is acceptable, i.e. the signal-to-noise ratio is sufficient.

Assuming $f_{n,m}(t)$ are the time-domain received signals for each combination of transmit (n) and receive (m) elements in the sequential case. $\delta_n^T(r)$ is the transmission delay applied to the nth element to achieve a focus at a point r. Also, $g_m(r,t)$ is the time-domain signal received on element

m for the parallel transmission of all elements delayed independently by $\delta_n^T(r)$. The frequency (ω) domain versions of $f_{n,m}(t)$ and $g_m(r,t)$ are given by $F_{n,m}(\omega) = \int_{t_r}^{t_r+T} f_{n,m}(t) e^{-i\omega t} dt$ and $G_m(\omega) = \int_{t_r}^{t_r+T} g_m(t)\, e^{-i\omega t} dt$, respectively.

The energy content of the fundamental is then found from integration of the amplitude squared across the frequency domain from $\frac{2}{3}\omega_0$ to $\frac{4}{3}\omega_0$. These integration limits are chosen to exclude nonlinear energy flux within the evaluated bandwidth and maximise the ultrasonic energy incident at the focal point. This is because the internal movement of energy to subharmonics or superharmonics does not contribute to the evaluation of fundamental energy loss. Consequently, the diffuse acoustic energy in the sequential focusing case E_s at focal point, r for an N element array is given as:

$$E_s(r) = \sum_{m=1}^{N} \left(\int_{\frac{2}{3}\omega_0}^{\frac{4}{3}\omega_0} \omega^2 \left| \sum_{n=1}^{N} F_{n,m}(\omega) e^{i\omega \delta_n^T(r)} \right|^2 d\omega \right). \tag{2.1}$$

Likewise, the parallel transmission energy E_p is calculated as follows:

$$E_p(r) = \sum_{m=1}^{N} \left(\int_{\frac{2}{3}\omega_0}^{\frac{4}{3}\omega_0} \omega^2 \, |G_k(r,\omega)|^2 d\omega \right). \tag{2.2}$$

Finally an image is formed by calculation of the nonlinear metric γ at a given imaging/focal point r [Potter et al., 2014]

$$\gamma(r) = \frac{E_s(r) - E_p(r)}{E_p(r)}. \tag{2.3}$$

The nonlinear metric γ at every focal point r is used to produce a full nonlinear image in the x-z plane (see figure 1(a) for axis definition). Alongside this a conventional TFM image (see fuller details in Subsection 1.4.1) of the same size is produced in order to visualise the linear features of the specimen, which the nonlinear imaging technique cannot display. The TFM image, $I(x, z)$, is given by:

$$I(x,z) = \left|\sum h_{n,m}\left(\frac{\sqrt{(x_n - x)^2 + z^2} + \sqrt{(x_m - x)^2 + z^2}}{c}\right)\right|, \tag{2.4}$$

where $h_{n,m}$ is the Hilbert transform of, $f_{n,m}$, the position of focal point $\boldsymbol{r}$ is defined in terms of x and z coordinates, c is the speed of sound and the summation is performed over all transmitters and receivers.

2.3 Experimental procedure

2.3.1 High cycle fatigue tensile test

As presented in figure 2.1(a), mild steel compact tension (CT) specimens were manufactured according to the ASTM standard E647-05 [ASTM International, 2006]. The initial notch was manufactured by electrical discharge machining (EDM) to create a stress concentration and is displayed in figure 2.1(b). The fuller details of its geometry are displayed in figure A.1. The type of the mild steel is chosen to be ASTM A36, which is commonly used in engineering industries for general structural purposes. The wave propagating speed in this steel has been found to be 5924 m/s by measuring the time at two successive peaks reflected from the back wall using A-scan. The load limits were then chosen to ensure that the specimen can fail in the high cycle fatigue regime. The maximum stress intensity factor K_{max} was selected as:

$$K_{max} = \frac{K_{IC}}{3}, \tag{2.5}$$

where K_{IC} = 65 MN/m$^{3/2}$ is the nominal fracture toughness of this steel [ASTM International, 2006]. The minimum stress intensity factor K_{min}, employing a stress ratio value of R=0.13 (where the stress ratio R is the ratio of the minimum and maximum load, P_{min} and P_{max}, per cycle), is estimated below:

$$K_{min} = RK_{max} = \frac{P_{min}}{P_{max}} K_{max}. \tag{2.6}$$

According to ASTM standard E647-05, the geometry factor of the CT specimen is given, and consequently the stress intensity factor range *ΔK* is given as:

$$\Delta K = \frac{\Delta P}{B\sqrt{W}} \frac{(2+\alpha)}{(1-\alpha)^{\frac{3}{2}}} (0.886 + 4.64\alpha - 13.32\alpha^2 + 14.72\alpha^3 - 5.6\alpha^4), \tag{2.7}$$

where $\Delta P = P_{max} - P_{min}$, *B* is the thickness of the specimen (25 mm) and *α*(=*a*/*W)* is the ratio of the distance from the load bearing point to the notch or crack tip (*a*=22 mm), and the width of CT specimen (*W*=50 mm). The dimensions of *B*, *a* and *W* are illustrated in figure 2.1(a).

Therefore, the load was varied between 2 kN and 15 kN (P_{min} and P_{max}) in a hydraulic tensile testing machine (Instron 8800MJ6272, UK) at a frequency of 3 Hz. In addition, once the test was stopped (in order to allow the linear and nonlinear ultrasonic imaging) after a prescribed number of cycles, the metallographic preparation was completed in the vicinity of the crack tip by fine grinding using silicon carbide paper as well as further fine abrasion using polishing cloth with a 3 µm monocrystalline diamond suspension. Note that acetone was used to clean the surface following each cycle of abrasion or polishing. After polishing to a scratch-free mirror finish, the microstructure around the crack was then observed by a microscope (Zeiss Axio Imager 2, Germany) and, consequently, the crack length was monitored periodically during the fatigue test.

2.3.2 Ultrasonic inspection

The ultrasonic inspections utilising NUI and TFM imaging were implemented by positioning an array on the top face above the end of notch as shown in figure 2.1(a). All the inspections were performed with a 64 element ultrasonic array (Imasonic, France) with nominal centre frequency of 5 MHz, (-6 dB bandwidth 86% of the centre frequency), and pitch of 0.63 mm, as well as an array controller (Peak NDT Micropulse FMC, UK). This experimental setup is consistent with the one from [Potter et al., 2014], which is expected to provide good sensitivity to linear and nonlinear features on the CT sample in close size. It should be noted that the gate start time, t_r, depends on the geometry of specimen, random noise and material properties, since the time to reach the diffuse field varies with these. By examining the efficacy of NUI on the given nonlinear and linear features on this CT specimen during experiments, empirically appropriate parameters for the NUI imaging were chosen as window length, T of 0.12 ms with the gate start time, t_r, at 0.1 ms, providing a compromise between diffuseness and signal-to-noise ratio. Note that the values of T and t_r were modified independently in this parametric study and the corresponding imaging performance was estimated by observing the nonlinear metric close to a fatigue crack relative to that of an undamaged area. Since the incoherent (i.e. time varying and random) noise has more influences on measurability of a diffuse wave at lower amplitude, reception gains for parallel and sequential transmission were adjusted correspondingly to ensure the consistency of their received amplitude intensity. Consequently, the parallel and sequential gains were selected as 42 dB and 59 dB respectively, which received similar amplitude at high intensity (without saturation). The voltage was input as 200 v to maximise the transmission energy, instrumentally leading to the largest difference in nonlinear response between parallel and sequential focusing. Sample bit rate was 16 bit/s and sampling frequency was 25 MHz, which provides sufficient horizontal and vertical precision of the digital waveform in this case. Also, the pulse repetition frequency was selected as 500 Hz, which allows the wave energy remaining in previous transmission cycle to dissipate for a longer period prior to the next firing. Furthermore, the TFM imaging technique was performed on the side of specimen parallel to the crack face (as presented in figure 2.1(a)). As a consequence of a larger reflecting surface in this orientation, this gives rise to the best case scenario for linear inspection, however it should be noted that this arrangement is often not practically realisable due to access limitations (e.g. single-sided access towards orientation of surface breaking cracks in application to pipeline and pressure vessel inspection).

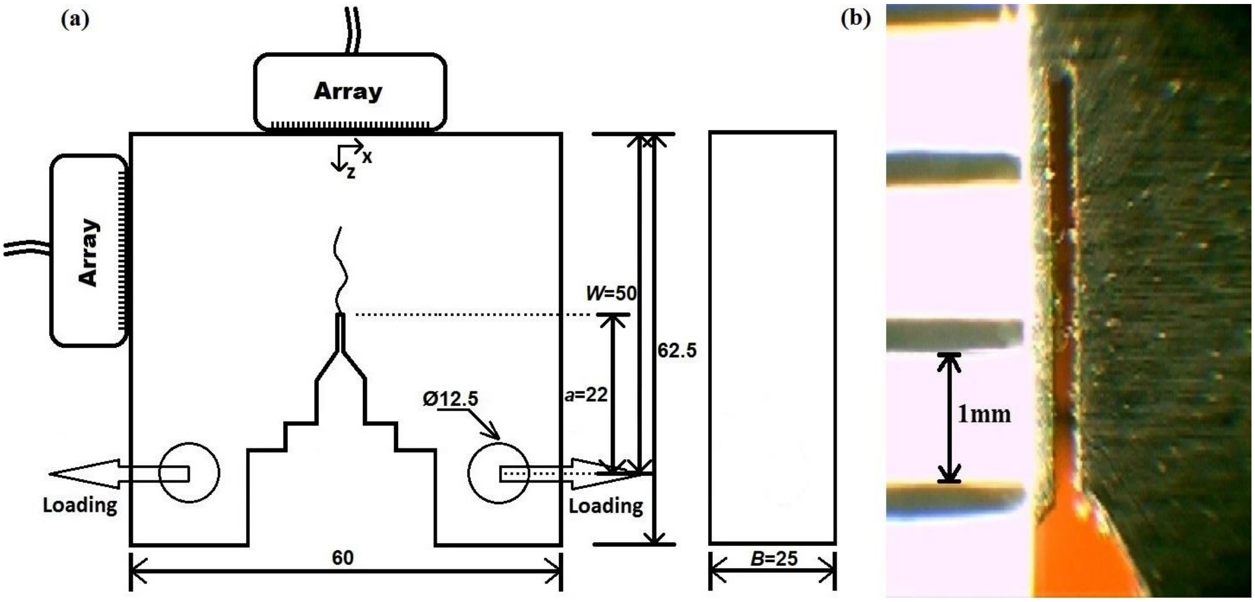

Figure 2.1. (a) Schematic diagram of nonlinear and linear phased array measurement configuration on CT specimen (dimensions in mm) and (b) photograph (zoomed in with a millimetre scale) of the 0.1 mm wide notch on the CT specimen before fatigue test.

2.4 Experimental results

2.4.1 Life monitoring

A mild steel CT specimen was subjected to cyclic loading in order to ascertain the performance of NUI and TFM imaging with crack growth. The fatigue test continued until the specimen failed with a prescribed opening angle, 5 degrees, in order to estimate the life span based on the specified high cycle fatigue loading. This allows linear and nonlinear metrics to be related to the fatigue life in addition to crack size.

Before the start of fatigue test, the specimen was inspected using linear TFM and the NUI technique, shown in figures 2.2(a) and (b) to understand the background noise level and the characteristics of the baseline geometric features.

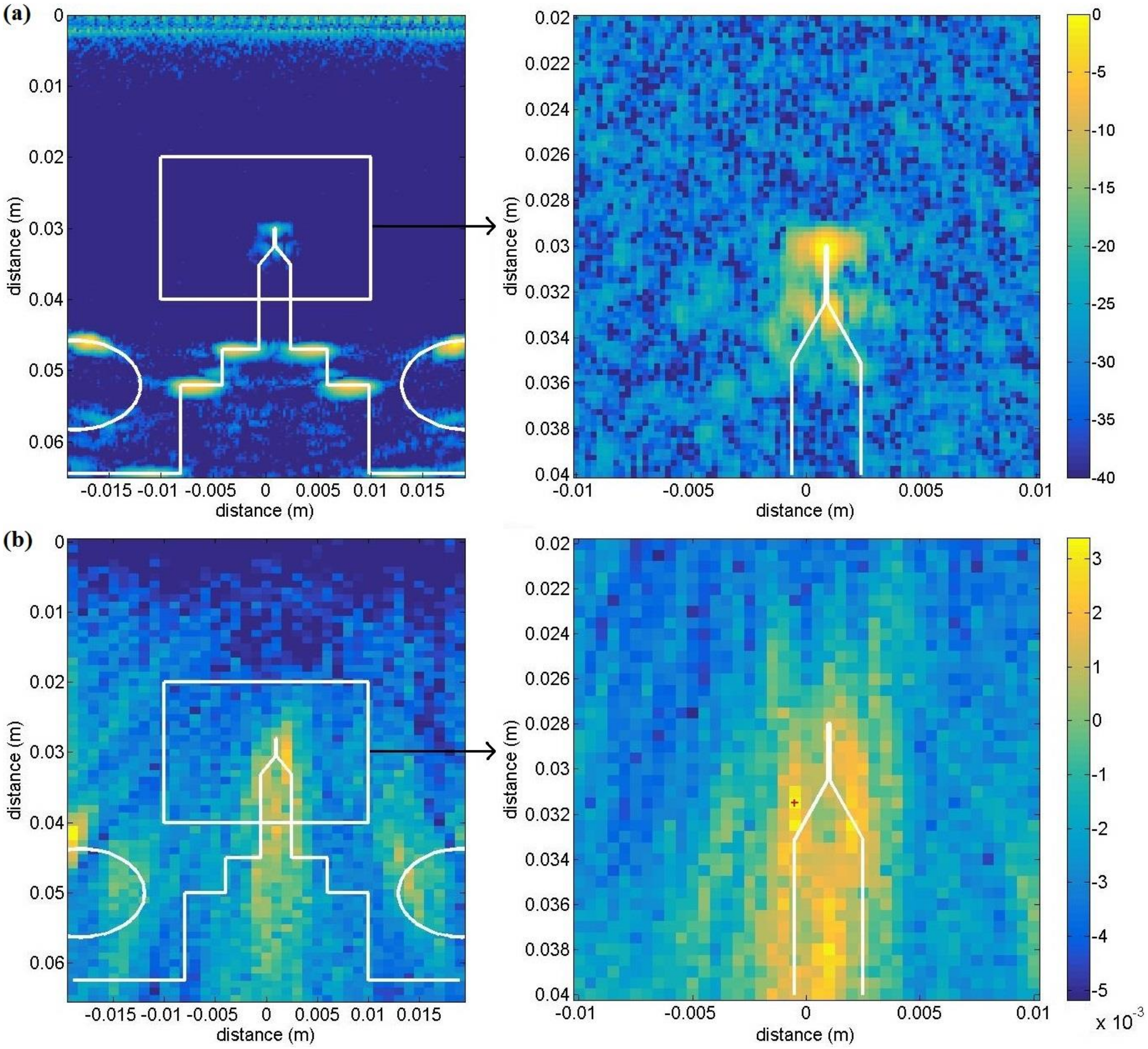

Figure 2.2. Nonlinear and linear images prior to loading. (a) Linear TFM images on a dB scale (b) Nonlinear images of the nonlinear metric, γ.

The grain structure of mild steel contributes to energy absorption, increasing the effect of incoherent (i.e. time varying and random) noise on diffuse field measurements as well as generating coherent (i.e. scattering form the grain structure) noise in linear images in comparison to finer grained materials such as Aluminium. Therefore, the background levels presented in figures 2.2(a) and (b), will inevitably mask some nonlinear and linear features and set detection thresholds. It is likely that time-variant perturbations to the system, for example through environmental changes, between parallel and sequential acquisitions also contribute to the nonlinear background levels. Additionally, in spite of higher reception gain used in sequential capture over the parallel one, incoherent noise still has a proportionally larger contribution to the, lower amplitude, sequential measurements since the amplitude of propagating sequential waves is more likely to be close to or below the noise floor. This leads to imperfect subtraction of parallel/sequential fields, reducing the ability to suppress linear features, as is evident by the presence of background response coinciding with linear features. As would be expected, the linear TFM image in figure 2.2(a) shows the linear scattering from the geometric features of the specimen and the amplitude in figure 2.2(b) gives an indication of how well these features are suppressed.

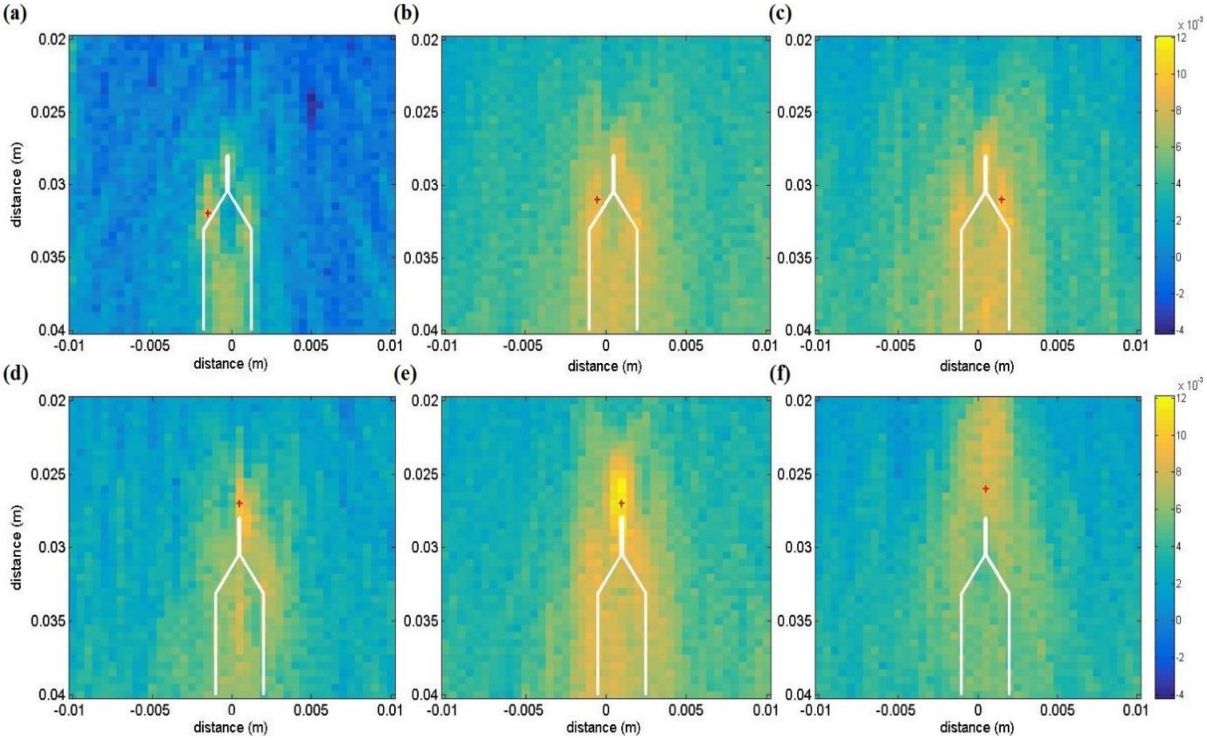

Figure 2.3. Nonlinear images in nonlinear metric γ at (a) 20000, (b) 30000, (c) 50000, (d) 70000, (e) 90000, and (f) 130000 cycles. Note that the red cross represents position of the maximum γ.

The fatigue experiments were stopped at the completion of 20000, 30000, 50000, 70000, 90000 and 130000 cycles in order to perform the NUI (see figures 2.3 (a-f)), with eventual failure occurring at 135500 cycles. Figures 2.3(a-c), cover the period up to 50000 cycles, which is thought to correspond to crack nucleation and initial growth. In this initial fatigue region, the amplitude of the nonlinear metric can be seen to increase by double the maximum background level with the maximum nonlinearity occurring in the vicinity of the initiation notch. Figures 2.3(d-f) show the position of maximum nonlinearity (indicated by the red cross) moving ahead of the initiation notch, suggesting more extensive cracking. In all cases, it is likely that the nonlinear response observed (up to four times the maximum background level) is predominantly a consequence of contact-acoustic effects [Cantrell and Yost, 2001]. Figure 2.3(f) shows that at 130000 cycles the position of maximum nonlinearity has reached 2 mm from the starter notch tip and its amplitude has decreased somewhat relative to earlier points in the fatigue life. This late-life amplitude effect is likely a consequence of the crack beginning to open as the sample nears failure, resulting in fewer contact points and reduced instances of nonlinear contact acoustic effects. The sample failed shortly after commencing cycling beyond 130000 cycles.

A linear TFM image was performed with the array located on the top of the sample as shown in figure 2.4(a) and this revealed no significant changes in linear scattering above the end of the initiation notch throughout the crack growth. Although some evidence of the defect is provided by shadowing effects close to notch tip caused by diffraction at the crack there is an unclear indication as well as no sizing information. This demonstrates a clear example of the NUI technique having increased sensitivity over a high performance traditional linear technique (i.e. TFM).

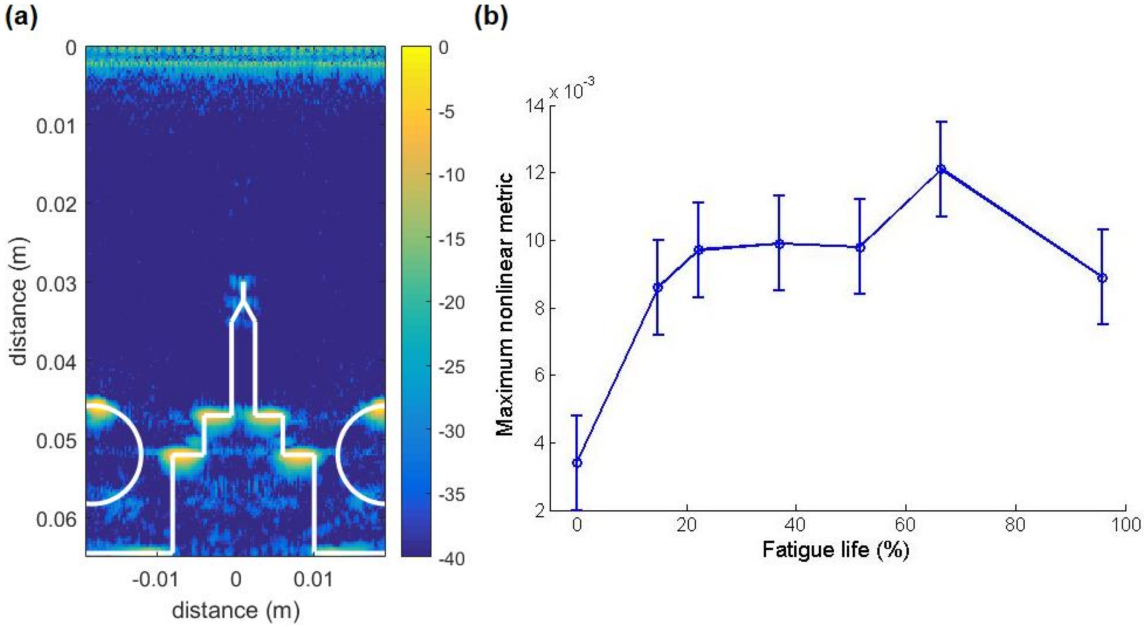

Figure 2.4. (a) Linear TFM image at 130000 cycles on a dB scale and (b) maximum nonlinear metric, γ, as a function of % fatigue life (error bar represents an averaged standard deviation).

As shown in figure 2.4(b), the relationship between change in the maximum acoustic nonlinearity and fatigue life demonstrates that the acoustic nonlinearity generally increases until it reaches around 70% of fatigue life). Error bars denote a single standard deviation of peak nonlinear amplitude. This standard deviation is calculated for multiple image acquisitions (between 3 and 5) at each sample point, then averaged over all points. The error bars provide a measure of repeatability for a specimen in a given state, but not between different specimens.

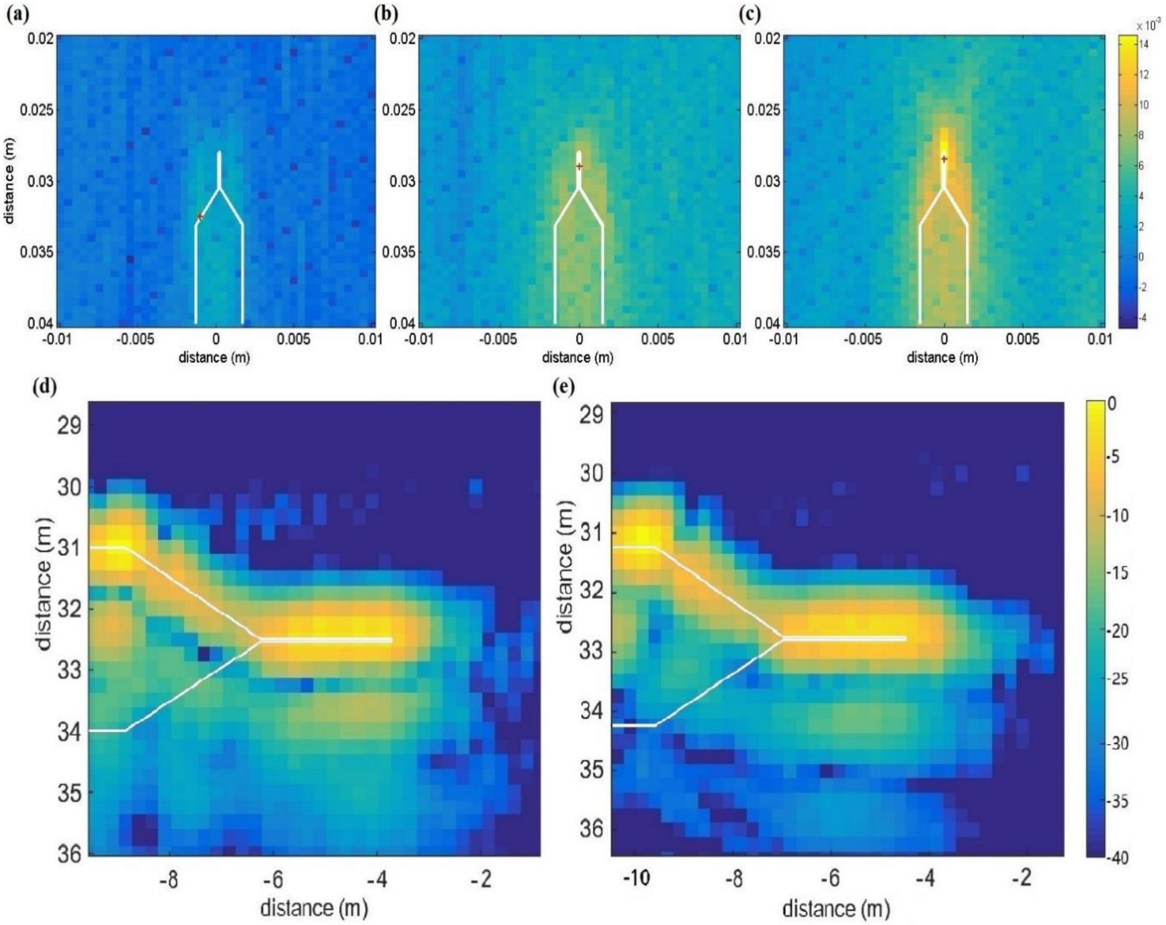

Figure 2.5. Nonlinear images in nonlinear metric, γ at (a) 5000, (b) 20000 and (c) 40000 cycles. Note that the red cross represents position of the highest γ. Linear images from left side view at (d) 0 and (e) 20000 cycles.

2.4.2 Early detection investigation

The previous study evaluated the efficacy of imaging throughout the whole fatigue life. A further test was conducted in order to more closely study early stages of crack growth and explore the limits of detectability. The loading step was reduced to 5000 cycles in order to ensure the early stage damage is monitored and detection performance could be investigated.

The results in figures 2.5(a-c) demonstrate nonlinear features consistent with those seen in Subsection 2.4.1. Initially the crack, which was barely visible in figure 2.6(a), could not be detected with NUI or the TFM technique. The earliest detection was at 20000 cycles where the maximum nonlinearity was near the end of the notch. The micrograph in figure 2.6(c) was taken at 20000 cycles and shows that the crack tip was at 251 µm above the initial notch end. The location of the maximum nonlinearity then remained within 1 mm of the crack tip from 20000 cycles to 40000 cycles. It should be noted that the fundamental transmitted wavelength is 1.2 mm, which potentially contributes to the error in its localisation. It should also be noted that in this experiment the crack propagation was more likely to generate small branches due to slight variations in loading condition caused by relatively frequent removal and mounting among all the steps. The branches which might not exist before 40000 cycles in the previous test may contribute to the small difference in acoustic nonlinearity observed when figures 2.3 and 2.5 are compared. Therefore, the difference in the maximum nonlinear metric at the same cycles (from figures 2.4, 2.7 and 2.9) results predominantly from sample-to-sample variations.

The features of diagonal spots as displayed in figures 2.5(a-c) are a consequence of reduced focused capture number (the number of focal point per parallel acquisition). When each set of parallel data is captured some energy from the previous parallel transmission remains, which increases the amount of energy recorded in the next set. The delay between sets of acquisitions is much longer, so that this energy dissipates. Consequently, the first pixel of each acquisition set possesses lower nonlinear metric. Note that although a decrease in pulse repetition frequency as well as a reduction in focused capture number could be used to suppress this effect the pulse repetition frequency has been selected as the lowest and a reduction in focused capture number increases total acquisition time, which also gives a rise to coupling change. From Subsection 2.4.2, a compromise focused capture number was chosen as 16 rather than 64 used in Subsection 2.4.1.

Figures 2.5(d) and (e) show the linear TFM images produced through positioning the array at the left side (see figure 2.1(a)). Despite the advantageous array positioning, the linear array imaging is not able to detect the increase in crack length clearly at 20000 cycles due to coherent noise and blurring due to the finite point spread function.

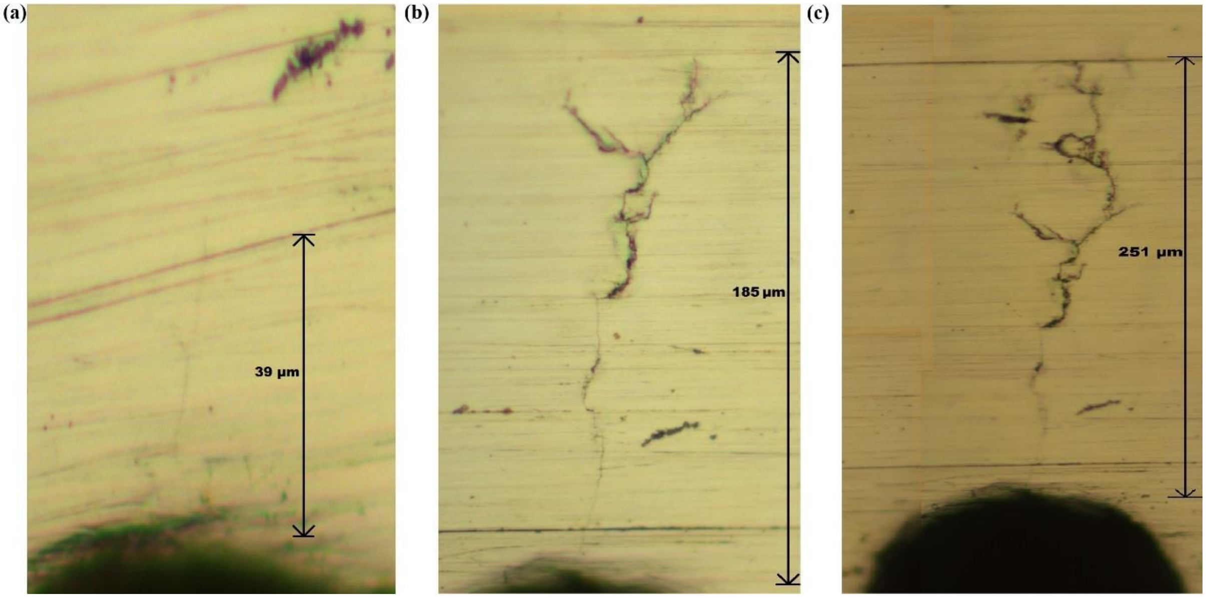

Figure 2.6. Micrographs of the fatigue crack at (a) 5000, (b) 15000, and (c) 20000 cycles. Note that the scale is different in each image.

Figures 2.7(a) and (b) show that the maximum nonlinearity at each early fatigue step increases with crack growth from 5000 cycles to 40000 cycles, which is consistent with the results in section 2.4.1. It can be seen that the crack tip became detectable from 15% of its fatigue life (20000 cycles). Here detectability was defined as the first measurement with a lower error bar that exceeded the upper error bar of the zero-load condition. From figure 2.7(a) this detection limit can be seen to correspond to a crack length of between 200-250 μm. It is also worth noting that nearly the whole of figure 2.7 is below the commonly quoted half-wavelength limit for linear detectability (i.e. 600 μm in this case).

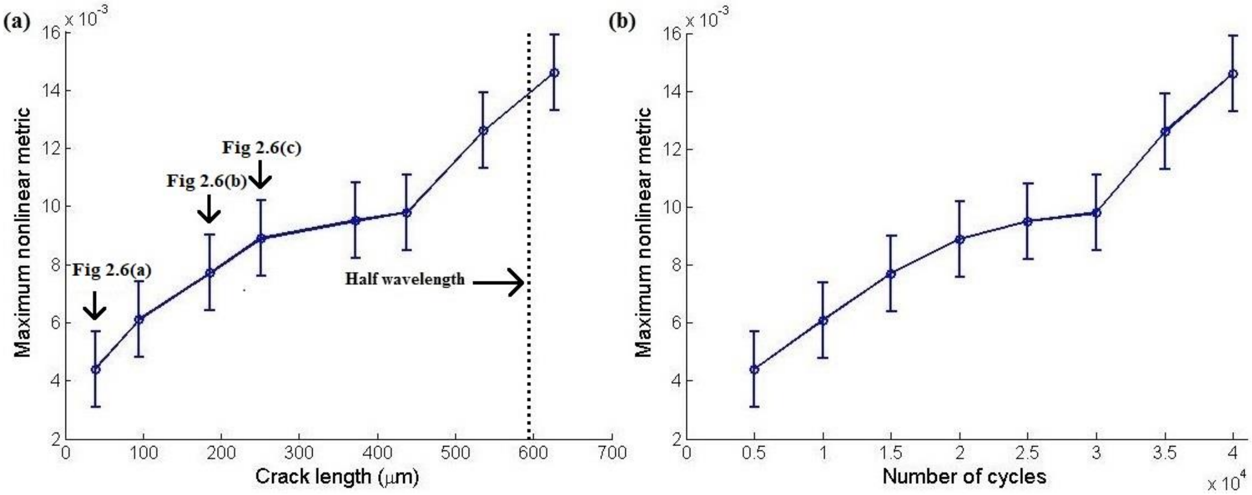

Figure 2.7. Maximum nonlinear metric γ during fatigue as a function of (a) crack length and (b) number of fatigue cycles (error bars represent an averaged standard deviation).

2.4.3 Sizing analysis

Though not diffraction limited in the classical sense, subwavelength geometric features cannot be resolved directly in a nonlinear image. For such features the image produced is that of the associated point spread function for the technique. The existence of the point spread function should arise from parallel and sequential focusing of long excitation pulses. For this very early stage crack growth, crack size may only be inferred from the amplitude of nonlinear response, as demonstrated in the previous section. As crack length increases beyond the order of half a wavelength, the region of nonlinear contrast within the image increases in size, allowing for direct sizing of defects from nonlinear images.

This section investigates the sizing of small cracks which corresponded here to loading from between 40000 and 100000 cycles. Figures 2.8(a-d) show the nonlinear images in this loading range at increments of 20000 cycles. Noticeably, the maximum magnitude of the nonlinear metric increases almost linearly with crack growth from 40000 cycles to 100000 cycles (as shown in figures 2.9(a) and (b)).

The position of peak nonlinear amplitude and the actual crack tip location as measured from micrographs are indicated in figure 2.8 as red and black crosses respectively. The location of highest nonlinearity is consistently at approximately 1 mm below the actual crack tip. This is not necessarily indicative of the location of maximum nonlinear response. When focusing at the crack tip, less of the crack lies under the footprint of the focal region (see figure 2.10), reducing the measured nonlinear response. Aside from this offset, the location of peak nonlinearity is seen to correspond very closely with the actual crack tip location measured from surface micrographs, as is shown in figure 2.9(c).

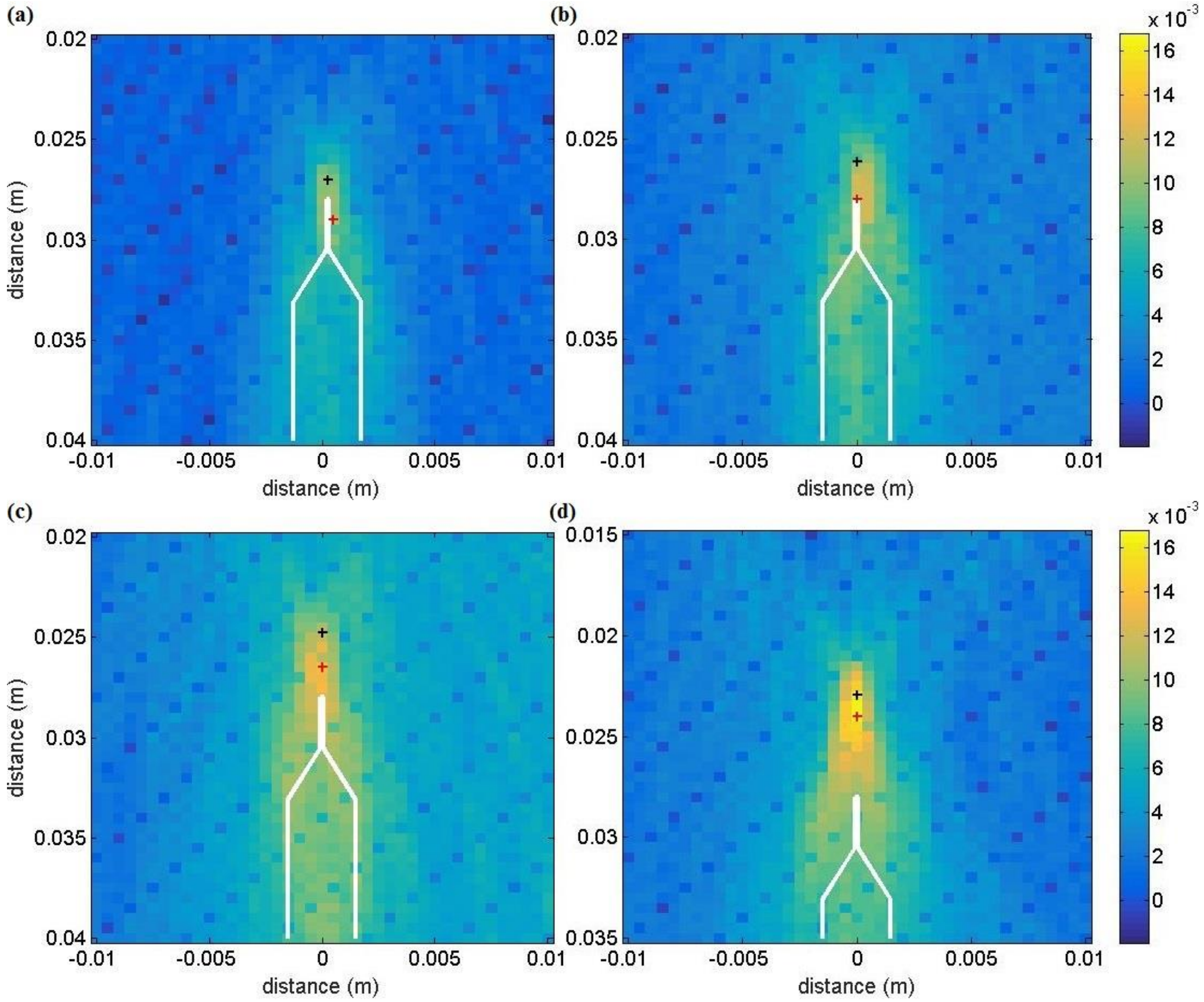

Figure 2.8. Nonlinear images in nonlinear metric γ at (a) 40000, (b) 60000, (c) 80000, and (d) 100000 cycles. Note that the red cross and black cross represent positions of the highest γ and the micrographically measured crack tip respectively.

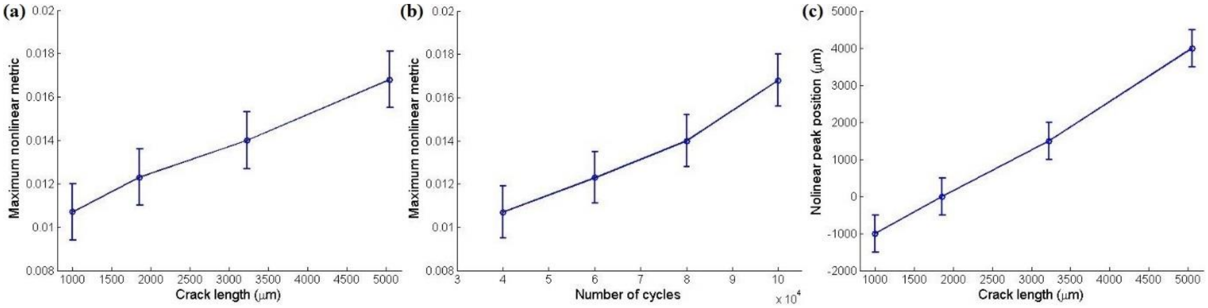

Figure 2.9. Maximum nonlinear metric γ during fatigue as a function of (a) actual crack length and (b) number of fatigue cycles. (c) Measured crack length from the NUI image (notch end to position of maximum nonlinear metric γ) during fatigue as a function of micrographically measured crack length (error bar represents an averaged standard deviation).

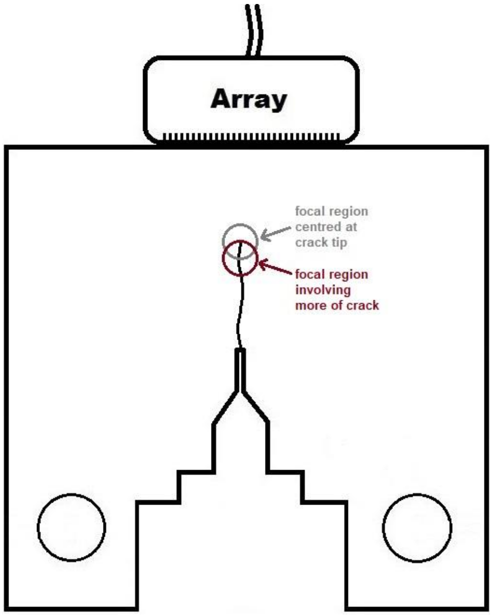

Figure 2.10. Illustration of focal region centred at or below crack tip.

2.5 Conclusions

The experimental results presented show that monitoring fatigue crack growth in mild steel using the NUI technique was effective from 15% fatigue life. The NUI technique was performed using a commercially available array and array controller. The same instrumentation was also used to simultaneously produce traditional high resolution linear TFM images. These linear images did not reveal any detectable changes throughout their fatigue life at the same inspection position. The amplitude of nonlinearity was shown to be a measure of progress of the very early stages of fatigue crack growth. The experiments showed that statistically significant amplitude increases were measurable for cracks of 250 μm length and greater. As crack growth continued the location of maximum nonlinearity was used to measure the extent of the cracking. For these larger cracks the NUI technique becomes a form of nonlinear imaging, mapping out the extent of a given crack. As the same phased array system (including an array probe connected to a controller) is used at the identical inspection point, linear and nonlinear images can be produced simultaneously, and these contain complementary information. The linear images will reveal essentially geometric information from sample boundaries and large defects, whereas the NUI images will reveal nonlinear features such as partially-closed cracks and crack tips. The NUI results were obtained with the array positioned directly above the crack, an orientation that typically results in poor linear imaging as the signals reflected directly from the crack tip are small. It has been noted however that the orientation used in NUI is beneficial as it reduces access limits relative to traditional linear array imaging (which would typically be performed as an angle inspection). The NUI technique therefore both improves sensitivity and reduces access limitations making it a viable prospect for *in-situ* or permanent fatigue monitoring of, for example, pipework or pressure vessel welds.

CHAPTER 3-OPTIMISATION OF NONLINEAR ULTRASONIC DIFFUSE ENERGY IMAGING

3.1 Introduction

The previous chapter demonstrates the performance of nonlinear ultrasonic diffuse energy imaging (NUI) on monitoring fatigue crack growth in mild steel. The results suggest that the crack can be detected from 15 % of its fatigue life and the technique was able to identify its size quantitatively. However, the parameters used in NUI (i.e., the reception bandwidth used in post-processing, gate start time, t_r and window length, T) were empirically determined by examining the technique on well-studied samples (i.e. the existence of a defect is known). In different industrial applications, the optimum parameters will vary on a case-by-case basis, predominantly depending on material properties, specimen geometry, boundary condition and instrumentation noise. In addition, volumetric defects, such as voids or inclusions, necessitate detection with a more sophisticated three-dimensional imaging method, in order to improve inspection efficacy and efficiency. Therefore, this chapter will describe a suite of parametric studies for optimising NUI in terms of its performance as well as methods for characterising a diffuse field and realising in three-dimensional imaging which will extend the practical applicability to different structures.

3.2 Key parameter study

In this section, four of the most important parameters: (1) aperture size of ultrasonic array, (2) data averaging in sequential transmission, (3) reception bandwidth and (4) centre frequency used in post-processing, were studied by changing one variable independently and examining its corresponding imaging performance with the proposed metric. The same experimental configuration as illustrated in figure 3.1 was used in this study. The core objective was to facilitate the appreciation of these parameters according to their signal-to-noise performance and design a strategy to choose the optimum parameters on a case-by-case basis.

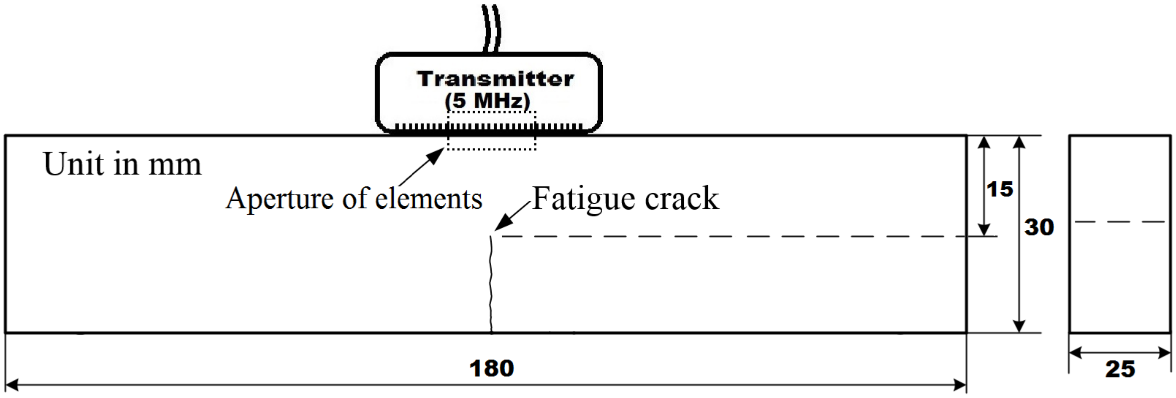

Figure 3.1. Schematic diagram of NUI measurement configuration on aluminium specimen subjected to fatigue tensile test (dimensions in mm).

The size of an aperture (middle subset of all the array elements as presented in figure 3.1) strongly affects the performance of the NUI method, so that an adequate size is particularly important for each practical application. Here an adaptive method is used to examine the aperture size required for different targets (e.g. a fatigue crack as shown in figure 3.1). Metrics used to assess the proposed method will be compared and discussed.

Data averaging is defined here as a repeat process of signal transmission and capture following by averaging over a number of repetitions. The number of averages (known as repetitions) delivers the suppression of incoherent noise. The incoherent noise is caused by many factors such as coupling conditions and electrical random noise from the instrument. However, averaging can reduce their amplitude level by a factor of $1/\sqrt{N}$ (equivalent to $1/N$ in energy), where N is the number of averages taken (i.e. number of firings in NUI). Sequential transmission is influenced more significantly by this noise due to the small amplitude of the emitted signal (i.e. only one element emits at a time). In parallel transmission multiple elements are fired and so the amplitude of the waves in the sample are larger (than for the sequential case) and hence less averaging is needed to obtain the same signal-to-noise-ratio.

To minimise the effect of incoherent noise, the other alternative is to apply different reception gains to sequential and parallel captures (a higher gain at sequential reception), so that the intensity of received amplitudes are matched (as shown in figure 3.2(a)), which means the contribution of random noise is approximately the same. Finally, the sequential data are normalised by applying the same reception gain used in parallel capture to obtain the actual energy (as presented in figure

3.2(b)). Since the number of firings in one parallel transmission cycle is N times higher than that in single sequential transmission cycle and the diffuse wave field arises from superposition of uncorrelated waveforms, the parallel diffuse field will have the root mean square (RMS) amplitude $\sqrt{N}$ times higher than the sequential, which would suggest a theoretical relative increase in reception gain of 18 dB for sequential captures of a 64-element array. But, this gain is not as reliable as the averaging, although it is much less time consuming as a consequence of less captures required. Specifically, errors (up to 3 dB) have been found to be present when the gain strategy is adopted and all the incoherent noise has to appear after the gain stage of the signal chain [Potter and Croxford, 2018].

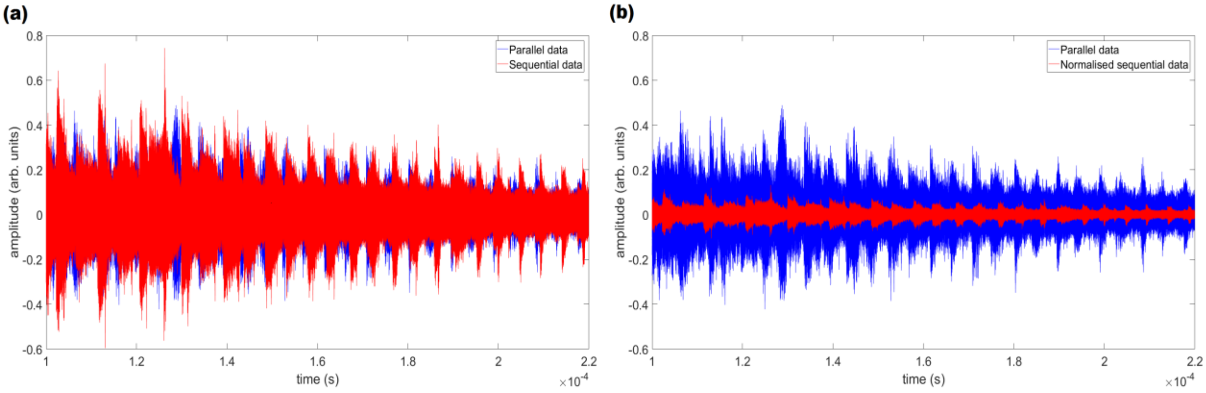

Figure 3.2. (a) Example time traces of parallel data (in blue line) and sequential data (in red line), and (b) example time traces of the same parallel data (in blue line) and the normalised sequential data (in red line).

Further, investigations into the post-processing filter used in NUI (as described in Chapter 1) will now be presented. The comprehensive studies on its bandwidth and centre frequency were conducted by evaluating the signal-to-noise performance with the proposed metric (signal-to-noise ratio for NUI). Again, these two parameters are chosen to effectively measure the remaining waves at the fundamental frequency by minimising the contributions from internal movement of energy within the evaluated bandwidth. Whilst a bandwidth with the size (no less than two-thirds of centre frequency) and a nominal transmission centre frequency can be applied to the filter, their optimum sizes are required to be estimated by a systematic method because the actual characteristics of transmitted waveforms differ from the nominal ones over time and a compromise between the largest size of fundamental bandwidth and the smallest contributions from side transmission bands necessitates a judgement to be made, depending on many potential factors such as the asymmetric shape of measured transmit-receive frequency spectrum, properties of the bulk materials, characteristics of nonlinear defects and nonlinear metrics.

3.2.1 Experimental setup

All these studies will be conducted with the compact tension (CT) specimen, which was made of Aluminium Al2014 and was designed to generate high cycle fatigue cracks (manufactured and loaded by Dr. Liaptsis from UNDT group at University of Bristol) [Liaptsis, 2008]. It was subjected to cyclic loading from 0.5 kN to 6 kN for 75000 loading cycles and the measured crack length was 15 mm finally (as presented in figure 3.1). All the inspections were performed with a 64 element ultrasonic array (Imasonic, France) with nominal centre frequency of 5 MHz, (-6 dB bandwidth 86% of the centre frequency), and pitch of 0.63 mm, as well as a commercial array controller (Peak NDT Micropulse FMC, UK). The standard parameters for the NUI method were implemented constantly as follows: window length, T of 0.12 ms, reception start time, t_r, at 0.1 ms, focused capture number of 64, sampling bit rate, of 16, sampling frequency, at 25 MHz, pulse width, of 100 ns, reception gain at 25 dB and pulse repetition frequency, at 500 Hz. Two mini clamps (Wilko, UK) were applied to keep the array probe in firm contact with the specimen consistently. In addition, the centre of probe was aligned to the centre of the specimen surface (i.e. right above the fatigue crack).

3.2.2 Array aperture and data averaging

An imaging performance indicator is important in order to explore the effect of parameters on the performance of the nonlinear metric. The signal-to-noise ratio implemented in a linear phased array imaging technique may use the ratio of the target reflection amplitude to the average of the background noise level in the image [Holmes et al., 2005]. In traditional linear imaging, background noise arises from the coherent noise (time invariant interference with, for example, the grain scattering and the scattering from different wave modes) and the incoherent noise (any time varying random process). For conventional linear or nonlinear imaging based on the recorded amplitude of a scattered wave, incoherent and coherent noise appears directly as noise within the image space. However, because the evaluated quantity in NUI is normalised relative statistical energy, the background noise should be defined differently. The measurable difference, arising from inequivalent contribution of relative noise for parallel and sequential focusing, has an offset in the resulting nonlinear image (as shown in figure 3.3) [Potter and Croxford, 2018]. Therefore, the root-mean-square value of the nonlinear metrics rather than the average of absolute value is preferred to measure the background noise as the sign has no real meaning.

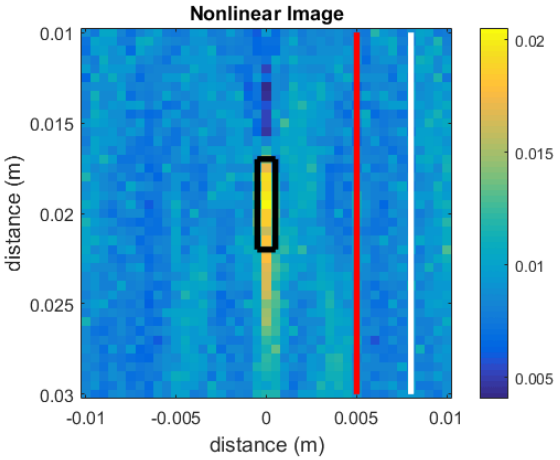

Figure 3.3. An example nonlinear diffuse energy image in nonlinear metric, γ.

The signal in signal-to-noise ratio (SNR) is defined as the peak nonlinear metric in the estimated target region and the noise is calculated from different sections of its surrounding pixels (as illustrated in figure 3.3). Notably, taking the peak nonlinear value from the cracked region allows the closest approximation to the measurement of a point-like nonlinear defect (the crack tip in this case). The black box in figure 3.3 indicates the cracked region in the well-known sample, however the peak nonlinear value in the whole image is thought to be selected for an unknown sample, which generally corresponds to the cracked region in a damaged structure. Further, four different signal-to-noise ratios, are proposed to evaluate the background noise level in a NUI image. The red and white lines in figure 3.3 are used to define different background noise, which are thought to cover different noise region in the nonlinear image. An example nonlinear image (as presented in figure 3.3), from which it can be seen that a discrete nonlinear elastic feature provides a nonlinearity much higher than the surrounding bulk material in nonlinear metric γ, is used to schematically explain definitions of the signal and the noise in SNRs as follows in table 3.1:

SNR(=Signal/Noise)	Signal	Noise
SNR_{all}	Peak nonlinear metric in the black box, indicating region around the crack tip	RMS value of the overall surrounding pixels (the entire undamaged region outside the black box)
SNR_{max}		Peak value of the pixels on the red line
SNR_{line}		RMS value of the pixels on the red line
SNR_{part}		RMS value of the pixels between the red line and the white line

Table 3.1. The definitions of signal and noise in each SNR.

Through generating a series of nonlinear images with different groups of array transmitters the sensitivity of aperture size can be examined. Their transmissions are achieved by electronically controlling the number of array elements, which are symmetric about the centre of the array, and their receptions keep consistent with the full capture mode (involving all the array elements in data capture).

The SNR_{all}, SNR_{max}, SNR_{line} and SNR_{part} measure the signal-to-noise performance with different selections of background noise. By examining the four different SNRs with changing aperture size and number of averages their significance can be evaluated comprehensively. Again, the averaging is only applied to the sequential transmission by capturing N sets of sequential data (N is the number of firings per parallel transmission cycle), for the sake of matched contribution from incoherent noise between parallel and sequential focusing. The aperture size was varied from 1 to 64. It was found experimentally that nonlinear metric, γ, regardless of the averaging was dominated significantly by the baseline of incoherent noise for under 8-elements because number of firings per parallel transmission cycle (i.e. number of averages in sequential transmission when the averaging is applied) is too small to generate signals above the noise floor. Therefore, noise suppression through averaging will have significance on this study only if the aperture size is adequate (e.g. not less than 8 here).

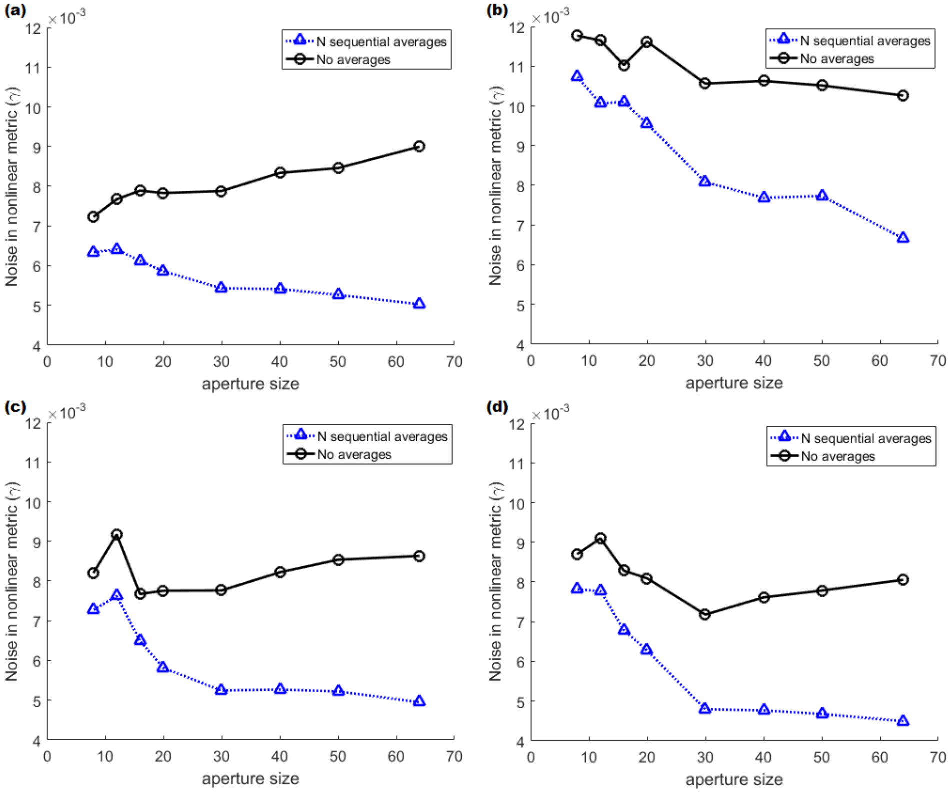

Figure 3.4. The background noise in nonlinear metric, γ, used in (a) SNR_{all}, (b) SNR_{max}, (c) SNR_{line} and (d) SNR_{part}.

The background noise used in SNR_{all}, SNR_{max}, SNR_{line} and SNR_{part} (representing overall noise, peak noise, linear noise and sectional noise sequentially) is first plotted against the aperture size (from 8 to 64) respectively in figures 3.4(a-d). The experimental results in figures 3.4(a-d) suggest that the noise after averaging (in blue lines) decreases with the aperture size and generally converges to 0.005 (except for the peak noise used in SNR_{max}) from the aperture size of 30. Again, the number of sequential averages, N, was equal to the number of firings in single cycle of parallel transmission, thereby matching the contribution from incoherent noise. Nevertheless, the noise without averaging in figures 3.4(a-d) behaves relatively constant with increasing aperture size. From figures 3.4(a-d), the change in ratio of noise with and without averaging in γ (roughly from

0.9 to 0.5) with increasing aperture size (equal to N from 8 to 64) implies close trend with the proposed optimum factor of $1/N$ (from 0.125 to 0.0156).

Note that the blue line indicates baseline noise from a nonlinear image with N sequential averages and the black line reflects the additional incoherent noise on top of the baseline noise due to no averaging performed at sequential transmission. In addition, the sequential averaging is thought to suppress the incoherent noise by the same level as the parallel focusing achieves. Therefore, the difference between blue and black lines provides an indication of the relative incoherent noise level between parallel and sequential focusing with the same reception gain. It should be noted that only the overall noise in figure 3.4(a) always increases gradually in the same manner as the theoretical perspective that the larger aperture size will reduce the relative incoherent noise between parallel and sequential focusing by higher factor (i.e. a symmetric relationship between the blue line and the black line is expected to be seen in figures 3.4(a-d)). As the symmetric relationship between the unaveraged background noise in the nonlinear metric and the averaged one is only observed from the overall noise as illustrated in figure 3.4(a) the following nonlinear imaging performance study will merely examine the $\mathrm{SNR}_{\mathrm{all}}$ as the most representative SNR.

Furthermore, the contribution of the relative incoherent noise between the averaged noise in the nonlinear metric and the unaveraged increases with the aperture size (see figure 3.5(a)). This exhibits good agreement with a model of theoretical incoherent noise contribution against aperture size [Potter and Croxford, 2018]. This model states that the theoretical incoherent noise contribution to the imaging metric γ can be expressed as a function of N and ϵ, where ϵ denotes a proportion of noise to the acoustic energy of a single sequential response. In addition, this relationship indicates that value of the theoretical incoherent noise contribution (i.e. relative incoherent noise between the averaged noise in nonlinear metric and the unaveraged) increases with aperture size.

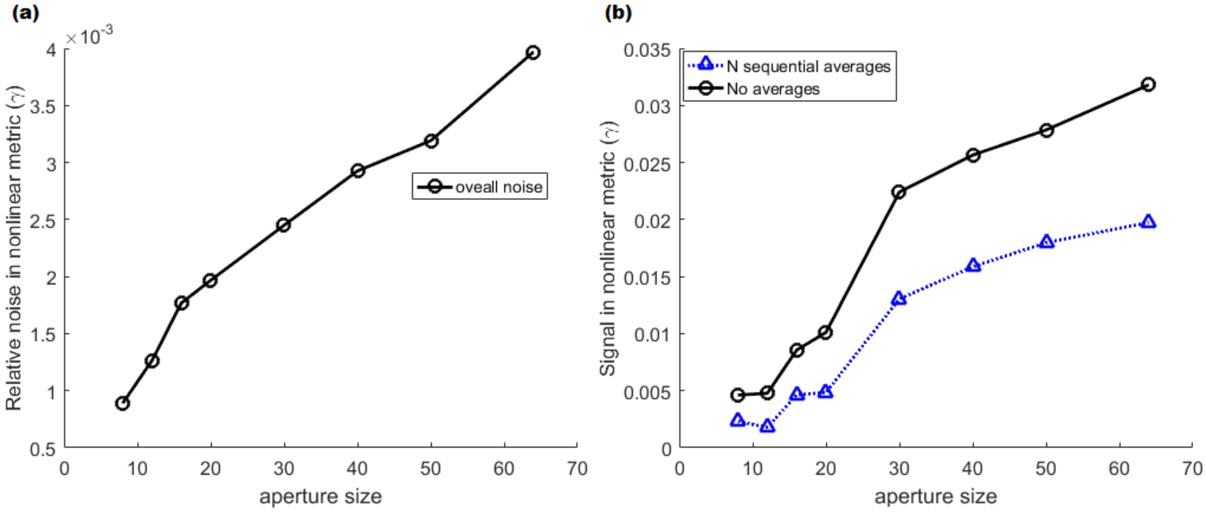

Figure 3.5. (a) The relative noise in nonlinear metric, γ and (b) the signal of $\mathrm{SNR}_{\mathrm{all}}$ in nonlinear metric, γ.

Again, the signal used in $\mathrm{SNR}_{\mathrm{all}}$ is calculated by taking the peak value from the specified region around the crack tip in corresponding nonlinear image with different aperture size and then plotted in figure 3.5(b). In addition, the blue and black lines in figure 3.5(b) indicate the signals in nonlinear metric with and without averaging in sequential transmission respectively. Their results suggest that sensitivity to the crack tip generally increases with the aperture size regardless of the averaging due to more total transmitted energy focused at the crack tip, however, the signal without averaging is notably larger than the one with averaging due to the superposition of their background noise and signal.

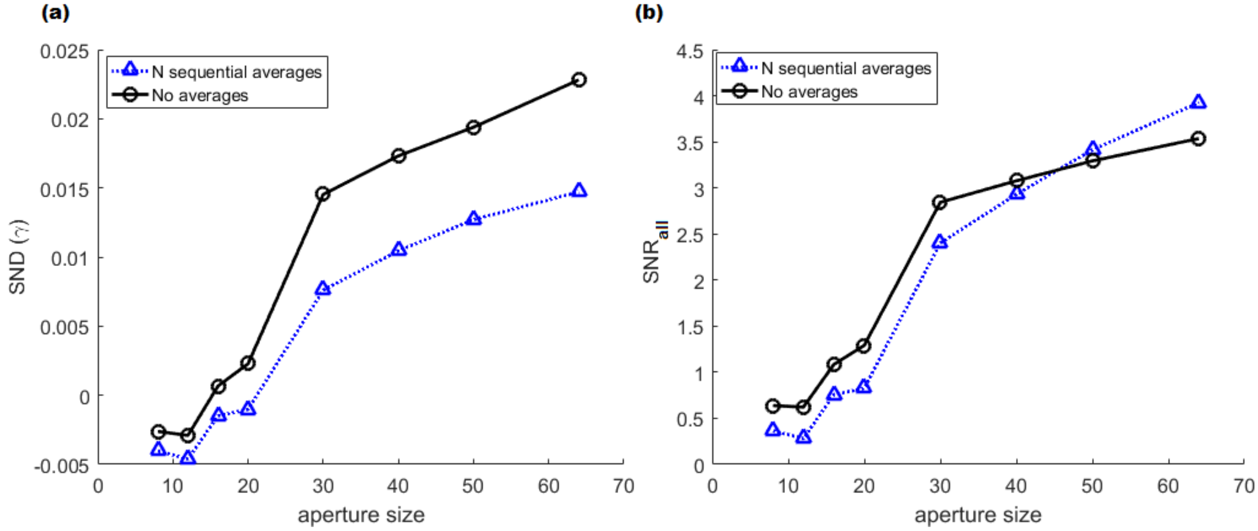

Figure 3.6. (a) The signal-to-noise difference, SND, in nonlinear metric γ, and (b) the signal-to-noise ratio, SNR_{all}.

The Signal-to-noise difference in nonlinear metric is initially examined by subtracting the corresponding overall noise from the signal. Its result as illustrated in figure 3.6(a) suggests that contributions of background noise as a proportion to its corresponding signal is always negligible because the trend is similar to that in figure 3.5(b). However, the relationship between SNR_{all} and aperture size (see figure 3.6 (b)) indicates that the background noise can be suppressed by greater percentage with increasing aperture size if the averaging is applied and the results displayed in figure 3.5(b) are compared. Consequently, the signal-to-noise performance can be improved significantly by taking averages in sequential transmission especially with a large aperture size.

3.2.3 Reception bandwidth and centre frequency

In post-processing as described in Section 2.2, reception bandwidth and centre frequency determine the imaging performance by balancing suppression of contributions from side transmission bands against maximisation of effective fundamental bandwidth, as a consequence of spectral leakage. Therefore, the SNR_{all} as the most promising indicator of imaging performance will be examined in this section. The generic strategy is to map SNR_{all} by post-processing the same parallel and sequential data and changing reception bandwidth and centre frequency in post-processing. Eventually, the map can be used to select the optimum reception band by locating the highest $\mathrm{SNR}_{\mathrm{all}}$ and this methodology is particularly useful in practice because of variations in the characteristics of the ultrasonic transducers, properties of materials and types of nonlinear defects and nonlinear metrics. For the experiment, the same aluminium sample was used to be inspected by the NUI technique and provide a set of sequential and parallel data (used for producing figure 3.7) in order to implement this bandwidth and centre frequency study.

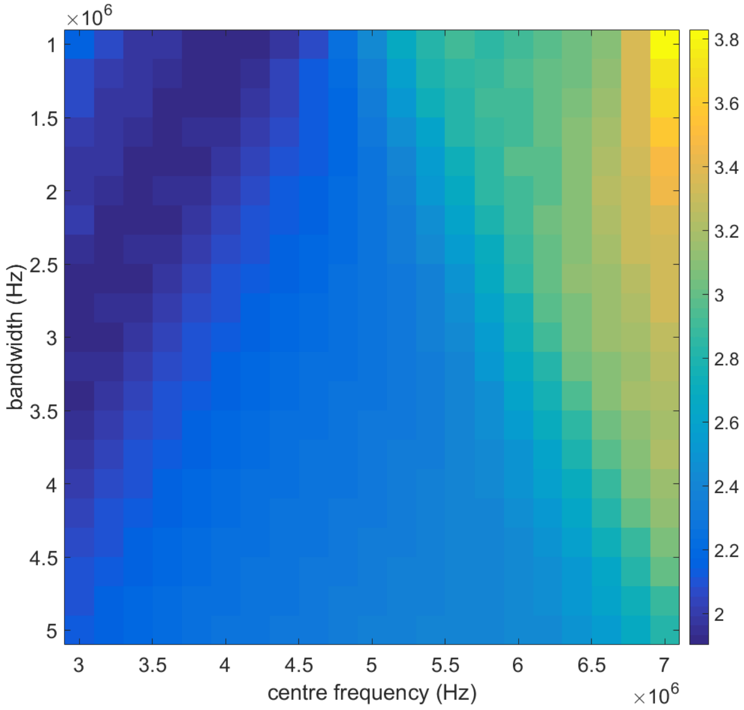

Figure 3.7. Map of $\mathrm{SNR}_{\mathrm{all}}$ with respect to the bandwidth (Hz) and the centre frequency (Hz).

From figure 3.7, it is found that the smaller bandwidth at any fundamental centre frequency between 4.8 MHz and 7 MHz always leads to the higher $\mathrm{SNR}_{\mathrm{all}}$ due to the smaller contributions from side transmission bands when the transmit-receive spectrum of this array specified by the manufacturer in figure 3.8 is considered. Hence, the opposite relationship should be expected from the results with the centre frequencies smaller than 4.8 MHz because of the higher contributions from their superharmonics (i.e. their frequency responses at lower frequencies are close to or less than those at their superharmonics). Furthermore, the higher centre frequency within the transmission band (e.g. 7 MHz) contributes to a higher $\mathrm{SNR}_{\mathrm{all}}$, which should be attributed to lower contributions from transmit-receive spectrum at corresponding superharmonic frequencies presented in figure 3.8 (i.e. the frequency responses at their superharmonics become negligible compared with themselves). In addition, a smaller wavelength as a consequence of higher centre frequency yields higher sensitivity to partially closed cracks. However, the highest SNR_{all} (equal to 6.824) appeared when the centre frequency is at 7.4 MHz and the bandwidth is 0.2 MHz (see figure 3.9 with the smaller range of effective bandwidth and the larger range of effective centre frequencies due to the upper limit equal to 12.5 MHz, half of sampling frequency) because the frequency response from 7.4 MHz drops to -6 dB (as shown in figure 3.8), which is considered to become too small in amplitude, and the subharmonic components within the transmission band has more contributions than its fundamental loss. Likewise, the lowest SNR_{all} (equal to 1.901) is seen with the centre frequency at 4 MHz and the bandwidth of 1 MHz due to significantly higher amplitude in superharmonic components. The corresponding NUI images with the lowest and the highest SNR_{all} are shown in figures 3.10 and 3.11 respectively, and then can be compared with the image using the standard band (bandwidth of 3.4 MHz and centre frequency of 5 MHz) in figure 3.12 in the same dynamic range. The NUI results suggest that a combination of higher centre frequency and lower bandwidth within thresholds can reduce the background noise by great amount (approximately 0.005 in nonlinear metric γ) in contrast to the imaging result with the standard band. Furthermore, it improved the signal from the cracks by 0.0071 in γ.

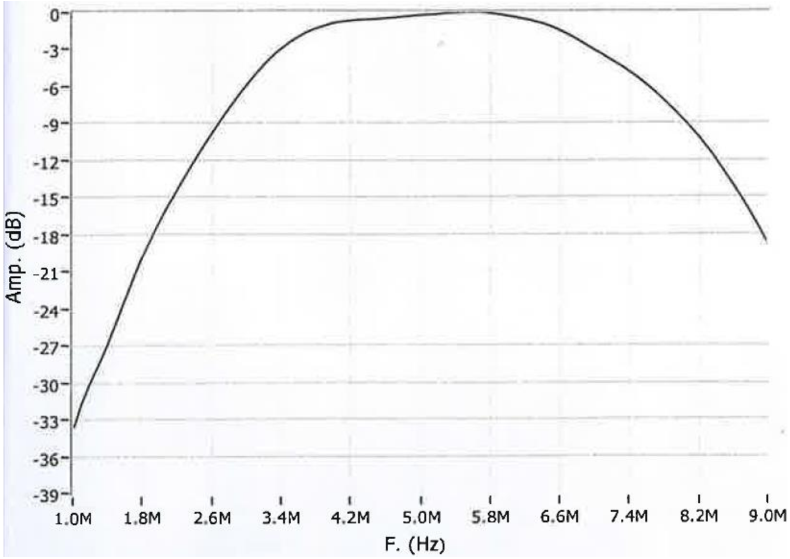

Figure 3.8. Transmit-receive spectrum specified by manufacturer (dB) against frequency (Hz).

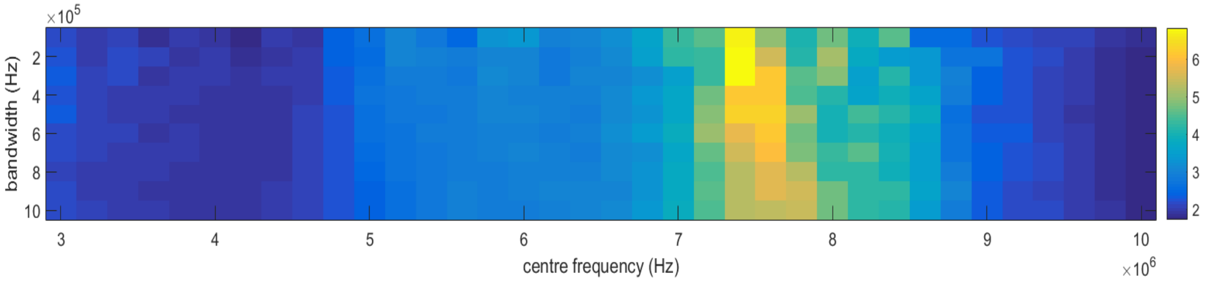

Figure 3.9. Map of $\mathrm{SNR}_{\mathrm{all}}$ with respect to the bandwidth (Hz) and the centre frequency (Hz).

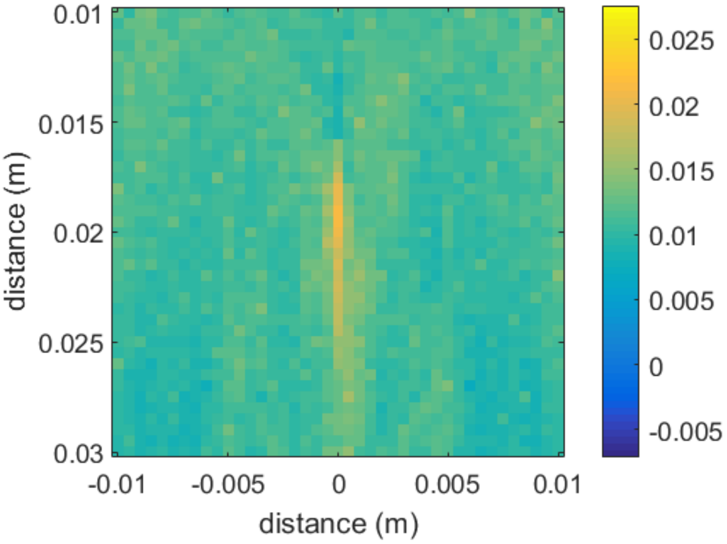

Figure 3.10. A nonlinear diffuse energy image with lowest $\mathrm{SNR}_{\mathrm{all}}$ in nonlinear metric, γ.

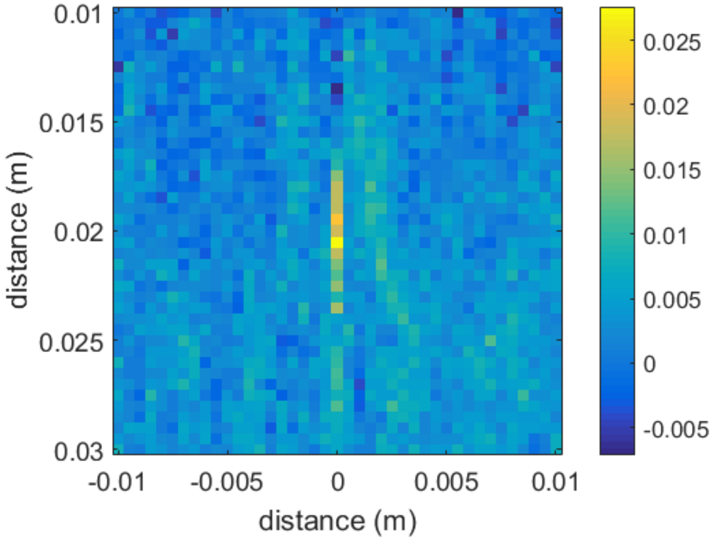

Figure 3.11. A nonlinear diffuse energy image with highest $\mathrm{SNR}_{\mathrm{all}}$ in nonlinear metric, γ.

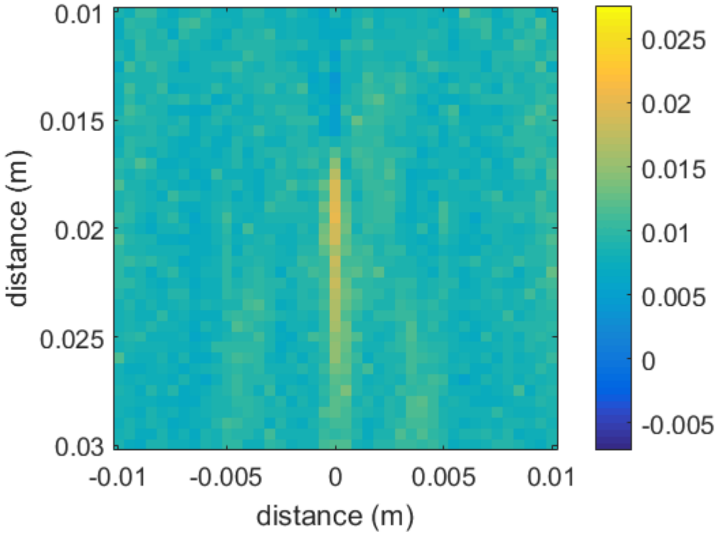

Figure 3.12. A nonlinear diffuse energy image with standard reception band in nonlinear metric, γ.

3.2.4 Conclusions

In order to quantify the NUI performance, the unique signal-to-noise ratio, $\mathrm{SNR}_{\mathrm{all}}$ is used to examine the effect of aperture size, data averaging, reception bandwidth and centre frequency. The results suggest that the selectivity of the crack tip increases with the aperture size as a consequence of stronger physical focusing at the crack tip. Whilst the signal without averaging is notably larger than the one with averaging the background noise can be suppressed significantly with increasing aperture size if the averaging is applied. Consequently, the NUI performance can be enhanced by taking averages in sequential transmission particularly with large aperture size.

Reception bandwidth and centre frequency in post-processing are found to predominantly determine the imaging performance. The generic approach is to map $\mathrm{SNR}_{\mathrm{all}}$ by examining single set of parallel and sequential data with different combinations of reception bandwidth and centre frequency. The results suggest that the smaller bandwidth gives rise to the higher $\mathrm{SNR}_{\mathrm{all}}$ at any centre frequency between 4.8 MHz and 7.8 MHz. Furthermore, the value of $\mathrm{SNR}_{\mathrm{all}}$ increases until the centre frequency increases to 7.8 MHz. The NUI results corresponding to the highest and the lowest $\mathrm{SNR}_{\mathrm{all}}$ values seen on the map suggest that the higher centre frequency associated with the smaller bandwidth can enhance the $\mathrm{SNR}_{\mathrm{all}}$ by significantly reducing the background noise.

3.3 Measurement and prediction of a diffuse wave field using a phased array

The prediction of the diffuse field is particularly important for NUI. If an idealised diffuse field is assumed the total transmitted energy is uniformly distributed throughout the structure [Evans and Cawley, 1999]. Therefore, the change in characteristics of wave energy due to the target nonlinear source can be measured subsequently at any point of the structure in diffuse field. However, the practical measurement of energy in diffuse field necessitates a compromise between the degree of diffuseness and SNR because of two competing effects. First, the acoustic field only slowly tends to the diffuse field state over time. Second, as wave propagation in real structures is dissipative and the acoustic energy is converted to other forms the SNR will decrease with time. Ultimately, compromising values of gate start time t_r and window length T used in NUI must be found such that an adequately diffuse field condition is realised and the amplitude is measurable, i.e. the SNR is sufficient. From this discussion it is apparent that the requirements are to maximise the transmitted amplitude, A and predict the earliest point at which the field can be approximated as a diffuse field state (i.e. the smallest value of t_r).

The acoustic source implemented throughout the experiments was the same ultrasonic phased array and the standard settings used in Subsection 3.2.1 were applied to the same array controller. A specimen made of the same materials (Aluminium 2014) was manufactured with the same geometry as the specimen used in Section 3.2 as illustrated in figure 3.1, in order to perform experimental confirmation of diffuse field generation as well as compare the experimental results with those output from numerical models. It should be noted that this undamaged sample facilitates simplicity and accuracy of the comparative study because diffuse-field theory predominantly relies on specimen geometry and properties of boundary and materials [Hodgson, 1996]. Furthermore, the predicted diffuse field can be directly related to the application on the cracked one.

Three different metrics used for diffuse field verification will be proposed and examined on analytical, experimental and numerical data. More specifically, the first two metrics evaluate the statistical variation in energy received simultaneously at different location, and the third metric measures the phase coherence of signals fired independently by two neighbouring transmitters. The analytical model is simulated random noise, which is thought to provide a representation of idealised diffuse state. The experiment was designed to measure and predict the formation of a diffuse field in a real structure. Last, the finite element model was created to emulate the wave propagation in the experiment as much as possible. The metrics will be compared in terms of reliability and limitations and then their applications on diffuse-field-dependent ultrasonic techniques using a phased array will be discussed.

3.3.1 Methods for verifying a diffuse field

Previous studies have concluded that the measured envelope area extracted from the signal envelopes can be indicative of the signal amplitude such that estimating whether a field is diffuse is then simply a case of mapping the variation of the envelop area across the surface of the structure [Evans and Cawley, 1999]. However, the technique was limited to measurement errors from repositioning the receiver because simultaneous sampling at a large number of positions were not realisable. With technological development, a phased array system that consists of multiple electronically controlled channels potentially enables the whole process to be completed without those limitations. Hence, it is advantageous to exploit its capability on diffuse field verification and ultimately integrate the measurement of diffuse field with those relevant NDT techniques using a phased array.

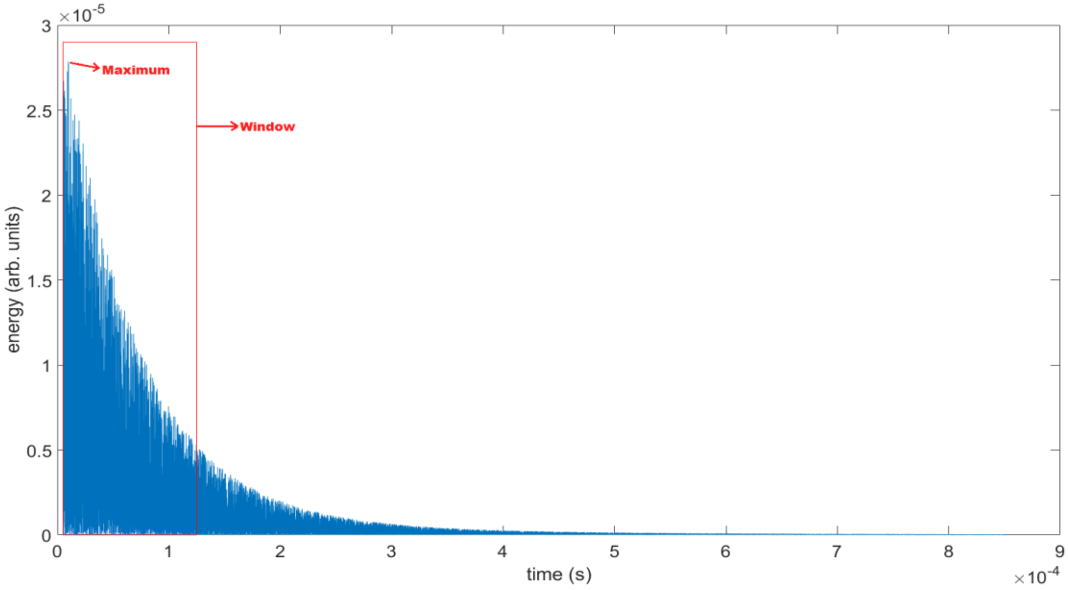

Figure 3.13. An example time trace of simulated incoherent noise for schematically illustrating the selection of windowed energy (with a window size, *T*) and the maximum energy in arbitrary units.

The acoustic source used throughout the experimental work was the same ultrasonic phased array used in Subsection 3.2.1. The full matrix capture (known as sequential transmission) was employed for completely utilising the array transmitters at as many locations as possible so that the diffusivity (i.e. the extent to which the field becomes truly diffuse) relative to the source locations can be taken into account. Although works [Evans and Cawley, 1999] reported that the envelope area measurement was favoured over maximum amplitude both will be examined more comprehensively and compared here. In addition, it is thought to evaluate spatial variations in energy rather than amplitude, which is attributed to the definition of a diffuse field. Last but not least, the energy area by calculating the integral of energy over the window (as illustrated in figure 3.13) and the maximum energy in the window are used in the first two metrics (η_{area} and η_{max}) respectively. Assuming $f_{n,m}(t)$ are the FMC time-domain received signals for each combination of transmit (n) and receive (m) elements in sizes of N_n and N_m respectively the metric for evaluating variations in energy area of windowed signals, η_{area}, can be expressed as:

$$\eta_{area} = 100 \sum_{n=1}^{N_n} \frac{\sigma\left(\int_{t_r}^{t_r+T} \left|f_{n,1\to N_m}(t)\right|^2 dt\right)}{N_n \overline{\int_{t_r}^{t_r+T} \left|f_{n,1\to N_m}(t)\right|^2 dt}} \%. \tag{3.1}$$

where σ denotes the standard deviation. Further, given that the maximum amplitude in each window of FMC signals is denoted as $f_{n,m}^{max}$ the metric for evaluating variations in maximum energy, η_{max} can be expressed as:

$$\eta_{max} = 100 \sum_{n=1}^{N_n} \frac{\sigma\left(\left|f_{n,1\to N_m}^{max}\right|^2\right)}{N_n \overline{\left|f_{n,1\to N_m}^{max}\right|^2}} \%. \tag{3.2}$$

Here, the above metrics were implemented to measure the normalised standard deviations of energy integrals and maximum energy respectively from the same time traces received by 64 elements. Note that the selection of transmitters will be discussed in Subsection 3.3.3 and the window length, T, was thought to be 0.12 ms, the empirical value used in NUI as stated in Subsection 3.2.1. Finally, their averaged value (termed η_{area} and η_{max}) were plotted against gate start time, t_r, in order to represent the degree of diffuseness with corresponding wave energy at different times. Previous experimental results state that the initial reflected signals account for most of the variation and it necessitates a delay to allow the energy to be evenly distributed [Evans and Cawley, 1999] and [Weaver, 1985]. Therefore, these two metrics should be expected to converge to a lower value with increasing t_r.

The other method was developed by considering the change in phase coherence evolved from coherent field to diffuse field. In diffuse field, all the signals could be expected to behave like white noise (i.e. the waves at different locations are uncorrelated to each other) [Evans and Cawley, 1999]. Furthermore, selection of the most representative wave sources to examine their relative phase coherence significantly determines the effectiveness of this method. This is because two neighbouring transmitters in an array are preferred over two transmitters far away from each other in terms of the similarity of their received signals in the same time window in a coherently scattered field. Therefore, the summation of their windowed signals fired independently by two neighbouring transmitters and received by all the elements in an array is approximate to twice of the either one in a coherently reflected field. However, the distribution of the reflected wave field is independent of the incident angle (i.e. random in amplitude and direction) in real structures, whereby the boundaries and the grains are diffuse reflectors. Hence, a diffuse field will be generated over time and the arrival of diffuse field can be indicated by evaluating the averaged change in phase coherence between propagating waves transmitted by all the combinations of two neighbouring elements and received by all the elements in a phased array.

Once the propagating waves from two neighbouring sources become uncorrelated in diffuse field, their summation is approximate to $\sqrt{2}$ times of each signals which can be attributed to random waveform combinations ($= \sqrt{n}A$) where n denotes number of component waveforms and A refers to amplitude of component waveform). A compensation factor of 2 is applied to the individual waveform, whereby the ratio of the individual amplified waveform to the resultant waveform in energy should be in a range of from 0.5 to 1 (suggest an evolution from coherent wave field to diffuse wave field). The metric is finally averaged from all the pairs of neighbouring transmission elements. As a consequence of calculating the windowed energy extracted from the same signals used in estimating η_{area} and η_{max}, the metric for evaluating the degree of their phase coherence, η_{phase}, may be written as follows:

$$\eta_{phase} = \sum_{n=1}^{N_n} \frac{2\sum_{m=1}^{N_m}\int_{t_r}^{t_r+T}\left|f_{n,m}(t)\right|^2 dt}{N_n \sum_{m=1}^{N_m}\left(\int_{t_r}^{t_r+T}\left|f_{n,m}(t)+f_{n\pm1,m}(t)\right|^2 dt\right)}. \tag{3.3}$$

3.3.2 Experimental generation of an evolution from coherent field to diffuse field

The array probe was positioned at the centre of top surface (the same layout as the one used in figure 3.1). As the incoherent noise has a significant effect on decayed signals in diffuse field and its contribution increases with time the reception gain should be altered to ensure the received amplitude from each set of captured data is always at the equivalently high level. The window length, T, for each FMC was set as 0.06 ms (half of the standard NUI window length used in Subsection 3.2.1), so as to frequently select the optimum reception gain corresponding to different gate start time, t_r. Further, the initial gate start time was chosen to 0.005 ms after which the crosstalk was no longer present and the first coherent reflections from boundaries start to emerge. It should be noted that the reception gains (used for maintaining the same contribution of incoherent noise as described in Section 3.2) were determined by finding the maximum received amplitude in each window close to 1 (the saturated value of the array controller). Then, twelve sets of FMC time traces were acquired sequentially with the parameters listed in table 3.2 and all the signals were normalised subsequently to 23 dB, used in the first capture. Note that the last set was indicated by capturing with the highest instrumental reception gain, 70 dB. Consequently, all the time traces stitched together to form one resulting set of FMC time traces from 0.005 ms to 0.85 ms.

An example time trace from a pair of neighbouring transmitters (elements 1 and 2) are presented in figure 3.14 and early time traces transmitted by element 1 and received by all the elements from 0.005 ms to 0.02 ms in dB scale are illustrated in figure 3.15. In addition, the longitudinal bulk wave and the surface wave can be confirmed by measuring their wave speed as approximately 6300 m/s and 2625 m/s respectively.

Gate start time, t_r (ms)	Reception gain (dB)	Maximum received amplitude (arb. units)
0.005	23	0.991
0.03	35	0.997
0.09	46	0.986
0.15	49	0.969
0.21	55	0.990
0.27	55	0.995
0.33	59	0.996
0.39	61	0.993
0.45	64	0.945
0.51	66	0.959
0.57	67	0.973
0.63	68	0.920
0.69	70	0.995

Table 3.2. The gate start time, reception gain and maximum amplitude corresponding to twelve sets of FMC time traces.

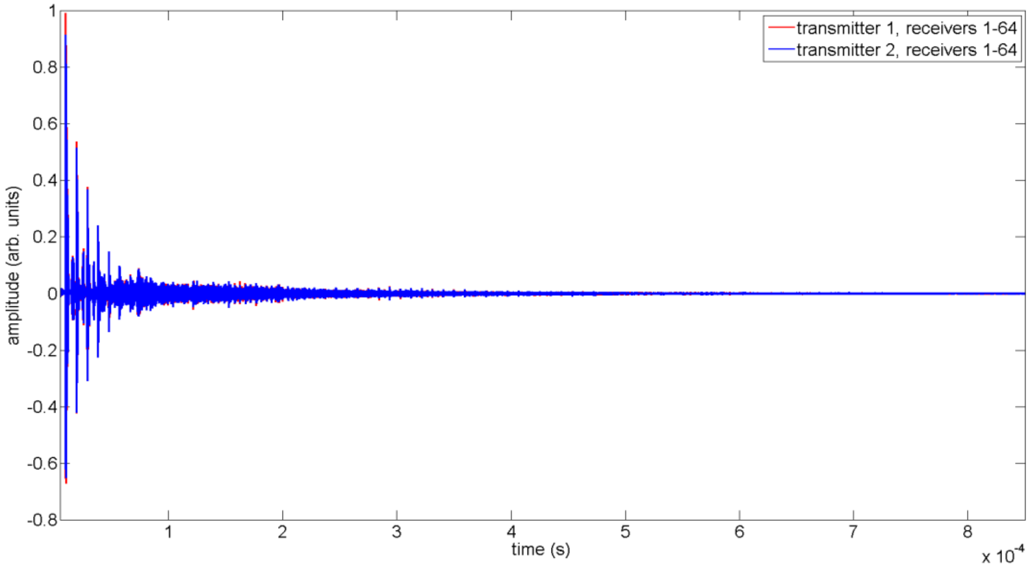

Figure 3.14. An example time trace from a pair of neighbouring transmitters (elements 1 and 2).

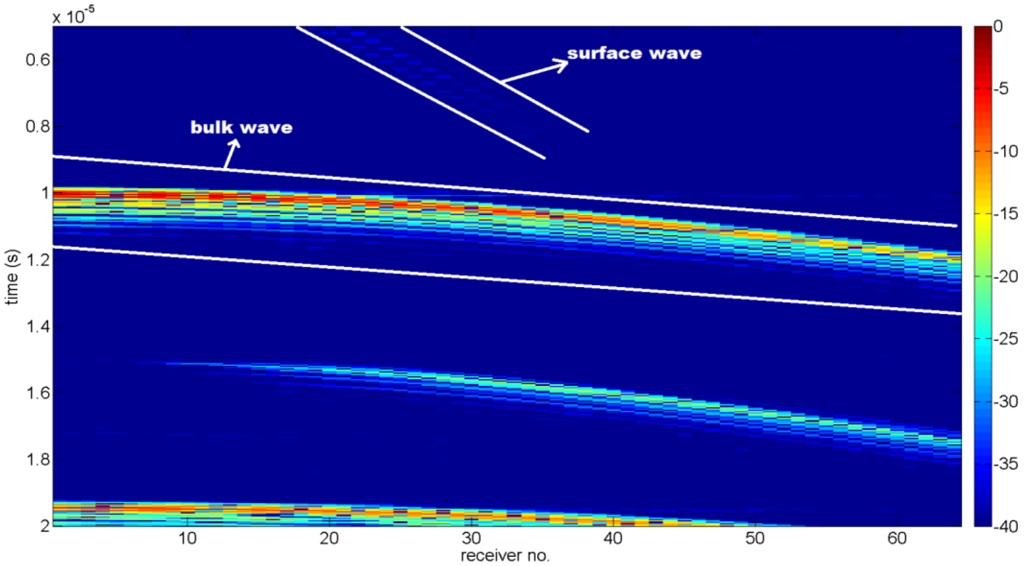

Figure 3.15. Early time traces transmitted by element 1 and received by all the elements from 0.005 ms to 0.02 ms in dB scale.

3.3.3 Numerical model of the wave field

Whilst all the commercially available finite element (FE) packages are limited in their ability to model diffuse reflectors in real structures the decayed wave propagation in a coherent field after intensive specular reflections and mode conversions can be simulated by the FE analysis, thereby examining the metrics on the simulated signals to understand the significance of their values especially in an early coherent field. Therefore, a FE model of the undamaged aluminium specimen with the same dimensions as displayed in figure 3.1 was built by using the FE package (ABAQUS/CAE 6.14-1). Specifically, the same arrangements (as illustrated in figure 3.16) and material properties (listed in table 3.3) as well as the approximated forced excitation at each transmitter using 5-cycle tone burst signals (generated from 5-cycle gaussian windowed sine wave with 5 MHz centre frequency and 10 MHz bandwidth) were applied to the dynamic explicit model.

Material	Aluminium 2014
Young's Modulus	73 GPa
Density	2800 kg/m^3
Poisson's ratio	0.33

Table 3.3. Material properties of aluminium 2014.

The model was simplified to two-dimensional plane strain geometry excited with left half of the array, due to the negligible element width in contrast to its length and the symmetric layout about the middle on top surface of the specimen. In addition, only three pairs of neighbouring transmitters at left, middle and right sides of the left-half array elements (the most representative ones to measure the diffuse field spatially) were selected as elements 1, 2, 16, 17, 31 and 32 (as illustrated in figure 3.16) in this FE model due to high computational cost per firing. At the reception, all the 64 elements were required for capturing the time traces from 0.005 ms to 0.85 ms (the same range as mentioned in Subsection 3.3.2), termed $f_{n,m}^{F}(t)$. The size of used quadrilateral-shaped element was determined on the basis of 20 nodes per wavelength (equal to 0.063 mm), which delivered sufficient accuracy for this numerical analysis. The enhanced hourglass and distortion control were employed in order to remove the effect of continuous residual vibrations at the wave source and the low frequency components. However, it was found that surface waves existed in the initial coherent wave field in the measured signals, which can be observed from example time traces transmitted by element 1 and received by all the elements from 0.005 ms to 0.02 ms (as shown in figure 3.17). In addition, the time traces fired by elements 1 and 2, and captured by all 64 elements are displayed in figure 3.18, which demonstrate that the initial surface waves propagating until 0.016 ms are overwhelmingly strong compared to the propagating bulk waves, but then they attenuate due to long lateral surface and mode conversions along with propagation. In practice, it is realised that the coupling and the excitation mode between the array elements (wave sources) and the structure can suppress the intensity of surface waves. Again, lack of diffuse reflectors such as boundaries and grains in the FE model leads to negligible change in phase coherence between the signals fired by two neighbouring transmitters over time.

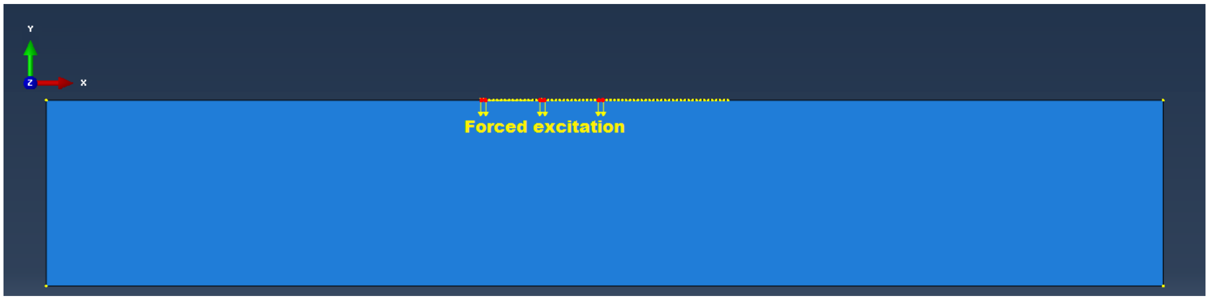

Figure 3.16. Schematic diagram of a 2D FE model.

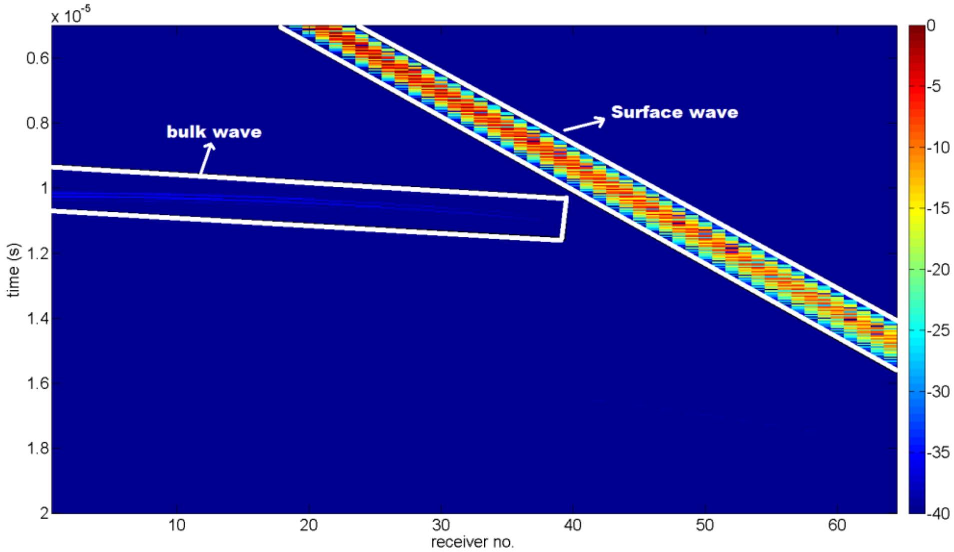

Figure 3.17. Example time traces transmitted by element 1 and received by all the elements from 0.005 ms to 0.02 ms.

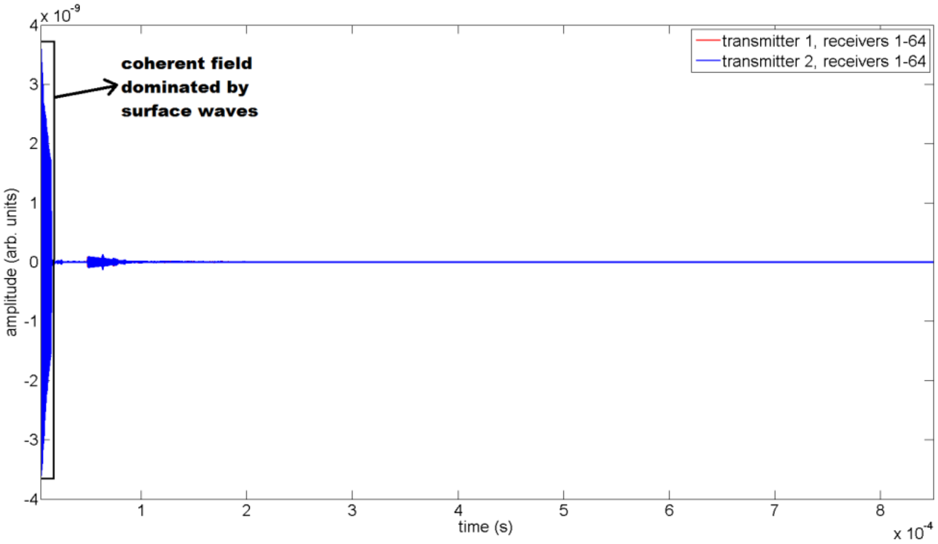

Figure 3.18. Time trace fired by elements 1 and 2, and captured by all 64 elements.

3.3.4 Analytical generation of a diffuse field

Since the behaviour of propagating waves in perfectly diffuse state is random, similar to that of white noise it is worth examining the proposed metrics on simulated random signals. This should deliver a benchmark for an idealised diffuse field, such that the evaluated experimental and numerical results can be better appreciated.

As illustrated in figure 3.19(a), the white noise, termed $f^{W}_{n,m}(t)$, can be simulated by generating uniformly distributed random variables within specified interval (from -0.4 to 0.4) using a standard programming language (MALTLAB R2016a) because incoherent signal is a zero-mean random process. In addition, the decay rate was extracted by fitting a two-term exponential model ($y_{n,m}(t) = o_1 e^{bt} + o_2 e^{dt}$, where o_1 and o_2 are amplitude factors, b and d are decay coefficients) to the stitched experimental FMC data set (an example time trace is displayed in figure 3.19(b)). These coefficients were calculated by using the 'Fit' function and specifying its type as 'exp2' in MATLAB software. Note that the two-term exponential model rather than a one-term model was selected due to better approximation of multi-mode wave decay. The simulated random signals in the same size of FMC data were multiplied by the corresponding exponential fits, $y_{n,m}(t)$ to obtain the decayed white noise, denoted as $\hat{f}^{W}_{n,m}(t)$, whereby the effect of attenuation in wave propagation on the proposed metrics can be quantified.

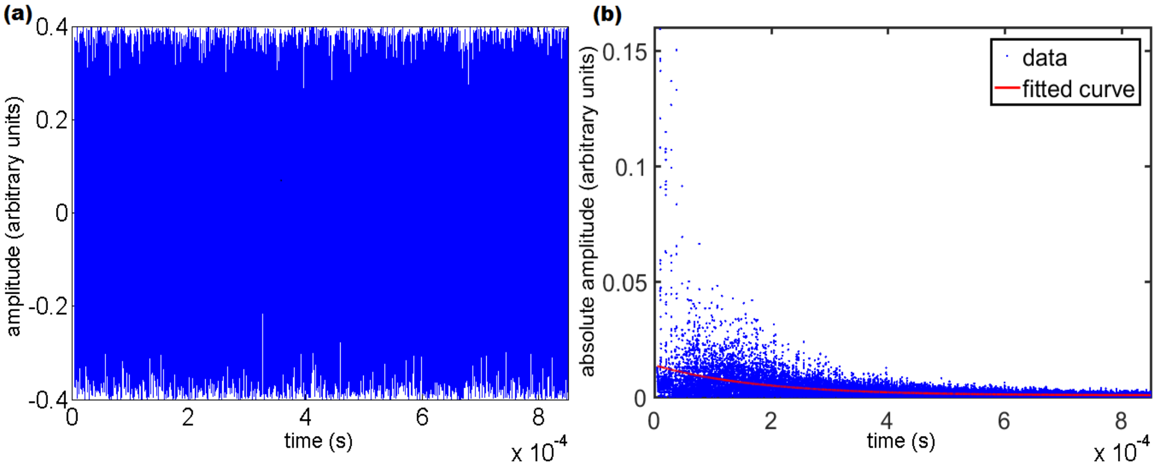

Figure 3.19. (a) Simulated white noise, $f^{W}_{n,m}(t)$ against time and (b) an example time trace including the exponential fit.

3.3.5 Methodology to predict a diffuse field using proposed metrics

The data obtained from experiments, FE and analytical simulations are now analysed with three proposed metrics, thereby delivering a systematic methodology for diffuse field prediction on any structure. In most of the ultrasonic applications, the fundamental frequency band is examined hence the wave propagation at the fundamental frequency in diffuse state is critical to these techniques. As a consequence, the metrics should assess the diffusivity of wave components particularly at the fundamental frequencies, which can be accomplished by introducing a gaussian windowed filter in post-processing.

Specifically, the experimental FMC signals, $f_{n,m}(t)$, the decayed white noise, $\hat{f}^{W}_{n,m}(t)$, the white noise, $f^{W}_{n,m}(t)$ and the FE signals, $f^{F}_{n,m}(t)$ were selectively processed by a gaussian windowed filter and then examined by three different metrics (η_{area}, η_{max} and η_{phase}),in order to predict a diffuse field (as illustrated in figure 3.20). The metrics were plotted against the gate start time, t_r, from 0.005 ms to 0.85 ms (this range was indicated by limits of hardware reception gain). In addition, the window length, T, was initially selected as 0.12 ms as a consequence of the standard parameter used in NUI. Therefore, the outcome of this process will help determine the earliest approach of the diffuse field as well as understand the underlying physics behind the formation of diffuse field in real structures.

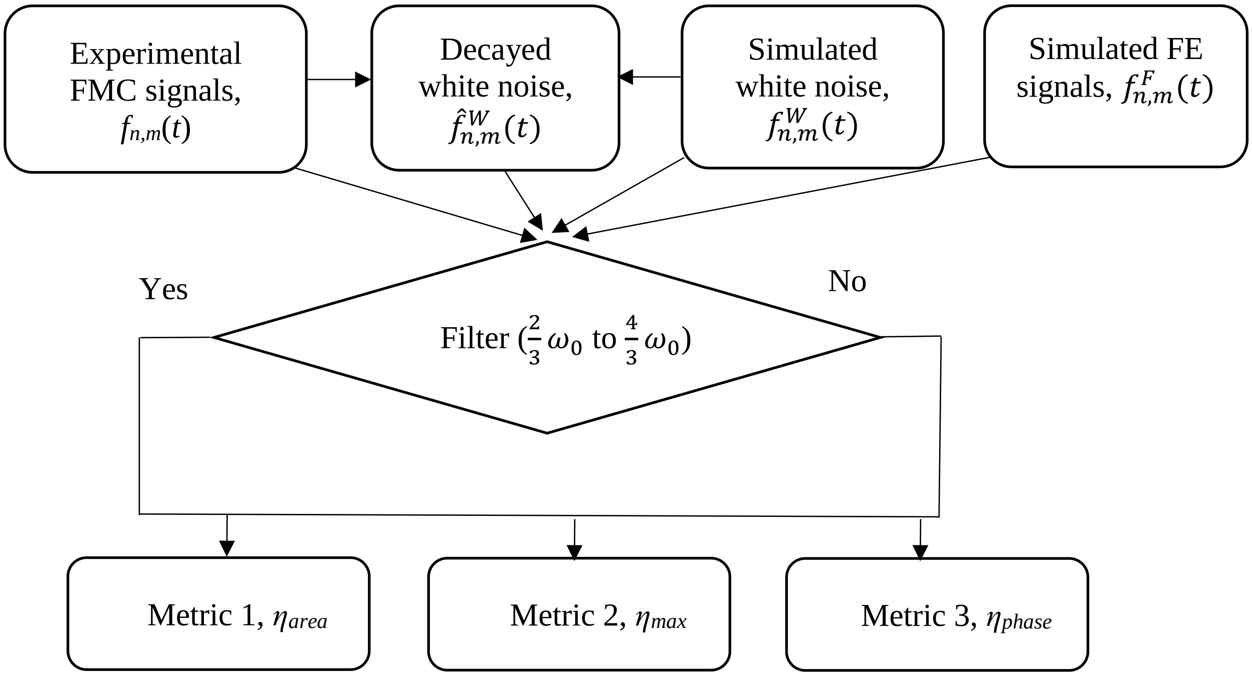

Figure 3.20. Flow chart of methodology for diffuse field verification.

First, the relationship between metric, η_{area}, and gate start time, t_r, is displayed in figure 3.21. This figures indicates the variations in windowed energy, which were post-processed from experimental FMC signals, FE signals and white noise. A gaussian windowed filter from $\frac{2}{3}\omega_0$ to $\frac{4}{3}\omega_0$ was selectively implemented to those data prior to evaluations through proposed metrics. The results in figures 3.21(a) and (b) suggest that the metric (η_{area}) on FE data after filtering is significantly determined by the coherent surface waves. This is confirmed by observing the declining pulsed features (indicated by blue lines in figures 3.21(a) and (b)) in every time increment about 0.07 ms (equal to the time required for capturing a pulse echo along the top surface). These features are thought to be attributed to the much higher attenuation rate of surface wave compared with other wave modes at fundamental frequencies as well as their overwhelmingly higher initial intensity seen in figures 3.17 and 3.18. Although the numerical model cannot encompass the essential conditions for generating diffuse field (e.g. diffuse reflectors) their results can imply the equivalent state to a diffuse field, developed by multi-mode wave components. This is because mode conversions continue to occur along with surface wave propagation, so that substantial regenerated waves and low frequency components (with lower attenuation rate) will be distributed uniformly in the structure (i.e. the mode conversions here have the same contributions as diffuse reflectors). Therefore, the FE data without filtering in post-processing can virtually deliver a converged value of η_{area} around 15% from gate start time at 0.1 ms (representing the significantly attenuated surface waves).

The results from simulated white noise in figure 3.21(b) indicate the benchmarks for an idealised diffuse field. Most importantly, the effect of exponential decay extracted from experimental data and the gaussian windowed filter has measurable contributions to the metric, η_{area}. Their corresponding influence can be observed in figure 3.22, which demonstrates that the incoherent signals within a narrow band tend to possess much higher value in η_{area} (i.e. less diffusivity), and the metric on decayed signals is likely to inherit the characteristics of their decay rate, which possibly is the cause of higher η_{area} in early wave field of experimental and FE data.

The metric, η_{area}, on experimental FMC signals in figure 3.21(b) suggest a good agreement with FE results and previously observed variation of the amplitude envelope measurements about 15 % [Evans and Cawley, 1999]. Specifically, the experimental results using the metric η_{area} suggest that a diffuse wave field occurs at 0.1 ms by observing the converged start point and the filtered data provide the higher value in η_{area} within predicted diffuse field, which is consistent to the observation from white noise. Most importantly, this predicted gate start time for a diffuse field is same as the empirical one used in Section 2.2 that delivers good NUI performance on crack detection.

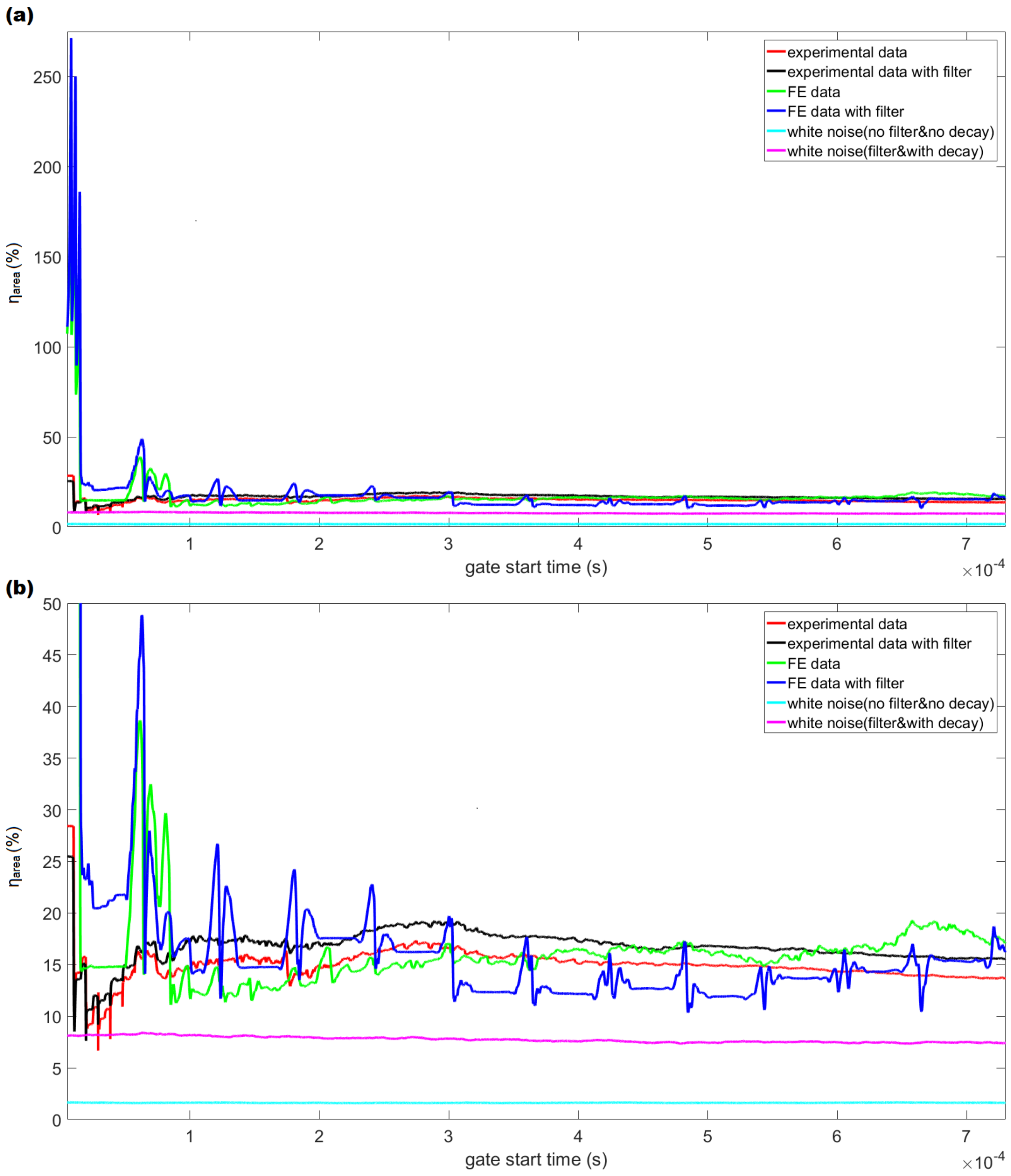

Figure 3.21. Diffuse field verification on white noise, FE data and experimental data using metric, η_{area} (a) full scale of η_{area} against gate start time and (b) the corresponding zoomed in view of smaller η_{area}.

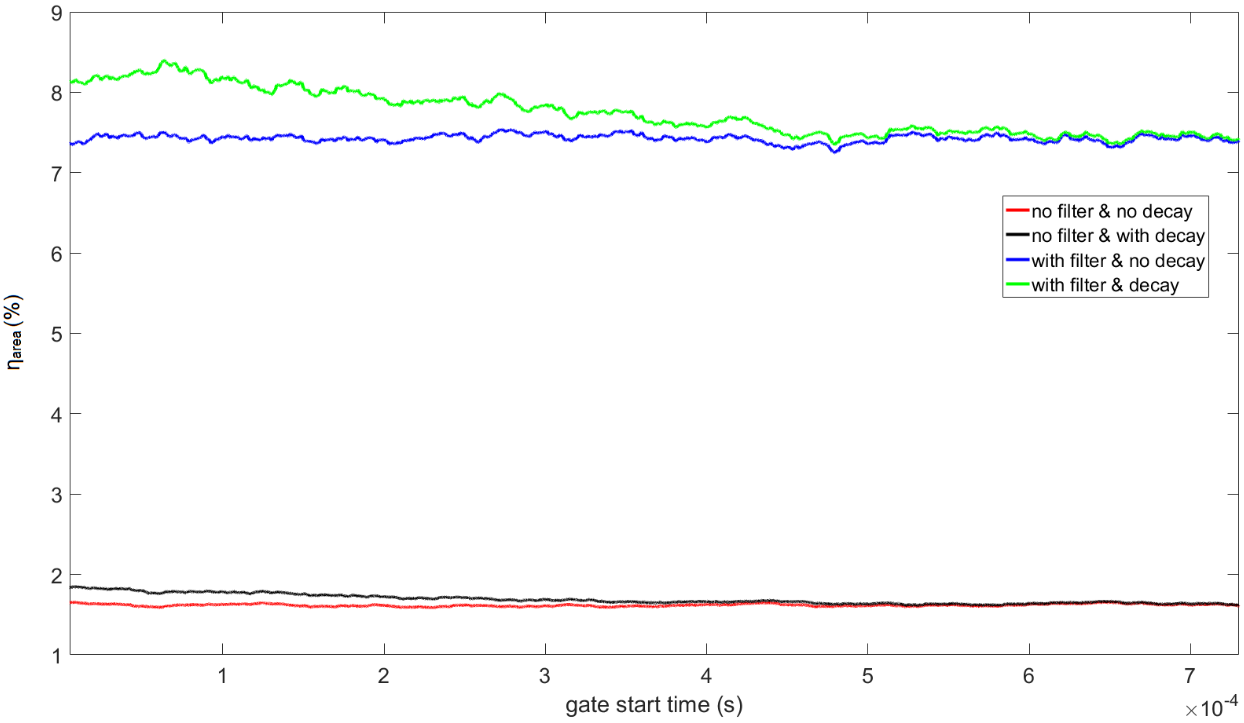

Figure 3.22. Diffuse field verification on white noise with or without filter and decay using metric, η_{area}.

The metric (η_{max}) indicating the variation in maximum energy is plotted in figures 3.23(a) and (b) with respect to gate start time, t_r. Its results are very similar to those in figures 3.21(a) and (b), but the overall variations increase by 20 percent and small fluctuations with increasing t_r due to too small number of samples in a statistical problem (i.e. when calculating the standard deviations of overall energy in a wave field). This fact will be confirmed later by the window size study (a converged relationship between η_{area} and window length T as presented in figure 3.25) Therefore, the metric (η_{area}) is favoured over the metric (η_{max}) as a consequence of the most representative measurement in overall wave field energy.

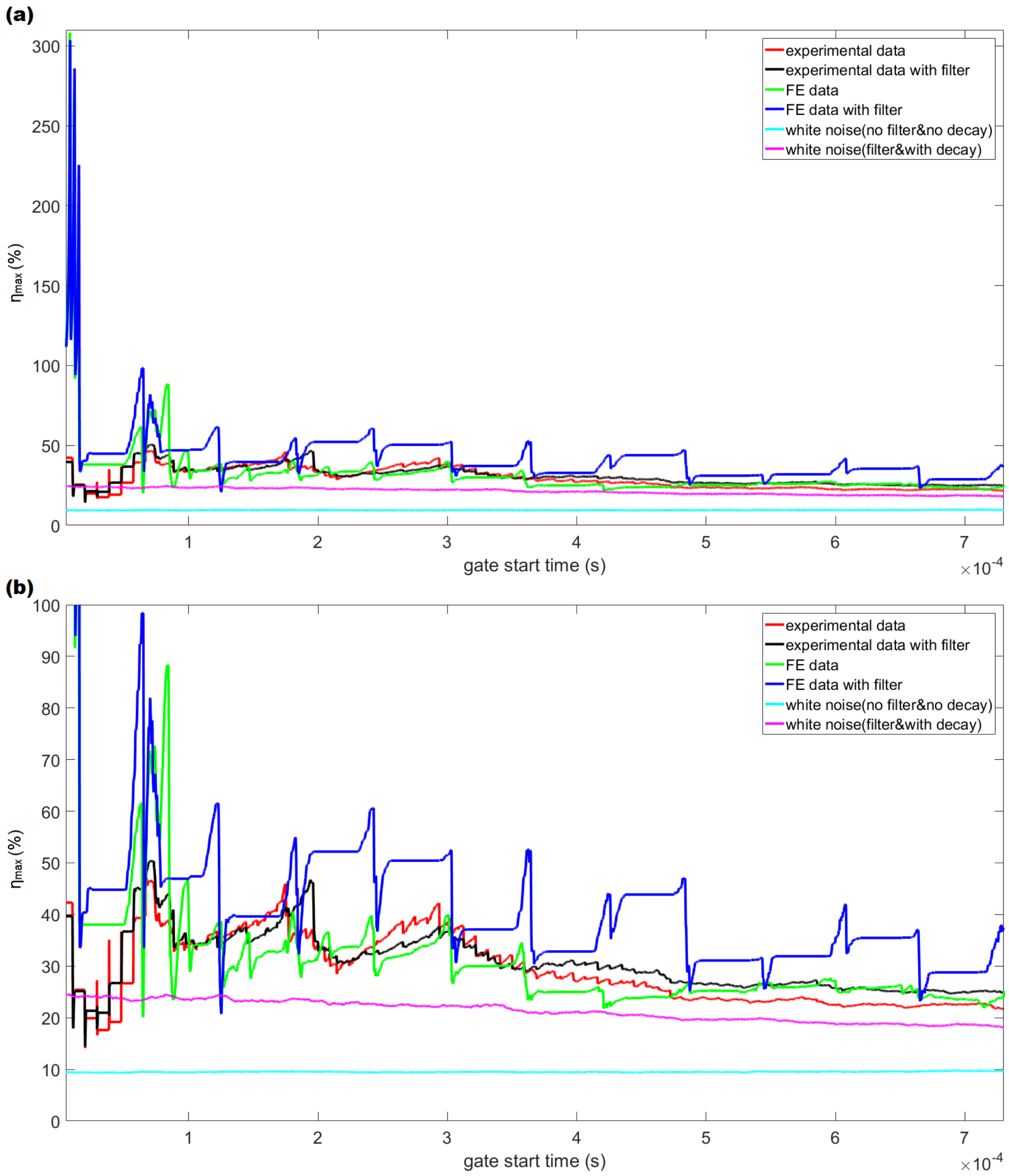

Figure 3.23. Diffuse field verification on white noise, FE data and experimental data using metric, η_{max} (a) full scale of η_{max} against gate start time and (b) the corresponding zoomed in view of smaller η_{max}.

The change in the metric (η_{phase}), by which the extent of phase coherence between signals fired by two neighbouring transmitters is reflected, with increasing t_r is displayed in figure 3.24. As mentioned in Subsection 3.3.1, the expected range in η_{phase}, indicating the change from coherent field to diffuse field, is from 0.5 to 1. The results from FE data with the filter suggest that the wave energy field of two neighbouring elements is always correlated in phase due to a converged value of 0.5. It has good agreement with the assumption of the metric, η_{phase}, because the FE model cannot incorporate diffuse reflectors so that the metric, η_{phase}, should be expected to remain at 0.5. Notably, the FE data without filtering has dramatic increase and decrease in η_{phase}. Those odd values (e.g. 1.5) of η_{phase} can be caused by the noise at uninterested frequencies due to dispersive errors in numerical analysis [Mullen and Belytschko, 1982]. Most importantly, the FE data within fundamental bandwidth should behave like coherently reflected signals.

As a consequence of a phase-dependent method, the filter and the attenuation rate barely have influence on white noise, which can be reflected by the overlapped curves (in cyan and magenta colours) in figure 3.24. Furthermore, the metric (η_{phase}) on white noise (uncorrelated signals) is consistently with a value of 1 as expected. For the experimental data, the filter also has little effect on this metric. The diffuse state might be indicated from t_r at 0.07 ms due to the corresponding η_{phase} value at 1 although the metric then decreases by approximately 0.15 and then converges to the value around 1.02. This small decrease is possibly because the surface waves not only attenuate more slowly than the bulk waves [Uenishi, 2017], but also become diffuse much later due to high aspect ratio of this structure (6:1). That is to say, the bulk waves initially at higher intensity will reach diffuse state earlier due to significantly more reflections from two horizontal boundaries closer to each other in y-direction (as illustrated in figure 3.16). This fact will be further confirmed by examining η_{phase} on a specimen with lower aspect ratio (1.04:1), as presented in figure 3.28. The metric, η_{phase}, evaluating both experimental data and FE filtered data have the small decrease in good agreement prior to the previously predicted diffuse field start time (0.1 ms), which might be attributed to the existing surface wave components in high intensity before 0.1 ms in figures 3.14 and 3.18.

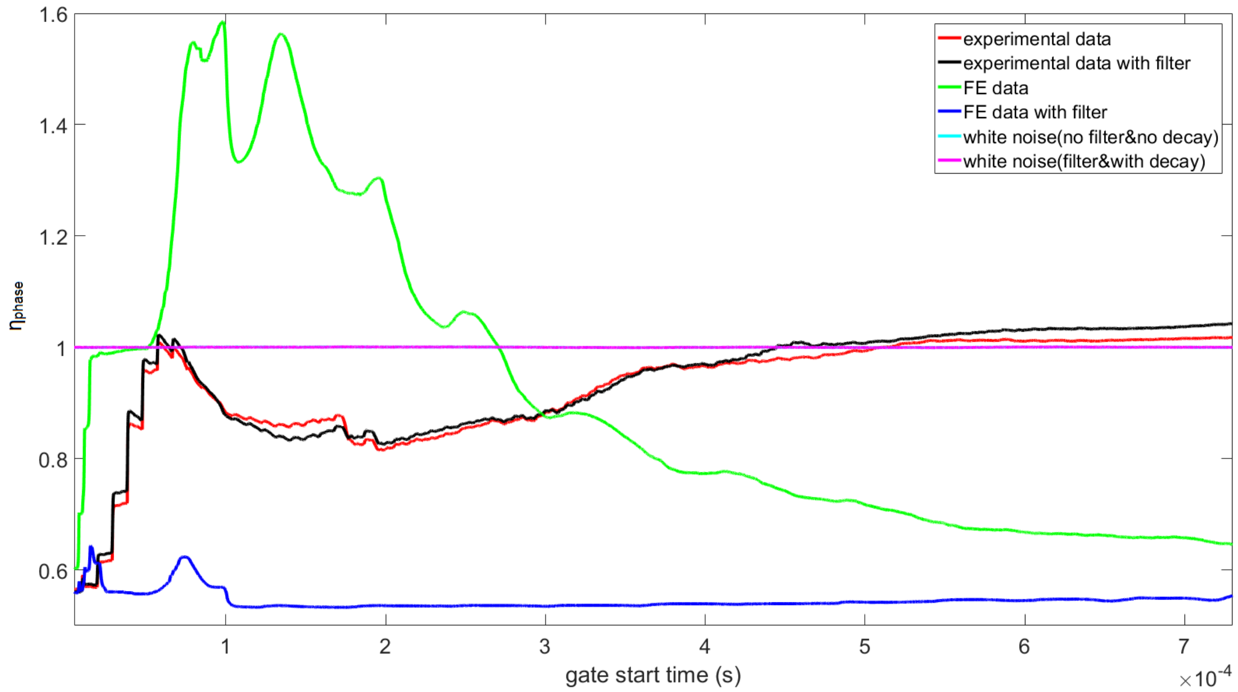

Figure 3.24. Diffuse field verification on white noise, FE data and experimental data using metric, η_{phase}.

The window length, T, is studied by plotting the metrics (η_{area} and η_{phase}) against t_r, because it is important to select the most representative samples in a predicted diffuse field with the smallest window required. In theory, the smaller number of sample (e.g. the single sample used in the metric η_{max}) are more likely to provide the large error when measuring standard deviations of the statistical energy in diffuse wave field. However, there should be an upper limit for the size of sample to be estimated, which delivers a saturation point, as a measure of the highest degree of diffuseness.

Therefore, the size of window length, T, was varied from 0.0004 ms to 0.2 ms. As presented in figure 3.25, the metric, η_{area}, was first plotted against t_r, in order to explore the effect of window size on variation between windowed energy received at different location. It clearly demonstrates that the relationship between the size of T and η_{area} is exponentially inverse. In particular, the η_{area} converges with increasing size of T from the empirical T with 0.12 ms (used in NUI imaging and previous studies) by observing the overlapped curves between T with 0.12 ms and 0.2 ms in figure 3.25. It should be also noted that the small size of T (e.g. 0.0004 ms and 0.002 ms) contributed to more fluctuations and larger offset. As a consequence of the results, the size of T with 0.12 ms is suggested to be used.

In addition, it was thought that the three neighbouring pairs of transmitters used in the simplified FE model should provide a good approximation to experimental FMC data. This assumption can be validated by examining the corresponding data extracted from the FMC data. Thus, the metric, η_{area}, examined the corresponding subset of experimental FMC data using the agreed T of 0.12 ms (encompassing the signals transmitted by transmitters 1, 2, 16, 17, 31 and 32 then received by all 64 receivers). The results in the metric, η_{area} in in figure 3.25 suggest that six transmitters, which are thought as the most representative ones, have close approximation to all the transmitters involved.

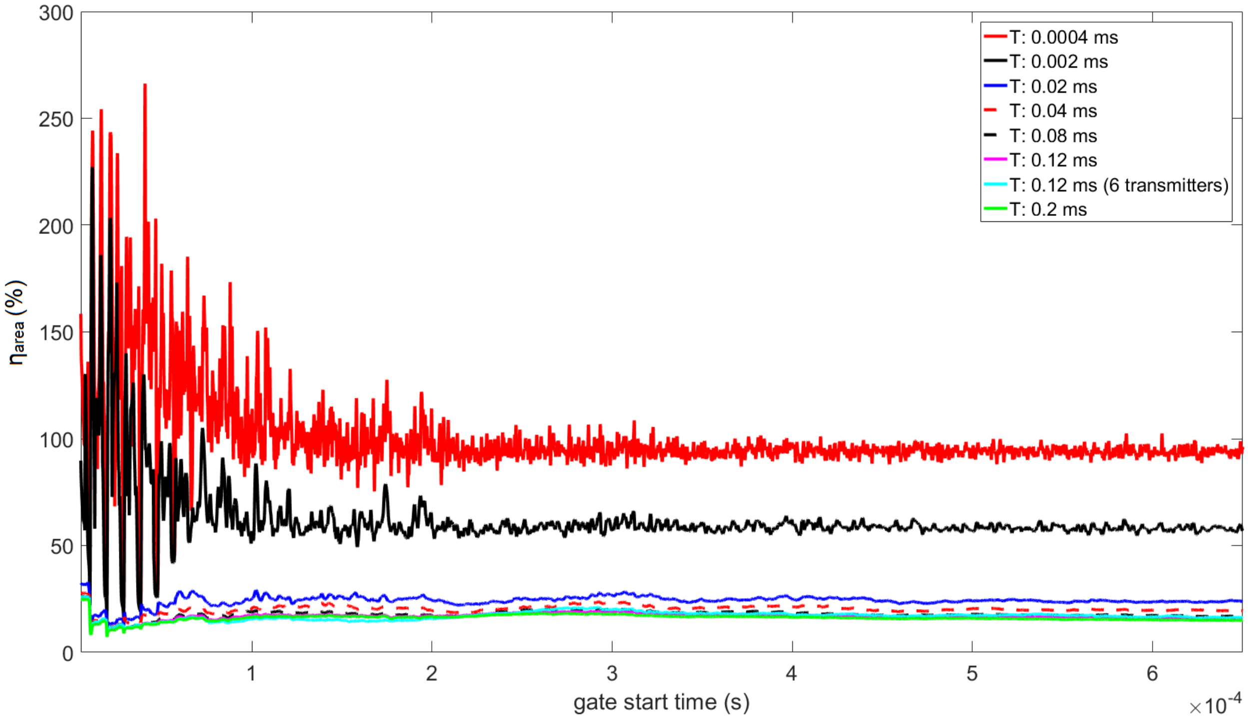

Figure 3.25. Diffuse field verification on experimental data with different window size using metric, η_{area}.

Similarly, the same window length study was performed by examining the metric, η_{phase} with increasing gate start time, t_r. The results in figure 3.26 suggest that the larger window size delivers more rapidly converged value in the idealised diffuse state with increasing t_r. In addition, the metric, η_{phase} becomes converged at T of 0.12 ms with increasing window size and the three neighbouring pairs was able to provide the same prediction of diffuse field as the entire array transmitters.

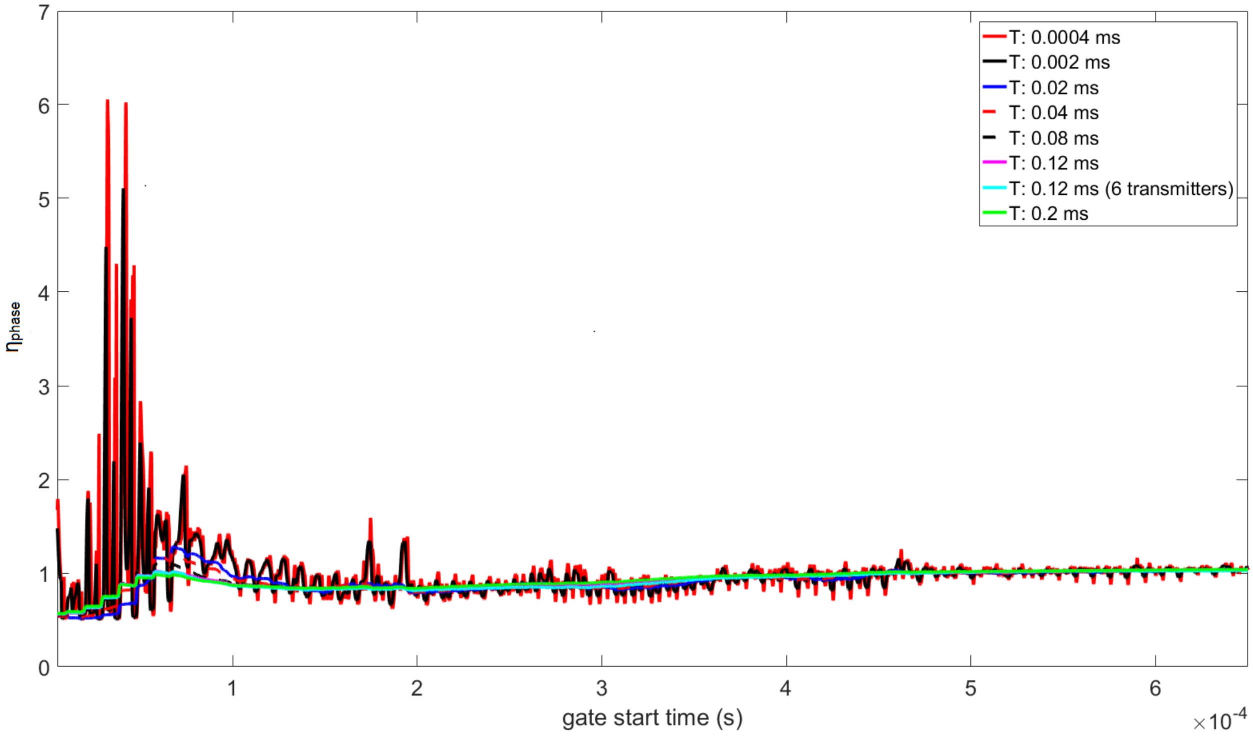

Figure 3.26. Diffuse field verification on experimental data with different window size using metric, η_{phase}.

Furthermore, the robustness of these two metrics is examined on the same steel CT specimen used in Subsection 2.4.2 for performing NUI technique on crack monitoring, whereby the size of T was used as 0.12 ms and the resulting time traces from 0.005 ms to 0.4 ms was combined from nine sets of FMC data were acquired independently with different gains (from 36 dB to 70 dB). Note that the white noise here is also produced from combining simulated random signal and exponential decay rate extracted from the experimental resulting time traces. The results in figure 3.27 demonstrate that the metric η_{area} on filtered experimental data implies good agreement with the empirical values used in Chapter 2 (T of 0.12 ms with the gate start time, t_r, at 0.1 ms) and that of filtered white noise by observing the converged start point at approximately 0.07 ms (where η_{area} is around 15 % as the indicated diffuse state). In addition, the metric η_{phase} as presented in figure 3.28 identifies the convergence to 0.95 (very close to the idealised diffuse state, 1) from around 0.07 ms in good agreement. It should be noted that the surface of this steel sample in contact with the probe has one-third length of the aluminium one, so that the state of surface waves is expected to become diffuse three times faster due to more reflections from boundaries. As a consequence, the small decrease observed after the predicted diffuse start time (0.07 ms) in figure 3.24 is probably attributed to the surface waves as discussed before.

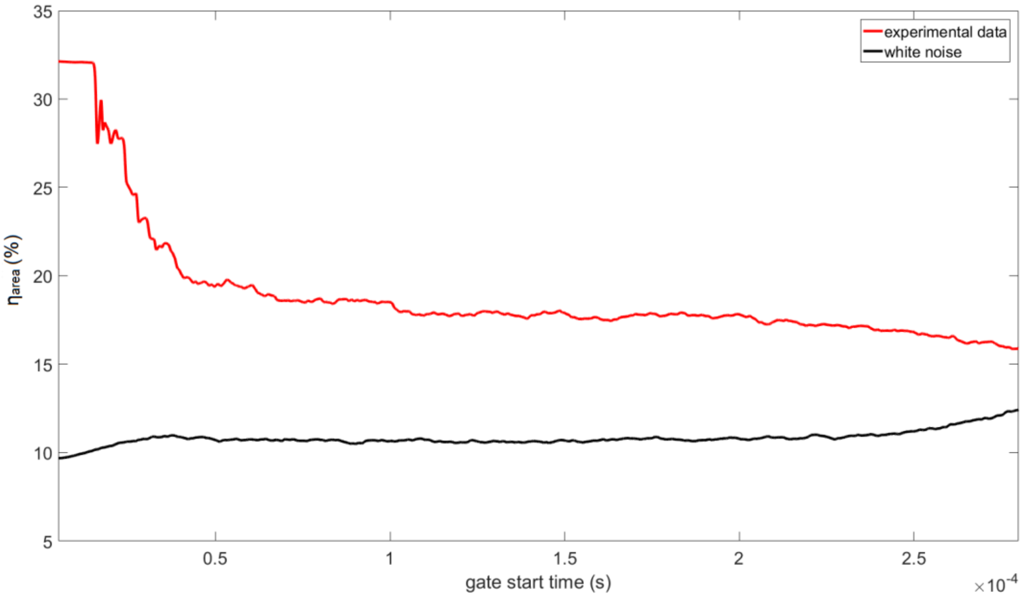

Figure 3.27. Diffuse field verification on white noise, FE data and experimental data using metric, η_{area}.

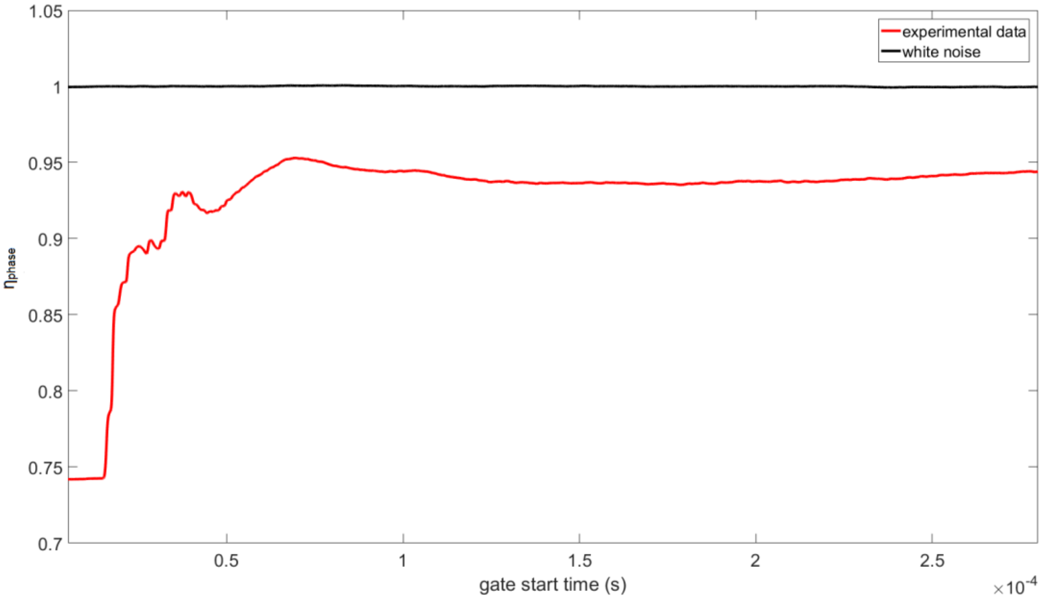

Figure 3.28. Diffuse field verification on white noise, FE data and experimental data using metric, η_{phase}.

3.3.6 Conclusions

The results from the aluminium specimen suggest that both of the metrics η_{area} and η_{phase} were able to effectively identify the change from coherent field to diffuse field of experimental signals according to the reference values generated from FE data, decayed white noise. Note that the effect of both the exponential decay extracted from experimental data and the gaussian windowed filter has been found to provide considerable contributions to the metrics. Consequently, the simulated white noise including both of them delivers the best approximation to the experimental data in terms of diffusivity indicated by the proposed metrics. In addition, the FE data was seen to provide no indication of diffuse state, which should be attributed to no diffuse reflectors included in the model. Furthermore, the effect of window size, T, was studied by using the same metrics η_{area} and η_{phase}. Its results demonstrated that the larger T delivered higher diffusivity and the preferred size of 0.12 ms indicated by the converged values of η_{area} and η_{phase} was consistent to the empirical value obtained from the experimental NUI performance on crack detection. Investigations using these two metrics were conducted on one of the steel CT specimens used in Chapter 2. The consistent results corresponding to empirical values were confirmed by observing the t_r, at which both η_{area} and η_{phase} converged to reference values of diffuse state.

In summary, both of the metrics η_{area} and η_{phase} on examining t_r and T demonstrated good agreements with their empirical values from the experimental NUI performance on crack detections of the same structures (one aluminium CT specimen and one steel CT specimen), hence, they are thought to be able to quantitatively predict the diffuse field start time as well as the optimum window size T by comparing their value with the idealised diffuse state (15 % for η_{area} and 1 for η_{phase}) and identifying the convergence start point. It should be noted that in some cases the surface waves might lead to errors in judging the diffuse state, particularly with excitation on a long surface of a structure.

3.4 Three-dimensional NUI technique

In order to allow the NUI to localise the acoustic nonlinearity in three-dimensional (3D) space of a specimen, a novel technique termed 3D NUI was developed. The principle is to control the array elements within a 2D array probe with independent delay laws, thereby achieving the physical and synthetic focusing (known as parallel and sequential focusing) at each volumetric pixel. Similarly, the difference in remaining fundamental energy between sequential and parallel cases within the diffuse field is exploited to calculate the nonlinear metric, γ at each focal point. The focal laws of transmission and reception requires recalculations of the distance between the transducer and each imaging pixel in three-dimensional coordinate system. A 96 element 2D array probe (Imasonic, France) was selected with the same nominal transmission frequency of 5 MHz. Specifically, this 2D array has 96 elements in a configuration of 3 rows and 32 columns, which provides an active area with a width in *y*-axis of 10 mm and a length of 32 mm in *x*-axis. This technique was implemented on the same aluminium sample with fatigue cracks used in Section 3.2, which was well studied by 2D NUI. A schematic diagram of this experimental configuration in *xyz*-space is presented in figure 3.29.

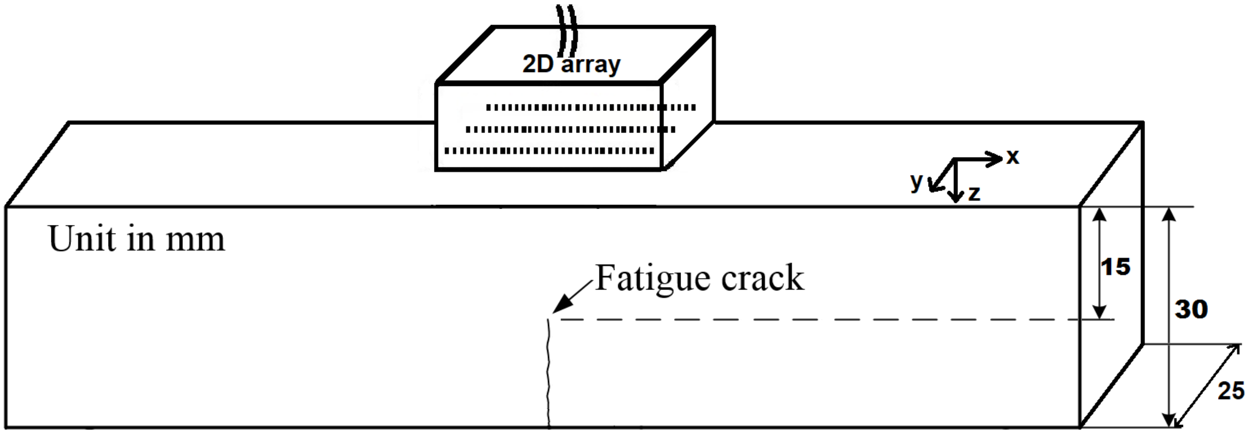

Figure 3.29. A schematic diagram of experimental setup used in 3D NUI measurement on a fatigue crack sample.

Using the optimal NUI parameters from Subsection 3.2.1, their value for this 3D NUI method was chosen as follows: window length, T of 0.12 ms, reception start time, t_r, at 0.1 ms, focused capture number of 16, sampling bit rate, of 16, sampling frequency, at 25 MHz, pulse width, of

100 ns, reception gains at 15 dB for parallel capture and 30 dB for sequential capture and pulse repetition frequency, at 500 Hz. In addition, the centre of probe was aligned to the centre of the specimen surface (the same arrangement as illustrated in figure 3.1).

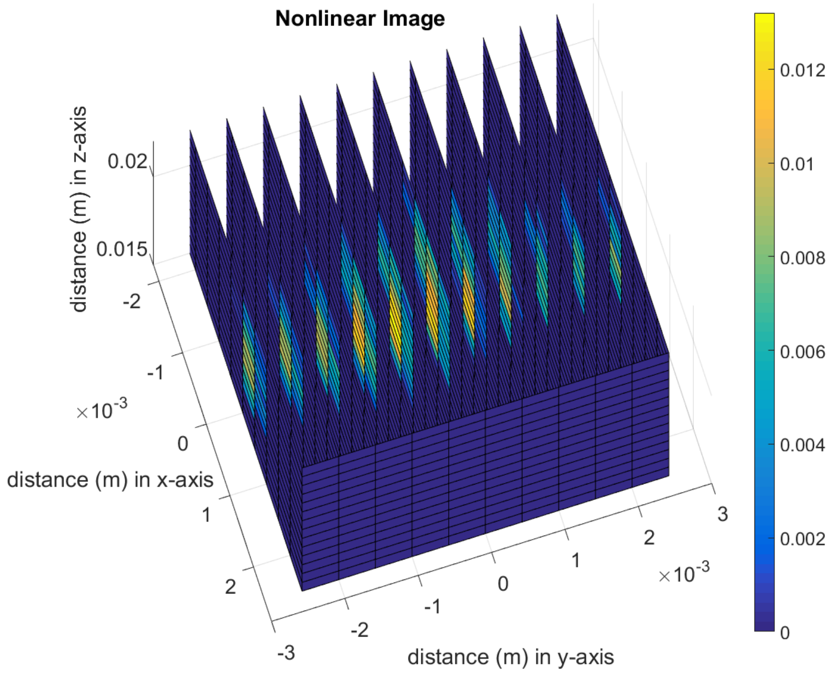

Figure 3.30. The nonlinear image from 3D NUI technique on aluminium sample in nonlinear metric, γ.

From figure 3.30, the through-thickness nonlinear features of the cracks, presented in manner of *x*-*z* plane slices, are in close proximity to the ones generated from previous 2D NUI technique (*x*-*z* plane). In addition, the results suggest that the imaging performance is depending on the amount of physical energy at focal point because the highest nonlinear metric (γ) appears in the centre of y-axis (which is on the middle slice displayed in figure 3.31).

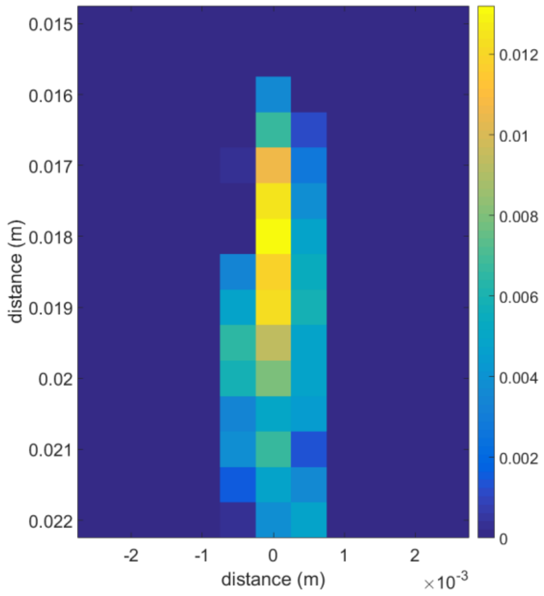

Figure 3.31. The middle slice of nonlinear image from 3D NUI technique in nonlinear metric, γ.

In practice, the 3D NUI with number of lateral array elements facilitates accurate localisation and quantification of the nonlinear defects sparsely distributed in 3D space below the inspection area. It also enhances the detectability of volumetrically variant defects in engineering structures, such as voids and inclusions.

CHAPTER 4- NONLINEAR COHERENT IMAGING

4.1 Introduction

In the present chapter, a form of amplitude and phase modulation imaging is explored which is shown to have distinct advantages over the above discussed methods in Subsection 1.4.2.6. In particular, an alternative approach is proposed to allow the effective separation of nonlinear and linear features in a nonlinear image without any requirement of a measurable diffuse field. In this study, one or two ultrasonic phased arrays are used to create a spatial map of nonlinearity by applying the process of parallel and sequential field subtraction (i.e. as used in nonlinear diffuse energy imaging, see Subsections 1.4.2.6.3 and 2.2 for fuller details), to the coherently scattered components of the field at the fundamental or subharmonic frequency. In parallel focusing the elements are fired with a pre-set delay law to cause a high intensity focus at the target pixel. In sequential focusing individual elements are fired in-turn and the full matrix of transmit-receive data is captured and synthetically focused at the pixel location in post-processing. The two resulting images would be linearly equivalent and therefore any differences in phase and amplitude can be attributed to nonlinearity. Hence, the proposed imaging metric here is the difference in coherently scattered amplitude for fields yielded from sequential and parallel focusing at each pixel location. In addition, effects arising from the nonlinearity inherent in the instrumentation are observed in the residual relative phase and amplitude at damage-free points. Processing is applied to remove these effects, greatly improving the suppression of linear scattering features. In addition, since physical focusing is only required once per pixel, this nonlinear coherent imaging (NCI) approach can shorten the time for data acquisition compared to another nonlinear amplitude-modulation imaging method developed by [Haupert et al., 2017] (see Subsection 1.4.2.6.2 for more details), which potentially allows the faster imaging of large structures.

4.2 Sequential and parallel fields

Two alternative modes of image formation are commonly employed with a typical commercially available array controller. In parallel transmission mode, all elements are fired near simultaneously in a pre-set sequence termed a delay law. The application of this mode results in a high intensity beam forming in the test structure which is then physically translated, steered or focused to form an image. Alternatively, in sequential mode each transmitter is fired independently and the time-domain signals from all the individual combinations of transmitter-receiver pairs are captured one after the other forming the so-called full matrix of inter-element responses. This full matrix can then be post-processed with the same delay laws used in parallel transmission. If the system is time invariant and the principle of linear superposition holds, these two modes of operation form linearly equivalent responses. However, elastic nonlinearity leads to differences in the fields produced by these two modes of focusing. This difference can be exploited to allow the measurement of material nonlinearity. It has been shown that elastic nonlinearity produces differences in the statistical diffuse energy of parallel and sequentially focused fields and this principle has been used to image fatigue cracks with the nonlinear diffuse energy method [Potter et al., 2014]. The first part of the present study examines the effect of the nonlinear elastic response of fatigue cracks on the relative properties of the coherently scattered components of the parallel and sequential fields

Assuming $f_{n,m}(t)$ are the time-domain received signals for each combination of transmit (n) and receive (m) elements in the sequential case. $\delta_n^T(r)$ is the transmission delay applied to the nth element to achieve a focus at a point, $r(x,z)$, which can be expressed as

$$\delta_n^T(r) = \frac{\sqrt{(x_n - x)^2 + z^2} - \sqrt{(x_a - x)^2 + z^2}}{c}, \tag{4.1}$$

where c denotes the longitudinal wave velocity of the material, x_a is the position of reference element in x-axis for the transmission delay law. $\delta_m^R(r)$ is the reception delay applied to the mth element to achieve the focus, which may be written as

$$\delta_m^R(r) = \frac{\sqrt{(x_m - x)^2 + z^2} - \sqrt{(x_b - x)^2 + z^2}}{c}, \tag{4.2}$$

where x_b is the position of reference element in x-axis for the reception delay law. The frequency (ω) domain version of $f_{n,m}(t)$ can be expressed as

$$F_{n,m}(\omega) = \int_0^{t_r} f_{n,m}(t) e^{-i\omega t} dt, \tag{4.3}$$

where t_r is the reception end time. Further, if $g_m(r,t)$ is the time-domain signal received on element m for the parallel transmission of all elements delayed independently by $\delta_n^T(r)$ then the frequency (ω) domain version of $g_m(r,t)$ is given by

$$G_m(\omega) = \int_0^{t_r} g_m(t)\, e^{-i\omega t} dt. \tag{4.4}$$

For a general nonlinear defect illuminated by ultrasonic waves, the interaction results in a transfer of energy from the fundamental frequency to subharmonics, superharmonics and modulation frequencies of the incident bandwidth. Regardless of the frequency component that the energy moves to, it is always lost from the transmission bandwidth, resulting in small changes to amplitude and phase of those frequency components. Hence, the relative difference in amplitude and phase of the transmission bandwidth for parallel and sequentially focused fields is now explored. Likewise, the gain at subharmonics is examined by measuring the difference in amplitude and phase of the reception bandwidth using a subharmonic array as receiver. In this study a narrow bandwidth from $\frac{5}{6}\omega_0$ to $\frac{7}{6}\omega_0$ was examined relative to the nominal centre frequency of the array probe at reception, ω_0. These limits are chosen to effectively measure either the remaining waves at the fundamental frequency or the increasing nonlinear subharmonic response by minimising the contributions from internal movement of energy within the evaluated bandwidth as well as suppressing the effect of spectral leakage (as discussed in Subsection 3.2.3). Consequently, the received time series in the sequential focusing case, $A_s(t)$, for an N element array is given as

$$A_s(t) = \int_{\frac{5}{6}\omega_0}^{\frac{7}{6}\omega_0} \left(\sum_{m=1}^{N} \left(\sum_{n=1}^{N} F_{n,m}(\omega) e^{i\omega\delta_n^T(r)} \right) e^{i\omega\delta_m^R(r)} \right) e^{-i\omega t} d\omega. \tag{4.5}$$

Likewise, the amplitude, $A_p(t)$, in the parallel focusing case is calculated as follows

$$A_p(t) = \int_{\frac{5}{6}\omega_0}^{\frac{7}{6}\omega_0} \left(\sum_{m=1}^{N} G_m(\omega)\, e^{i\omega\delta_m^R(r)} \right) e^{-i\omega t} d\omega. \tag{4.6}$$

4.3 Pulse-echo nonlinear coherent imaging

4.3.1 Experimental procedure

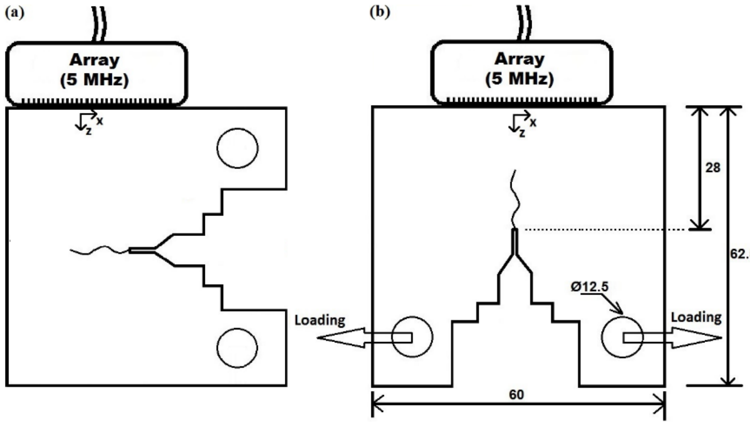

Figure 4.1. Schematic diagrams of pulse-echo configurations with array placed on (a) the right-hand side and (b) the top of the compact test specimen.

The effect of fatigue cracks on the time domain responses, $A_s(t)$ and $A_p(t)$ is first examined. The same type of CT specimens used in Chapter 2 were manufactured and the fatigue test with the same loading conditions described in Subsection 2.3.1 was conducted in order to relate linear and nonlinear metrics to the crack size. Furthermore, before the fatigue test, the same metallographic preparation described in Subsection 2.3.1 was performed around the electro-discharge machined (EDM) starter-notch. The microstructure around the crack was then observed by a microscope

(Zeiss Axio Imager 2, Germany) and, consequently, the crack length was measured periodically during the fatigue test.

The ultrasonic measurements were implemented through positioning an array on the faces of the CT specimen as shown in figures 4.1(a) and (b) and operating it in pulse-echo mode. It should be noted that the arrangement in figure 4.1(a) provides the best-case scenario for capturing the fundamental signals reflected from closed cracks since the cracks grown by the cyclic tension present a larger reflecting surface in this orientation. However, the efficacy of imaging by positioning the array above the cracks in figure 4.1(b) is also examined as this is often the only option in many industrial application scenarios, due to access restrictions. All the measurements were performed with a 64 element ultrasonic array (Imasonic, France) with nominal center frequency of 5 MHz, (-6 dB bandwidth 68% of the centre frequency), and pitch of 0.6 mm, using a commercial array controller (Micropulse, Peak NDT, UK). Aside from the selection of sampling frequency and reception gains, all of the parameters were chosen to be consistent with those used in NUI described in Subsection 2.3.2, as a consequence of the identical transmission modes in use. The sampling frequency was increased to 50 MHz due to the analysis of coherently scattered field. Further, the reception gains for sequential and parallel captures were used as 33 and 10 respectively to effectively measure the signals without the occurrence of instrument saturation.

As with other amplitude modulation methods defined in Subsection 1.4.2.6.2, the proposed coherent nonlinear imaging method relies on the presence of linear scatterer in the vicinity of nonlinear defect in order for the distorted component of the field to be returned to the transducer. This suggests that the nonlinearities cannot be detected until the linear scattering features are formed (i.e. the detection is less sensitive to the very early closed cracks). Therefore, the arrangement in figure 4.1(a) is particularly beneficial as the orientation allows stronger linear reflections from the cracks. With this arrangement, our proposed technique demonstrated its ability to localise the crack tip and size the cracks throughout the fatigue life. The underlying physics behind the nonlinear image is now explored to understand the nonlinear responses. Two fundamental physical quantities (absolute amplitude and phase), of which the nonlinear image consists, were studied over the considered bandwidth.

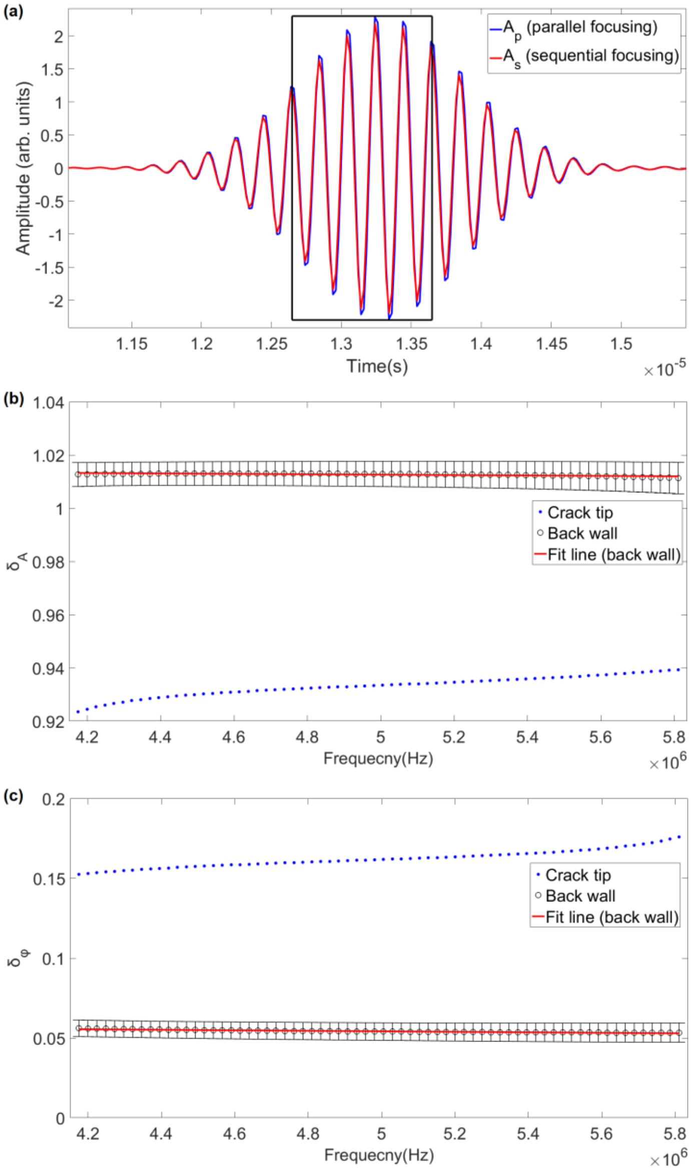

Figure 4.2. At 30000 loading cycles, (a) time traces for a pixel at the crack tip. The rectangular box denotes the portion of the signal that was analysed in the frequency domain. (b) amplitude ratio, δ_A, at crack tip and back wall, and (c) relative phase in radians, δ_φ against frequency at the crack tip and back wall. Note that error bars denote standard deviations of the metrics at multiple linear points selected from back wall at the given frequency.

Example parallel and sequential time traces ($A_p(t)$ and $A_s(t)$), produced by focusing at the crack tip in a CT specimen with a crack of length of 695 μm are shown in in figure 4.2(a). The relative properties of the fields are analysed in the frequency domain in figure 4.2(b) and (c) from which is can be seen that the parallel and sequential fields obtained from a pixel at the crack tip show differences in both amplitude and phase. Note that 5-cycle gaussian windowed signals centered at focal time, t_f in figure 2(a) were post-processed for this frequency analysis.

The amplitude ratio between sequential and parallel focusing is first studied which is defined as

$$\delta_A(\omega) = \frac{|A_s(\omega)|}{|A_p(\omega)|}. \tag{4.7}$$

Figure 4.2(b) shows the amplitude ratio, $\delta_A(\omega)$ over the post-processed frequency band (one third of the centre frequency), from which it can be seen that the ratio is below unity indicating that the amplitude of the parallel field is higher than that of the sequential field. This finding is somewhat counter-intuitive as it has been previously shown, for example through diffuse energy imaging [Potter et al., 2014], that the total energy loss from the fundamental component is higher in the parallel transmission case. It is possible that the apparent increase in amplitude is a consequence of interference effects between the distorted and undistorted components of the field. A similar observed amplitude increase has also been observed using the amplitude modulation approach to coherent nonlinear imaging [Ikeuchi et al., 2013]. The relative phase between sequential and parallel focusing is then evaluated as

$$\delta_\varphi(\omega) = \angle A_s(\omega) - \angle A_p(\omega). \tag{4.8}$$

Figure 4.2(c) shows that the relative phase, $\delta_\varphi(\omega)$ when focused at the crack tip increases significantly. For comparison, multiple linear points selected from back wall, considered as undamaged areas, were chosen to understand the background level, and results suggest that all of their relative phases remain at a lower level. Note that the linear points here are defined as those pixels on the back wall, which possess amplitude of $A_s(t_f)$ larger than 0.5 in arbitrary units. The difference in phase and amplitude between the back wall measurements can be attributed to the bulk material nonlinearity, coupling and, more significantly, the nonlinearity of the instrumentation. Nonetheless, the observed differences suggest that the relative phase and amplitude allow for the characterisation and localisation of the nonlinear defect.

4.3.2 Nonlinear coherent imaging metrics

4.3.2.1 Amplitude

Given that it is observed that nonlinear elasticity induces measurable differences in the coherently scattered component of parallel and sequentially focused fields, this is now used a basis for nonlinear imaging. First, the complex amplitude of the focal point *r* in the sequential case, I_s is given as

$$I_s(x,z) = A_s(t_f), \tag{4.9}$$

This sequential imaging is equivalent to a conventional linear total focusing method image. Similarly, the complex amplitude of the focal point *r* in the parallel case I_p is given by

$$I_p(x,z) = A_p\left(t_f\right), \tag{4.10}$$

Finally an image is formed from calculation of the nonlinear amplitude metric ζ at a given imaging/focal point $\zeta(x,z)$ by subtracting the parallel and sequential amplitudes as follows

$$\zeta(x,z) = \left|I_s(x,z) - I_p(x,z)\right|. \tag{4.11}$$

Figures 4.3(a) and (b) present the sequential and parallel images ($|I_s(x,z)|$ and $\left|I_p(x,z)\right|$ respectively) of the region around the EDM starter-notch tip and fatigue crack. These images, which are linearly equivalent, are seen to be indistinguishable, even in the presence of crack growth. The subtracted image, $\zeta(x,z)$ in figure 4.3(c) is seen to suppress the linear geometric features, revealing the nonlinear response of the fatigue crack with the maximum nonlinearity located close to the crack tip. This imaging process is termed as pulse-echo amplitude NCI. It is noted that the residual amplitude of the subtracted fields used to form the nonlinear image is predominantly from the observed differences in phase rather than amplitude. This can be attributed to small changes in phase producing large residual amplitudes when the responses are subtracted. Some evidence is provided later in the corresponding results through using only the phase differences as the imaging metric (see the method discussed in Subsection 4.3.2.2 as well as more imaging results in figures 5.7(a-j) and figures 5.8(a-j)).

Although reduced through subtraction, the suppression of linear features is imperfect. This is thought to be a consequence of both the bulk material nonlinearity and that of the instrumentation, specifically the ability of the instrument to produce identical waveforms in both parallel and sequential transmission modes. This was seen in figures 4.2(b) and (c) as differences in amplitude and phase for fields focused on the specimen back wall which is thought to act as a purely linear reflector. To compensate for these effects, the relative amplitude and phase of the baseline measurements is first averaged for multiple points on the back wall. This baseline response is then approximated through a linear fit in the frequency domain, indicated by the red lines in figures 4.2(b) and (c). Note that the linear fit can be replaced by direct use of each average value due to negligible differences of them for back wall. These approximate baseline phase and amplitude terms are denoted $\hat{\delta}_{\varphi}(\omega)$ and $\hat{\delta}_{A}(\omega)$ respectively. The influence of instrument nonlinearity can be removed by applying a correction for the relative phase and amplitude arising from the instrument to the sequential focused amplitude, which as follows

$$\hat{A}_s(\omega) = \frac{A_s(\omega)}{\hat{\delta}_A(\omega)} e^{-i\hat{\delta}_{\varphi}(\omega)}, \tag{4.12}$$

where $\hat{A}_s(\omega)$ denotes the corrected sequential amplitude in frequency domain. Hence, the improved complex amplitude in time domain of the focal point r in the sequential case $\hat{I}_s$ is given as

$$\hat{I}_s(x, z) = \hat{A}_s(t_f). \tag{4.13}$$

An improved image is then obtained by computing the new nonlinear amplitude metric $\hat{\zeta}$ with the compensated amplitude in the sequential case as follows

$$\hat{\zeta}(x,z) = \left|\hat{I}_s(x,z) - I_\mathrm{p}(x,z)\right|. \tag{4.14}$$

Figure 4.3(d) shows the nonlinear image with the instrumentation compensation from which it can be seen that the background levels drop approximately from 0.2 to 0.02 in nonlinear metric.

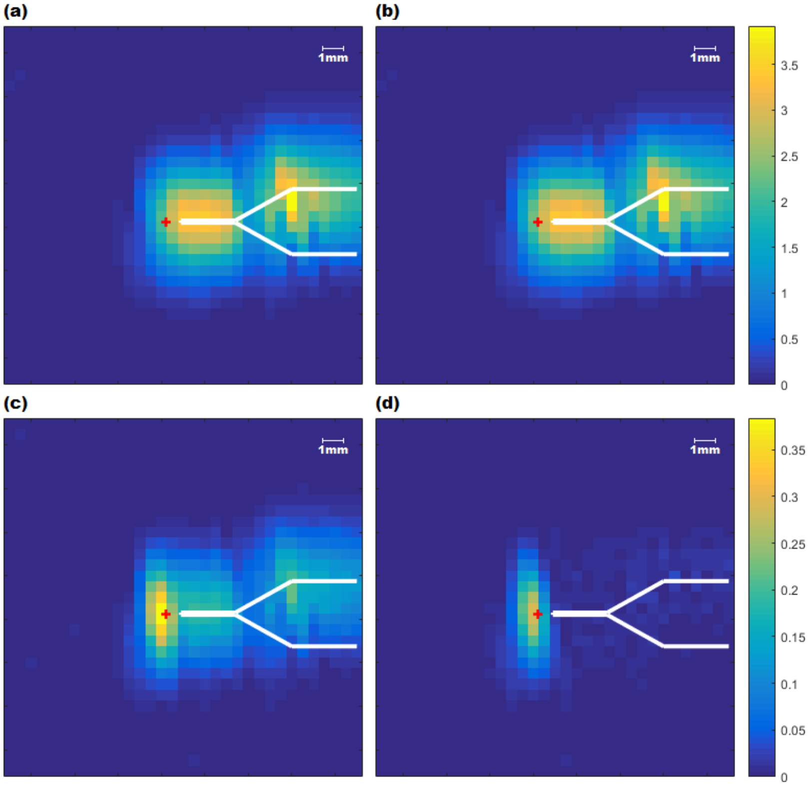

Figure 4.3. At 30000 loading cycles, (a) linear sequential image, $|I_s|$ and (b) parallel image $\left|I_p\right|$ in arbitrary units, (c) image of the nonlinear metric, ζ and (d) image of the nonlinear metric with instrumentation compensation applied, $\hat{\zeta}$. The inspection configuration is as illustrated in figure 4.1(a). The red cross indicates the micrographically measured crack tip and the geometry of the EDM starter notch is shown with white lines.

4.3.2.2 Phase

As a consequence of significant differences in the phase component between parallel and sequentially focused fields, their differences are extracted and then exploited for nonlinear imaging. Note that it is necessary to limit the interference from background noise by identifying the backscatterers on a linear image with a threshold (e.g. $I_s(x,z)$ in figure 4.3(a) is not less than 2 in this case) and then mapping the indicated clean area in the nonlinear phase image as zero. An intuitive way to achieve the phase imaging is to directly use phase component $\varphi_s(x,z)$ of complex amplitude $I_s(x,z)$ at every pixel in sequential case (in equation (4.9)) as follows

$$\varphi_s(x,z) = \angle A_s(t_f), \tag{4.15}$$

Likewise, phase component $\varphi_p(x,z)$ of complex amplitude $I_p(x,z)$ in parallel case (in equation (4.10)) is given by

$$\varphi_p(x,z) = \angle A_p(t_f), \tag{4.16}$$

Consequently, an image is formed from calculation of the nonlinear phase metric ζ_φ in radians at a given imaging/focal point $\zeta_\varphi(x,z)$ by subtracting the parallel and sequential amplitudes as follows

$$\zeta_\varphi(x,z) \ = \angle A_s(t_f) - \angle A_p(t_f). \tag{4.17}$$

Figures 4.4(a) and (b) display the sequential and parallel images of the same imaging area near the crack and the notch. These linear images (representing $\varphi_s(x,z)$ and $\varphi_p(x,z)$) appear indistinguishable making it hard to extract any information about the crack. However, the subtracted image in figure 4.4(c) reveals the nonlinear response around the crack tip, which is comparable to the result in figure 4.3(c). This imaging process is referred to pulse-echo phase NCI. It is noted that this nonlinear phase metric ζ_φ provides higher selectivity of the crack tip over ζ by reducing the averaged background noise level from -6 dB to -9 dB.

Similarly, the instrument noise is then reduced by applying the same approximate baseline phase term $\hat{\delta}_\varphi(\omega)$ used in Subsection 4.3.2.1 to the sequentially focused amplitude as follows

$$\tilde{A}_s(\omega) = A_s(\omega)e^{-i\hat{\delta}_\varphi(\omega)}, \tag{4.18}$$

An enhanced nonlinear phase image is then realised by calculating the corrected nonlinear phase metric $\tilde{\zeta}_\varphi$ in radians with the compensated phase component in the sequentially focused amplitude as follows

$$\tilde{\zeta}_\varphi(x,z) = \angle\, \tilde{A}_s(t_f) - \angle\, A_p(t_f). \tag{4.19}$$

Figure 4.4(d) presents the nonlinear image with the instrumentation compensation from which it can be seen that the background levels drop approximately from 0.06 to 0.002 in the nonlinear phase metric.

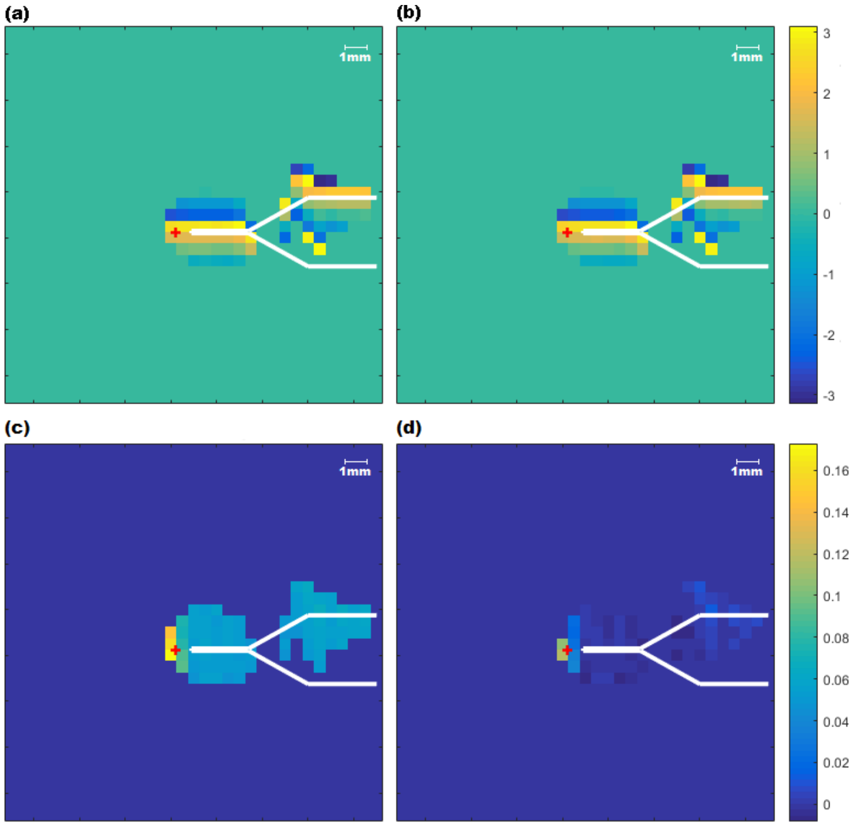

Figure 4.4. At 30000 loading cycles, (a) linear sequential image, $\angle A_s(x,z)$ and (b) linear parallel image, $\angle A_p(x,z)$ in radians, (c) image of the nonlinear metric, ζ_φ in radians and (d) image of the nonlinear metric with instrumentation compensation applied, $\tilde{\zeta}_\varphi$ in radians. The inspection configuration is as illustrated in figure 4.1(a). The red cross indicates the micrographically measured crack tip and the geometry of the EDM starter notch is shown with white lines.

4.4 Pitch-catch nonlinear coherent imaging

4.4.1 Experimental procedure

Since this section aims to analyse the forward scattered field generated by the equivalent setup and method, the imaging methods and metrics used in this section are consistent with those described in Section 4.3. However, the experimental configurations used here (as presented in figures 4.5(a)) differs from the pulse-echo arrangement used in Section 4.3. Note that the same array used in Section 4.3 is positioned at the identical inspection location as the transmitter in this section. Consequently, only the reception delay $\delta_m^R(r)$ requires the recalculations due to the change in position of the receiver. Whilst both of the pitch-catch configurations presented in figures 4.5(a) and (b) are often impractical in application to structures with single-sided access, there are still many critical engineering components with double-sided access (e.g. turbine blades). Additionally, it is worth investigating the nonlinear phenomenon of forward scattered field prior to the formation of linear defects.

4.4.1.1 Fundamental measurement

The pitch-catch configuration is expected to be the most sensitive to crack closure as the entire wave front passing through the closed cracks is allowed to be captured by positioning another array on the opposite side. Specifically, the same array used in pulse-echo NCI imaging was implemented as the transmitter in pitch-catch configuration. In addition, a 64-element ultrasonic array (Imasonic, France) with nominal centre frequency of 5 MHz, (-6 dB bandwidth 86% of the centre frequency) and pitch of 0.63 mm was used as the receiver for pitch-catch NCI fundamental imaging. The schematic diagram in figure 4.5(a) presents the arrangement of the pitch-catch fundamental measurement.

4.4.1.2 Subharmonic measurement

The subharmonic imaging was achieved by employing a 64-element ultrasonic array (Imasonic, France) with nominal centre frequency of 2.5 MHz, (-6 dB bandwidth 66% of the centre frequency) and pitch of 0.5 mm at reception. The schematic diagram in figure 4.5(b) describes the layout of the pitch-catch subharmonic measurement.

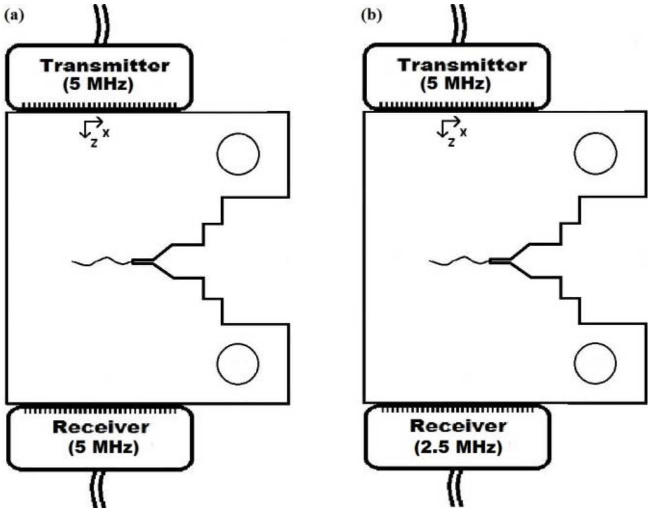

Figure 4.5. Schematic diagrams of (a) pitch-catch fundamental configuration and (b) pulse-echo subharmonic configuration.

4.4.2 Sequential and parallel fields

Likewise, their example parallel and sequential time traces (($A_p(t)$ and $A_s(t)$)) produced by focusing at the crack tip in the same CT sample are shown in in figure 4.6(a) and figure 4.7 (a). The relative properties of the fundamental and subharmonic wave fields are analysed in the frequency domain in figures 4.6(b) and (c) and figures 4.7(b) and (c) respectively from which it can be seen that the parallel and sequential fields obtained from pixels at the crack tip present significantly larger differences in both amplitude and phase in contrast to those from linear points. As a consequence of the measured through-transmission field, the linear points here are defined as those pixels within the clean area (i.e. undamaged region containing no linear scatterers), which possess amplitude of $A_s(t_f)$ larger than 0.5 in arbitrary units. Again, gaussian windowed signals centered at focal time, t_f in figure 4.6(a) and figure 4.7(a) were post-processed for this frequency analysis.

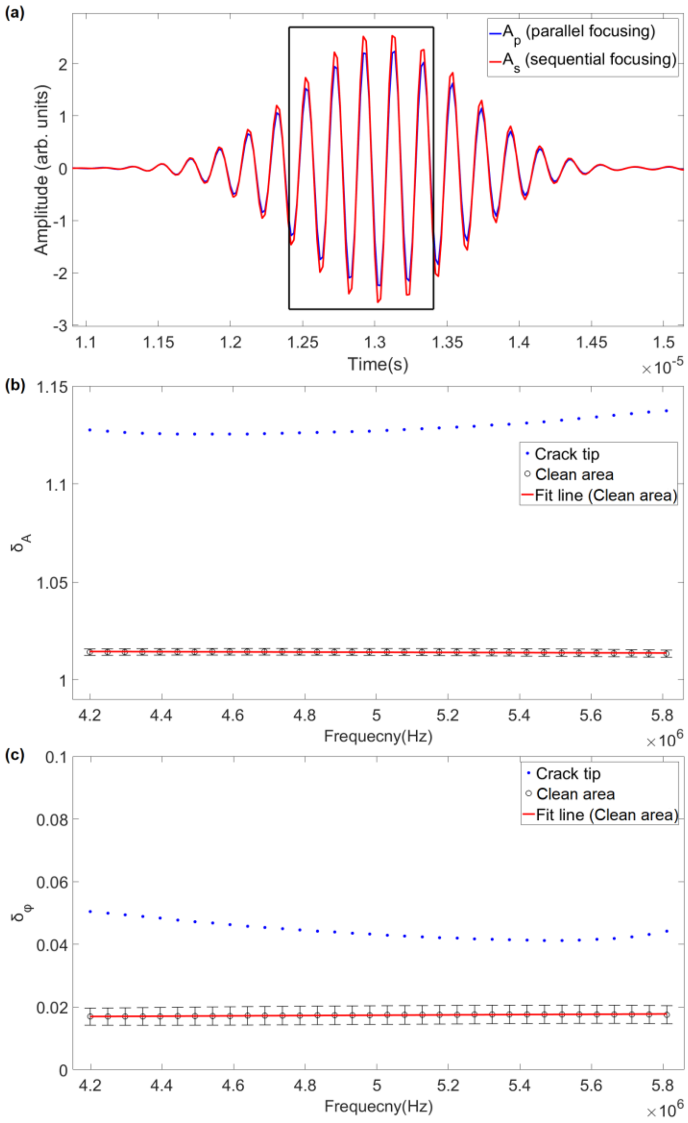

Figure 4.6. Pitch-catch fundamental measurement at 30000 loading cycles, (a) time traces for a pixel at the crack tip. The rectangular box denotes the portion of the signal that was analysed in the frequency domain. (b) amplitude ratio, δ_A, at crack tip and linear points, and (c) relative phase in radians, δ_φ against frequency at the crack tip and linear points. Note that error bars denote standard deviations of the metrics at multiple linear points selected from clean area at the given frequency.

Notably, the amplitude ratio between sequential and parallel focusing δ_A at the crack tip in the fundamental and subharmonic measurements of pitch-catch NCI (as presented in figure 4.6(b) and figure 4.7(b) respectively) increases by 0.2 and 0.1 respectively compared to that of the pulse-echo measurement (see figure 4.2(b)). As a consequence, this delivers remarkable contributions to the same nonlinear metric, ζ as indicated in equation (4.11). This observation (i.e. the amplitude of the parallel field is higher than that of the sequential field) as presented in figure 4.6(b) and figure 4.7(b) shows consistent nonlinear phenomenon with the diffuse energy imaging (NUI) results in which the remaining fundamental energy of the parallel focusing at the crack tip is much less than that of the sequential one.

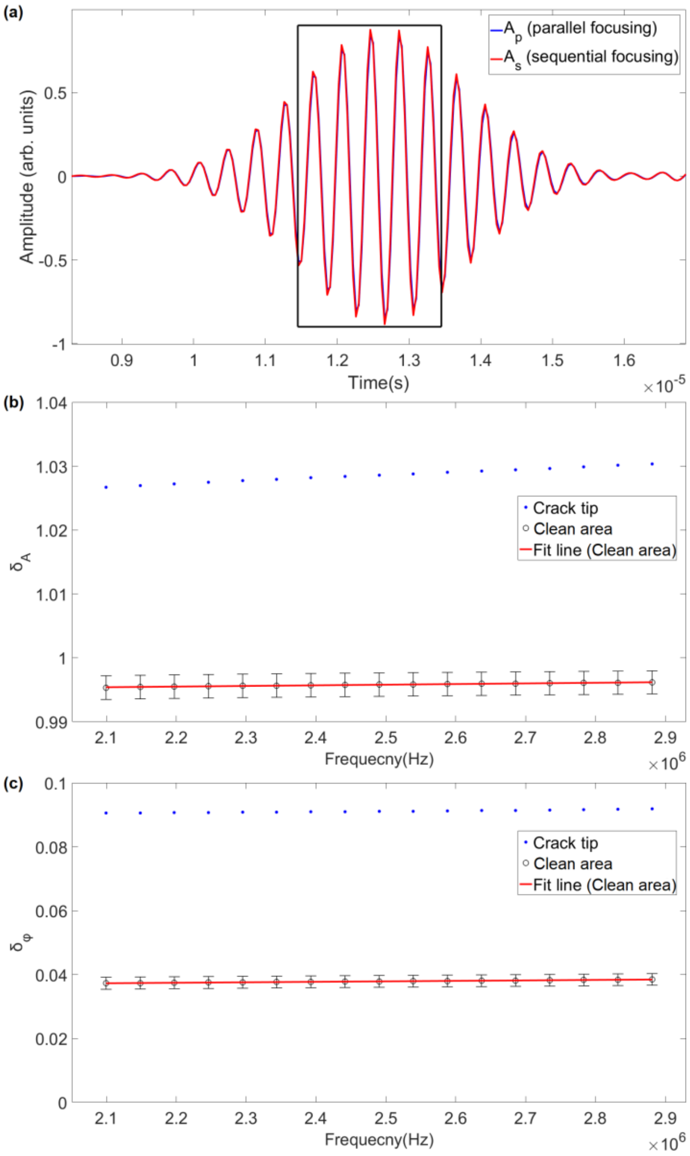

Figure 4.7. Pitch-catch subharmonic measurement at 30000 loading cycles, (a) time traces for a pixel at the crack tip. The rectangular box denotes the portion of the signal that was analysed in the frequency domain. (b) amplitude ratio, δ_A, at crack tip and linear points, and (c) relative phase in radians, δ_φ against

frequency at the crack tip and linear points. Note that error bars denote standard deviations of the metrics at multiple linear points selected from clean area at the given frequency.

On the other hand, the phase difference between the parallel and sequential focusing δ_φ at the crack tip in pitch-catch fundamental and subharmonic measurements at the crack tip reduces by 0.11 and 0.07 respectively relative to that in pulse-echo approach. As a consequence, the phase imaging here is thought to be ineffective for measuring the nonlinearity. This difference in amplitude and phase between backscattered and through-transmission fundamental components induced by closed cracks might be attributed to the nonlinear directivity function at the crack interface. Most importantly, these differences seen in pitch-catch configurations can be also used to image the elastic nonlinearity. All of δ_A and δ_φ at crack tip produced by different NCI methods are summarised in the table 4.1. In addition, it is worth noting their relative change at linear point (back wall or clean area) between each method is much smaller compared with that at crack tip.

Type of NCI	δ_A at crack tip	δ_A at back wall or clean area	δ_φ at back wall or clean area	δ_φ at back wall or clean area
Pulse echo	0.93	1.00	0.16	0.05
Pitch catch (fundamental measurement)	1.13	1.02	0.05	0.02
Pitch catch (subharmonic measurement)	1.03	1.00	0.09	0.04

Table 4.1. A summary of amplitude ratio, δ_A and relative phase in radians, δ_φ at crack tip and linear point (back wall or clean area) produced by different types of NCI methods.

4.4.3 Imaging results

The complex amplitude metrics used in pulse-echo NCI ($\zeta(x,z)$ and $\hat{\zeta}(x,z)$) can be equivalently applied to the pitch-catch fundamental and subharmonic measurements (termed as pitch-catch fundamental NCI and pitch-catch subharmonic NCI respectively). Figures 4.8(a) and

(b) show the pitch-catch fundamental sequential and parallel images ($|I_s(x,z)|$ and $|I_p(x,z)|$) of the same region around the notch and the crack as the area indicated in figures 4.3(a-d). Note that the absolute amplitude in these linear metrics implies the capability to propagate through the paths between transmitter and receiver. Although these two images, which are linearly identical, are seen to be indistinguishable the subtracted image in figure 4.8(c) is seen to suppress the linear features and reveal the nonlinear response of the fatigue crack with the maximum value in the vicinity of the crack tip. Furthermore, figure 4.8(d) shows the nonlinear image with the same instrumentation compensation process from which it can be seen that the background levels reduce roughly from 0.06 to 0.01 in nonlinear metric. For such nonlinear features the image produced is that of the dominant change in amplitude, small phase offset and associated point spread function for the technique.

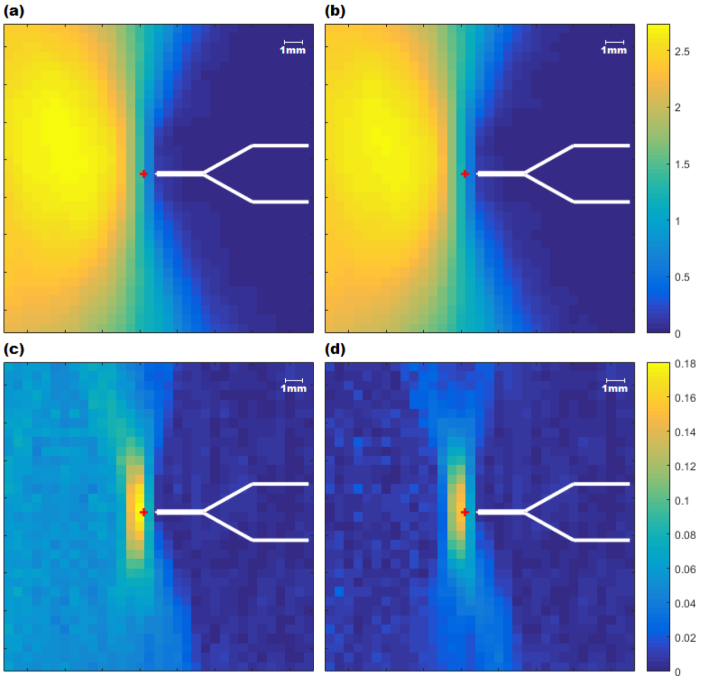

Figure 4.8. Pitch-catch fundamental NCI at 30000 loading cycles, (a) sequential image, $|I_s|$ and (b) parallel image, $|I_p|$ in arbitrary units, (c) image of the nonlinear metric, ζ and (d) image of the nonlinear metric with instrumentation compensation applied, $\hat{\zeta}$. The inspection configuration is as illustrated in figure 4.5(a). The red cross indicates the micrographically measured crack tip and the geometry of the EDM starter notch is shown with white lines.

Likewise, the linear and nonlinear images from the subharmonic measurement are displayed in figures 4.9(a-d). Their features can be related to those in figures 4.8(a-d). As a consequence of partial fundamental loss, the nonlinear subharmonic responses indicated by nonlinear images in figures 4.9(c) and (d) behave somewhat weaker than the nonlinear fundamental responses measured by those in figures 4.8(c) and (d). This is also seen from the smaller δ_φ and δ_A at the crack tip observed in figures 4.7(b) and (c). Therefore, the NCI of fundamental waves is thought to deliver the highest selectivity to elastic nonlinearity.

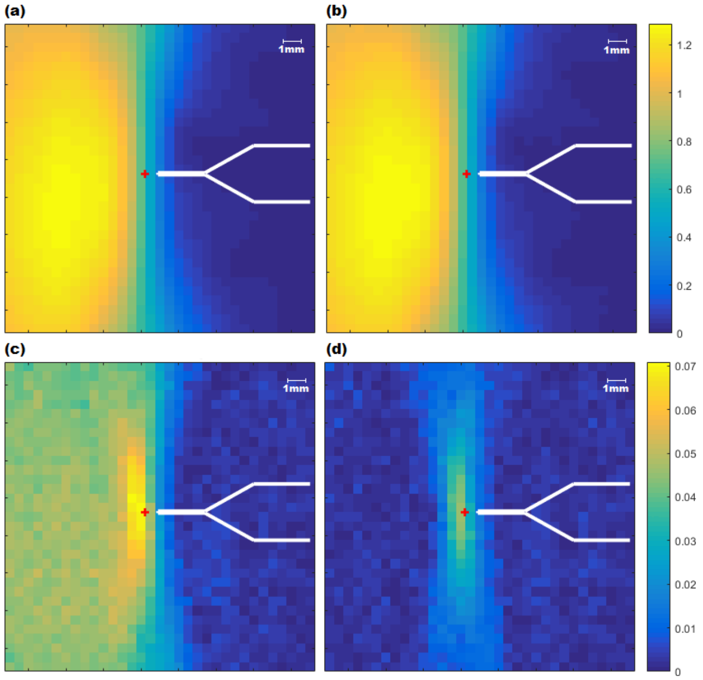

Figure 4.9. Pitch-catch subharmonic NCI at 30000 loading cycles, (a) sequential image, $|I_s|$ and (b) parallel image $|I_p|$ in arbitrary units, (c) image of the nonlinear metric, ζ and (d) image of the nonlinear metric with instrumentation compensation applied, $\hat{\zeta}$. The inspection configuration is as illustrated in figure 4.5(b). The red cross indicates the micrographically measured crack tip and the geometry of the EDM starter notch is shown with white lines.

4.5 Conclusions

A group of coherent nonlinear ultrasonic imaging (NCI) techniques are proposed to effectively localise and quantify the extent of cracking by evaluating differences in parallel and sequentially focused fields. Specifically, the first NCI method using pulse-echo amplitude measurement (referred to pulse-echo amplitude NCI) is developed based upon the overall nonlinear responses in absolute amplitude and phase. This method allows the linear sequential and parallel images (indicated by $|I_s(x,z)|$ and $|I_p(x,z)|$ respectively), to reveal essentially geometric information from sample boundaries and large defects. Additionally, the subtracted nonlinear images reveal nonlinear features such as partially-closed cracks and crack tips (measured by the amplitude metric of NCI, ζ). Further, the second NCI method (termed pulse-echo phase NCI) only measures the phase component of the nonlinear responses and then exploits it to images the cracks. The results suggest that it can improve the selectivity of cracks by suppressing the averaged background noise level from -6 dB (measured by ζ) to -9 dB (measured by the phase metric of NCI, ζ_φ). Last, another two variants of NCI techniques using the different arrangement (known as pitch-catch fundamental NCI and pitch-catch subharmonic NCI) are developed by measuring forward scattered amplitude at the opposite side using the amplitude metric , ζ. This configuration also demonstrates its sensitivity to crack closure by capturing the waves at either subharmonic or fundamental frequencies. However, this method (i.e. the imaging approach of forward scattered field) principally depends on the difference in the absolute amplitude (rather than the phase used in pulse-echo configuration) between sequential and parallel focusing. Furthermore, the NCI of fundamental waves is seen to deliver the highest selectivity of acoustic nonlinearity. Last but not least, all of the NCI methods discussed above can be optimised by suppressing the instrumentation noise estimated from the baseline measurements of relative phase and absolute amplitude at the back wall. The results of NCI (produced by using the optimised amplitude and phase metrics $\hat{\zeta}$ and $\tilde{\zeta}_\varphi$ on the same type of sample) suggest that this technique without the use of a measurable diffuse field potentially provides higher signal-to-noise performance over the NUI technique using the same instrumentation.

CHAPTER 5-INVESTIGATIONS INTO THE APPLICATIONS OF NONLINEAR COHERENT IMAGING

5.1 Introduction

Since chapter 4 has presented the potential of four proposed nonlinear coherent imaging (NCI) methods (known as pulse-echo amplitude NCI, pulse-echo phase NCI, pitch-catch fundamental NCI and pitch-catch subharmonic NCI) on detecting a fatigue crack grown in a mild steel specimen, this chapter further examines their capability of crack sizing and early detection through periodic monitoring of crack growth from 0 to 100,000 cycles (*circa* 74% of fatigue life) in the same type of specimen. Their efficacy of crack detection is studied and then compared, in order to explore the detection limits and the applications. In addition, the effect of inspection angle (i.e. dependence of linear scattering) is also investigated for the pulse-echo measurement along with nonlinear ultrasonic diffuse energy imaging (NUI) for comparison purpose. Here the loading step was chosen as 10,000 cycles in order to allow the microstructural change and detection limits to be explored by all of the NCI approaches.

Last, the SBCs grown in two existing aluminium specimens were inspected by the pulse-echo amplitude NCI, in order to explore the detectability of SBCs in application to pressure vessel and pipeline inspection. These samples possess close type of defects and similar geometry compared with those engineering components. Furthermore, a preliminary study of the relationship between the change in relative phase ($\hat{\delta}_\varphi$) as well as amplitude ratio ($\hat{\delta}_A$) and the crack size is conducted.

5.2 Monitoring fatigue crack growth

Before conducting the fatigue test described in Subsection 2.3.1, the baselines of relative phase ($\hat{\delta}_{\varphi}$) and amplitude ratio ($\hat{\delta}_{A}$) from linear points across the back wall or those through the clean materials were evaluated for pulse-echo and pitch-catch methods respectively, in order to compensate for the instrument nonlinearity (as described in Sections 4.3 and 4.4). The baseline parameters, $\hat{\delta}_{\varphi}$ and $\hat{\delta}_{A}$, acquired for the 0-cycle case are used in the image formation of each subsequent loading step. In addition, the same metallographic preparation and the identical micrography described in Subsection 2.3.1 were performed in this study. All of the micrographic results in this study are presented in figures (A.2-A.11). In order to quantify the performance of all the types of NCI relative to that of linear sequential (TFM) and NUI methods, a unified signal-to-noise ratio, SNR_1 is defined as the maximum absolute value in each imaging metric from the crack (indicated by micrography) to its peak absolute value from the EDM starter notch, as the nearest linear reference feature.

5.2.1 Pulse-echo nonlinear coherent imaging

The experimental apparatus as mentioned in Subsection 4.3.1 is implemented in this study. Figures 5.1(a-j) show images obtained with sequential imaging, denoted as $\left|\hat{I}_s(x,z)\right|$ (indicated in equation 4.13) from 10000 cycles to 100000 cycles. Before 50000 cycles, the crack at the early stages are barely detectable due to their small size (maximum 1.3 mm) relative to the fundamental wavelength (1.2 mm). Beyond 50000 cycles, the cracks are detectable and can be sized from these sequential images.

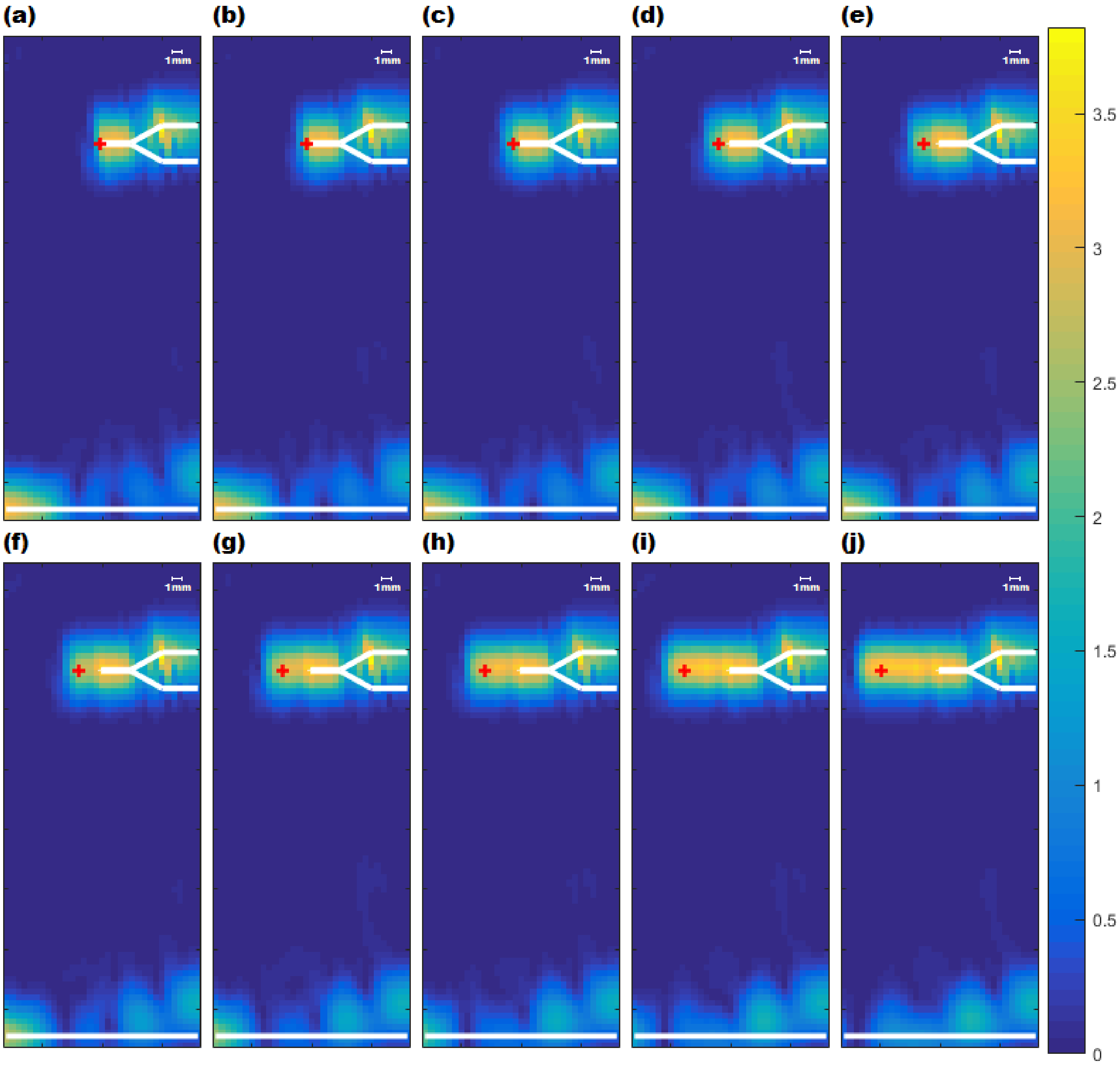

Figure 5.1. Linear sequential (i.e. TFM) images, $|\hat{I}_S(x,z)|$ in arbitrary units at (a) 10000 cycles, (b) 20000 cycles, (c) 30000 cycles, (d) 40000 cycles, (e) 50000 cycles, (f) 60000 cycles, (g) 70000 cycles, (h) 80000 cycles, (i) 90000 cycles and (j) 100000 cycles. The inspection configuration is as illustrated in figure 4.1(a) and the red cross marks the micrographically measured crack tip.

In contrast, the coherent nonlinear images, $\hat{\zeta}(x,z)$ obtained using equation 4.14 in figures 5.2 (a-j) show sensitivity to cracks as well as high selectivity of nonlinear features at an earlier stage in the fatigue life. The crack was first distinguishable at 20,000 cycles (indicated by a magnitude of 0.082 in the nonlinear amplitude metric $\hat{\zeta}$ higher by a factor of 5 compared with the peak value on the starter notch observed at current and previous stages (i.e. SNR_1 is equal to 5)), which corresponded to a crack length of 0.35 mm as shown in figure 5.4(b). Notably, both the nonlinear and linear images in its late fatigue life (as shown in figures 5.1(g-j) and 5.2(g-j)) indicate the crack-like features beyond the crack tip micrographically measured on the surface. This is thought to be attributed to the through-thickness crack curvature (a natural behavior with fatigue crack propagation [Peng et al., 2018]). It is also confirmed by opening the same CT specimen at 135500 cycles used in Subsection 2.4.1 and obtaining the crack front profile in which the side crack front is up to approximately 2 mm less than the middle, as shown in figure 5.2(a). Consequently, the indicated crack tip from ultrasonic measurements over the through-thickness crack font is expected to be farther from the notch.

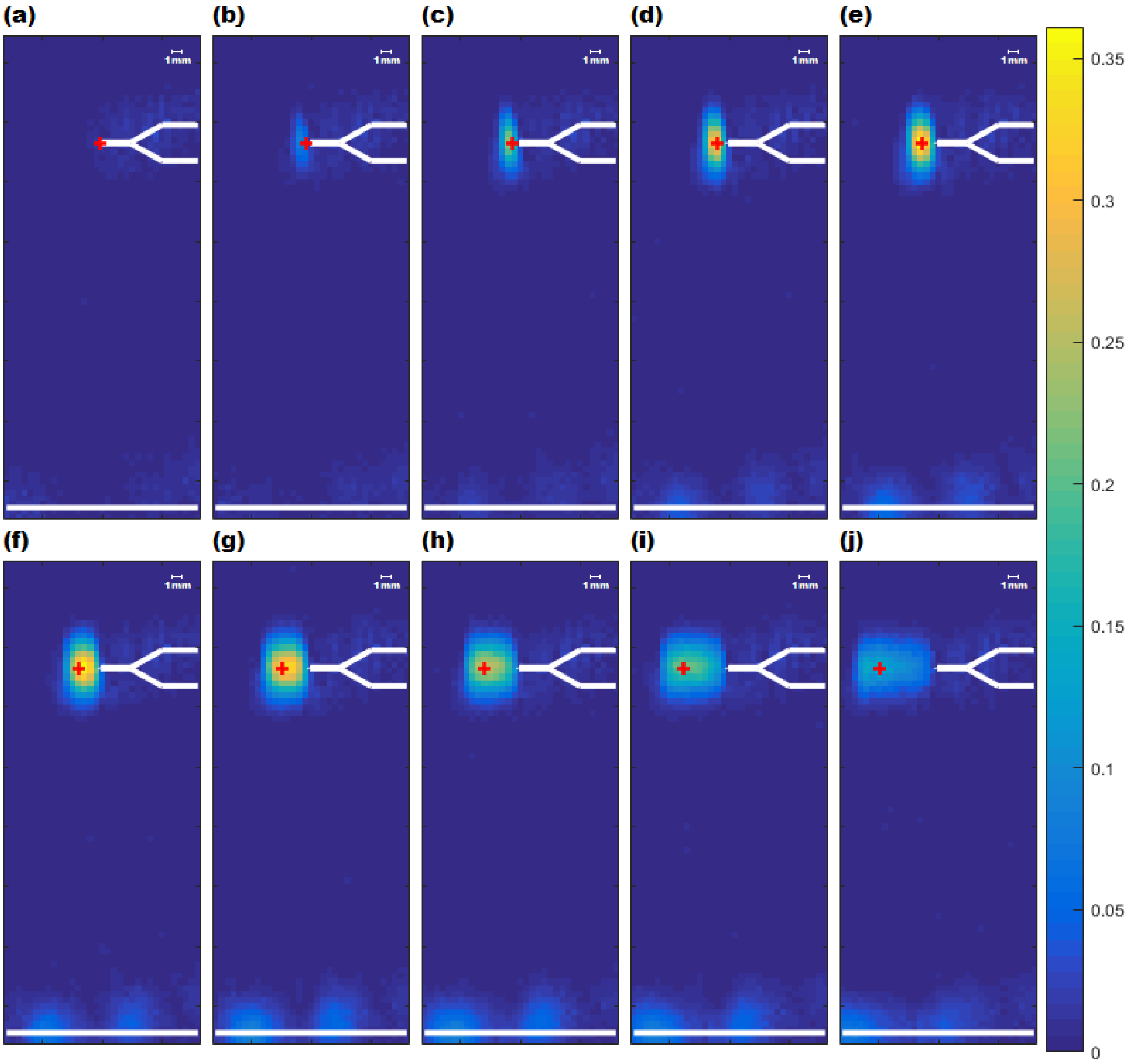

Figure 5.2. Nonlinear images in nonlinear amplitude metric, $\hat{\zeta}$ at (a) 10000 cycles, (b) 20000 cycles, (c) 30000 cycles, (d) 40000 cycles, (e) 50000 cycles, (f) 60000 cycles, (g) 70000 cycles, (h) 80000 cycles, (i) 90000 cycles and (j) 100000 cycles. The inspection configuration is as illustrated in figure 4.1(a) and the red cross marks the micrographically measured crack tip.

It is worth noting that selectivity of nonlinear defects seen in figures 5.2(b-d) in these early stages (e.g. 20000 cycles) is improved significantly by the instrumentation compensation in figure 5.3(a), without which the uncorrected nonlinear amplitude metric, ζ, from cracks was at the same level as those from back wall in figure 5.3(b). Subsequently, from figures 5.2(a-j) it can be observed that the peak nonlinear metric is seen to increase until 60000 cycles and then start to decrease gradually. It can also be seen that the position of the peak nonlinear metric at each stage is consistently close to the micrographically measured crack tip (marked as a red cross). Furthermore, the results suggest the crack started to become progressively more open (i.e. the nonlinear metric is decreasing and the linear metric is increasing) from 60000 cycles, which is consistent with the increased linear amplitude seen in the corresponding linear images in figures 4.1(b-j). This late-life amplitude effect is thought to be due to fewer contact points across the crack faces leading to reduced instances of nonlinear contact acoustic effects (described in Subsection 1.4.2.2). Note that the change in relative phase δ_φ has a significantly greater effect than the relative amplitude δ_A on the nonlinear imaging metric (before 60000 cycles), which indicates that the nonlinear phase response is more sensitive to cracks at the early stages. This effect will be inferred later by the imaging results in the nonlinear phase metric, $\tilde{\zeta}_\varphi$ (see figures 5.6 (a-j)).

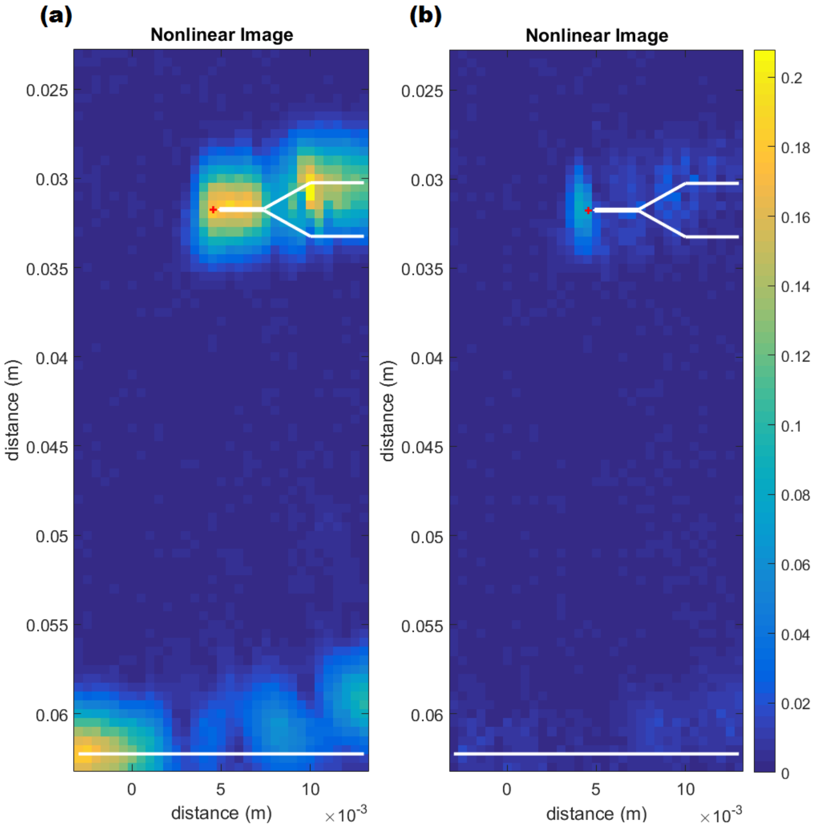

Figure 5.3. Nonlinear images at 20000 cycles where the crack size was 0.35 mm (a) in nonlinear amplitude metric, ζ and (b) in improved nonlinear amplitude metric $\hat{\zeta}$. The inspection configuration is as illustrated in figure 4.1(a) and the red cross marks the micrographically measured crack tip.

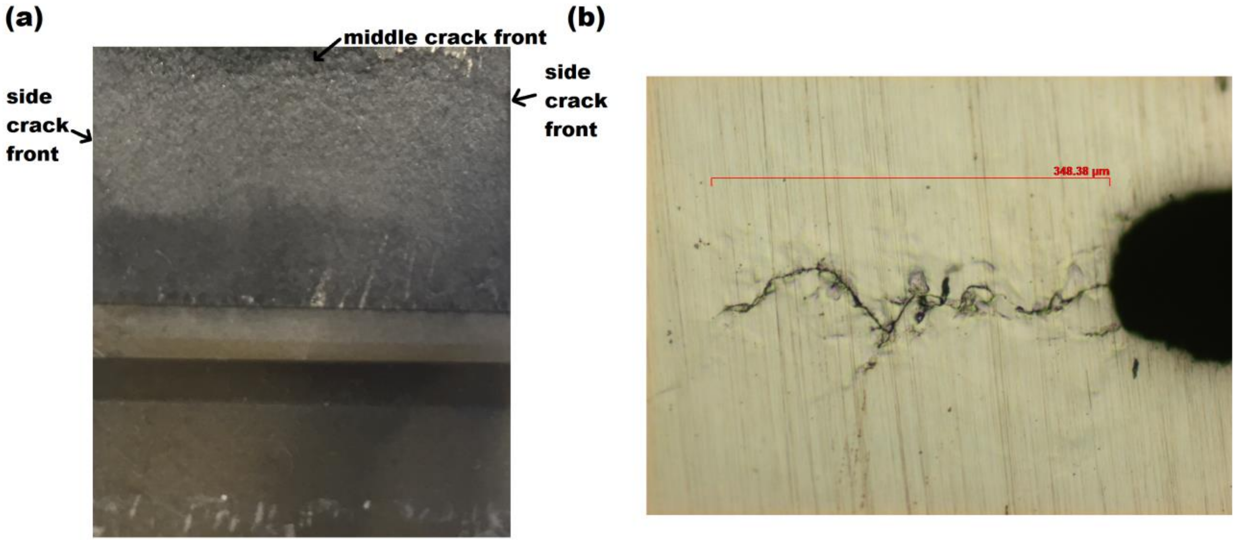

Figure 5.4. (a) Photo of through-thickness crack curvature at 135500 cycles (b) micrograph of the fatigue crack at 20000 cycles.

Figure 5.5(a) shows the relationship between the maximum nonlinear metric (obtained from the images shown in figures 5.2(a-j)) and the loading cycles. The error bars denote the standard deviation across multiple repeat (between 5 and 8) measurements on the same sample and so indicate measurement consistency. Furthermore, another four identical type of specimens were loaded to 30000 cycles (resulting in crack lengths varying between 515 μm and 750 μm, as presented in figure 5.6) and the measured maximum nonlinear metric shown as the red point in Figure 5.5(a). Their mean and standard deviation are calculated over all specimens using 5 repeat measurements on each sample each. This then provides some indication of the repeatability between different specimens, but is thought primarily to reflect the statistical variance of crack growth between samples. Also, figure 5.5(b) shows the ability of pulse-echo amplitude NCI to predict the location of the crack tip from 20000 cycles (the starting point where the crack of 0.35 mm was detectable).

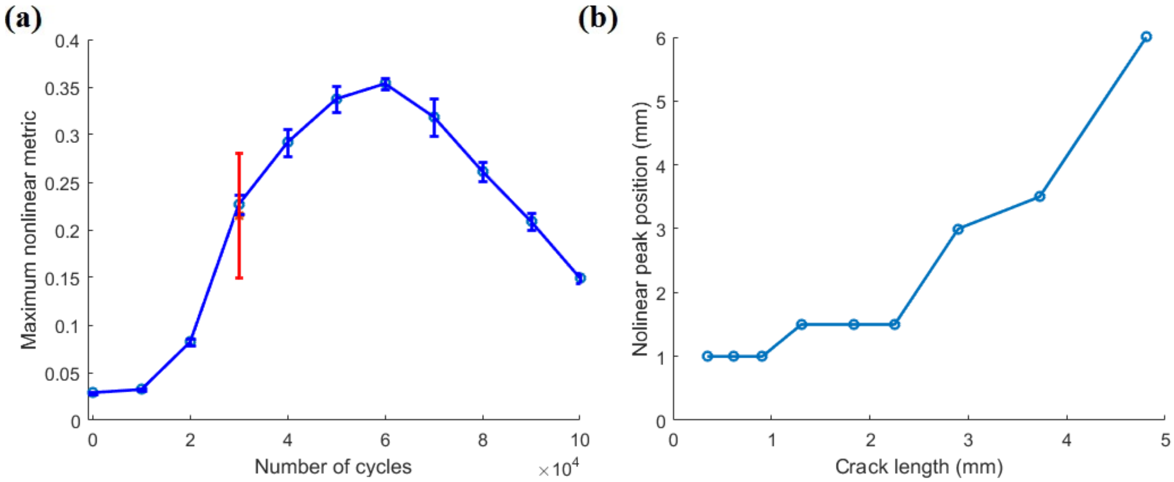

Figure 5.5. Maximum nonlinear amplitude metric $\hat{\zeta}$ during fatigue as a function of (a) number of fatigue cycles (blue and red error bars represent standard deviations of multiple measurements on the single specimen and across five specimens respectively). (b) Measured crack length in mm from the nonlinear image (notch end to position of maximum nonlinear metric $\hat{\zeta}$) during fatigue as a function of micrographically measured crack length in mm.

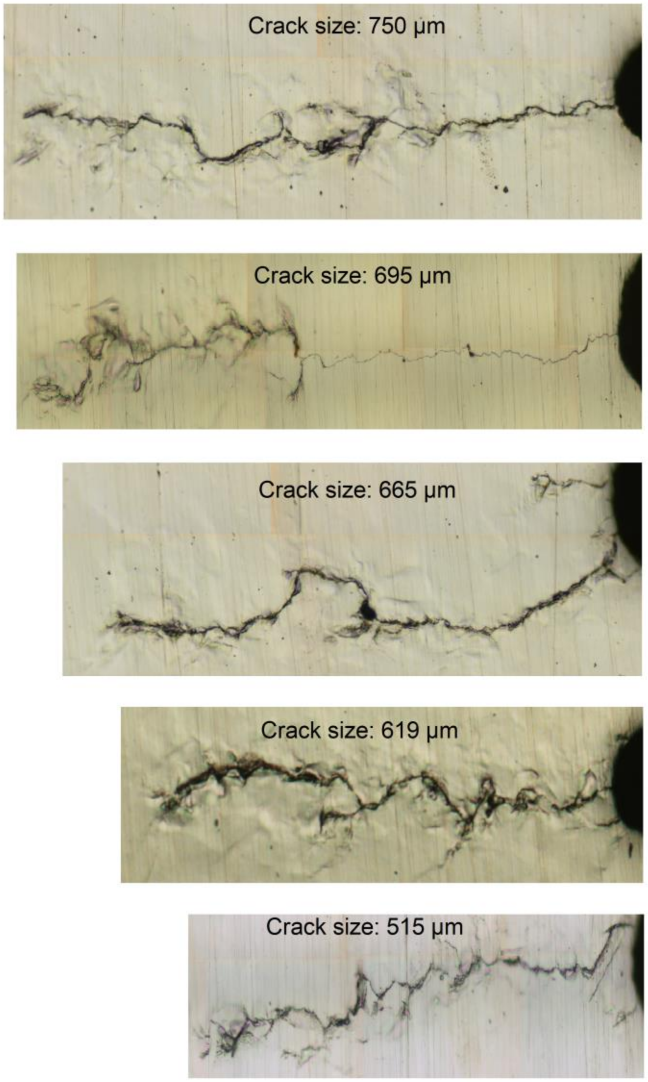

Figure 5.6. Micrographs of five different fatigue cracks in the same type of CT specimens at 30000 cycles.

The nonlinear images formed by the pulse-echo phase NCI are presented in figures 5.7(a-j)) and show similar nonlinear responses corresponding to those in figures 5.2(a-j). Note that the interference from background noise in the nonlinear phase image is limited by identifying the backscatterers on the corresponding linear sequential image, $\hat{I}_s(x,z)$ with a threshold (magnitude of each pixel in figures 5.1(a-f) is not smaller than 2 in this case). Consequently, the effective signal-to-noise ratio of pulse-echo phase NCI can be also defined as the ratio of the absolute value of the peak nonlinear phase metric, $\tilde{\zeta}_\varphi$ around the nonlinear defect to the absolute value of the peak nonlinear phase metric, $\tilde{\zeta}_{\varphi}$ from EDM starter notch. For comparison purpose, the resulting images produced by subtracting the absolute amplitude of parallel case, $\left|I_p(x,z)\right|$ (defined in equation 4.10) from the corrected absolute amplitude of sequential case $\left|\hat{I}_s(x,z)\right|$ are presented in figures 5.8(a-j)). The images in figure 5.8(b-f) demonstrate that the differences between their absolute amplitude, resulting in negative magnitude reveal the elastic nonlinearity of fatigue cracks in the middle of the fatigue life. It is also worth noting that the amplitude of back wall increases significantly, which implies that the forward scattered field, subjected to some possible distortion, leads to the higher amplitude loss in parallel case. The distortion might be attributed to the weakened focusing at the crack interface by the effect of point spread function. This finding shows good agreement with the results using pitch-catch fundamental NCI in figure 4.6(b). Furthermore, the results in nonlinear phase metric, $\tilde{\zeta}_{\varphi}$ (in figure 5.7(a-j)) agree well with the previous statement (in Subsection 4.3.2.1) in which the remaining amplitude of the subtracted backscattered fields used to yield the nonlinear image $\hat{\zeta}$ is principally from the differences in phase rather than absolute amplitude.

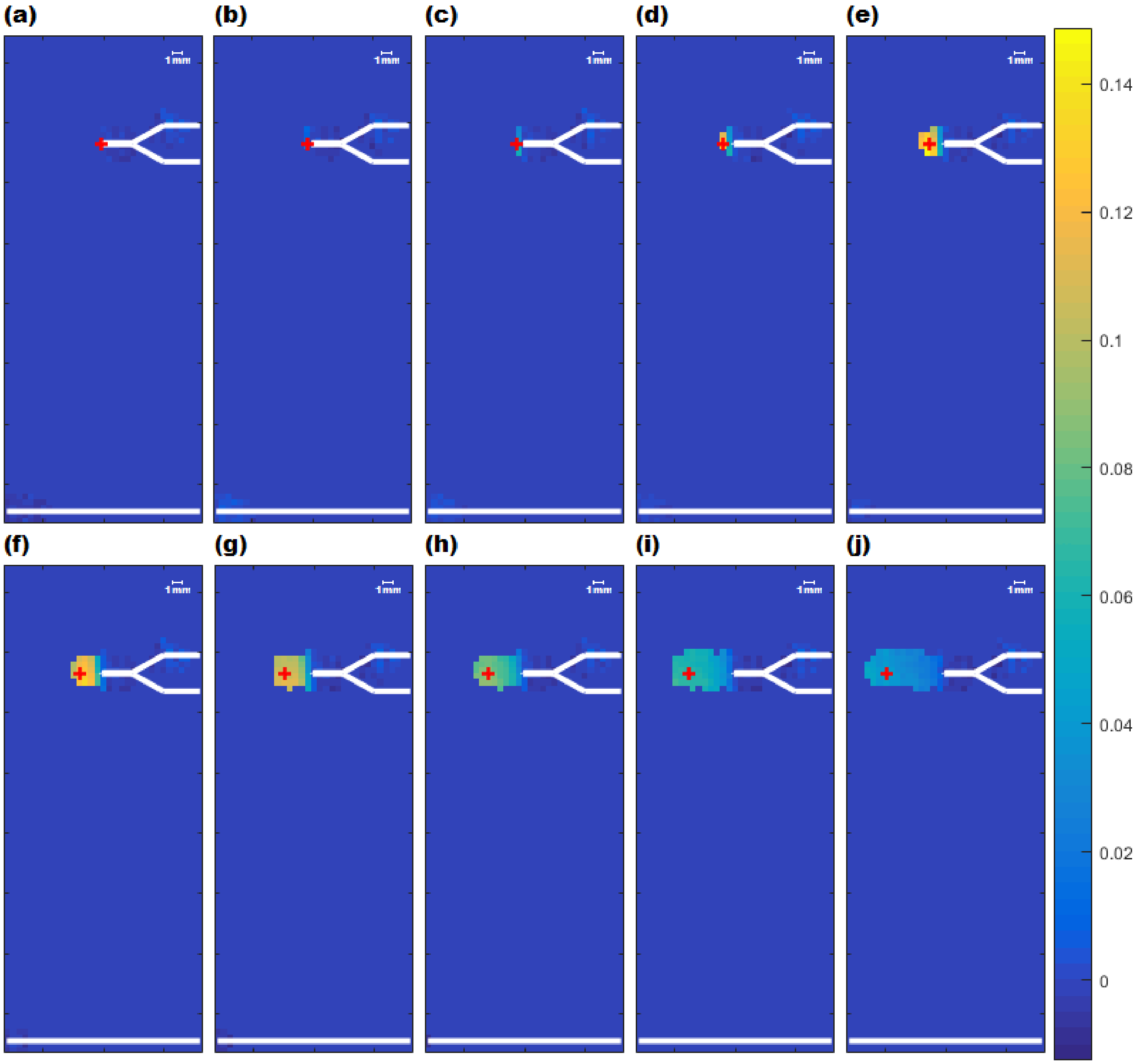

Figure 5.7. Nonlinear images in nonlinear phase metric, $\tilde{\zeta}_{\varphi}$ at (a) 10000 cycles, (b) 20000 cycles, (c) 30000 cycles, (d) 40000 cycles, (e) 50000 cycles, (f) 60000 cycles, (g) 70000 cycles, (h) 80000 cycles, (i) 90000 cycles and (j) 100000 cycles. The inspection configuration is as illustrated in figure 4.1(a) and the red cross marks the micrographically measured crack tip.

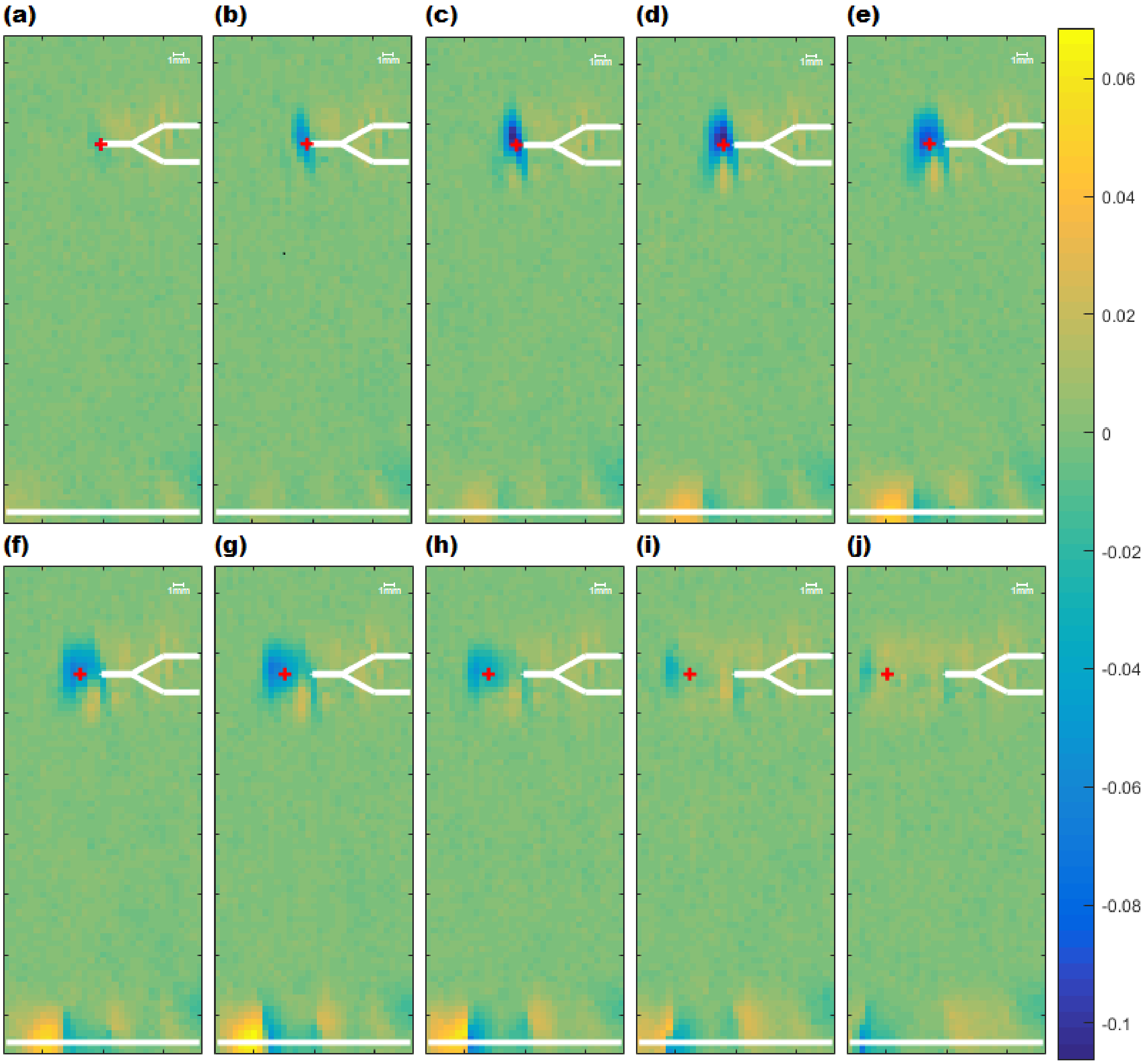

Figure 5.8. The resulting images by subtracting $|I_p(x,z)|$ from $|\hat{I}_s(x,z)|$ at (a) 10000 cycles, (b) 20000 cycles, (c) 30000 cycles, (d) 40000 cycles, (e) 50000 cycles, (f) 60000 cycles, (g) 70000 cycles, (h) 80000 cycles, (i) 90000 cycles and (j) 100000 cycles. The inspection configuration is as illustrated in figure 4.1(a) and the red cross marks the micrographically measured crack tip.

5.2.2 Dependence on linear scattering

Inspections performed in which the array insonifies the crack face at normal incidence, as illustrated in figure 4.1(a), are particularly well suited to the presented coherent nonlinear imaging method because the specular reflection from the crack face allows the nonlinear information contained in the wave to be returned to the receiver. Naturally, due to access limits, such a configuration is not always possible and consequently it is important to evaluate performance for less favourable inspection angles. To this end, imaging was performed with the array positioned such that it predominantly insonifies the crack tip as illustrated in figure 4.1(b). Linear sequential (i.e. TFM) and coherent nonlinear images for 0 and 100,000 cycles are shown in figures 5.9(a-d). Figure 5.9(a) shows that the magnitude, $|\hat{I}_s|$ (defined in equation 4.13) around the starter-notch in the linear sequential image is approximately 10% of those from the geometric features. As the crack grows, the signals reflected from the EDM starter notch become weaker as the transmitted signals are first diffracted by the crack tip. Additionally, the crack tip itself is seen to exhibit only very weak linear scattering. Figure 5.9(d) shows that at 100000 cycles, the nonlinear coherent image, $\hat{\zeta}(x, z)$ shows a feature at the starter-notch tip that is not seen at 0 cycles (i.e. figure 5.9(c)). This is thought to be due to the incident field being nonlinearly distorted by the crack and then subsequently being linearly scattered by the starter-notch tip (see fuller details in Subsection 1.4.2.6). No features within the coherent nonlinear image are seen to correspond to the crack tip for this inspection angle, meaning that although there is some indication of a nonlinear feature, no defect sizing is information is provided.

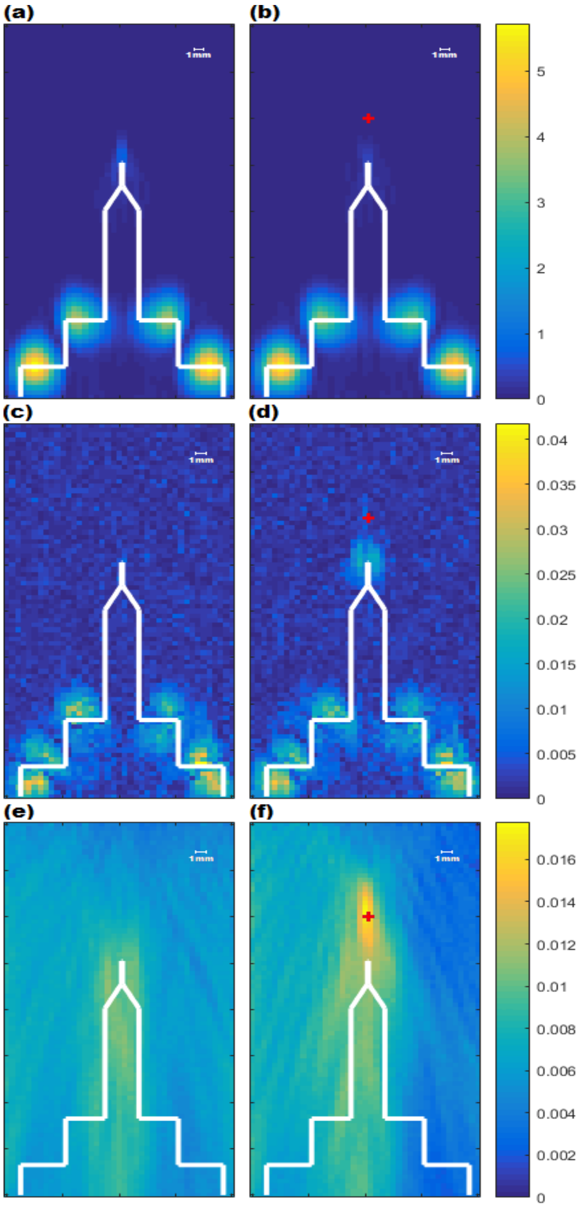

Figure 5.9. Linear sequential images, $\left|\hat{I}_S(x,z)\right|$ in arbitrary units at (a) 0 cycle and (b) 100,000 cycles. Nonlinear images in nonlinear amplitude metric, $\hat{\zeta}$ at (c) 0 cycle and (d) 100,000 cycles. Nonlinear diffuse energy images in nonlinear metric, γ (e) 0 cycle and (f) 100,000 cycles. The inspection configuration is as illustrated in figure 4.1(b) and the red cross marks the micrographically measured crack tip.

To confirm that the observed reduced performance of the coherent nonlinear method due to an unfavourable incident angle is a consequence of the reduced linear scattering as opposed to a reduction in the nonlinear response at this inspection angle, results are also obtained using the NUI method. NUI is a technique which is independent of local linear scattering (see more details in

Subsection 1.4.2.6.3) and consequently can be used to separate the nonlinear response of the defect. The NUI imaging method is implemented with the same experimental apparatus using a time domain window length of 0.12 ms with the reception start time at 0.1 ms. Nonlinear diffuse energy images for 0 and 100000 cycles are shown in figures 5.9(e) and (f) respectively. It can be clearly seen that there is a nonlinear response that is in agreement with the location of the fatigue crack and not the location of the starter-notch tip. This confirms that nonlinear distortion of the field still occurs from this inspection angle. From this investigation it is apparent that it is the absence of strong linear scattering in the vicinity of the defect that reduces detectability using the pulse-echo amplitude NCI. These results support the hypothesis that NCI methods rely on the convolution of nonlinear distortion with the linear scattering response of defects. While it is clear that the necessity for linear scattering close to the inspection point represents a distinct disadvantage in comparison to nonlinear diffuse energy imaging, the lack of a requirement for a measurable diffuse state makes this coherent imaging approach more widely applicable in practice.

Most importantly, it is realised in figure 5.10 that the pulse echo phase NCI is particularly useful when the signals weakly backscattered from the crack. For example, the surface breaking area in figures 5.9(a) and (b) are barely visible and their nonlinear information in figures 5.9(c) and (d) is hidden by other strong linear backscattered components in the subtracted nonlinear amplitude image, $\hat{\zeta}(x,z)$. Specifically, the corrected nonlinear amplitude metric $\hat{\zeta}$ is used to measure the amplitude difference rather than the amplitude ratio of two focusing (i.e. the metric is unnormalised to one of their amplitude). As a consequence of imperfect linear subtraction, the linear residual features in a nonlinear image, $\hat{\zeta}(x,z)$ (seen in bottom region of figure 5.9(d) corresponding to the highly linear scatterers in 5.7 (b)) dominates the imaging performance. That is to say, the absolute amplitude of residual linear features in the subtracted image, $\hat{\zeta}(x,z)$ is directly proportional to their amplitude in corresponding linear image, $\left|\hat{I}_s(x,z)\right|$. Hence, the increase in backscattered amplitude amplifies the differences in amplitude between parallel and sequential focusing due to small residual instrument nonlinearities despite the instrumentation compensation. The amplitude-dependent effect remains as artefacts in the nonlinear amplitude image after the subtraction.

However, the nonlinear metric, $\tilde{\zeta}_{\varphi}$ for phase NCI is thought to reveal elastic nonlinearities hidden behind weak backscatterer by eliminating the effect of imperfect amplitude subtraction.

Figures 5.10 (a-j) present the nonlinear images from 10000 cycles to 100000 cycles, using pulse-echo phase NCI with the same configuration in figure 4.1(b), from which it can be seen that the detectability of the cracks near the notch tip starts at 30000 cycles. As presented in figure 5.10(d), the peak value of $\tilde{\zeta}_\varphi$(equal to 0.0596) is seen in the vicinity of the crack tip at 40000 cycles. Subsequently, the nonlinear metric $\tilde{\zeta}_\varphi$ close to the notch tip decreases with increasing number of cycles. These observations are consistent with the results using $\hat{\zeta}(x, z)$ (see figures 5.2(a-j)) and $\tilde{\zeta}_\varphi(x, z)$ (see figures 5.7(a-j)) in different arrangement. Note that the interference from background noise is limited by identifying the backscatterers on the corresponding linear sequential image with a threshold of 0.4 (e.g. $\hat{I}_s(x, z)$ in figures 5.9(a) and (b) is not smaller than 0.4). The results in figure 5.10 suggest good agreement with the hypothesis that the amplitude-dependent effect does not exist in the pulse-echo phase NCI.

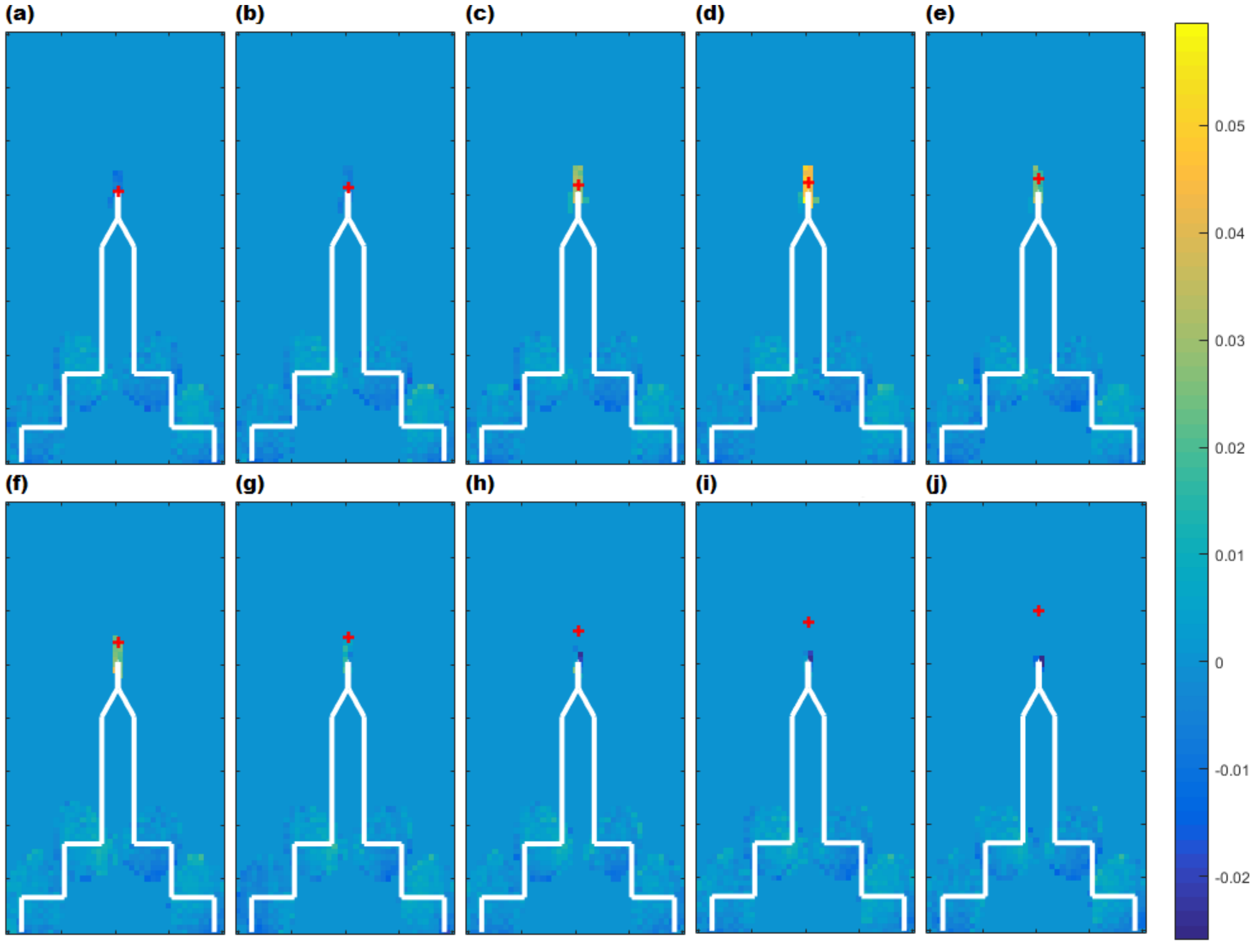

Figure 5.10. Nonlinear images in nonlinear phase metric, $\tilde{\zeta}_{\varphi}$ at (a) 10000 cycles, (b) 20000 cycles, (c) 30000 cycles, (d) 40000 cycles, (e) 50000 cycles, (f) 60000 cycles, (g) 70000 cycles, (h) 80000 cycles, (i) 90000 cycles and (j) 100000 cycles. The inspection configuration is as illustrated in figure 4.1(b) and the red cross marks the micrographically measured crack tip.

5.2.3 Pitch-catch nonlinear coherent imaging

This study is conducted in order to explore the capability of forward scattered field as a measure of elastic nonlinearity induced by different sizes of fatigue cracks. In addition, through this study the imaging results can be compared with those from pulse-echo NCI, thereby determining the detection limits and applicability of each NCI method. The experimental procedures for pitch-catch fundamental NCI and pitch catch subharmonic NCI (as described in Subsection 4.4.1) are used in this study. Their experimental configurations are illustrated in figures 4.5(a) and (b) respectively. The pitch-catch fundamental NCI is expected to detect the crack earlier than the pulse-echo method by capturing through-transmission signals distorted at crack closure. This is because this method does not necessitate the formation of partially open cracks to backscatter the nonlinearly distorted waves. In addition, the pitch-catch subharmonic NCI is implemented on this crack monitoring, in order to understand the change in nonlinear subharmonic response with increasing crack size although its response corresponds to part of fundamental loss.

5.2.3.1 Fundamental measurement

Figures 5.11 (a-j) display linear images yielded by linear sequential (TFM) imaging, $\left|\hat{I}_s(x,z)\right|$ (indicated in equation 4.13) from 10000 cycles to 100000 cycles. In contrast to the pulse echo method, pitch-catch sequential imaging results are difficult to reveal the actual size of cracks throughout its fatigue life. The change in linear images with increasing cycles predominantly arises from the forward field scattered by the growing cracks. It can be seen that the amplitude of through-transmission waves is decreasing with increasing crack length.

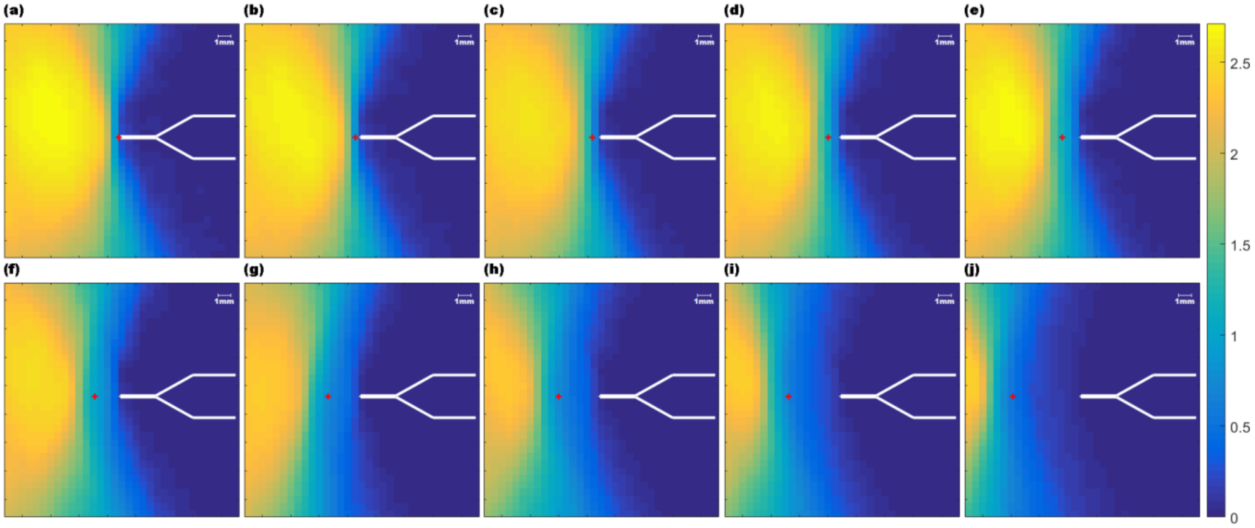

Figure 5.11. Linear sequential images, $\left|\hat{I}_s(x,z)\right|$ in arbitrary units at (a) 10000 cycles, (b) 20000 cycles, (c) 30000 cycles, (d) 40000 cycles, (e) 50000 cycles, (f) 60000 cycles, (g) 70000 cycles, (h) 80000 cycles, (i) 90000 cycles and (j) 100000 cycles. The inspection configuration is as illustrated in figure 4.5(a) and the red cross marks the micrographically measured crack tip.

However, the pitch-catch nonlinear images, $\hat{\zeta}(x,z)$ obtained using equation 4.14 in figures 5.12 (a-j) reveal presence of cracks and deliver high selectivity of nonlinear features from 20000 cycles in the fatigue life. The detection of the crack tip starts at 20000 cycles (indicated by a magnitude (0.055) in the nonlinear metric $\hat{\zeta}$ higher by a factor of 3 compared with the peak value on the starter notch observed at current and previous stages (i.e. SNR_1 is equal to 3) is same as that of pulse-echo NCI. Notably, the highest nonlinearity (equal to 0.2205 in $\hat{\zeta}$) throughout its fatigue life is seen at 50000 cycles, which appears slightly earlier than that from pulse-echo measurement. Subsequently, the nonlinearities measured by $\hat{\zeta}$ decrease at increasing rate with the number of cycles. It should be noted that the nonlinear responses observed in nonlinear images, $\hat{\zeta}(x,z)$ are principally attributed to the difference in absolute amplitude between sequential and parallel focusing. Some evidence is provided by similar features seen in the resulting images (as presented in figure 5.13(a-j)) generated through the subtraction of parallel absolute amplitude, $\left|I_p(x,z)\right|$ from sequential absolute amplitude, $\left|\hat{I}_s(x,z)\right|$. Furthermore, the nonlinear phase images, $\tilde{\zeta}_\varphi(x,z)$ in figure 5.14(a-j) also show that the pitch-catch fundamental NCI is not dependent on the phase change of parallel and sequential focusing, due to unclear indication of elastic nonlinearity from the growing cracks. Note that the interference from background noise in the nonlinear phase images is limited by identifying the backscatterers on the corresponding linear sequential image with a threshold of 0.5 (magnitude of each pixel in figures 5.11(a-f) is not smaller than 0.5 in this case).

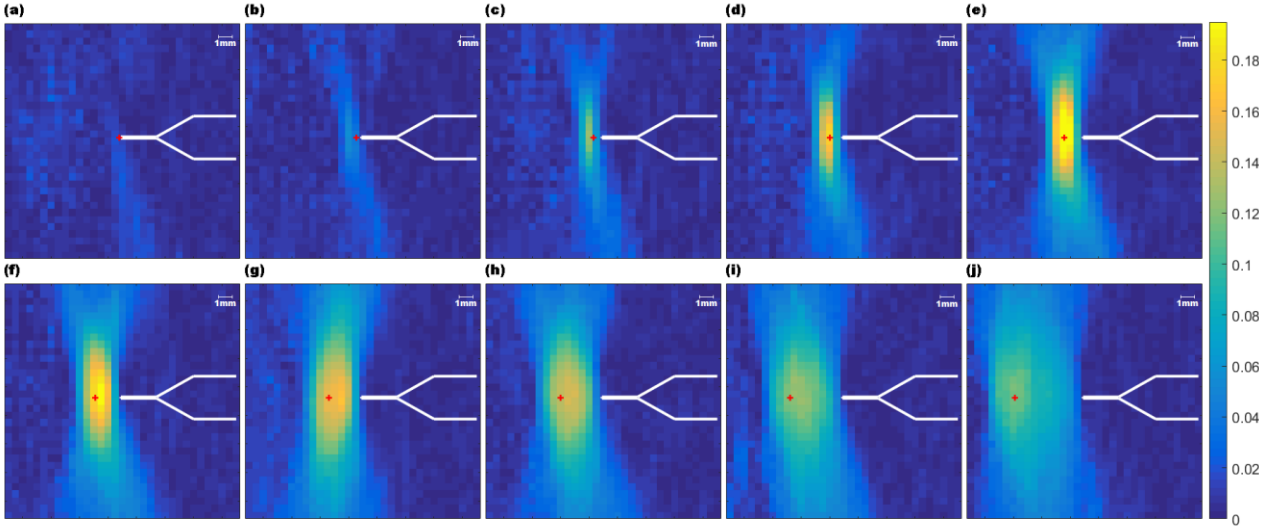

Figure 5.12. Nonlinear images in nonlinear amplitude metric, $\widehat{\zeta}$ at (a) 10000 cycles, (b) 20000 cycles, (c) 30000 cycles, (d) 40000 cycles, (e) 50000 cycles, (f) 60000 cycles, (g) 70000 cycles, (h) 80000 cycles, (i) 90000 cycles and (j) 100000 cycles. The inspection configuration is as illustrated in figure 4.5(a) and the red cross marks the micrographically measured crack tip.

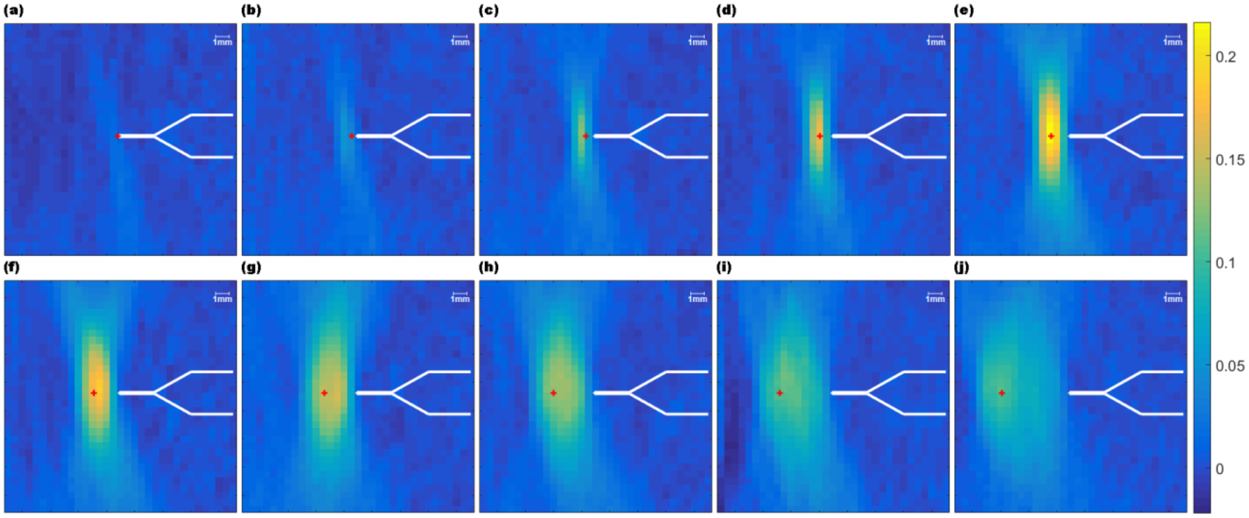

Figure 5.13. The resulting images by subtracting $|I_p(x,z)|$ from $|\hat{I}_s(x,z)|$ at (a) 10000 cycles, (b) 20000 cycles, (c) 30000 cycles, (d) 40000 cycles, (e) 50000 cycles, (f) 60000 cycles, (g) 70000 cycles, (h) 80000 cycles, (i) 90000 cycles and (j) 100000 cycles. The inspection configuration is as illustrated in figure 4.5(a) and the red cross marks the micrographically measured crack tip.

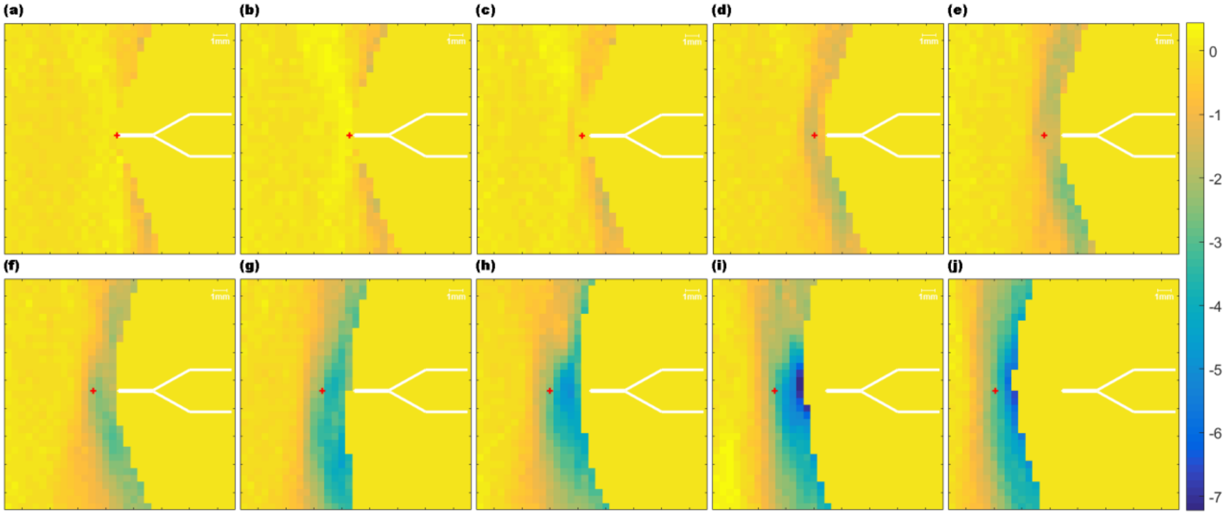

Figure 5.14. Nonlinear images in nonlinear phase metric, $\tilde{\zeta}_{\varphi}$at (a) 10000 cycles, (b) 20000 cycles, (c) 30000 cycles, (d) 40000 cycles, (e) 50000 cycles, (f) 60000 cycles, (g) 70000 cycles, (h) 80000 cycles, (i) 90000 cycles and (j) 100000 cycles. The inspection configuration is as illustrated in figure 4.5(a) and the red cross marks the micrographically measured crack tip.

5.2.3.2 Subharmonic measurement

Figures 5.15(a-j) present similar linear features (as seen in figures 5.11(a-j)) generated from sequential (i.e. TFM) subharmonic imaging, $\left|\hat{I}_s(x,z)\right|$ (see equation 4.13) from 10000 cycles to 100000 cycles. As a consequence of the similar features, these linear results might predominantly arise from the linear subharmonic components within transmission bandwidth. Since the region of closed cracks in these linear sequential images does not exhibit any notably high magnitude the nonlinear subharmonic responses induced by the cracks are thought to be negligible compared to the linear subharmonic components, so that the nonlinearity of cracks cannot be determined by the change in linear images.

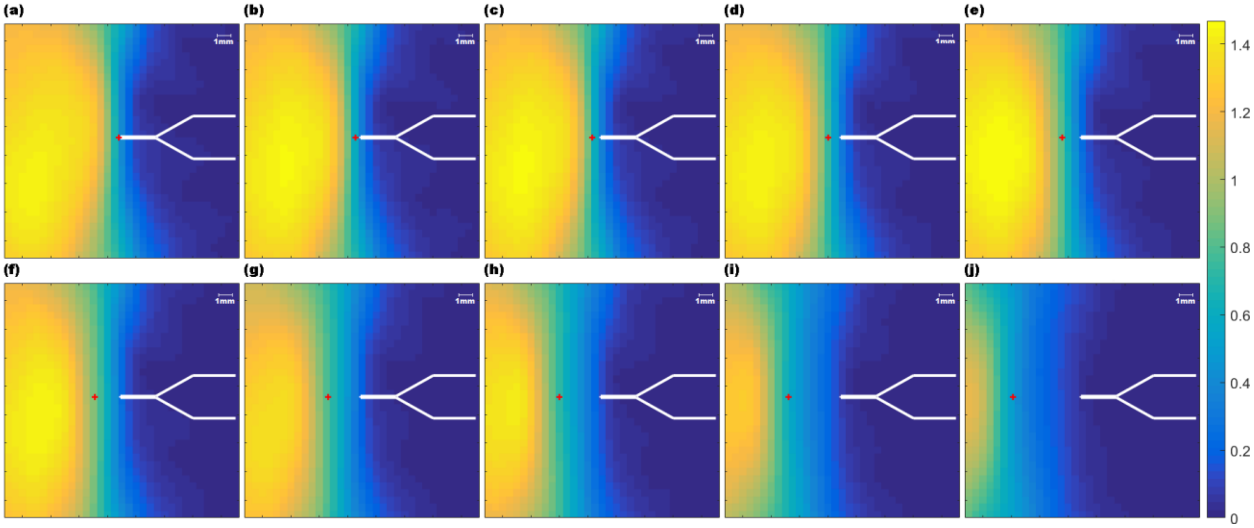

Figure 5.15. Linear sequential images, $\left|\hat{I}_s(x,z)\right|$ in arbitrary units at (a) 10000 cycles, (b) 20000 cycles, (c) 30000 cycles, (d) 40000 cycles, (e) 50000 cycles, (f) 60000 cycles, (g) 70000 cycles, (h) 80000 cycles, (i) 90000 cycles and (j) 100000 cycles. The inspection configuration is as illustrated in figure 4.5(b) and the red cross marks the micrographically measured crack tip.

However, the subtracted nonlinear images, $\hat{\zeta}(x,z)$ obtained using equation 4.14 in figures 5.16 (a-j) reveal comparable nonlinear features (to those observed in figures 5.12) around the cracks and deliver high detectability of crack tip from 30000 cycles in the fatigue life. By comparing with the detectability (earlier detection at 20000 cycles) of pulse-echo NCI and pitch-catch fundamental NCI, the delay in detecting the crack is primarily due to small portion of nonlinear responses evaluated in subharmonic NCI. Specifically, the earliest detection point at 30000 cycles is indicated by a magnitude (0.043) of the nonlinear metric $\hat{\zeta}$ higher by a factor of 4 relative to the highest background level seen at current and previous stages. Notably, the nonlinearities measured by $\hat{\zeta}$ increase to its highest value (equal to 0.1387) at 80000 cycles, which appears much later than those from pulse-echo and pitch-catch fundamental measurements. Subsequently, the nonlinearities indicated by $\hat{\zeta}$ also decrease at increasing rate with increasing crack size. Again, the nonlinear responses seen in nonlinear amplitude images, $\hat{\zeta}(x,z)$ primarily arise from the difference in absolute amplitude between sequential and parallel focusing (seen in figure 4.7 (b)). Some evidence is provided by similar features seen in the resulting images (as presented in figure 5.17(a-j)) generated through the subtraction of parallel absolute amplitude, $\left|I_p(x,z)\right|$ from sequential absolute amplitude, $\left|\hat{I}_s(x,z)\right|$. It is worth noting that the nonlinear phase images, $\tilde{\zeta}_\varphi(x,z)$ in figure 5.18(b-g) show that the pitch-catch subharmonic NCI is sometimes dependent on the phase change of parallel and sequential focusing, due to increasing $\tilde{\zeta}_\varphi$ with growing cracks (from 20000 cycles to 70000 cycles), as a measure of elastic nonlinearity. Note that the interference from background noise in the nonlinear phase images is limited by identifying the backscatterers on the corresponding linear sequential image with a threshold of 0.5 (magnitude of each pixel in figures 5.15(a-f) is not smaller than 0.5 in this case).

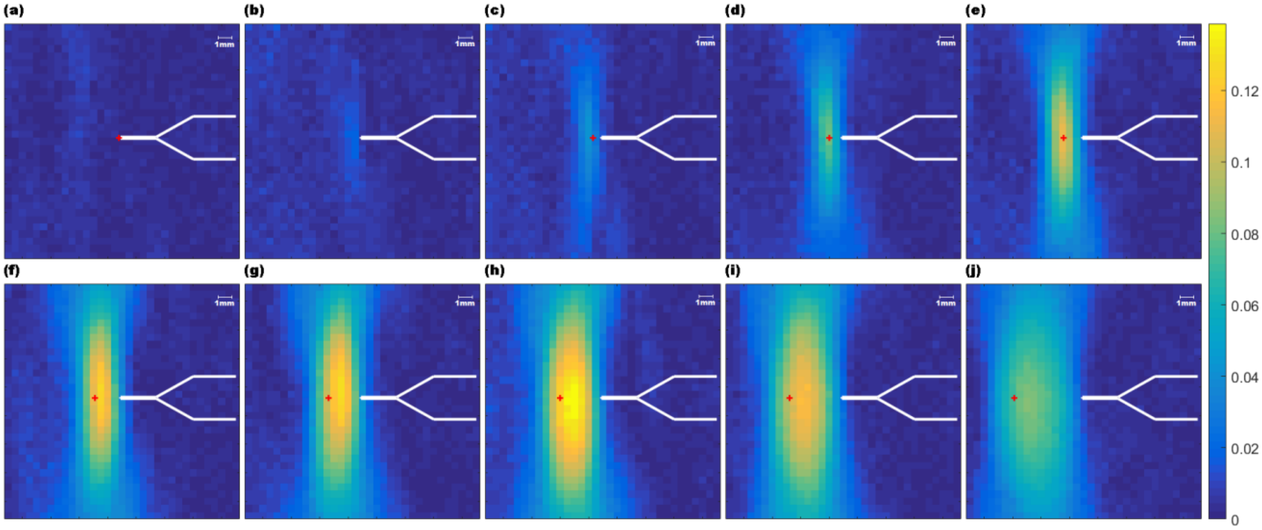

Figure 5.16. Nonlinear images in nonlinear amplitude metric, $\hat{\zeta}$ at (a) 10000 cycles, (b) 20000 cycles, (c) 30000 cycles, (d) 40000 cycles, (e) 50000 cycles, (f) 60000 cycles, (g) 70000 cycles, (h) 80000 cycles, (i) 90000 cycles and (j) 100000 cycles. The inspection configuration is as illustrated in figure 4.5(b) and the red cross marks the micrographically measured crack tip.

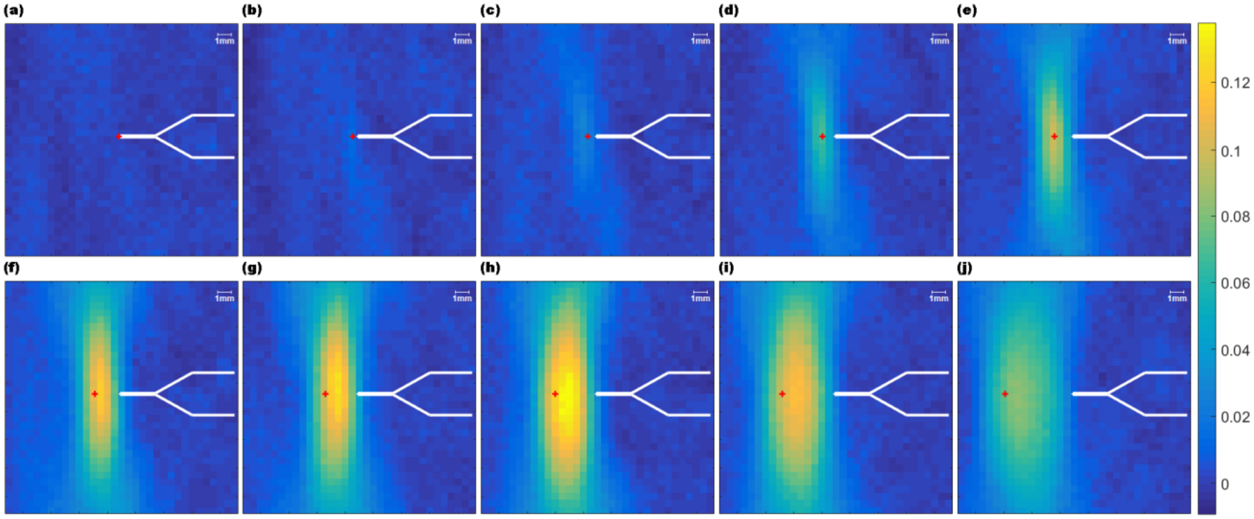

Figure 5.17. The resulting images by subtracting $|I_p(x,z)|$ from $|\hat{I}_s(x,z)|$ at (a) 10000 cycles, (b) 20000 cycles, (c) 30000 cycles, (d) 40000 cycles, (e) 50000 cycles, (f) 60000 cycles, (g) 70000 cycles, (h) 80000 cycles, (i) 90000 cycles and (j) 100000 cycles. The inspection configuration is as illustrated in figure 4.5(b) and the red cross marks the micrographically measured crack tip.

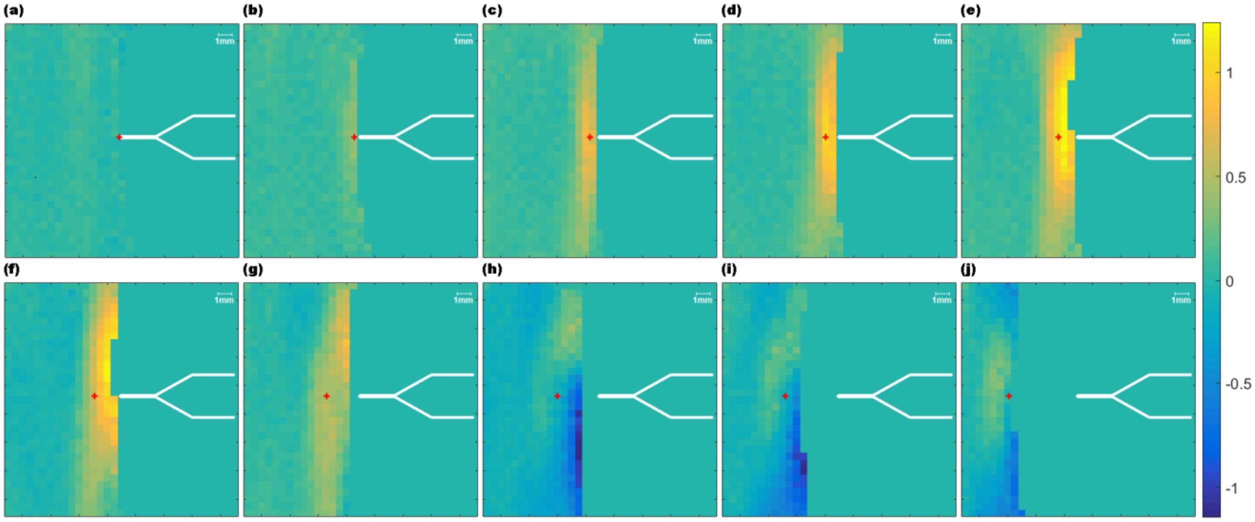

Figure 5.18. Nonlinear images in nonlinear phase metric, $\tilde{\zeta}_{\varphi}$at (a) 10000 cycles, (b) 20000 cycles, (c) 30000 cycles, (d) 40000 cycles, (e) 50000 cycles, (f) 60000 cycles, (g) 70000 cycles, (h) 80000 cycles, (i) 90000 cycles and (j) 100000 cycles. The inspection configuration is as illustrated in figure 4.5(b) and the red cross marks the micrographically measured crack tip.

5.2.4 Conclusions

A family of coherent nonlinear ultrasonic imaging techniques (known as pulse-echo amplitude NCI, pulse-echo phase NCI, pitch-catch fundamental NCI and pitch-catch subharmonic NCI) were used to effectively localise and quantify the extent of cracking by predominantly evaluating differences in phase or absolute amplitude of parallel and sequentially focused fields. In pulse-echo case, the linear sequential and parallel (i.e. TFM) images reveal essentially geometric information from sample boundaries and large defects, whereas all the types of coherent nonlinear amplitude images reveal nonlinear features such as partially-closed cracks and crack tips. The ability of pulse-echo and pitch-catch NCI to effectively monitor fatigue crack growth has been demonstrated (as presented in Figures 5.2, 5.7 and 5.12) on fatigue cracking in mild steel from a crack length of 350 μm (circa. 15% of fatigue life). Localisation of the crack tip was realisable by observing the peak nonlinear metric with an accuracy of less than 1 mm.

Further, it was manifested that significant improvements in linear feature suppression through appropriate compensation for instrumentation nonlinearity could provide the ability to better distinguish the nonlinear defect from other geometric (i.e. linear) features particularly in their early fatigue life (e.g. at 20000 cycles as presented in figures 5.3(a) and (b)). By studying the influence of inspection angle, in conjunction with NUI measurements, evidence was provided to show that the performance of pulse-echo NCI methods is dependent on the convolution of nonlinear distortion with the linear scattering response of defects. Nonetheless, the pulse-echo phase measurements of NCI demonstrate its unique capability on improving detectability by revealing nonlinear responses in phase from those weak backscattered signals. In addition, the pitch-catch fundamental and subharmonic NCI measurements also demonstrate that the forward scattered fields can be used to monitor crack growth and improve the detectability at early stages. Note that the pitch-catch fundamental and subharmonic NCI technique principally rely on the difference in absolute amplitude (the same basis used in NUI).

No. of cycles	SNR_1 (linear sequential, TFM)	SNR_1 (pulse-echo amplitude NCI)	SNR_1s (pulse-echo phase NCI)	SNR_1 (pitch-catch fundamental NCI)	SNR_1 (pitch-catch subharmonic NCI)	SNR_1 (NUI)
10000	0.527	0.706	0.122 (right) 0.923 (top)	1.334	1.392	1.019
20000	0.747	3.572	1.730 (right) 1.021 (top)	3.807	3.176	1.039
30000	0.805	7.060	6.789 (right) 3.397 (top)	8.336	3.140	1.050
40000	0.880	10.186	15.110 (right) 5.183 (top)	8.873	3.317	1.065
50000	0.926	13.131	15.392 (right) 7.042 (top)	15.041	4.270	1.133
60000	0.909	17.903	16.445 (right) 8.836 (top)	15.105	3.519	1.133
70000	0.976	13.926	12.275 (right) 1.624 (top)	11.139	3.073	1.152
80000	0.963	10.609	9.475 (right) 2.185 (top)	9.465	3.519	1.172
90000	0.987	9.376	6.931 (right) 2.043 (top)	10.740	5.404	1.316
100000	1.006	5.245	4.265 (right) 2.287 (top)	9.881	6.985	1.422

Table 5.1. Signal-to-noise ratios, SNR_1s produced by NCI, linear sequential TFM and NUI technique on monitoring crack growth.

Most importantly, the imaging performance of all the types of NCI metrics (defined in equation 4.14 and 4.19), NUI metric (defined in equation 2.3) as well as the linear sequential (TFM) imaging metric (defined in equation 4.13 and using the configuration as displayed in 4.1(a)) on monitoring crack growth is quantitatively summarised in table 5.1 by using the SNR_1 (defined earlier in Section 5.2) to estimate their selectivity. Note that two SNR_1s from the nonlinear phase images (referred to ‘right’ and ‘top’ in table 5.1) are produced by the pulse-echo phase NCI using the configurations in figures 4.1(a) and (b) respectively. Specifically, the SNR_1s are produced from the imaging results on the same CT specimen as presented in figures 5.1(a-j), 5.2(a-j), 5.7(a-j), 5.10(a-j)), 5.12(a-j), 5.16(a-j) and A.12 respectively. As indicated in table 5.1, the pulse-echo amplitude NCI, the pulse-echo phase NCI as well as the pitch-catch deliver the most effective quantification of the crack size by showing the significantly increasing SNR_1 from the early stage of the fatigue life to the middle stage and then the decreasing SNR_1 with the increasing fatigue cycles.

This reliance of linear scattering is a limitation of the pulse-echo NCI technique not present for NUI imaging. However, the principal disadvantage to the NUI technique is the necessity for a measurable diffuse state. This prevents the applicability to large structures and highly attenuating materials, for which the signal amplitude would become immeasurable by the time a diffuse state is formed. Therefore, it is unlikely to be effective in heavy industry applications. Furthermore, the NCI techniques outperform the NUI method in terms of the signal-to-noise ratio (as presented in table 5.1) and the measurement consistency if figures 2.4(b) and 5.5(a) are compared. In numerous engineering industries, a linear backscatterer is often realisable because the crack usually initiates from the surface of structures, which is known as surface breaking crack (SBC). Consequently, despite the observed limitations, the NCI techniques considered here are practically more widely applicable than NUI. Last but not least, the pitch-catch fundamental and subharmonic NCI have presented their ability on monitoring cracks, so that their potentials are worth to being further explored by considering ray-tracing using single array, thereby improving its applicability.

5.3 Detection of surface breaking cracks

The NCI results described in Subsection 5.2.2 suggest that the pulse-echo amplitude NCI necessitate a linear scatterer to backscatter the signals distorted by nonlinear defects (e.g. closed cracks). Surface breaking crack (SBC) induced by fatigue loading, seen in many aged engineering structures (e.g. pipelines, bearings and pressure vessels), satisfies the requirements of pulse-echo NCI. The linear NDT techniques cannot distinguish the early stage cracks from linear discontinuities near the surface. Therefore, the pulse-echo amplitude NCI technique is now explored on samples with surface breaking cracks generated by fatigue tests. In order to quantify the performance of pulse-echo amplitude NCI relative to that of linear sequential (TFM) method, signal-to-noise ratio, SNR_2 is defined as the maximum absolute value in each imaging metric from the area of the SBC to its peak absolute value from the back wall, at which the SBC locates.

5.3.1 Three-point bending specimen

The single-edge notched bend aluminium (2014-T6) specimen of dimensions 342 mm × 76 mm × 31.5 mm, used in previous works for SBC inspection [Peng et al., 2018], is examined by pulse-echo NCI technique. The same ultrasonic phased array used in Chapter 4.2 was positioned on the top face perpendicular to the crack face (as illustrated in figure 5.19). Fatigue cracks were grown until the length were about 6 mm. Subsequently, SBCs were fabricated by machining along the dashed line shown in Figure 5.19 to remove the EDM starter notch and keep the fatigue cracks of a size of 3 mm. Finally, further material was then removed by 0.5 mm in depth from the back wall of this specimen. Therefore, the pulse-echo amplitude NCI was conducted on this specimen with back wall at two different depths (38.5 mm and 38 mm) in order to confirm its detectability of the SBC dependent on the depth of back wall and explore the nonlinear responses from different part of the cracks.

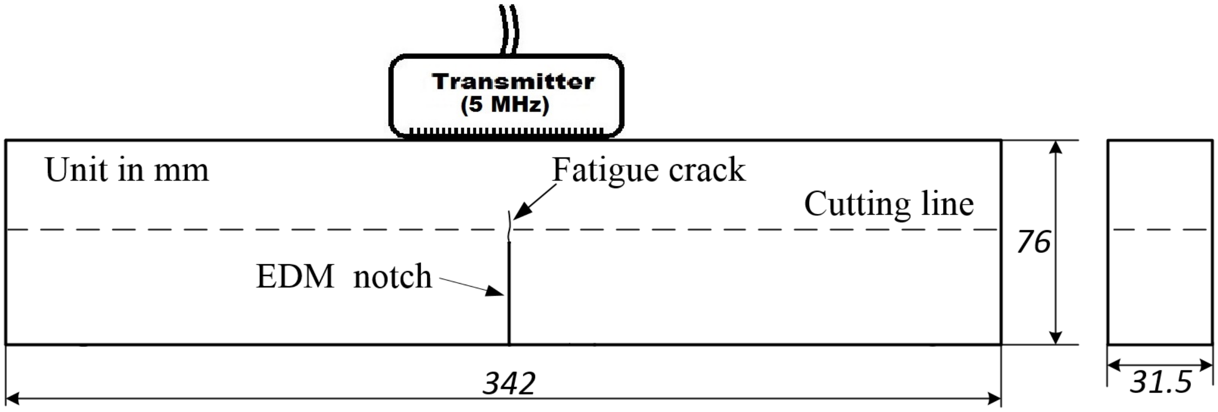

Figure 5.19. Schematic diagram of pulse-echo NCI measurement configuration on specimen subjected to three-point bending fatigue test (dimensions in mm).

Figures 5.20(a) and (b) present the linear sequential images $\hat{I}_s(x,z)$ with back walls in two different depth (38.5 mm and 38 mm respectively) from which it can be seen that the back wall, indicated by the peak value on each image, shifts upward by 0.5 mm (one-pixel size). In addition, the discontinuities around the centre of back wall seen in linear images arise from the SBCs. Nonetheless, the features seen in the linear image cannot estimate the source of the shadowing effects as a consequence of inability to characterise the surface discontinuities. The separation of linear and nonlinear modalities is not achievable in the case of linear imaging. In practice it is however important to distinguish a closed crack from other small linear scatterers.

Figure 5.20(c) and (d) show the nonlinear images with instrumentation compensation computed from the pixels on back wall. The results in nonlinear metric $\hat{\zeta}$ suggest that the SBCs can be selectively detected, and its maximum nonlinear responses appear in the vicinity of the surface. Figures 5.21(a-d) present the amplitude ratio $\delta_A(\omega)$ (defined in equation 4.7) and the relative phase $\delta_\varphi(\omega)$ (defined in equation 4.8) at SBC and back wall against frequency from which it can be seen that high amplitude ratio $\delta_A(\omega)$ dominates the nonlinear response at the SBC. Previous results in Chapter 4.3 suggest that the NCI by measuring forward scattered field depends on the amplitude ratio of parallel and sequential focusing. Therefore, the observed nonlinear features in figures 5.20(c) and (d) are thought to be attributed to the forward field being nonlinearly distorted by the closed cracks and subsequently being linearly scattered by the back wall. Furthermore, the highly negative value of $\delta_\varphi(\omega)$ seen in figures 5.21(b) and (d) is also in agreement with previous results in Subsection 5.2.2, indicated by notably negative $\tilde{\zeta}_\varphi$, near the notch tip (i.e. surface) obtained from the same experimental configuration, as shown in figures 5.10(h-j). Hence, the part of a fatigue crack close to the surface (i.e. crack initiation area) tends to yield negative phase difference (with a factor of at least 2 stronger than small negative background noise) indicated by $\tilde{\zeta}_\varphi$ or $\delta_\varphi(\omega)$ with the inspection angle illustrated in figures 4.1(b) and 5.19.

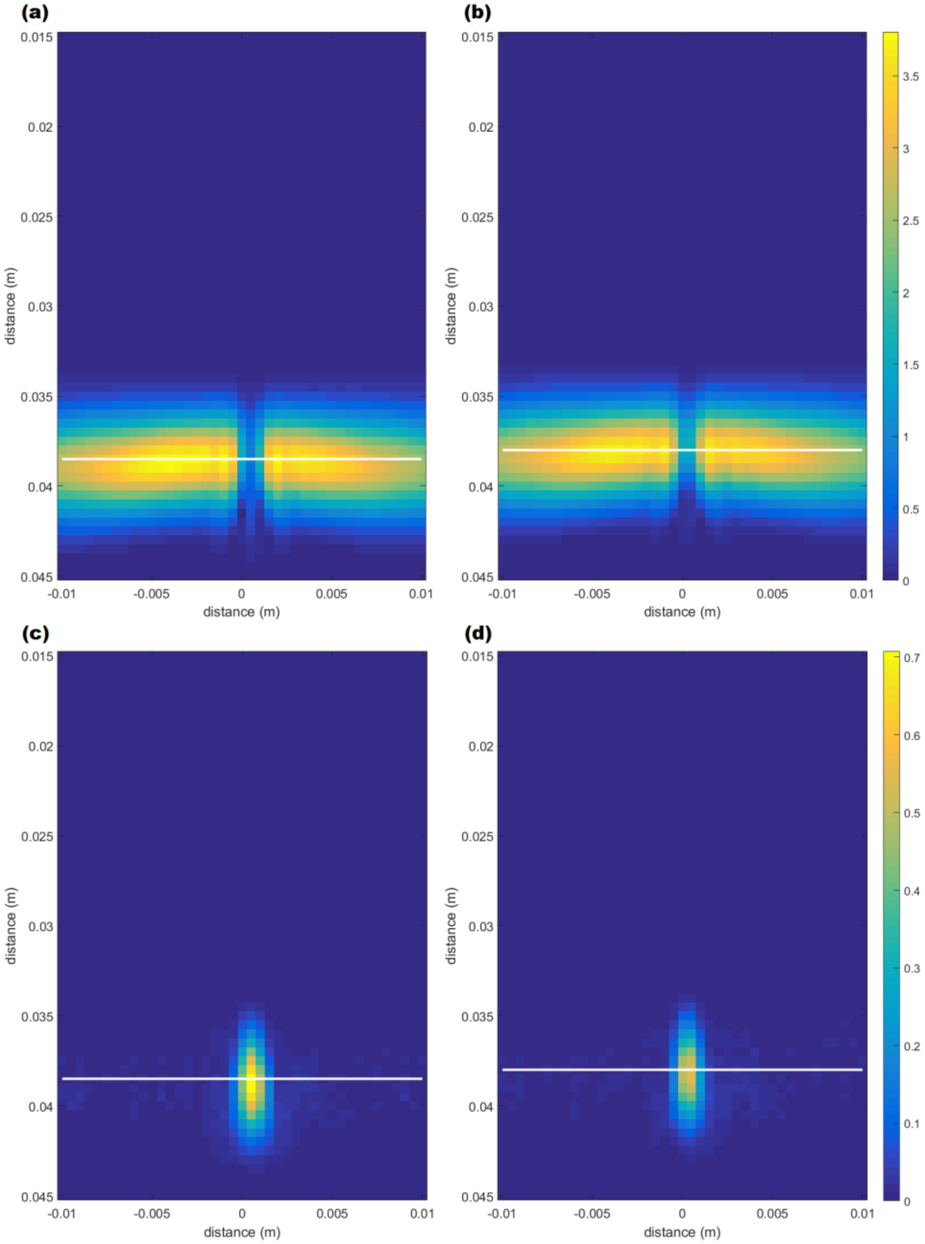

Figure 5.20. Linear sequential (TFM) images, $|\hat{I}_s(x,z)|$ in which the back wall is at a depth of (a) 38.5 mm and (b) 38 mm in arbitrary units. Nonlinear images using pulse-echo amplitude NCI in which the

back wall is at a depth of (c) 38.5 mm and (d) 38 mm in nonlinear amplitude metric, $\hat{\zeta}$. The inspection configuration is as illustrated in figure 5.19. The location of the back wall is shown with white line.

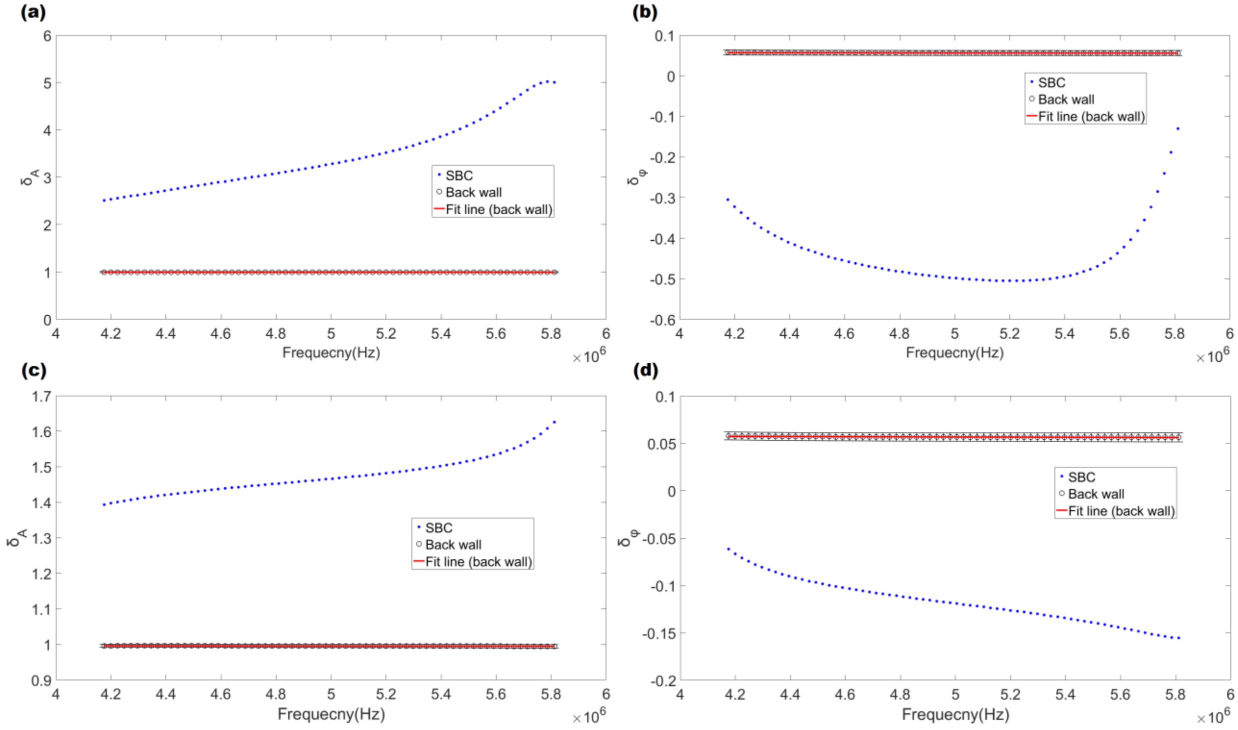

Figure 5.21. (a) Amplitude ratio, δ_A and (b) relative phase in radians, δ_φ against frequency at a SBC and undamaged back wall at a depth of 38.5 mm. (c) Amplitude ratio, δ_A and (d) relative phase in radians, δ_φ against frequency at a SBC and undamaged back wall at a depth of 38 mm. Note that error bars denote standard deviations of the metrics at multiple linear points selected from back wall at the given frequency.

5.3.2 Compact tension specimen

The other feasibility study was conducted on an appropriate example (the same aluminium sample with two drilled holes used in [Potter et al., 2014]). As shown in figure 5.22, the fatigue cracks in this sample were first grown by cyclic tensile load with the same procedure described in Subsection 3.2.1. Subsequently, one hole was drilled over the front part of the cracks approximately 2.5 mm away from the crack tip to emulate surface break cracking. An identical hole, as a linear reference, was drilled at the same depth about 15 mm away. Previous NUI results demonstrate that only the fatigue crack tip is selectively imaged and neither of the holes are visible.

To detect this artificial SBC the pulse-echo amplitude NCI technique is examined on the sample with the same experimental arrangement used in NUI (described in Subsection 2.3.2). Figure 5.23 shows the linear sequential image $\hat{I}_s(x,z)$ from which it can be seen that the linear scattering is presented corresponding to the actual geometries of the back wall and two drilled holes. The existence of SBC cannot be confirmed from the linear image. However, the nonlinear image $\hat{\zeta}$ (as shown in figure 5.24) reveals the actual position of SBC by measuring backscattered signals containing the nonlinearities generated from the SBC. Figures 5.25(a) and (b) demonstrates that the NCI results here rely on both the amplitude ratio and phase difference of two focusing, which might be attributed to the combined effect of backward and forward scattered nonlinear distortions.

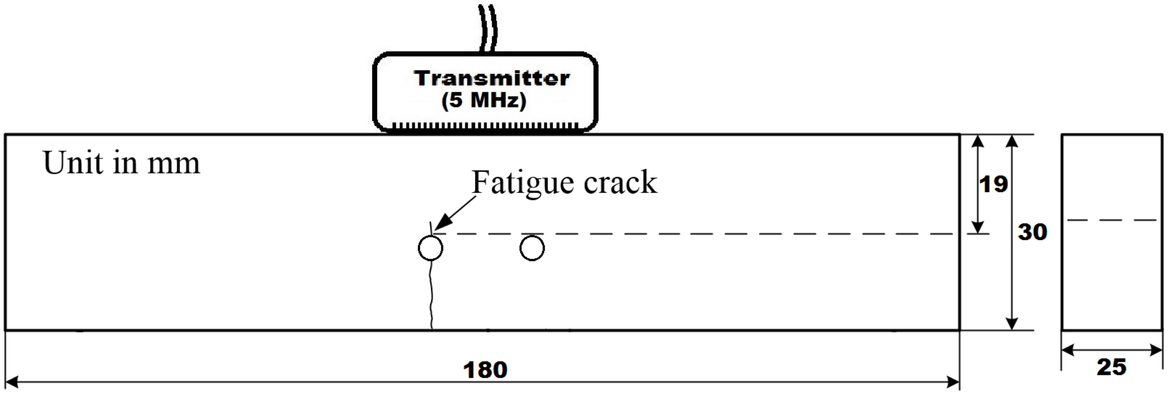

Figure 5.22. Schematic diagram of pulse-echo NCI measurement configuration on specimen subjected to fatigue tensile test (dimensions in mm).

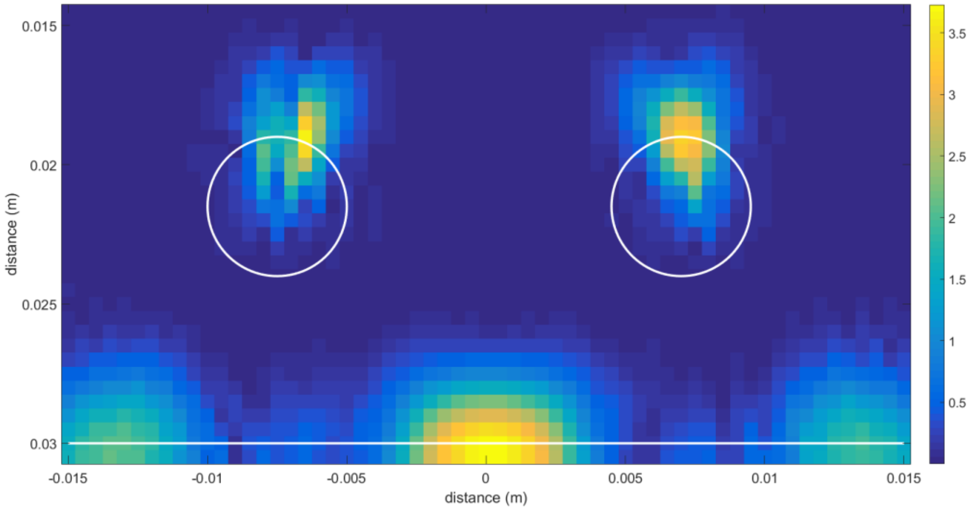

Figure 5.23. Linear sequential image, $\left|\hat{I}_S(x,z)\right|$ in arbitrary units. The inspection configuration is as illustrated in figure 5.22. The location of the back wall and two drilled holes are shown with white lines.

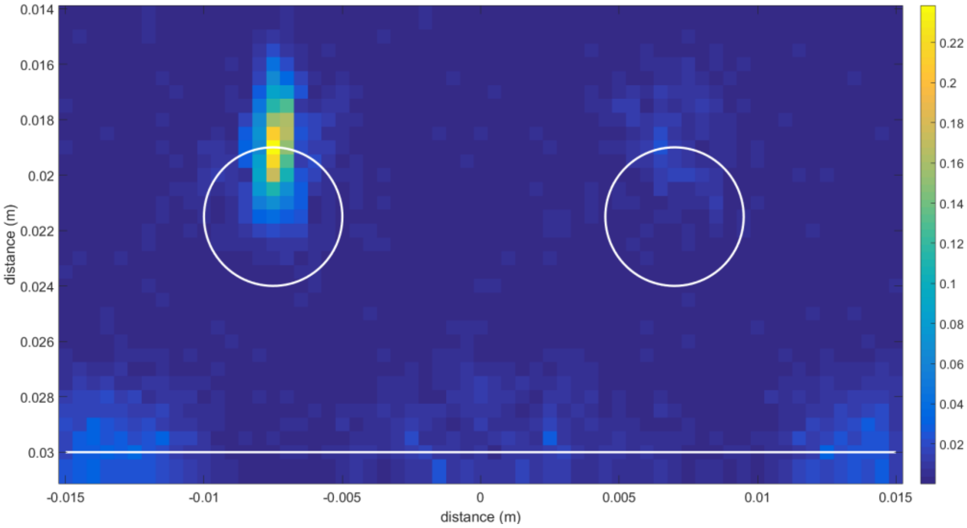

Figure 5.24. Nonlinear image using pulse-echo amplitude NCI in nonlinear amplitude metric, $\hat{\zeta}$. The inspection configuration is as illustrated in figure 5.22. The location of the back wall and two drilled holes are shown with white lines.

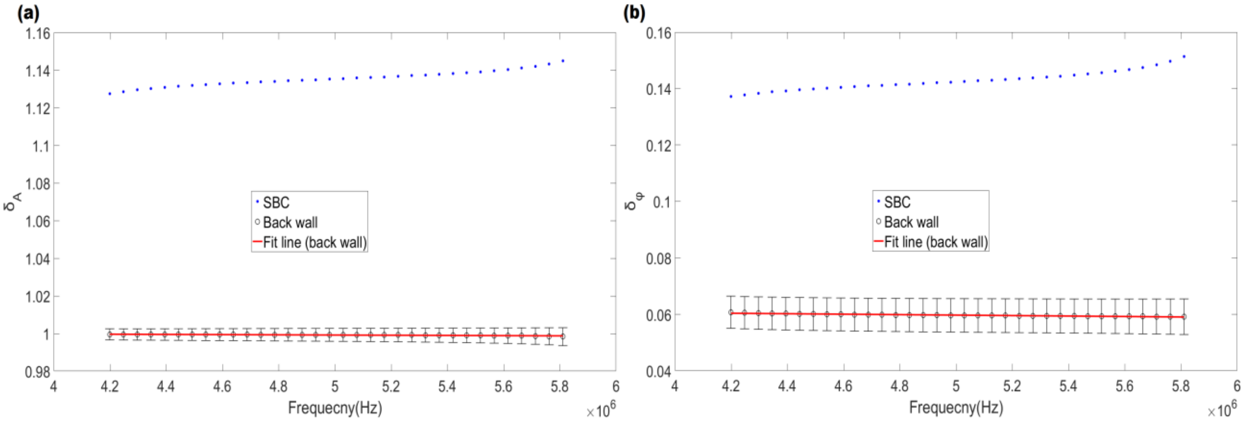

Figure 5.25. (a) Amplitude ratio, δ_A and (b) relative phase in radians, δ_φ against frequency at a SBC and undamaged back wall.

5.3.3 Conclusions

As presented in table 5.2, the detectability of SBCs grown in two aluminium specimens using pulse-echo amplitude NCI technique can be improved significantly if the signal-to-noise ratio, SNR_2 of nonlinear amplitude metric, $\hat{\zeta}$ and the linear sequential (TFM) metric, $\hat{I}_s$ are compared. The results demonstrate that the existence of strong linear backscatterers near the surface allows the nonlinear responses from SBC in forms of phase and absolute amplitude to be measured. The nonlinear responses measured by $\hat{\zeta}$ are thought to arise from the combined effect of back and forward scattered nonlinear distortions. The consistent nonlinear phenomenon in phase is seen in results from both the steel CT specimen and the aluminium specimen subjected to three-point bending fatigue test (as presented in figures 5.10(h-j)) and figures 5.21(b) and (d) respectively). Specifically, their results suggest that the phase difference between sequential and parallel focusing, measured by δ_φ or $\tilde{\zeta}_\varphi$ at the cracked surface tend to become positive in sign with decreasing distance from the crack initiation area to the crack tip.

Finally, the cracked surface 2.5 mm away from the crack tip (in an aluminium sample with a 15 mm long crack) was examined by the metric, $\hat{\zeta}$. For a cracked area much closer to the crack tip (indicated by a percentage of the overall crack length, equal to 16 % in this case), the pulse-echo amplitude NCI results might be dependent on both measurable amplitude ratio and significantly stronger phase difference in positive sign of two focusing.

Sample	SNR_2 (linear sequential, TFM)	SNR_2 (pulse-echo amplitude NCI)
Three point bend specimen with a 3 mm long SBC	0.461	16.006
Three point bend specimen with a 2.5 mm long SBC	0.439	9.807
Compact tension specimen	0.462	7.27

Table 5.2. Signal-to-noise ratio, SNR_2 produced by pulse-echo amplitude NCI and linear sequential TFM technique on detecting SBCs.

CHAPETER 6- CONCLUSIONS

This chapter summarises the key findings described in the previous chapters. In addition, this chapter proposes some recommendations for further work on nonlinear imaging for non-destructive testing and describe possible multidisciplinary applications of this research.

6.1 Conclusions

In Chapter 2, a systematic monitoring process was designed for examining nonlinear ultrasonic diffuse energy imaging (NUI) and total focusing method (TFM) techniques on detecting fatigue cracks in three identical compact tension (CT) steel specimens. The experimental results presented show that monitoring fatigue crack growth in mild steel using the NUI technique was effective from 15% fatigue life. The NUI technique was performed using a commercially available array and array controller. The same instrumentation was also used to simultaneously produce traditional high resolution linear TFM images. These linear images did not reveal any detectable changes in these early stages of fatigue. The amplitude of nonlinearity was shown to be a measure of progress of the early stages (15%-50% fatigue life) of fatigue crack growth. The experiments showed that statistically significant amplitude increases were measurable for cracks of 250 μm length and greater. As crack growth continued the location of maximum nonlinearity was used to measure the extent of the cracking. For larger cracks (i.e. greater than 250 μm) the NUI technique becomes a form of nonlinear imaging, mapping out the extent of a given crack. As the same instrumentation is used, linear and nonlinear images can be produced simultaneously and these contain complementary information. Whilst the linear images will reveal essentially geometric information from sample boundaries and large defects, the NUI images will reveal nonlinear features such as partially-closed cracks and crack tips. The NUI results were obtained with the array positioned directly above the crack, an orientation that typically results in poor linear imaging as the signals reflected directly from the crack tip are small. It is noted that the orientation (i.e. array directly above the defect) used in NUI is potentially beneficial as it reduces access limits relative to traditional linear array imaging (which would typically be performed as an angle inspection). The NUI technique therefore both improves sensitivity and reduces access limitations making it a viable prospect for *in-situ* or permanent fatigue monitoring of, for example, pipework or pressure vessel welds.

In research prior to this thesis, the parameters used in NUI were empirically determined by examining the technique on specific, well known samples (i.e. the existence of a defect is known). As a consequence, Chapter 3 presented multiple optimisations of NUI technique through a detailed parametric study, wave field characterisation and three-dimensional imaging. In order to quantify the NUI performance of fatigue cracks, the unique signal-to-noise ratio, SNR_{all} was decided to examine the effect of aperture size, data averaging, reception bandwidth and centre frequency. The results suggest that the selectivity of the crack tip (relative to linear geometric features) increases with the aperture size as a consequence of stronger physical focusing at the crack tip. Whilst the signal (as a superposition of elastic nonlinearity and incoherent noise) without averaging is notably larger than the one with averaging the background noise can be suppressed by a greater percentage if the averaging is applied. Therefore, the NUI performance can be improved significantly by taking N (equal to aperture size) averages in sequential transmission and using a large aperture size.

Reception bandwidth and centre frequency in post-processing principally determine the imaging performance. This is a consequence of a compromise between suppression of contributions from side transmission bands and maximisation of the effective fundamental bandwidth. The generic approach is to map SNR_{all} by examining single set of parallel and sequential data with different combinations of reception bandwidth and centre frequency. The results demonstrated that the smaller bandwidth resulted in the higher SNR_{all} at any centre frequency between 4.8 MHz and 7.8 MHz in a specific case. Furthermore, the value of SNR_{all} increased until the centre frequency rose to 7.8 MHz. The upper threshold of centre frequency was found to be determined by transducer bandwidth at no less than -8 dB. The NUI results corresponding to the highest and the lowest SNR_{all} values seen on the map suggest that the higher centre frequency combined with the smaller bandwidth can improve the SNR_{all} through significantly reducing the background noise by 50%.

The prediction of the diffuse field state is also important for the NUI technique. Furthermore, the same phased array used in NUI can be implemented to measure the diffuse field more efficiently and effectively compared with previous works using single transducers [Evans and Cawley, 1999]. The measurement of energy in diffuse field is used to predict the time at which a diffuse state is first reached (i.e. estimation of the smallest gate start time t_r). This is important as the SNR decreases with time. As a consequence, three metrics (as measures of variations in energy area, η_{area}, maximum energy, η_{max}, and phase coherence, η_{phase}) used for diffuse field verification were proposed and examined on analytical, experimental and numerical data. The analytical data was formed by using the white noise as a representation of a perfectly diffuse state. In addition, the finite element (FE) and experimental data were obtained by transmitting and receiving signals in sequential mode on an undamaged aluminium sample. The simulated FE signals were used to indicate early and late state of coherent wave field. Therefore, the efficacy of these three metrics was examined by comparing the experimental results with FE results and simulated white noise. The results suggest that both of the metrics η_{area} and η_{phase} were able to effectively identify the change from coherent field to diffuse field of experimental signals according to the reference values generated from FE data and decayed white noise. Furthermore, the effect of window size, T, was studied by using the same metrics η_{area} and η_{phase}. Its results demonstrated that the larger T delivered higher diffusivity and the preferred size of 0.12 ms indicated by the convergence of η_{area} and η_{phase} was consistent with the empirical value obtained from the experimental optimisation of NUI performance on crack detection. Eventually, investigations using these two metrics were conducted on one of the steel CT specimens used in Chapter 2. The results corresponding to empirical values (i.e. optimal t_r at 0.1 ms and optimal T in 0.12 ms) were confirmed by observing the t_r, at which both η_{area} and η_{phase} converged to reference values of diffuse state. This then demonstrated that both η_{area} and η_{phase} can quantitatively predict the diffuse field start time as well as the optimal window size T by comparing their magnitude with the optimum diffuse state (15 % for η_{area} and 1 for η_{phase}) and estimating the convergence start point.

In order to allow the NUI to explicitly reveal 3D information about size and profile of nonlinear defects (e.g. closed fatigue cracks) a novel technique termed 3D NUI was developed. This technique is particularly important for improving the detectability of volumetric defects, i.e. defects other than planar cracks. The principle is to control the array elements within a 2D array probe with independent delay laws, thereby achieving the physical and synthetic focusing (known as parallel and sequential focusing) at each volumetric pixel. This technique was implemented on the aluminium sample used in Section 3.2 and the results show that the imaging performance is depending on the amount of physical energy at focal point because the highest nonlinear metric (γ) appeared in the centre of y-axis (middle of its thickness). In practice, 3D NUI with multiple lateral array elements is thought to bring the benefits of accurate localisation and quantification for the cracks in changing size and locations through thickness of the structure. 3D NUI technique may also improve the inspection efficiency over the traditional 3D scanning techniques.

In Chapter 4, four different forms of coherent nonlinear ultrasonic imaging (NCI) were proposed to effectively localise and quantify the extent of cracking by evaluating differences in parallel and sequentially focused fields. The first NCI method (termed pulse-echo amplitude NCI) was developed based upon the relative nonlinear responses in absolute amplitude and phase of two focused fields. This technique reveals nonlinear features such as partially-closed cracks and crack tips in the subtracted nonlinear images (measured by the amplitude metric of NCI, ζ). Further, the second NCI method (referred to pulse-echo phase NCI) only measures the phase information of the nonlinear responses and then exploits it to images the cracks. The results suggest that it can improve the selectivity of cracks by suppressing the averaged background noise level from -6 dB (measured by the amplitude metric ζ) to -9 dB (measured by the phase metric of NCI, ζ_φ). The essentially geometric information from sample boundaries and large defects can be also presented with the same apparatus in the linear sequential and parallel images (indicated by linear amplitude metrics, $|I_s(x,z)|$ and $\left|I_p(x,z)\right|$ respectively).

Two further variants of NCI techniques using the different arrangement (known as pitch-catch fundamental NCI and pitch-catch subharmonic NCI) were also developed by measuring forward scattered amplitude at the opposite side using the amplitude metric , ζ. This configuration also demonstrated its sensitivity to crack closure by capturing the waves at either subharmonic or fundamental frequencies. However, it was found that this method (i.e. the use of forward scattered field) predominantly relied on the difference in the absolute amplitude (not the phase) between sequential and parallel focusing.

Furthermore, the NCI of fundamental waves were seen to deliver the highest selectivity of acoustic nonlinearity. The NCI methods mentioned above were then optimised by suppressing the instrumentation noise obtained from the baseline measurements of relative phase and absolute amplitude at the back wall. The corrected amplitude and phase metrics are termed as $\hat{\zeta}$ and $\tilde{\zeta}_\varphi$ respectively.

In Chapter 5, a substantial number of experimental works were performed on a range of samples, thereby exploring the applications of NCI techniques as well as their repeatability and accuracy of detecting defects. The capability of pulse-echo NCI methods to effectively monitor fatigue crack growth was first demonstrated on fatigue cracking in mild steel from a crack length of 350 μm (circa. 15% of fatigue life). The results also suggest that the pulse-echo methods, using metrics $\tilde{\zeta}_{\varphi}$ and $\hat{\zeta}$, predominantly rely on the nonlinear responses in phase. Localisation of the crack tip from 20000 cycles to 100000 cycles was achieved by identifying the maximum nonlinear metric with an accuracy of less than 1 mm. This error (up to 1 mm) was attributed to the existing through-thickness curvature at the crack fronts. Furthermore, significant improvements in linear feature suppression were realised through instrumentation noise compensation, delivering the capability to more clearly distinguish the nonlinear defect from other geometric (i.e. linear) features especially in their early fatigue life (e.g. at 20000 cycles, 15% fatigue life).

Through studying the effect of inspection angle, in conjunction with NUI measurements, it was shown that the performance of pulse-echo NCI methods is dependent on the convolution of nonlinear distortion with the linear scattering response of defects. This dependence of linear scattering is a limitation of the pulse-echo NCI technique not present for NUI imaging. Nonetheless, the main disadvantage to the NUI technique is the reliance of a measurable diffuse state. This prevents the applicability to large structures and highly attenuating materials, for which the signal amplitude would become immeasurably small by the time a diffuse state is formed. As a consequence, it is unlikely to be applicable in heavy industry applications. Such situations necessitate the use of the early-time, coherent component of the field instead. Furthermore, the NCI techniques significantly improve the signal-to-noise ratio and the measurement consistency compared with the NUI method. In many engineering industries, the crack generally initiates from the surface of structures (e.g. rail, pipeline, pressure vessel and bearing), so that a linear backscatterer is often realisable and detectable. Notably, the pulse-echo phase NCI presented the enhanced detectability by extracting nonlinear phase information from weak scattering at the notch tip. Results from monitoring the crack growth with pulse-echo phase NCI suggest that the nonlinearities close to surface breaking area measured by $\tilde{\zeta}_{\varphi}$ increased until 40000 cycles and then decreased to detectable magnitude in opposite sign. Therefore, the pulse-echo NCI technique considered here is practically more widely applicable than NUI.

In addition, the pitch-catch fundamental and subharmonic NCI measurements using $\hat{\zeta}$ demonstrated that the forward scattered fields were able to monitor the crack growth as well and improve the selectivity at late stages (e.g. the signal-to-noise ratio at 100000 cycles is enhanced by a factor of 2 when the pitch-catch fundamental NCI and pulse echo amplitude NCI are compared in table 5.1). Note that the pitch-catch methods principally depend on the difference in absolute amplitude (the same basis used in NUI). The imaging results of the various types of NCI on the steel CT sample throughout its fatigue life suggest that this technique without the use of a measurable diffuse field potentially provides 3-18 times higher signal-to-noise performance over the NUI technique using the same instrumentation.

The improvement in the detectability of surface breaking crack (SBC) using pulse-echo amplitude NCI technique was further confirmed by examining the metric $\hat{\zeta}$on two aluminium specimens with fatigue cracks of different size at the back wall. The results demonstrated that the existence of strong linear backscatterers near the surface could allow the nonlinear responses from SBC in forms of phase and absolute amplitude to be measured. The nonlinear responses measured by $\hat{\zeta}$ are thought to arise from the combined effect of back and forward scattered nonlinear distortions. The consistent nonlinear phenomenon in phase was seen in results from both the steel CT specimen and the aluminium specimen subjected to three-point bending fatigue test. These preliminary studies conclude that the metric used in pulse-echo amplitude NCI, $\hat{\zeta}$ also rely on different part of the cracks and the SBCs are thought to be detectable by the pulse-echo NCI with a broad range of inspection angle. The advantages and the disadvantages are summarised in the table 6.1.

Method	Damage sensitivity	Advantages	Disadvantages
Pulse-echo amplitude NCI	Partially closed crack or closed crack	Highest SNR. Through depth imaging. Single-sided access.	Backscatterer required close to the target
Pulse-echo phase NCI	Partially closed crack or closed crack	Second highest SNR. Through depth imaging. Single-sided access.	Backscatterer required close to the target
Pitch-catch fundamental NCI	Partially closed or closed crack	Good SNR. Through depth imaging.	Double-sided access
Pitch-catch subharmonic NCI	Partially closed or closed crack	Through depth imaging.	Double-sided access
NUI	Partially closed or closed crack	Through depth imaging. Single-sided access.	Measurable diffuse field required. Lowest SNR and repeatability.

Table 6.1. Summary of a comparative study for nonlinear ultrasonic phased array techniques.

6.2 Future work

1) The optimisation methods described in Chapters 3 and 4 are suitable for integration with the corresponding nonlinear imaging approaches (NUI and NCI), thereby achieving an automated process from identification of the optimum parameters to visualisation of the area of interest. For example, prior to implementation of NUI technique on an unknown structure, the diffuse field prediction method using the metrics η_{area} and η_{phase} can first determine the optimum values of t_r and T by comparing their experimental results to the idealised diffuse state (15 % for η_{area} and 1 for η_{phase}) and identifying the convergence start point. This automated and adaptive process will greatly improve the efficiency and the simplicity of practical inspections across a broad range of structures without prior knowledge of these nonlinear imaging techniques.

2) As a consequence of promising NCI experimental results seen in Chapters 4 and 5, it is recommended to develop numerical methods (e.g. finite difference and finite element approaches), thereby better understanding the underlying physics behind those novel nonlinear phenomena. The next step would be to quantitatively relate the nonlinear metrics $\tilde{\zeta}$ and $\tilde{\zeta}_{\varphi}$ to microfeatures, roughness, corrosion and closure degrees of cracks by multiple experimental and numerical models, which must be designed carefully to provide specified characteristics of cracks. Ultimately, this research might contribute to the understanding of NCI results (in Chapters 5.1 and 5.2) with respect to different parts and types of cracks from different inspection angles (e.g. the detectable negative magnitude in $\tilde{\zeta}_{\varphi}$ seen in the cracked area far from the crack tip). This would facilitate the defect characterisation, thereby assessing the severity of nonlinear defects.

3) The nonlinear information contained in the forward scattered field warrants further exploration by developing multi-mode sequential and parallel focusing method using single array, thereby possibly improving its applicability and detectability. Notably, preliminary studies using pitch-catch subharmonic measurement investigated longitudinal-shear and longitudinal-longitudinal cases [Potter et al., 2016]. The results suggest that the scattered shear subharmonic field delivers larger amplitude than the scattered longitudinal subharmonic field. However, this ray-tracing technique, in conjunction with analysis of possible mode conversions (e.g. longitudinal-shear case) necessitate the prior knowledge of possible scatterer location and orientation.

4) It is worth exploring the applications of NCI in other fields (e.g. medical diagnosis). Notably, the microbubble contrast agent, as an efficient nonlinear backscatterer, is widely used to significantly enhance the visualisation and the quantification of tissue perfusion and vascularity. Its capability of measuring small amounts of slow-moving blood, usually in fast-moving tissue backgrounds, is significantly desirable in the clinical diagnosis of cancer and cardiovascular diseases. Previous works reported that considerable imaging errors that arose from the ultrasound propagation path between transducer and area of interest were existing in the medical imaging techniques (e.g. pulse inversion and amplitude modulation methods) [Tang and Eckersley, 2006]. Therefore, the NCI approach provides the potentials to improve the selectivity of targeted microbubbles by eliminating the interference with nonlinear medium including tissues and bubbles in post-processing. The improvement in the detectability of targeted microbubbles would enable more effective diagnosis of cardiovascular diseases and cancer. However, the application of NCI in vivo must be optimised in terms of frame rate and focal laws.

5) The classical nonlinearity (e.g. plastic deformation and creep) can be explored by pitch-catch NCI methods. Some preliminary studies were performed on a plastically deformed sample and a reference sample in undamaged condition as well as the same dimensions. A rectangular bar (in 360 mm × 50 mm × 21 mm) was subjected to a static load of 23 kN, whereby the 2 mm maximum plastic deformation was generated at the centre. Note that the spans of top and bottom loading pins (arranged symmetrically about the centre of the bar) were chosen as 94 mm and 250 mm respectively. Subsequently, the middle part in 110 mm long was cut from the sample (as shown in Figure 6.1) for the ultrasonic inspection. The NCI configuration used in the pitch-catch fundamental measurement was implemented in this study (as illustrated in Figure 6.1). The results in Figures 6.2(a-d) suggest that the standard focal law used in parallel and sequential focusing calculated by using the fixed wave velocity did not work on the plastically deformed samples due to non-uniform distribution of plasticity (i.e. unpredictable change in wave speed) in the four-point bend bar [Kim et al., 2015]. The change in wave speed can be confirmed by the discontinuities of through-transmission amplitude in x-direction (as presented in Figure 6.2(b)) because the change in elasticity (i.e. the difference between the nominal velocity and the actual one) significantly determines the data retrieval from time traces. The discontinued features can also be correlated to the residual stress profile (reconstructed from the measured displacement) estimated by [Kim et al., 2015]. Therefore, the NCI measurement of non-uniform plasticity necessitates calibration of

the focal law based upon prior knowledge of velocity distribution in the inspection area. The alternative solution might be longer transmission pulses (i.e. pulses with narrower transmission bandwidth) produced by a flexible array controller with arbitrary waveform generator. The realisation of NCI for the classical nonlinearity leads to a significant breakthrough in residual stress measurements, which could replace the impractical or destructive approaches (e.g. neutron diffraction and deep-hole drilling).

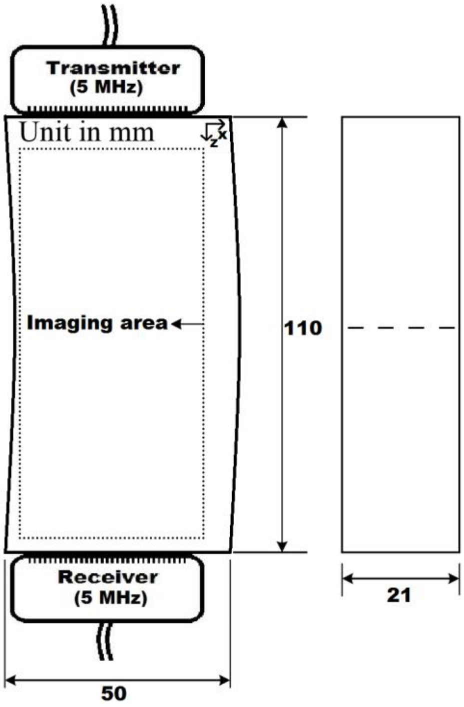

Figure 6.1. Schematic diagram of pitch-catch NCI measurement configuration on specimen subjected to four-point bending fatigue test (dimensions in mm).

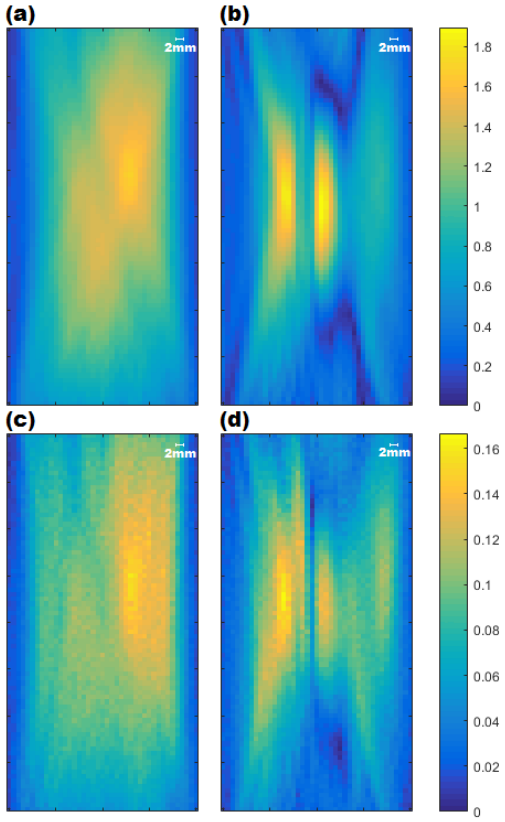

Figure 6.2. Linear sequential images in arbitrary units, of the same area (a) before deformation and (b) after deformation. Nonlinear images in nonlinear amplitude metric, ζ, of the same area (c) before deformation and (d) after deformation.

REFERENCES

Alston, J., Croxford, A., Potter, J. & Blanloeuil, P., 2018. Nonlinear non-collinear ultrasonic detection and characterisation of kissing bonds. *NDT & E International,* Volume 99, pp. 105-116.

Amura, M., Meo, M. & Amerini, F., 2011. Baseline-free estimation of residual fatigue life using a third order acoustic nonlinear parameter. *The Journal of the Acoustical Society of America,* Volume 130, pp. 1829-1837.

Angelsen, B. A. J. et al., 1995. Which transducer array is best?. *European Journal of Ultrasound,* Volume 2, pp. 151-164.

Baby, S. et al., 2008. Creep damage assessment in titanium alloy using a nonlinear ultrasonic technique. *Scripta Materialia,* Volume 59, pp. 818-821.

Bannouf, S., Robert, S., Casula, O. & Prada, C., 2013. *Data set reduction for ultrasonic TFM imaging using the effective aperture approach and virtual sources.* s.l., s.n., p. 012007.

Bateman, T., Mason, W. P. & McSkimin, H. J., 1961. Third-order elastic moduli of germanium. *Journal of Applied Physics,* Volume 32, pp. 928-936.

Becher, H. & Burns, P. N., 2012. *Handbook of contrast echocardiography: Left ventricular function and myocardial perfusion.* s.l.:Springer Science & Business Media.

Bermes, C., Kim, J.-Y., Qu, J. & Jacobs, L. J., 2007. Experimental characterization of material nonlinearity using Lamb waves. *Applied physics letters,* Volume 90, p. 021901.

Best, S. R., Croxford, A. J. & Neild, S. A., 2014. Pulse-echo harmonic generation measurements for non-destructive evaluation. *Journal of Nondestructive Evaluation,* Volume 33, pp. 205-215.

Blackshire, J. L., Sathish, S., Na, J. & Frouin, J., 2003. *Nonlinear laser ultrasonic measurements of localized fatigue damage.* s.l., s.n., pp. 1479-1488.

Blanloeuil, P. et al., 2016. Closed crack imaging using time reversal method based on fundamental and second harmonic scattering. *Wave Motion,* Volume 66, pp. 156-176.

Blum, F., Jarzynski, J. & Jacobs, L. J., 2005. A focused two-dimensional air-coupled ultrasonic array for non-contact generation. *NDT & E International,* Volume 38, pp. 634-642.

Breazeale, M. A. & Ford, J., 1965. Ultrasonic studies of the nonlinear behavior of solids. *Journal of Applied Physics,* Volume 36, pp. 3486-3490.

Breazeale, M. A. & Thompson, D. O., 1963. Finite-amplitude ultrasonic waves in aluminum. *Applied Physics Letters,* Volume 3, pp. 77-78.

Brock-Fisher, G. A., Poland, M. D. & Rafter, P. G., 1996. *Means for increasing sensitivity in non-linear ultrasound imaging systems.* s.l.:Google Patents.

Brotherhood, C. J., Drinkwater, B. W. & Dixon, S., 2003. The detectability of kissing bonds in adhesive joints using ultrasonic techniques. *Ultrasonics,* Volume 41, pp. 521-529.

Cantrell, J. H., 2003. Fundamentals and applications of nonlinear ultrasonic nondestructive evaluation. In: *Ultrasonic nondestructive evaluation.* s.l.:CRC Press, pp. 377-448.

Cantrell, J. H., 2004. *Substructural organization, dislocation plasticity and harmonic generation in cyclically stressed wavy slip metals.* s.l., s.n., pp. 757-780.

Cantrell, J. H. & Yost, W. T., 1994. Acoustic harmonic generation from fatigue-induced dislocation dipoles. *Philosophical magazine A,* Volume 69, pp. 315-326.

Cantrell, J. H. & Yost, W. T., 2001. Nonlinear ultrasonic characterization of fatigue microstructures. *International Journal of fatigue,* Volume 23, pp. 487-490.

Chen, Z. et al., 2014. Mixing of collinear plane wave pulses in elastic solids with quadratic nonlinearity. *The Journal of the Acoustical Society of America,* Volume 136, pp. 2389-2404.

Cosgrove, D. & Lassau, N., 2010. Imaging of perfusion using ultrasound. *European journal of nuclear medicine and molecular imaging,* Volume 37, pp. 65-85.

Courtney, C. R. P., Drinkwater, B. W., Neild, S. A. & Wilcox, P. D., 2008. Factors affecting the ultrasonic intermodulation crack detection technique using bispectral analysis. *NDT & E International,* Volume 41, pp. 223-234.

Croxford, A. J., Wilcox, P. D., Drinkwater, B. W. & Nagy, P. B., 2009. The use of non-collinear mixing for nonlinear ultrasonic detection of plasticity and fatigue. *The Journal of the Acoustical Society of America,* Volume 126, pp. EL117--EL122.

Demčenko, A., Akkerman, R., Nagy, P. B. & Loendersloot, R., 2012. Non-collinear wave mixing for non-linear ultrasonic detection of physical ageing in PVC. *NDT & E International,* Volume 49, pp. 34-39.

Deng, M. & Pei, J., 2007. Assessment of accumulated fatigue damage in solid plates using nonlinear Lamb wave approach. *Applied physics letters,* Volume 90, p. 121902.

Eckersley, R. J., Chin, C. T. & Burns, P. N., 2005. Optimising phase and amplitude modulation schemes for imaging microbubble contrast agents at low acoustic power. *Ultrasound in medicine \& biology,* Volume 31, pp. 213-219.

Evans, M. J. & Cawley, P., 1999. Measurement and prediction of diffuse fields in structures. *The Journal of the Acoustical Society of America,* Volume 106, pp. 3348-3361.

Felice, M. V., Velichko, A. & Wilcox, P. D., 2014. Accurate depth measurement of small surface-breaking cracks using an ultrasonic array post-processing technique. *NDT & E International,* Volume 68, pp. 105-112.

Fierro, G. P. M. & Meo, M., 2015. Residual fatigue life estimation using a nonlinear ultrasound modulation method. *Smart Materials and Structures,* Volume 24, p. 025040.

Gedroits, A. & Krasilnikov, V., 1963. Finite-amplitude elastic waves in solids and deviations from Hooke's law. *Soviet Phys. JETP,* Volume 16, pp. 1122-1126.

Granato, A. v. & Lücke, K., 1956. Theory of mechanical damping due to dislocations. *Journal of applied physics,* Volume 27, pp. 583-593.

Haupert, S., Renaud, G. & Schumm, A., 2017. Ultrasonic imaging of nonlinear scatterers buried in a medium. *NDT & E International,* Volume 87, pp. 1-6.

Hodgson, M., 1996. When is diffuse-field theory applicable?. *Applied Acoustics,* Volume 49, pp. 197-207.

Holmes, C., Drinkwater, B. W. & Wilcox, P. D., 2005. Post-processing of the full matrix of ultrasonic transmit--receive array data for non-destructive evaluation. *NDT & E International,* Volume 38, pp. 701-711.

Horinouchi, S. et al., 2012. Evaluation of closed stress corrosion cracks in Ni-based alloy weld metal using subharmonic phased array. *Japanese Journal of Applied Physics,* Volume 51, p. 07GB15.

Hughes, D. S. & Kelly, J. L., 1953. Second-order elastic deformation of solids. *Physical review,* Volume 92, p. 1145.

Hurley, D. C. & Fortunko, C. M., 1997. Determination of the nonlinear ultrasonic parameter using a Michelson interferometer. *Measurement Science and Technology,* Volume 8, p. 634.

Ikeuchi, M., Jinno, K., Ohara, Y. & Yamanaka, K., 2013. Improvement of closed crack selectivity in nonlinear ultrasonic imaging using fundamental wave amplitude difference. *Japanese Journal of Applied Physics,* Volume 52, p. 07HC08.

Jeong, H., Cho, S., Zhang, S. & Li, X., 2018. Acoustic nonlinearity parameter measurements in a pulse-echo setup with the stress-free reflection boundary. *The Journal of the Acoustical Society of America,* Volume 143, pp. EL237--EL242.

Jiao, J., Lv, H., He, C. & Wu, B., 2017. Fatigue crack evaluation using the non-collinear wave mixing technique. *Smart Materials and Structures,* Volume 26, p. 065005.

Jiao, J. P., Drinkwater, B. W., Neild, S. A. & Wilcox, P. D., 2009. Low-frequency vibration modulation of guided waves to image nonlinear scatterers for structural health monitoring. *Smart Materials and structures,* Volume 18, p. 065006.

Johnson, G. C., 1981. Acoustoelastic theory for elastic--plastic materials. *The Journal of the Acoustical Society of America,* Volume 70, pp. 591-595.

Kim, H. K., Coules, H. E., Pavier, M. J. & Shterenlikht, A., 2015. Measurement of highly non-uniform residual stress fields with reduced plastic error. *Experimental Mechanics,* Volume 55, pp. 1211-1224.

Kim, J.-Y., Jacobs, L. J., Qu, J. & Littles, J. W., 2006. Experimental characterization of fatigue damage in a nickel-base superalloy using nonlinear ultrasonic waves. *The Journal of the Acoustical Society of America,* Volume 120, pp. 1266-1273.

Korobov, A. I., Izosimova, M. Y. & Odina, N. I., 2015. Diagnostics of metal plates with residual stresses and defects by nonlinear scanning laser vibrometry. *Acoustical Physics,* Volume 61, pp. 293-300.

Korshak, B. A., Solodov, I. Y. & Ballad, E. M., 2002. DC effects, sub-harmonics, stochasticity and “memory” for contact acoustic non-linearity. *Ultrasonics,* Volume 40, pp. 707-713.

Lambert, J. et al., 2012. *Performance evaluation of total focusing method on GPP and GPU.* s.l., s.n., pp. 1-8.

Landau, L. D. & Lifshitz, E. M., 1986. Theory of Elasticity, vol. 7. *Course of Theoretical Physics*, Volume 3, p. 109.

Liaptsis, D., 2008. *The ultrasonic detectability and sizing of rough partially closed cracks in real structures / Dimosthenis Liaptsis..* s.l.:s.n.

Lim, H. J. & Sohn, H., 2015. Fatigue crack detection using structural nonlinearity reflected on linear ultrasonic features. *Journal of Applied Physics*, Volume 118, p. 244902.

Lim, H. J., Song, B., Park, B. & Sohn, H., 2015. Noncontact fatigue crack visualization using nonlinear ultrasonic modulation. *NDT & E International*, Volume 73, pp. 8-14.

Liu, S., Croxford, A. J., Neild, S. A. & Zhou, Z., 2011. Effects of experimental variables on the nonlinear harmonic generation technique. *IEEE transactions on ultrasonics, ferroelectrics, and frequency control,* Volume 58.

Macovski, A., 1979. Ultrasonic imaging using arrays. *Proceedings of the IEEE,* Volume 67, pp. 484-495.

Matlack, K. H., Kim, J.-Y., Jacobs, L. J. & Qu, J., 2015. Review of second harmonic generation measurement techniques for material state determination in metals. *Journal of Nondestructive Evaluation,* Volume 34, p. 273.

Meo, M., Polimeno, U. & Zumpano, G., 2008. Detecting damage in composite material using nonlinear elastic wave spectroscopy methods. *Applied composite materials,* Volume 15, pp. 115-126.

Meo, M. & Zumpano, G., 2005. Nonlinear elastic wave spectroscopy identification of impact damage on a sandwich plate. *Composite structures,* Volume 71, pp. 469-474.

Meziane, A., Norris, A. N. & Shuvalov, A. L., 2011. Nonlinear shear wave interaction at a frictional interface: Energy dissipation and generation of harmonics. *The Journal of the Acoustical Society of America,* Volume 130, pp. 1820-1828.

Moussatov, A., Gusev, V. & Castagnede, B., 2003. Self-induced hysteresis for nonlinear acoustic waves in cracked material. *Physical review letters,* Volume 90, p. 124301.

Mullen, R. & Belytschko, T., 1982. Dispersion analysis of finite element semidiscretizations of the two-dimensional wave equation. *International Journal for Numerical Methods in Engineering,* Volume 18, pp. 11-29.

Murnaghan, F. D., 1937. Finite deformations of an elastic solid. *American Journal of Mathematics,* Volume 59, pp. 235-260.

Nagy, P. B., 1998. Fatigue damage assessment by nonlinear ultrasonic materials characterization. *Ultrasonics,* Volume 36, pp. 375-381.

Njiki, M. et al., 2013. *A real-time implementation of the total focusing method for rapid and precise diagnostic in non destructive evaluation.* s.l., s.n., pp. 245-248.

Ohara, Y. et al., 2010. *Monitoring growth of closed fatigue crack using subharmonic phased array.* s.l., s.n., pp. 903-909.

Ohara, Y., Endo, H., Mihara, T. & Yamanaka, K., 2009. Ultrasonic measurement of closed stress corrosion crack depth using subharmonic phased array. *Japanese Journal of Applied Physics,* Volume 48, p. 07GD01.

Ohara, Y. et al., 2011. Nonlinear ultrasonic imaging method for closed cracks using subtraction of responses at different external loads. *Ultrasonics,* Volume 51, pp. 661-666.

Ohara, Y. et al., 2007. Imaging of closed cracks using nonlinear response of elastic waves at subharmonic frequency. *Applied Physics Letters,* Volume 90, p. 011902.

Ohara, Y., Mihara, T. & Yamanaka, K., 2006. Effect of adhesion force between crack planes on subharmonic and DC responses in nonlinear ultrasound. *Ultrasonics,* Volume 44, pp. 194-199.

Ohara, Y. et al., 2010. *Ultrasonic imaging of stress corrosion crack formed in high temperature pressurized water using subharmonic phased array.* s.l., s.n., p. 045007.

Ohara, Y. et al., 2017. High-selectivity imaging of closed cracks in a coarse-grained stainless steel by nonlinear ultrasonic phased array. *NDT & E International,* Volume 91, pp. 139-147.

Papazian, J. M. et al., 2007. Sensors for monitoring early stage fatigue cracking. *International journal of fatigue,* Volume 29, pp. 1668-1680.

Park, C.-S., Kim, J.-W., Cho, S. & Seo, D.-c., 2016. A high resolution approach for nonlinear sub-harmonic imaging. *NDT & E International,* Volume 79, pp. 114-122.

Peng, C., Bai, L., Zhang, J. & Drinkwater, B. W., 2018. The sizing of small surface-breaking fatigue cracks using ultrasonic arrays. *NDT & E International,* Volume 99, pp. 64-71.

Potter, J. & Croxford, A. J., 2018. Characterization of Nonlinear Ultrasonic Diffuse Energy Imaging. *IEEE transactions on ultrasonics, ferroelectrics, and frequency control,* Volume 65, pp. 870-880.

Potter, J. N., Croxford, A. J. & Wilcox, P. D., 2014. Nonlinear ultrasonic phased array imaging. *Physical review letters,* Volume 113, p. 144301.

Pruell, C., Kim, J.-Y., Qu, J. & Jacobs, L. J., 2009. Evaluation of fatigue damage using nonlinear guided waves. *Smart Materials and Structures,* Volume 18, p. 035003.

Sasaki, R. et al., 2005. Simulation and analysis of subharmonics and tail effect for ultrasonic nondestructive evaluation of closed cracks. *Japanese journal of applied physics,* Volume 44, p. 4389.

Sboros, V. & Tang, M. X., 2010. The assessment of microvascular flow and tissue perfusion using ultrasound imaging. *Proceedings of the Institution of Mechanical Engineers, Part H: Journal of Engineering in Medicine,* Volume 224, pp. 273-290.

Shull, D. J., Kim, E. E., Hamilton, M. F. & Zabolotskaya, E. A., 1995. Diffraction effects in nonlinear Rayleigh wave beams. *The Journal of the Acoustical Society of America,* Volume 97, pp. 2126-2137.

Simpson, D. H., Chin, C. T. & Burns, P. N., 1999. Pulse inversion Doppler: a new method for detecting nonlinear echoes from microbubble contrast agents. *IEEE transactions on ultrasonics, ferroelectrics, and frequency control,* Volume 46, pp. 372-382.

Solodov, I., Wackerl, J., Pfleiderer, K. & Busse, G., 2004. Nonlinear self-modulation and subharmonic acoustic spectroscopyfor damage detection and location. *Applied physics letters,* Volume 84, pp. 5386-5388.

Solodov, I. Y., 1998. Ultrasonics of non-linear contacts: propagation, reflection and NDE-applications. *Ultrasonics,* Volume 36, pp. 383-390.

Solodov, I. Y. & Korshak, B. A., 2001. Instability, chaos, and “memory” in acoustic-wave--crack interaction. *Physical review letters,* Volume 88, p. 014303.

Solodov, I. Y., Krohn, N. & Busse, G., 2002. CAN: an example of nonclassical acoustic nonlinearity in solids. *Ultrasonics,* Volume 40, pp. 621-625.

Standard, A. S. T. M., n.d. *E647-05, 2006,“Standard Test Method for Measurement of Fatigue Crack Growth Rates”, ASTM International, West Conshohocken, PA.* s.l.:s.n.

Sun, L., Kulkarni, S. S., Achenbach, J. D. & Krishnaswamy, S., 2006. Technique to minimize couplant-effect in acoustic nonlinearity measurements. *The Journal of the Acoustical Society of America,* Volume 120, pp. 2500-2505.

Suzuki, T., Hikata, A. & Elbaum, C., 1964. Anharmonicity due to glide motion of dislocations. *Journal of Applied Physics,* Volume 35, pp. 2761-2766.

Su, Z. et al., 2014. Acousto-ultrasonics-based fatigue damage characterization: Linear versus nonlinear signal features. *Mechanical Systems and Signal Processing,* Volume 45, pp. 225-239.

Tang, M.-X. & Eckersley, R. J., 2006. Nonlinear propagation of ultrasound through microbubble contrast agents and implications for imaging. *IEEE transactions on ultrasonics, ferroelectrics, and frequency control,* Volume 53.

Taylor, L. H. & Rollins Jr, F. R., 1964. Ultrasonic study of three-phonon interactions. I. Theory. *Physical Review,* Volume 136, p. A591.

Thomas, R., Drinkwater, B. W. & Liaptsis, D., 2005. The reflection of ultrasound from partially contacting rough surfaces. *The Journal of the Acoustical Society of America,* Volume 117, pp. 638-645.

Thompson, R. B. & Tiersten, H. F., 1977. Harmonic generation of longitudinal elastic waves. *The Journal of the Acoustical Society of America,* Volume 62, pp. 33-37.

Toupin, R. A. & Bernstein, B., 1961. Sound waves in deformed perfectly elastic materials. Acoustoelastic effect. *The Journal of the Acoustical Society of America,* Volume 33, pp. 216-225.

Tsuda, H., Lee, J.-R. & Guan, Y., 2006. Fatigue crack propagation monitoring of stainless steel using fiber Bragg grating ultrasound sensors. *Smart materials and structures,* Volume 15, p. 1429.

Uenishi, K., 2017. Rupture, waves and earthquakes. *Proceedings of the Japan Academy, Series B,* Volume 93, pp. 28-49.

Ulrich, T. J., Johnson, P. A. & Guyer, R. A., 2007. Interaction dynamics of elastic waves with a complex nonlinear scatterer through the use of a time reversal mirror. *Physical review letters,* Volume 98, p. 104301.

Van Den Abeele, K. E.-A., Johnson, P. A. & Sutin, A., 2000. Nonlinear elastic wave spectroscopy (NEWS) techniques to discern material damage, part I: nonlinear wave modulation spectroscopy (NWMS). *Journal of Research in Nondestructive Evaluation,* Volume 12, pp. 17-30.

Weaver, R. L., 1985. Diffuse elastic waves at a free surface. *The Journal of the Acoustical Society of America,* Volume 78, pp. 131-136.

Wells, P. N. T., 1992. Ultrasonics: a window into biomedical science. *Ultrasonics,* Volume 30, pp. 3-7.

Wilson, S. R. & Burns, P. N., 2010. Microbubble-enhanced US in body imaging: what role?. *Radiology,* Volume 257, pp. 24-39.

Yamanaka, K., Mihara, T. & Tsuji, T., 2004. Evaluation of closed cracks by model analysis of subharmonic ultrasound. *Japanese journal of applied physics,* Volume 43, p. 3082.

Yan, Z. & Nagy, P. B., 2000. Thermo-optical modulation for improved ultrasonic fatigue crack detection in Ti--6Al--4V. *NDT & E International,* Volume 33, pp. 213-223.

Yost, W. T. & Breazeale, M. A., 1974. Ultrasonic nonlinearity parameters and third-order elastic constants of germanium between 300 and 77° K. *Physical Review B,* Volume 9, p. 510.

Zener, C., 1948. *Elasticity and anelasticity of metals.* s.l.:University of Chicago press.

Zhang, J., Drinkwater, B. W. & Wilcox, P. D., 2011. Effects of array transducer inconsistencies on total focusing method imaging performance. *NDT & E International,* Volume 44, pp. 361-368.

Zhang, J., Drinkwater, B. W., Wilcox, P. D. & Hunter, A. J., 2010. Defect detection using ultrasonic arrays: The multi-mode total focusing method. *NDT & E International,* Volume 43, pp. 123-133.

Zhang, J., Xuan, F.-z. & Xiang, Y., 2013. Dislocation characterization in cold rolled stainless steel using nonlinear ultrasonic techniques: A comprehensive model. *EPL (Europhysics Letters)*, Volume 103, p. 68003.

APPENDIX A

CAD drawing regarding the geometry of the compact tension (CT) specimens, made of mild steel used in chapters 2, 3, 4 and 5:

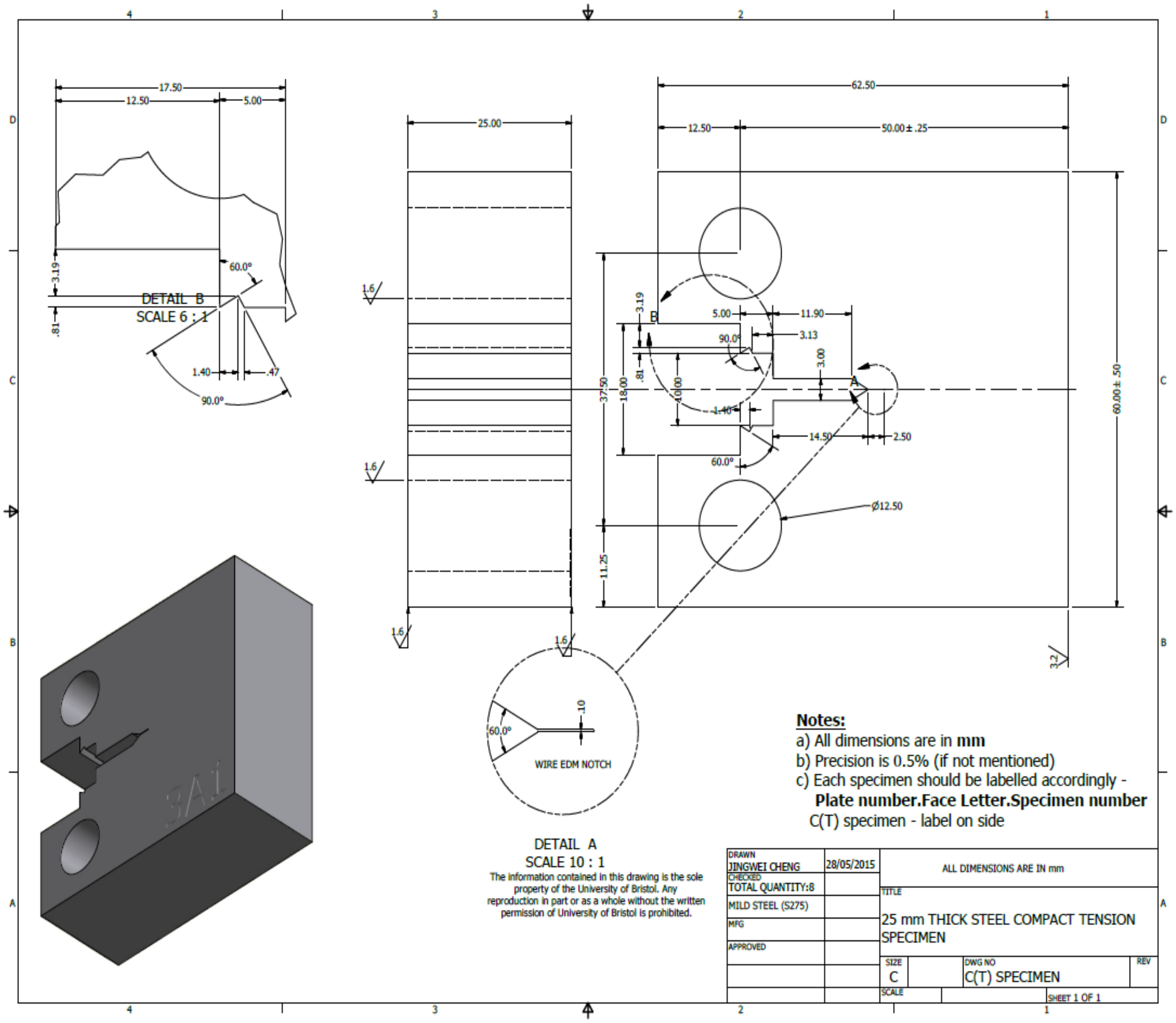

The information contained in this drawing is the sole property of the University of Bristol. Any reproduction in part or as a whole without the written permission of University of Bristol is prohibited.

Notes:

a) All dimensions are in **mm**

b) Precision is 0.5% (if not mentioned)

c) Each specimen should be labelled accordingly -
Plate number.Face Letter.Specimen number
C(T) specimen - label on side

DRAWN
JINGWEI CHENG
28/05/2015
CHECKED
TOTAL QUANTITY:8
MILD STEEL (S275)
MFG
APPROVED
ALL DIMENSIONS ARE IN mm
TITLE
25 mm THICK STEEL COMPACT TENSION SPECIMEN
SIZE
C
DWG NO
C(T) SPECIMEN
REV
SCALE
SHEET 1 OF 1

Figure A.1. The geometry of CT specimen.

The micrographs for the fatigue crack grown in the compact tension (CT) specimen from 10000 cycles to 100000 cycles in Section 5.2:

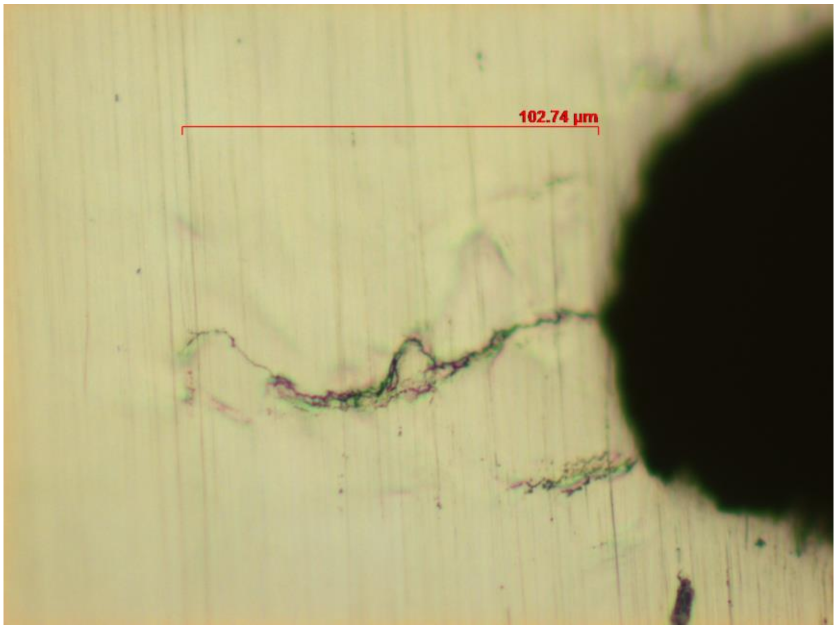

Figure A.2. Micrograph of the fatigue crack at 10000 cycles of 0.1 mm.

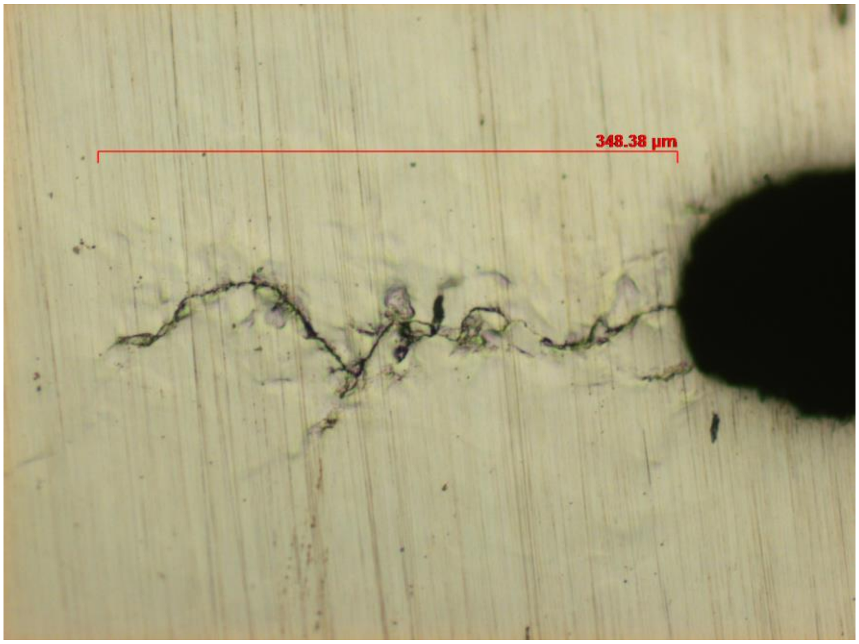

Figure A.3. Micrograph of the fatigue crack at 20000 cycles of 0.35 mm.

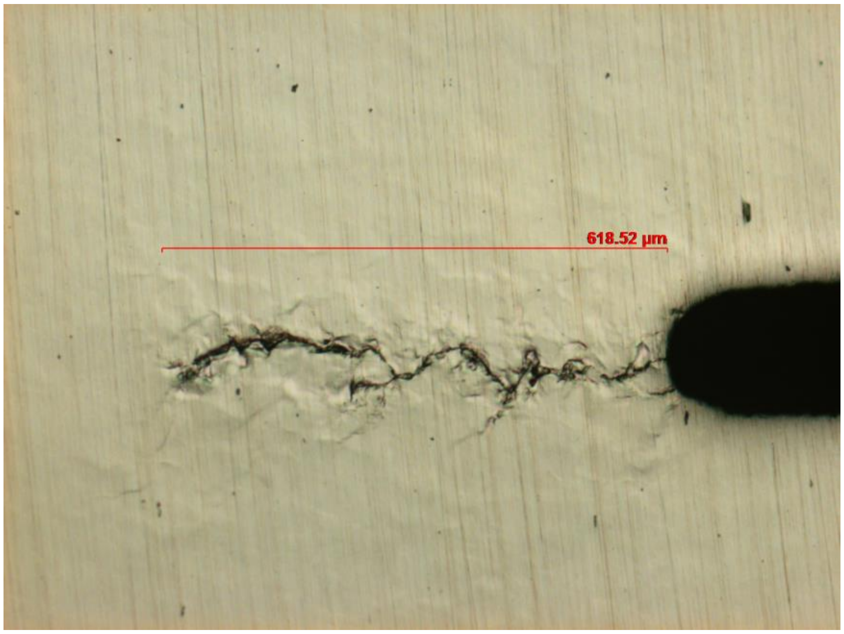

Figure A.4. Micrograph of the fatigue crack at 30000 cycles of 0.62 mm.

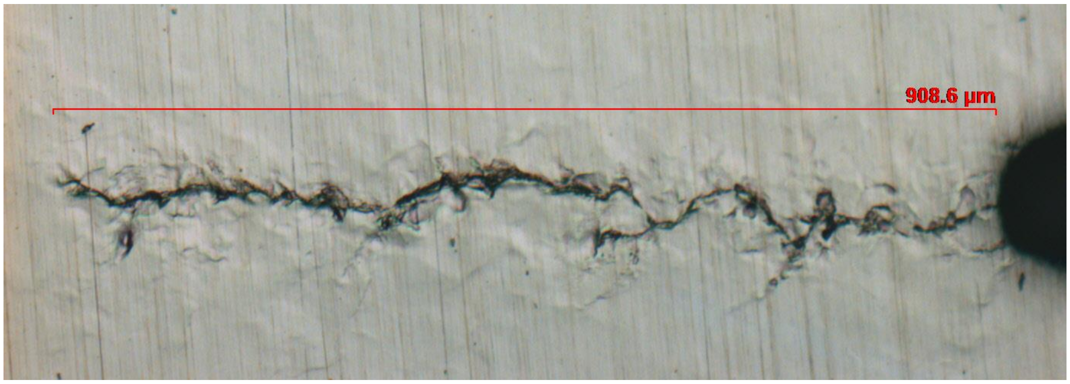

Figure A.5. Micrograph of the fatigue crack at 40000 cycles of 0.91 mm.

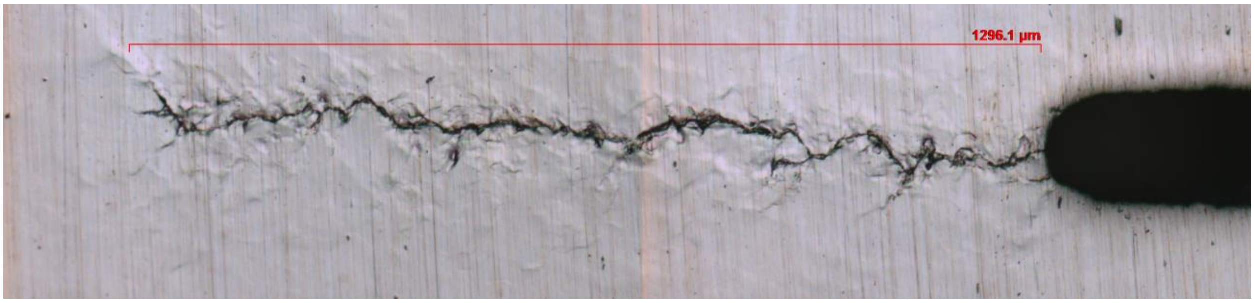

Figure A.6. Micrograph of the fatigue crack at 50000 cycles of 1.3 mm.

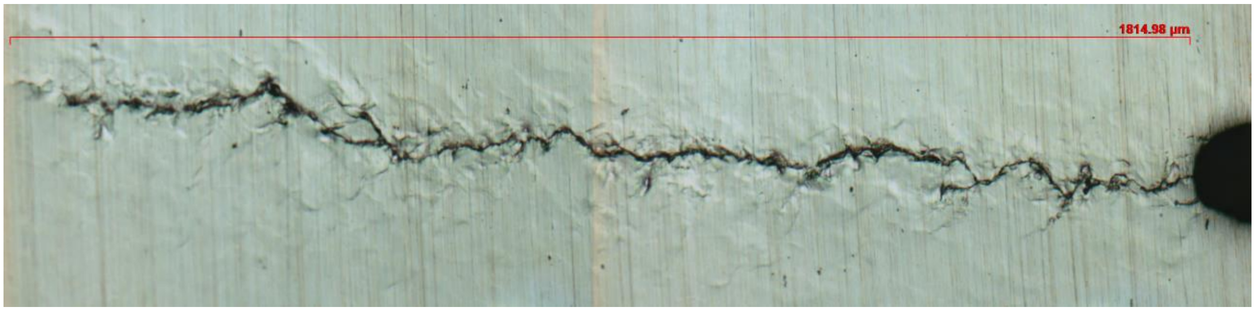

Figure A.7. Micrograph of the fatigue crack at 60000 cycles of 1.8 mm.

Figure A.8. Micrograph of the fatigue crack at 70000 cycles of 2.26 mm.

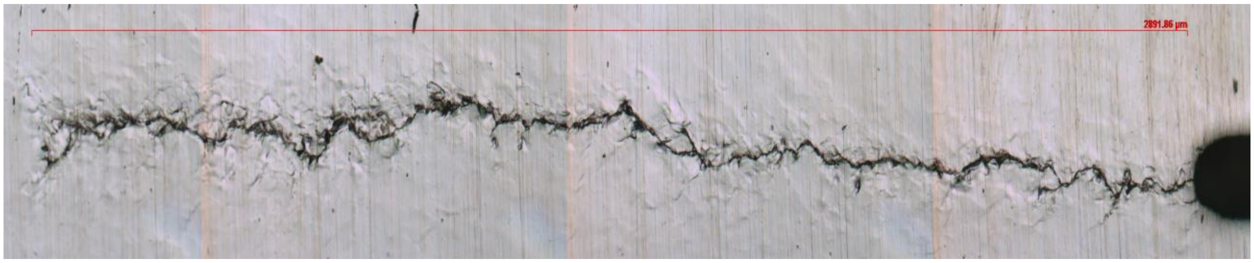

Figure A.9. Micrograph of the fatigue crack at 80000 cycles of 2.89 mm.

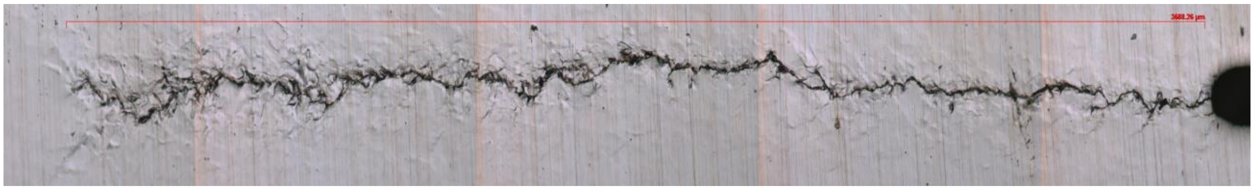

Figure A.10. Micrograph of the fatigue crack at 90000 cycles of 3.69 mm.

Figure A.11. Micrograph of the fatigue crack at 100000 cycles of 4.82 mm.

The nonlinear ultrasonic diffuse energy imaging (NUI) results for the fatigue crack grown in the compact tension (CT) specimen from 10000 cycles to 100000 cycles in Section 5.2:

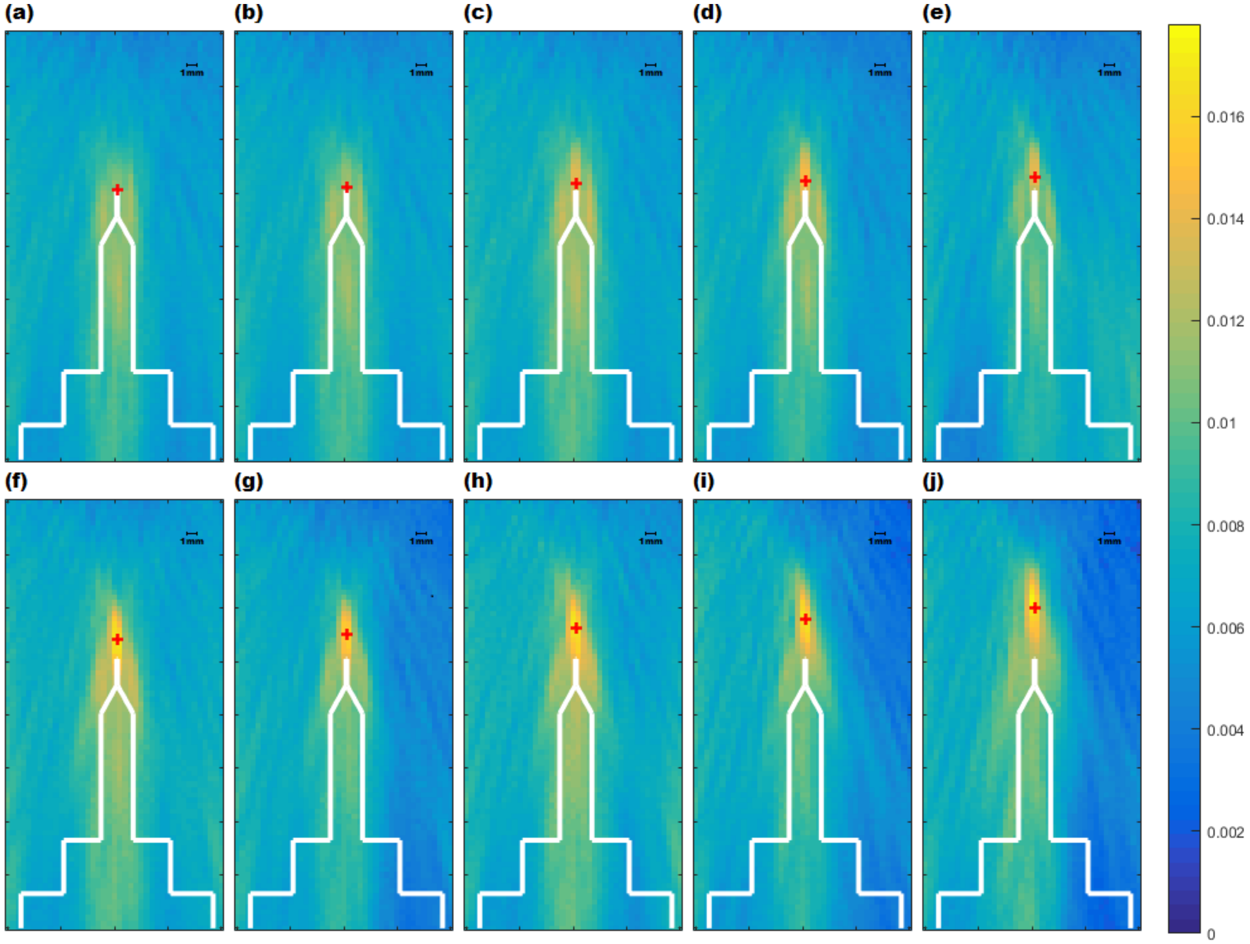

Figure A.12. Nonlinear images in nonlinear diffuse energy metric, γ at (a) 10000 cycles, (b) 20000 cycles, (c) 30000 cycles, (d) 40000 cycles, (e) 50000 cycles, (f) 60000 cycles, (g) 70000 cycles, (h) 80000 cycles, (i) 90000 cycles and (j) 100000 cycles. The inspection configuration is as illustrated in figure 4.1(a) and the red cross marks the micrographically measured crack tip.

APPENDIX B

The works presented in this thesis has been transferred to the following publications till now:

Cheng, J., Potter, J. N., Croxford, A. J. & Drinkwater, B. W., 2017. Monitoring fatigue crack growth using nonlinear ultrasonic phased array imaging. *Smart Materials and Structures,* Volume 26, p. 055006.

Cheng, J., Potter, J. N. & Drinkwater, B. W., 2018. The parallel-sequential field subtraction technique for coherent nonlinear ultrasonic imaging. *Smart Materials and Structures,* Volume 27, p. 065002.

Cheng, J., Potter, J. N. & Drinkwater, B. W., 2018. *The parallel-sequential field subtraction techniques for nonlinear ultrasonic imaging.* s.l., s.n., p. 070001.

Croxford, A. J., Cheng, J. & Potter, J. N., 2016. *Nonlinear phased array imaging.* s.l., s.n., p. 98052B.

Potter, J., Chen, J., Drinkwater, B. & Croxford, A., 2016. Ultrasonic array imaging of contact-acoustic nonlinearity. *The Journal of the Acoustical Society of America,* Volume 140, pp. 3325-3325.